



University  
of Glasgow

Dobson, Katherine Joanna (2006) *The zircon (U-Th)/He thermochronometer: development and application of thermochronometers in igneous provinces.*

PhD thesis

<http://theses.gla.ac.uk/4460/>

Copyright and moral rights for this thesis are retained by the author

A copy can be downloaded for personal non-commercial research or study, without prior permission or charge

This thesis cannot be reproduced or quoted extensively from without first obtaining permission in writing from the Author

The content must not be changed in any way or sold commercially in any format or medium without the formal permission of the Author

When referring to this work, full bibliographic details including the author, title, awarding institution and date of the thesis must be given

**The zircon (U-Th)/He thermochronometer:  
development and application of  
thermochronometers in igneous provinces**

**Katherine Joanna Dobson  
B.Sc. (Hons.), Durham**

**Thesis presented for the degree of Doctor of Philosophy (Ph.D.)**

**University of Glasgow**

**Department of Geographical & Earth Sciences**

**September 2006**

**© Katherine J. Dobson, 2006**

# **Dedication**

**in memory of my grandfather**

**Frederick John Dobson**

## Abstract

The zircon (U-Th)/He thermochronometer has a closure temperature of approximately 200°C [Reiners, 2005], and bridges the gap between the Ar-Ar and apatite fission track thermochronometers. This chronometer therefore has a wide range of potential applications, and will enable the recognition of cooling events beyond the resolution of existing techniques. However, zircon thermochronometry remains poorly utilised because of challenging analytical protocols, compounded by overly simplistic interpretive procedures. This study presents an improved routine methodology for the determination of zircon (U-Th)/He ages, and a more rigorous approach to the interpretation of (U-Th)/He age data.

Zircons commonly exhibit strong and variable zonation of U and Th. Crystals used for (U-Th)/He require correction for helium loss by  $\alpha$ -recoil, a correction that is based on the assumption that all crystals have homogeneous U and Th distributions. This assumption can introduce significant age bias into the  $\alpha$ -recoil corrected age in zoned crystals, and lead to poor age reproducibility. Characterisation of U and Th zonation in zircon is therefore essential for accurate  $\alpha$ -recoil correction, and to prevent over-dispersion of the data. The uncertainties for unknown zircon (U-Th)/He ages are currently calculated from the age reproducibility of the Fish Canyon Tuff zircon standard. Detailed characterisation of U and Th zonation the Fish Canyon Tuff zircon using Cathodoluminescence and Secondary Ion Mass Spectrometry shows that the poor age reproducibility ( $\pm 9.1 - 17.8 \%$ ,  $2\sigma$ ) is entirely consistent with the strong, variable and complex U and Th zonation observed within the crystal population. The Fish Canyon Tuff is a age standard for determining the quality of analytical procedures, and its use will limit the temporal resolution of the zircon (U-Th)/He technique.

This study presents a detailed consideration of the effects of geometry, U- and Th-zonation and diffusion on zircon (U-Th)/He ages. The errors introduced by assuming homogeneity are quantified, and the difficulties associated with the characterisation of U and Th zonation in zircon samples are addressed in a qualitative and quantitative assessment. When these issues are fully considered, the (U-Th)/He age distribution of unknown samples can be understood, and (U-Th)/He ages can be interpreted with confidence. Using these more rigorous interpretive techniques, it has

been possible to accurately determine the (U-Th)/He ages of zircons from the Palaeogene Hebridean Igneous Province. This data has been used in conjunction with apatite thermochronometry (fission track and (U-Th)/He) to constrain the low temperature cooling history of the region.

Many igneous provinces are deeply eroded, and large volumes of the volcanic products have been removed. The early Palaeogene Hebridean Igneous Province is a type example of such a province, and the volume of former volcanic products, the timing and the rate of cooling and exhumation are poorly constrained. In the Hebridean Igneous Province this denudation has removed much of the basaltic lava pile and has exposed the plutonic complexes emplaced at its base. This thermochronological investigation of these plutonic sequences shows that the initial cooling was very rapid. This is consistent with field evidence for shallow level emplacement, accompanied by extensive hydrothermal activity and syn-, and post-intrusive denudation. The new data from the zircon (U-Th)/He, apatite fission track, and apatite (U-Th)/He thermochronometers identifies a previously unresolved pulse of magmatic activity that occurred at approximately 47 Ma, significantly after the initiation of rifting, and the cessation of voluminous shallow level intrusion in the Hebridean Igneous Province. The timing of a short-lived low temperature event observed in the plutonic units on the islands of Rum (80 - 90°C peak temperature), and Skye (120 - 180°C peak temperature), correlates with a cooling episode of more than 200°C at the St Kilda Central Complex, 100 km further to the west. These post-rifting cooling events corroborate published radiometric ages from small volume intrusions elsewhere on the UK continental margin, and voluminous basaltic volcanism in the Rockall Trough. The magmatic event recognised in the onshore plutonic units has important local and regional implications for the volume of post-rift magmatic activity in the North Atlantic, and identifies a potentially unconsidered component to LIP magmatism. The identification of these low temperature events can only be achieved through the application of high resolution low temperature thermochronology.

# Table of contents

<b>Dedication</b> .....	<b>i</b>
<b>Abstract</b> .....	<b>ii</b>
<b>Table of contents</b> .....	<b>iv</b>
<b>List of figures</b> .....	<b>xi</b>
<b>List of tables</b> .....	<b>xv</b>
<b>List of abbreviations</b> .....	<b>xvii</b>
<b>Acknowledgements</b> .....	<b>xviii</b>
<b>Declaration</b> .....	<b>xx</b>
<b>Chapter 1 : Introduction</b> .....	<b>1</b>
<b>Chapter 2 : The principles of thermochronology</b> .....	<b>5</b>
2.1 Introduction .....	5
2.2 Apatite fission track thermochronology.....	7
2.2.1 Fission track formation.....	7
2.2.2 Fission track annealing .....	7
2.2.3 The determination of apatite fission track ages .....	9
2.2.4 Zeta calibration .....	10
2.2.4.1 Annealing and AFT ages.....	10
2.2.5 Fission track length distributions.....	11
2.2.5.1 Cf irradiation .....	12
2.3 Zircon fission track thermochronology .....	12
2.3.1 Zircon fission track annealing .....	13
2.3.2 The accumulation of radiation damage in zircon .....	14
2.3.2.1 Fission fragments .....	14
2.3.2.2 Recoil of heavy nuclides .....	14
2.3.2.3 Recoil of $\alpha$ -particles .....	15
2.3.3 Annealing and radiation damage .....	15
2.3.3.1 Radiation damage and etching response .....	16
2.4 Apatite (U-Th)/He thermochronology.....	17
2.4.1 Helium production .....	17
2.4.2 Helium diffusion in apatite.....	19

2.4.3 Alpha particle ejection ( $\alpha$ -recoil) .....	21
2.4.3.1 Alpha implantation.....	24
2.4.4 Modelling diffusion and ejection .....	25
2.4.5 Zonation .....	26
2.4.5.1 Zonation in mineral standards.....	26
2.5 Zircon (U-Th)/He thermochronology .....	27
2.5.1 Helium diffusion in zircon.....	27
2.5.2 Radiation damage.....	29
2.5.3 Alpha particle ejection ( $\alpha$ -recoil) .....	30
2.5.4 U and Th zonation in zircon .....	30
2.5.5 Mineral standards .....	30
2.6 Summary.....	31
<b>Chapter 3 : Analytical techniques .....</b>	<b>32</b>
3.1 Introduction .....	32
3.2 Mineral separation.....	32
3.3 Sample characterisation .....	33
3.4 Apatite fission track analytical procedures.....	33
3.5 Apatite (U-Th)/He analytical procedure.....	34
3.5.1 Crystal selection and encapsulation .....	34
3.5.2 Furnace extraction and He analysis .....	36
3.5.3 Laser extraction and He analysis .....	37
3.5.4 U and Th analysis .....	37
3.5.5 Reproducibility of the Durango apatite standard .....	38
3.6 Zircon (U-Th)/He analytical procedures.....	38
3.6.1 Crystal selection .....	38
3.6.1.1 The impact of inclusions on zircon (U-Th)/He ages .....	39
3.6.2 Aliquot preparation.....	40
3.6.3 He extraction.....	40
3.6.4 Existing methodologies for U and Th recovery.....	41
3.6.4.1 Flux Melting .....	41
3.6.4.2 Acid Digestion .....	42
3.6.5 A routine methodology for U and Th recovery.....	42
3.6.5.1 Zircon dissolution .....	42
3.6.5.2 U-Th purification and ICP-MS analysis .....	43
3.6.5.3 The U and Th blank.....	44
3.6.5.4 U and Th uptake into the sample solution.....	44
3.6.6 The (U-Th)/He age of the Fish Canyon Tuff zircon .....	45
3.6.6.1 Comparison with the existing (U-Th)/He age dataset .....	47
3.6.6.2 The origin of the anomalously young FCT zircon (U-Th)/He ages .....	47
3.6.6.3 The poor reproducibility of the FCT zircon (U-Th)/He ages .....	49

3.7 Summary.....	49
<b>Chapter 4 : The treatment of zircon (U-Th)/He data .....</b>	<b>50</b>
4.1 Introduction .....	50
4.2 Current techniques and sources of error .....	50
4.3 Crystal measurement.....	51
4.3.1 Unbroken crystals .....	51
4.3.1.1 Crystal geometries observed during this study.....	51
4.3.2 Broken crystals .....	53
4.3.2.1 Broken crystal geometries observed during this study .....	53
4.4 The calculation of surface area-to-volume ratio.....	54
4.4.1 Simplification to pinacoidal geometries .....	55
4.4.2 Simplification of pyramid-terminated geometries.....	57
4.4.2.1 Simplification of more complex geometries .....	57
4.5 The $F_T$ calculation .....	58
4.5.1 The determination of geometry specific $F_T$ .....	58
4.6 Geometry and the $\alpha$ -recoil correction .....	60
4.6.1 $\alpha$ -recoil from tetragonal geometries.....	60
4.6.2 The effect of aspect ratio .....	62
4.6.3 $\alpha$ -recoil from orthorhombic geometries.....	63
4.6.3.1 Correlation of modelling techniques.....	63
4.6.4 The relationship between $\beta$ and $F_T$ .....	65
4.6.4.1 The relationship between $F_T$ and $W_1/W_2$ .....	67
4.6.5 $\alpha$ -recoil from more complex geometries .....	69
4.6.5.1 The limitations of the current modelling techniques.....	70
4.6.5.2 Translation of complex geometries .....	71
4.7 U and Th zonation and the $\alpha$ -recoil correction.....	71
4.7.1 Modelling U and Th zonation .....	72
4.7.1.1 Simple U and Th zonation.....	72
4.7.1.2 Simple zonation in idiomorphic crystals .....	74
4.7.1.3 Complex U and Th zonation.....	78
4.7.1.4 The limitations of existing modelling techniques.....	79
4.8 Recoil and diffusion and zircon (U-Th)/He ages .....	80
4.8.1.1 Modelling diffusive loss of He in zircon .....	80
4.8.1.2 The limitations of the DECOMP model .....	81
4.8.2 The effect of recoil and diffusion on zircon (U-Th)/He ages .....	82
4.8.2.1 The effect of recoil and diffusion on (U-Th)/He ages in zoned zircon.....	84
4.8.2.2 Correct translation of tetragonal zonation into the spherical model.....	86
4.8.2.3 U and Th zonation and variable diffusion kinetics.....	87
4.8.2.4 Applied forward modelling of zircon (U-Th)/He data.....	87
4.9 Determining U and Th zonation in zircon.....	87

4.9.1 Qualitative assessment of U and Th zonation .....	88
4.9.1.1 Fission-track distributions.....	88
4.9.1.2 Cathodoluminescence.....	90
4.9.1.3 Charge contrast imaging .....	91
4.9.1.4 Scanning electron microscopy .....	92
4.9.1.5 Electron back scatter diffraction .....	93
4.9.1.6 Other imaging techniques .....	93
4.9.2 Quantitative assessment of U and Th zonation.....	93
4.9.2.1 Optical microscopy.....	94
4.9.2.2 Raman spectroscopy .....	94
4.9.2.3 Electron microprobe spectroscopy.....	95
4.9.2.4 Laser ablation ICP-MS .....	95
4.9.2.5 Secondary Ion Mass Spectrometry .....	96
4.9.3 The characterisation of zircon samples .....	96
4.10 Conclusions.....	96
4.10.1 Improved treatment of zircon (U-Th)/He data.....	97
4.10.1.1 Improving the uncertainty associated with the $F_T$ correction .....	97
4.10.1.2 Improving the uncertainty by applying the $F_Z$ correction.....	98
4.10.2 Interpretation of zircon (U-Th)/He ages in unknowns.....	98
4.10.3 Closing comments .....	101
<b>Chapter 5 : The Fish Canyon Tuff zircon .....</b>	<b>102</b>
5.1 Introduction .....	102
5.2 Potential causes of poor reproducibility .....	102
5.3 The Fish Canyon Tuff zircons: sample description.....	103
5.3.1 Chemical characterisation of the FCT zircons.....	104
5.4 Qualitative assessment of zonation in the FCT zircon.....	105
5.4.1 Charge contrast imaging of the FCT zircon.....	106
5.4.2 EBSD imaging of the FCT zircon.....	107
5.4.3 Zircon fission track distribution .....	107
5.4.4 Optical cathodoluminescence.....	108
5.4.5 SEM Cathodoluminescence .....	110
5.4.5.1 Type 1 zonation: complex high contrast zonation patterns.....	111
5.4.5.2 Type 2 zonation: complex moderate contrast zonation patterns .....	113
5.4.5.3 Type 3 zonation: inclusion influenced .....	113
5.4.5.4 Type 4 zonation: high CL rims .....	113
5.4.5.5 Type 5 zonation: high CL cores .....	113
5.4.5.6 Type 6 zonation: homogenous CL emission.....	114
5.5 Quantifying U and Th zonation in the FCT zircon.....	114
5.5.1 The distribution of U and Th .....	116
5.5.1.1 The correlation of U, Th and CL intensity .....	118

5.5.1.2 The correlation of trace elements and CL intensity .....	120
5.5.1.3 The quantification of typical zonation patterns .....	122
5.5.1.4 Extended correlation of U, Th and CL intensity .....	125
5.5.1.5 Insensitivity in the correlation .....	125
5.6 CL as a proxy for U and Th .....	126
5.7 Inter-sample correlation of the CL proxy .....	126
5.8 Calculating $F_z$ for the FCT zircon.....	131
5.8.1 Model parameters .....	132
5.8.2 Model results.....	133
5.8.2.1 Limitations of the modelling .....	135
5.8.3 Discussion .....	136
5.9 Re-evaluation of the FCT zircon as a (U-Th)/He standard .....	140
5.9.1.1 The use of standards in zircon (U-Th)/He analysis.....	140
5.10 Implications for the (U-Th)/He analyses of unknowns .....	141
<b>Chapter 6 : The post-magmatic evolution of the HIP .....</b>	<b>143</b>
6.1 Introduction.....	143
6.2 Regional setting & the magmatic evolution .....	143
6.3 The post-magmatic evolution of the HIP .....	146
6.3.1 The existing hypothesis .....	148
6.3.1.1 Evidence for rapid cooling .....	148
6.3.1.2 Evidence for the timing, volume, and rate of denudation .....	149
6.3.2 Questioning the existing hypothesis.....	150
6.3.2.1 Existing low temperature thermochronology in the HIP .....	150
6.3.2.2 Late stage magmatic activity in the North Atlantic.....	152
6.3.3 Testing the hypothesis .....	153
6.4 A thermochronological investigation of the HIP.....	156
6.4.1 Zircon (U-Th)/He analysis of the Muck Tuff.....	157
6.4.1.1 Zonation and $\alpha$ -recoil for the Muck Tuff .....	158
6.4.1.2 Using CL as a proxy for U and Th zonation in HIP zircons .....	160
6.4.2 Zircon (U-Th)/He analysis in the HIP .....	160
6.4.2.1 Ardnamurchan .....	163
6.4.2.2 Rum.....	164
6.4.2.3 Mull.....	165
6.4.2.4 Skye .....	167
6.4.2.5 Summary .....	170
6.4.3 Apatite fission track analysis.....	171
6.4.3.1 Mull & Ardnamurchan.....	171
6.4.3.2 Rum.....	171
6.4.3.3 Skye .....	173
6.4.3.4 Fission track length distributions.....	174

6.4.4 Apatite (U-Th)/He analysis .....	175
6.4.4.1 Rum.....	177
6.4.4.2 Skye .....	177
6.5 Interpretation of multi-chronometer data: Rum.....	180
6.5.1 Geological constraints .....	181
6.5.1.1 Geological and thermochronological inconsistency.....	181
6.5.2 Modelling of the multi-chronometer data .....	181
6.5.3 Synthesis .....	185
6.6 Interpretation of multi-chronometer data: Skye .....	185
6.6.1 Expansion to include the existing thermochronology.....	186
6.6.1.1 Zircon fission track data .....	186
6.6.1.2 Apatite fission track.....	189
6.6.2 Synthesis .....	189
6.7 The St Kilda Central Complex .....	189
6.7.1 Geological setting.....	190
6.7.2 Thermochronological investigation of the St Kilda Complex .....	191
6.7.2.1 Interpretation of the zircon and apatite (U-Th)/He data .....	192
6.8 The post-magmatic evolution of the HIP: Insight and implications.....	193
6.8.1 Possible sources for a mid-Eocene thermal anomaly.....	195
6.9 The HIP in the global context .....	200
6.9.1 Low temperature thermochronology in LIPs.....	201
6.10 Testing the hypothesis .....	203

## Appendices

<b>Appendix A : Column Calibration .....</b>	<b>204</b>
A.1 Calibration procedures.....	204
A.2 Resin preparation .....	206
A.3 Column chemistry procedure .....	206
A.3.1 Column preparation .....	206
A.3.2 Column chemistry procedure .....	207
A.3.3 Column cleaning.....	207
<b>Appendix B : The calculation of geometry specific <math>\beta</math>.....</b>	<b>208</b>
B.1 Complex crystal geometries.....	208
B.2 The body of the crystal .....	208
B.3 The terminations.....	209
B.3.1 Type iii terminations.....	211
B.3.2 Type i and ii terminations .....	214
B.3.3 Type iv terminations.....	215

---

B.3.4 Type v terminations.....	215
B.3.5 Type vi terminations.....	216
B.4 Type E crystal geometries .....	217
<b>Appendix C : Model concentration profiles for the FCT.....</b>	<b>219</b>
<b>Appendix D : Radiometric ages from the HIP &amp; surrounding area.....</b>	<b>222</b>
<b>Appendix E : Modelling the cooling of the plutonic complexes .....</b>	<b>224</b>
E.1 Initial model conditions .....	224
E.2 Intrusion characteristics.....	225
E.2.1 Rum .....	225
E.2.2 Skye .....	225
<b>Appendix F : Geological maps of the HIP &amp; sample localities.....</b>	<b>226</b>
<b>Appendix G : Apatite fission track data .....</b>	<b>232</b>
G.1 The radial plots for HIP samples.....	232
G.2 Raw AFT data for Rum.....	236
G.2.1 Single grain age data.....	236
G.3 Confined track length measurements .....	236
G.3.1 Frequency plot of track length measurements.....	237
G.3 Raw AFT data for Mull.....	237
G.4 Raw AFT data for Ardnamurchan .....	239
G.5 Raw AFT data for Skye .....	241
<b>References .....</b>	<b>242</b>

## List of figures

### Chapter 2

Figure 1	The closure temperatures of geochronometric systems .....	6
Figure 2	The modelled track length distributions for different thermal histories .....	12
Figure 3	The effect of increasing alpha radiation dose on annealing, and the PAZ.....	16
Figure 4	The Arrhenius plot for helium diffusion in apatite. ....	20
Figure 5	The variation of the apatite (U-Th)/He closure temperature.....	21
Figure 6	A schematic representation of $\alpha$ -recoil from apatite crystals. ....	22
Figure 7	The Arrhenius plot for helium diffusion in zircon .....	28
Figure 8	The helium partial retention zone for apatite and zircon. ....	29

### Chapter 3

Figure 9	The helium extraction line used for apatite and zircon (U-Th)/He analysis.....	35
Figure 10	The capsules used for zircon (U-Th)/He analysis. ....	40
Figure 11	The Parr bomb, and microcapsules used for zircon dissolution.....	43
Figure 12	The (U-Th)/He data set for the FCT zircon.....	48

### Chapter 4

Figure 13	The typical geometries seen in primary magmatic zircon. ....	52
Figure 14	The measurements required to calculate $\beta$ . ....	52
Figure 15	$\beta$ calculated using pinacoidal and idiomorphic equations (tetragonal).....	56
Figure 16	$\beta$ calculated using pinacoidal and idiomorphic equations (orthorhombic).....	56
Figure 17	$\beta$ calculated using average and and geometry specific termination length.....	57
Figure 18	The geometrical construct of the Hourigan <i>et al.</i> (2005) model. ....	59
Figure 19	The relationship between $F_T$ and $\beta$ for tetragonal crystals .....	61
Figure 20	The $F_T$ calculated by Hourigan <i>et al.</i> (2005) and Farley (2002). ....	62
Figure 21	The modelling parameters used during this study .....	64
Figure 22	The dependence of $F_T$ on $\beta$ and $W_1/W_2$ . ....	66
Figure 23	$F_T$ calculated from the tetragonal and geometry-specific fitting parameters. ....	67
Figure 24	The relationship between $W_1/W_2$ and the fitting parameters $a$ and $b$ .....	68
Figure 25	Complex crystal geometry and the $\alpha$ -recoil correction. ....	70
Figure 26	The model of self similar zonation used to calculate a 3-D $\alpha$ productivity matrix ...	72
Figure 27	The dependence of $F_z$ on zonation in tetragonal crystals. ....	73

Figure 28	The age bias introduced by assuming homogeneity in tetragonal crystals:.....	75
Figure 29	The age bias introduced by assuming homogeneity in orthorhombic crystals: (I). ...	76
Figure 30	The age bias introduced by assuming homogeneity in orthorhombic crystals: (II) ...	77
Figure 31	Complex zonation styles in natural zircon. ....	79
Figure 32	Effect of recoil and diffusion on zircon (U-Th)/He ages: homogeneous crystals .....	83
Figure 33	Effect of recoil and diffusion on zircon (U-Th)/He ages: heterogeneous crystals. ....	85
Figure 34	The translation between effective and measured rim position in tetragonal crystals.	86
Figure 35	Zonation in zircons from the Tardree Rhyolite. ....	89
Figure 36	CL images of Tardree Rhyolite zircon. White scale bars are 50µm. ....	91
Figure 37	A comparison of the CCI and CL images of a zoned zircon .....	92
Figure 38	A comparison of BSE and CL images of a zoned zircon .....	92
Figure 39	Examples of the diffraction patterns obtained during EBSD analysis of zircon. ....	93
Figure 40	Zonation in birefringence observed in Sri Lankan zircons .....	94
 <b>Chapter 5</b>		
Figure 41	A comparison of BSE and CL images of the Fish Canyon Tuff. ....	105
Figure 42	Charge contrast images of the FCT zircon.....	106
Figure 43	BSE and false colour EBSD images of the FCT zircon.....	107
Figure 44	The distribution of zircon fission tracks within the Fish Canyon Tuff.....	108
Figure 45	A representative selection of optical CL images of FCT zircons.....	109
Figure 46	Panchromatic SEM CL images of the zonation in FCT zircons. ....	112
Figure 47	The CL images of the crystals on which SIMS analysis was performed.....	115
Figure 48	An approximate U and Th concentration profile from zircon FCT 1.....	118
Figure 49	An approximate U and Th concentration profile for zircon FCT 2.....	118
Figure 50	The relationship between U, Th and CL emission for FCT 1, FCT 2, and FCT 3... ..	119
Figure 51	The relationship between CL and trace element composition for FCT zircons.....	121
Figure 52	The relationship between Dy/U, Dy/Th and Dy/eU with CL .....	121
Figure 53	A SIMS traverse along the c-axis of a FCT zircon showing typical zonation. ....	123
Figure 54	The distribution of the measured trace elements in FCT4. ....	124
Figure 55	The inter-crystal correlation of CL intensity and U and Th concentration. ....	125
Figure 56	Panchromatic CL images of the Muck Tuff zircons.....	127
Figure 57	The relationship between CL intensity and the composition of the MT zircons. ....	128
Figure 58	The relationship between CL intensity and the eU, and Dy/eU of the MT zircons..	129
Figure 59	The relationship between CL intensity and eU for the MT and FCT zircons.....	130
Figure 60	The age biases for modelled FCT zircon zonation profiles.....	133
Figure 61	The age biases from zoned FCT zircon of different sizes.....	134
Figure 62	The age biases calculated for crystals with complex oscillatory zonation .....	135
Figure 63	The predicted distribution of the age bias in the FCT zircon population. ....	137
Figure 64	Predicted age bias for the FCT zircons (full dataset) .....	139
Figure 65	Predicted age bias for the FCT zircons (S.U.E.R.C.).....	139

**Chapter 6**

Figure 66	A geological map of the North Atlantic Igneous Province .....	144
Figure 67	The geology of the Hebridean Igneous Province. ....	145
Figure 68	The magmatic evolution of the HIP. ....	147
Figure 69	The localities of published AFT and ZFT analyses from Skye .....	151
Figure 70	The modelled cooling of the Rum Central Complex.....	155
Figure 71	The modelled cooling of the Skye Central Complex. ....	156
Figure 72	Panchromatic SEM CL images of zircons from the Muck Tuff.....	158
Figure 73	Panchromatic SEM CL images of zircons from AR13, Ardnamurchan.....	163
Figure 74	Panchromatic SEM CL images of zircons from the AM1, Mull.....	165
Figure 75	Panchromatic SEM CL images of zircons from ML5, Mull.....	166
Figure 76	Panchromatic SEM CL images of zircons from ML3, Mull.....	166
Figure 77	Panchromatic SEM CL images of zircons from SC, Skye.....	167
Figure 78	Panchromatic SEM CL images of zircons from the SKM & S03-06.....	168
Figure 79	Panchromatic SEM CL images of zircons from GBM, Skye .....	169
Figure 80	Inverse modelling of the apatite fission track data from R03-11 using AFTSolve... 173	
Figure 81	The effect zonation may have on the confined tracks revealed during etching. ....	174
Figure 82	Representative apatites collected from the HIP. ....	176
Figure 83	SEM BSE image of an apatite crystal separated from SKM-04.....	180
Figure 84	Inverse modelling of multi-chronometer data from the RCC (I).....	183
Figure 85	Inverse modelling of multi-chronometer data from the RCC (II).....	184
Figure 86	A geological map of the St Kilda Central Complex. ....	190
Figure 87	Palaeo-reconstruction of the North Atlantic at ~ 55 Ma.....	197
Figure 88	Palaeo-reconstruction of the North Atlantic at ~ 47 Ma.....	198
Figure 89	The North Atlantic at present day.....	199
Figure 90	Full palaeo-spreading rates for the Mid Atlantic Ridge .....	200

**Appendices**

Figure 91	The natural U and Th measured in each sequential elution fraction.....	204
Figure 92	Column calibration. ....	205
Figure 93	Typical crystal and termination geometries seen in magmatic zircon. ....	208
Figure 94	The measurements needed for $\beta$ , volume of the crystal.....	209
Figure 95	The measurements required for $\beta$ , projected termination height .....	210
Figure 96	The measurements required for $\beta$ , Type iii terminations.....	213
Figure 97	The measurements required for $\beta$ , Type i and ii terminations.....	214
Figure 98	The measurements required for $\beta$ , Type v terminations .....	215
Figure 99	The measurements required for $\beta$ , Type vi terminations.....	217
Figure 100	The measurements required for $\beta$ , Type E crystals .....	217
Figure 101	The model FCT concentration profiles from the CL images.....	220
Figure 102	The model FCT concentration profiles generated from crystal FCT 4 .....	221
Figure 103	The geology of the Ardnamurchan Central Complex and surrounding area.....	226
Figure 104	The geology of Rum. ....	227

---

Figure 105	The geology of the Skye Central Complex.....	228
Figure 106	The geology of the Mull Central Complex .....	229
Figure 107	The offshore Seamounts in the Northeast Atlantic.....	230
Figure 108	Radial plots for apatite from the Rum Central Complex.....	232
Figure 109	Radial plots for apatite from the Ardnamurchan Central Complex.....	233
Figure 110	Radial plots for apatite from the Mull Central Complex.....	234
Figure 111	Radial plots for apatite from the Skye Central Complex .....	235
Figure 112	The apatite fission track frequency distribution .....	237

## List of tables

### Chapter 2

Table 1	Series averaged alpha particle stopping distances in common accessory minerals. ...	22
Table 2	The (U-Th)/He ages of the Fish Canyon Tuff zircon standard.....	31

### Chapter 3

Table 3	The (U-Th)/He ages and Th/U of Durango apatite determined at S.U.E.R.C. ....	38
Table 4	The (U-Th)/He age of the Fish Canyon Tuff zircons by furnace extraction .....	46
Table 5	The (U-Th)/He age of the FCT by laser extraction. ....	47

### Chapter 4

Table 6	The Farley (2002) fitting parameters for the equation $F_T = 1 + a\beta + b\beta^2$ .....	58
Table 7	The typical elemental contribution to the total number of $\alpha$ -particles generated.....	60
Table 8	The fitting parameters for the equation $F_T = 1 + a\beta + b\beta^2$ for tetragonal crystals.....	61
Table 9	The fitting parameters for the equation $F_T = 1 + a\beta + b\beta^2$ for orthorhombic crystals...	65

### Chapter 5

Table 10	Selected SHRIMP spot analyses from the FCT zircon.....	105
Table 11	Elemental data from the SIMS analyses of zircons FCT 1, FCT 2 and FCT 3.....	117
Table 12	Elemental data from the SIMS analysis of zircon FCT 4.....	124
Table 13	Elemental data from SIMS analysis of the MT zircons. ....	128

### Chapter 6

Table 14	Published apatite fission track data from Skye .....	151
Table 15	Published zircon fission track ages from the Skye Central Complex .....	152
Table 16	Zircon (U-Th)/He analyses of the Muck Tuff.....	158
Table 17	The $F_z$ correction for the Muck Tuff (U-Th)/He ages. ....	159
Table 18	Zircon (U-Th)/He data from the HIP.....	161
Table 19	New AFT data from the HIP.....	172
Table 20	Apatite (U-Th)/He analyses from the HIP. ....	177
Table 21	A comparison of the U-Pb, ZFT and AFT ages from individual plutons. ....	187

---

<b>Table 21</b>	<b>A comparison of the U-Pb, ZFT and AFT ages from individual plutons.....</b>	<b>187</b>
<b>Table 22</b>	<b>Zircon and apatite (U-Th)/He ages from the St Kilda Complex.....</b>	<b>192</b>

### **Appendices**

<b>Table 23</b>	<b>The relative natural abundance of Pt isotopes.....</b>	<b>205</b>
<b>Table 24</b>	<b>Segmented perimeter, perimeter normal lengths and slope heights.....</b>	<b>213</b>
<b>Table 25</b>	<b>The conversion from CL intensity to U and Th content.....</b>	<b>219</b>
<b>Table 26</b>	<b>Selected radiometric ages from the HIP, Ireland and the offshore UK margin.....</b>	<b>223</b>
<b>Table 27</b>	<b>The input parameters used to perform the Heat 3D simulations.....</b>	<b>224</b>
<b>Table 28</b>	<b>A summary of the samples and lithologies analysed during this study.....</b>	<b>231</b>
<b>Table 29</b>	<b>Single grain ages from sample R11, Harris Bay, Rum.....</b>	<b>238</b>
<b>Table 30</b>	<b>Confined track length measurements from sample R11, Harris Bay, Rum.....</b>	<b>238</b>
<b>Table 31</b>	<b>Single grain ages from sample ML5, Mull.....</b>	<b>237</b>
<b>Table 32</b>	<b>Single grain ages from sample ML2, Mull.....</b>	<b>238</b>
<b>Table 33</b>	<b>Single grain ages from sample AR13, Ardnamurchan.....</b>	<b>239</b>
<b>Table 34</b>	<b>Single grain ages from sample AR2, Ardnamurchan.....</b>	<b>240</b>
<b>Table 35</b>	<b>Single grain ages from sample S03-03, Glamaig, Skye.....</b>	<b>241</b>
<b>Table 36</b>	<b>Single grain ages from sample SKM04, Marsco, Skye.....</b>	<b>241</b>

## List of abbreviations

### Abbreviation

ACC	Ardnamurchan Central Complex
AFT	Apatite Fission Track
AHe	Apatite (U-Th)/He
BSE	Back Scatter Electron
CCI	Charge Contrast Imaging
CL	Cathodoluminescence
EBSD	Electron Back Scatter Diffraction
ELF	Eigg Lava Field
EMP	Electron Microprobe
FCT	Fish Canyon Tuff
$F_T$	$\alpha$ -recoil correction for homogeneous U and Th distribution
$F_z$	$\alpha$ -recoil correction for heterogeneous U and Th distribution
ZFT	Zircon Fission Track
HIP	Hebridean Igneous Province
ICP-MS	Inductively Coupled Plasma Mass Spectrometry
LA-ICP-MS	Laser Ablation Inductively Coupled Plasma Mass Spectrometry
MCC	Mull Central Complex
MLF	Mull Lava Field
NAIP	North Atlantic Igneous Province
PAZ	Partial Annealing Zone
PRZ	Partial Retention Zone
RCC	Rum Central Complex
REE	Rare Earth Element
$R_L$	Length of the body of the crystal (i.e. not terminations)
SCC	Skye Central Complex
SEM	Scanning Electron Microscopy
SIMS	Secondary Ion Mass Spectrometry
SLF	Skye Lava Field
$T_L$	Total crystal length
TR	Tardree Rhyolite
$T_1$ and $T_2$	Termination lengths
$W_1$ and $W_2$	Mutually perpendicular crystal widths
ZHe	Zircon (U-Th)/He

## Acknowledgements

Firstly I would like to thank the organisations that made this research possible. This study was funded by a NERC Ph.D. studentship award number NER/S/A/2002/10370, in CASE partnership with STATOIL, and I received additional financial support from the Volcanic & Magmatic Studies Group, the Geochemistry Group and the Department of Geographical & Earth Sciences in order to attend international conferences. All of whom are gratefully acknowledged. This work would also not have been possible without the support, assistance and motivation provided by my supervisors: Dr. Brian Bell, Prof. Paul Bishop, Dr. Tim Dempster, and Dr. Fin Stuart (listed here in alphabetical order). Their insight has provided me with as many questions as answers, and their help during all stages of this project has been invaluable. Special thanks should go to Fin for the extra motivation required to get me through the developmental stages of this project and to Tim, for invaluable comment on this thesis during all stages of its “development”.

I would also like to thank Dr. Jurgen Foeken, David Vilbert and Sorcha Diskin for their assistance, and my mental health, during my months at S.U.E.R.C. Thanks also to Dr. Rob Ellam. Special thanks go to Dr. Valerie Olive for her advice, and without her help the zircon (U-Th)/He procedure would not have been possible. I am also indebted to Dr. Cristina Persano for answering endless questions, and owe her several bottles of very good wine for her training and assistance at all stages of this project. I owe her several more for her perseverance with my “difficult” AFT samples. Without Dr. Richard Hinton the detailed sample characterisation of the FCT, and large parts of this study would not have been possible.

Thanks should go to all those people who have provided me with suggestions for good sample localities, and help during sample collection. As well as my supervisors, I have persuaded several other people to act as pack horses, and I thank them all. I would especially like to thank Dr. Henry Emeleus for all his assistance during the planning of the fieldwork, and Dr. John Faithful for his unique ability to find a particular kind of grey rock, on a grey hill, on a very grey day. My thanks also go to Dr. Lynne Chambers, Dr. John Valley, Dr. Mike Hamilton, Dr. Ray Donelick and Chris Ravey all of whom provided crucial samples, and saved me hours of mineral separation. Thanks also to Dr. Andrew Carter for the images of the FCT zircon.

The staff and postdocs in the Gregory Building have always helped when they can, but John Gillece, Dr. Jeff Harris, and Prof. Rod Brown deserve individual thanks, as does Kenny Roberts for fixing everything several times over. I would also like to thank Claire Torney and Craig Barrie.

All the postgraduates, past and present, who have shared an office with me have made spending time in the lab enjoyable, and when the work wasn't going too well there was always someone around to cheer me up, or to help me drown my sorrows. I am especially grateful to Sally, for sharing both an office and a flat for the last three years, and providing friendship, good (if hazy) memories of Grand Slam rugby matches, and company on the commute to East Kilbride.

Without my parents' belief that I would get this thesis submitted in time, it probably wouldn't have been. I would like to thank them for the emotional and financial support that made it possible for me to get to this stage; but also for their appreciation of castles, mountains, B&B's (mainly the breakfasts), and fine Scottish beer. I would also like to thank my brother and my Grandma for their help over the course of the last four years. Finally I must thank Davie. He has put up with me and my mess through the stresses and strains of the last four years. He has provided me with absolutely everything, from field assistance to a place to live, and has given me endless love and support.

Thank you all.

## **Declaration**

The material presented in this thesis is the result of the independent research undertaken by myself between October 2002 and July 2006. This work was supervised by Dr. Brian Bell, Dr. Tim Dempster, Dr. Fin Stuart and Prof. Paul Bishop. All work by other researchers that is quoted in this thesis is given full acknowledgement in the text.

**Katherine J. Dobson**

**September 2006**

# 1

## Introduction

The development of the radiometric dating techniques over the last century has enabled scientists to quantify the timescales involved in many geological processes. The absolute ages from “geochronology” have provided the quantitative framework of modern geology, and changed the way that we understand the evolution of the Earth’s surface. As new radiometric techniques are developed, we are able to develop an ever more detailed understanding of the geological processes that shape the world around us. The continued expansion of geochronology has led to the development of techniques that can provide quantitative information about geological events that occur long after the formation of the rock, and allow the determination of detailed thermal histories for individual samples. All geochronometers use the relationship between the rate of radioactive decay and the thermally-controlled rate at which the radiogenic daughter products are lost through diffusion. The change from open- to closed-system behaviour is gradual, and so the time-integrated concentration of a given daughter product is related to the thermal history that the sample has experienced [Green *et al.*, 1989; Lovera *et al.*, 1989; Wolf *et al.*, 1996]. For most chronometers, this change occurs at temperatures well above 200°C. However, in some systems (e.g. Ar-Ar, fission-track and (U-Th)/He), closure occurs at lower temperatures, and these systems are therefore sensitive to the cooling of rocks in the shallow crust [see reviews in Reiners & Ehlers, 2005; Braun *et al.*, 2006].

“Thermochronology” can determine the transport of a sample relative to isothermal surfaces; either as the position of the isotherm moves relative to a stationary rock column, or as the sample is transported vertically through a constant thermal structure. These low temperature thermochronological techniques can be used to extract information about the timing and rate of the geological processes controlling denudation, and are powerful tools in the investigation and understanding of landscape evolution [e.g. Braun, 2005]. The modelling and interpretive techniques used to extract geologically significant information from thermochronological data sets are becoming ever more detailed and complex, keeping pace with the development of new and more precise thermochronometric methods [see reviews in Reiners & Ehlers, 2005; Braun *et al.*,

2006]. Low-temperature thermochronology can now be used to constrain the rate and timing of many shallow crustal processes.

Recent advances in low-temperature thermochronology have enabled the development of the zircon (U-Th)/He dating system [Reiners *et al.*, 2002; Reiners, 2005]. This system records cooling through ~ 170 - 200°C, and so provides thermal constraints beyond the resolution of existing thermochronometric techniques (for example, Ar-Ar, fission track). The development of the zircon (U-Th)/He system, therefore, improves the ability of researchers to constrain geological processes affecting the upper levels of the crust. At present, the technique remains under-utilised because of the challenging analytical procedures, and poor understanding of many of the issues that must be considered before accurate geological interpretation can be attempted.

This study aims to resolve aspects of the low temperature post-magmatic evolution of the Palaeogene Hebridean Igneous Province (HIP), in order to achieve an understanding of the landscape evolution in response to the intensive magmatism on the continental margin of the incipient north-east Atlantic rift. Denudation is known to have occurred across the region, and has exposed the plutonic roots of Palaeogene volcanoes, however the timing and extent of this denudation remains poorly constrained. Published zircon fission track analyses from the HIP have been used to suggest elevated geothermal gradients existed for ~ 10 Myr [Lewis *et al.*, 1992], in contradiction to other studies that predict rapid denudation and unroofing immediately after plutonic emplacement [see reviews in Bell & Williamson, 2002; Emeleus & Bell, 2005].

Constraining the unroofing of the HIP requires an understanding of the changing thermal structure in the upper (< 5 km) crust associated with the late-stage, low temperature cooling of the magmatic system. The application of multiple low temperature thermochronometers to individual samples will allow the timing and rate of the post-magmatic cooling to be determined, and can provide important extra information on the late stage cooling across the HIP. This investigation will complement the limited apatite and zircon fission track data from the province [Lewis *et al.*, 1992], and provide further constraint on the post-magmatic evolution.

The principles governing the fission track and (U-Th)/He dating techniques are presented in Chapter 2. A variety of analytical problems make the existing zircon (U-Th)/He methodologies unsuitable for use in many laboratories, including S.U.E.R.C., and so the development of a suitable analytical protocol was undertaken. The resulting procedure, presented in the latter part of Chapter 3, can be applied by the majority of (U-Th)/He laboratories and permits the routine application of this thermochronometer. With the ability to perform (U-Th)/He age determinations established, several issues must be considered before accurate interpretation of (U-Th)/He data can be achieved. Many of the controls governing the loss of helium from natural crystals, such as the effect of

crystal geometry, and U and Th zonation, are only beginning to be addressed [e.g. Hourigan *et al.*, 2005].

To enable the accurate interpretation of isotopic data from the range of natural crystals analysed during this study, a detailed investigation of the geometry and zonation dependence of (U-Th)/He data was performed, and the implications for the reproducibility of replicate analyses assessed (Chapter 4). This appraisal highlights the significance of the characterisation of zircon samples if accurate interpretation of the (U-Th)/He data is to be achieved, but also shows that, where geometry and zonation are accurately known, the uncertainty associated with any individual (U-Th)/He ages is much reduced.

Despite the level of precision that is possible for individual analyses, the true uncertainty associated with the (U-Th)/He ages of “unknowns” is generally calculated from the relative reproducibility of known mineral standards. The standard that has been adopted for the (U-Th)/He system is the Fish Canyon Tuff [Reiners *et al.*, 2002; Tagami *et al.*; Reiners *et al.*, 2004; Reiners]. This was selected because it is widely used as a standard for both zircon and apatite fission track techniques, and so can be used as an inter-thermochronometer calibration tool. The mean zircon (U-Th)/He age for the Fish Canyon Tuff is  $28.3 \pm 3.1$  Ma ( $2\sigma$ ,  $\pm 11.2$  %,  $n = 129$ ), and is within error of both the zircon fission track ( $27.9 \pm 2.2$  Ma) and apatite fission track ( $26.8 \pm 4.2$  Ma) ages; however, the poor reproducibility is substantially greater than typical analytical uncertainties ( $< 3$  %). This has consequences for the determination of (U-Th)/He ages from unknown samples. Uncertainties in (U-Th)/He ages are generally calculated from the relative reproducibility of known mineral standards, and so while the origin of this poor reproducibility remains unknown, the suitability of the Fish Canyon Tuff sample as a (U-Th)/He standard must be questioned.

A detailed characterisation of the Fish Canyon Tuff shows that over 98 % of all crystals have a heterogeneous distribution of U and Th. Minor and subtle zonation has been proposed as one mechanism that can account for the poor reproducibility of this sample [e.g. Reiners, 2005], but the high resolution qualitative and quantitative characterisation presented in Chapter 5 shows that zonation is often extreme, with the U and Th concentrations measured on individual zones ranging from *c.* 15 ppm to 5000 ppm. Intra-crystalline variation in U and Th contents by up to two and a half orders of magnitude can have a significant effect on the proportion of helium lost through  $\alpha$ -recoil. Techniques that can be used for the assessment of heterogeneity in U and Th have been assessed and, while the effect of the heterogeneous distribution on the calculated (U-Th)/He age will vary on a crystal specific basis, the significance of under and overestimating the  $\alpha$ -recoil correction in both the Fish Canyon Tuff and other samples has been investigated.

The application of these techniques allows a more confident interpretation of zircon (U-Th)/He data from unknown samples than has previously been possible; and enables the potential of this technique to be harnessed for the study of the post-magmatic evolution of the HIP, as well as volcanic provinces, worldwide. The results of the thermochronological investigation of the HIP are presented in Chapter 6.

In summary, this research aims to provide a methodology for the acquisition, understanding and modelling of zircon (U-Th)/He data, which considers all the additional complexities associated with the zircon system. It also aims to quantitatively constrain the post-magmatic evolution of the Hebridean Igneous Province, and will explore the local, regional and global implications of the study.

# 2

## The principles of thermochronology

### 2.1 Introduction

Radioactive isotopes are present in trace amounts in many common minerals, and undergo radioactive decay at known rates, to produce daughter products, such as other isotopes and crystal lattice damage. The accumulation of these products is the basis of absolute geochronology [e.g. Rutherford, 1905]. At high temperatures, thermally-activated diffusion prevents the accumulation of these daughter products within the host mineral, but as temperature decreases, the rate of diffusion reduces. The temperature at which the rate of diffusive loss of the daughter product equals the rate of production is defined as the “closure temperature” ( $T_C$ ), and is specific to each parent-daughter-mineral dating system (Figure 1) [Dodson, 1973]. Below this temperature there is a net accumulation of daughter products within the crystal lattice, and when the rate of decay, and the concentration of the parent isotope are known, the concentration of the daughter products can be used as a chronometer, recording the time of cooling through  $T_C$ . Diffusion becomes decreasingly efficient at lower temperatures, and the loss of the daughter product eventually becomes negligible over geological time-scales ( $10^5 - 10^8$  Myr). When the rate of cooling through this temperature range is rapid, the age recorded by the geochronometers, effectively dates a geologically instantaneous event. However, when cooling is slow, prolonged partial diffusion reduces the concentration of daughter product and interpretation of the measured ages becomes more complicated.

In many lower temperature mineral systems (e.g. mica  $^{40}\text{Ar}$ - $^{39}\text{Ar}$ , apatite fission track, and apatite (U-Th)/He) the temperature range over which partial diffusive loss of the daughter products occurs has been measured [Gleadow & Duddy, 1981; Harrison *et al.*, 1985; Hames & Bowring, 1994; Brandon *et al.*, 1998; Wolf *et al.*, 1998; Reiners & Spell, 2002]. In these dating systems, the ability to model the partial loss of daughter products with time and temperature during cooling, allows the extraction of information about both the timing and rate of that cooling. Many thermochronometers can be applied to complex mineral assemblages, with each mineral-

thermochronometer combination having a different  $T_c$ . Within each thermochronometer-mineral combination, further variation may be caused by variation in chemical composition, grain size or other factors such as accumulated radiation damage. The application of multiple thermochronometers in a rock specimen, can therefore be used to constrain detailed and complex thermal histories and/or the timing of cooling.

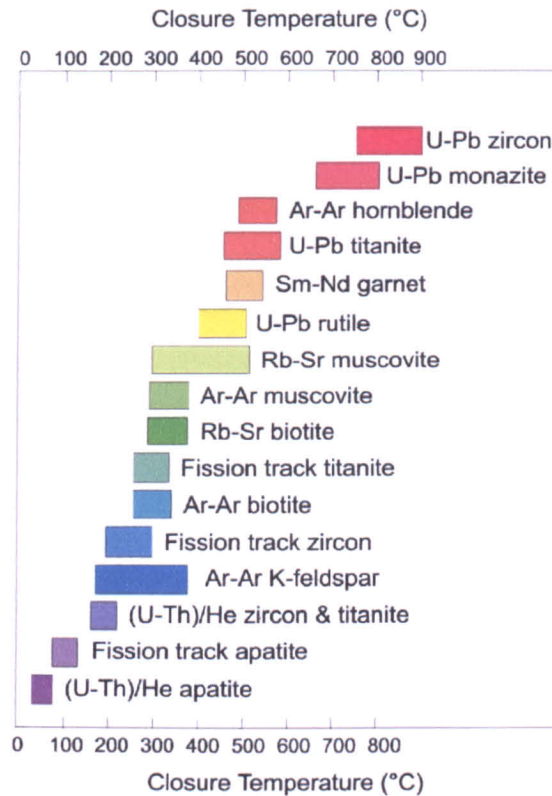


**Figure 1 - The closure temperatures of geochronometric systems. [after <http://4thermochronology.syr.edu/>]**

Of the commonly used thermochronometers, the lowest closure temperatures are recorded by the fission track and (U-Th)/He systems when they are applied to apatite and zircon. These record cooling from  $\sim 300^\circ\text{C}$  to  $\sim 30^\circ\text{C}$  [Gallagher *et al.*, 1998; Farley, 2002; Donelick *et al.*, 2005; Reiners, 2005; Tagami, 2005], temperatures that are typical of the upper few kilometres of the crust (1 - 10 km with geothermal gradients of 30 - 60°C/km). Consequently, these thermochronometers are used to constrain very low temperature cooling histories, and shallow crustal processes. This chapter provides an overview of the theoretical basis of both the fission track and (U-Th)/He thermochronometers, as applied to apatite and zircon.

## 2.2 Apatite fission track thermochronology

The apatite fission track (AFT) thermochronometer has become the most widely used thermochronometer over the ~ 30 years since it was first developed [Wagner, 1968; Naeser & Faul, 1969; Fleischer *et al.*, 1975; Wagner, 1981].

### 2.2.1 Fission track formation

Approximately one in every two million  $^{238}\text{U}$  nuclei undergoes spontaneous nuclear fission, splitting into two approximately equally sized, highly-charged fragments. These move away from the point of fission in opposite directions, producing a linear zone of damage; a fission track [Fleischer *et al.*, 1975]. These narrow (few nm) tracks can be revealed by a chemical etching process that preferentially dissolves the damaged zones [Donelick, 1995], and observed at high magnification. The other fissile nuclides ( $^{235}\text{U}$ ,  $^{232}\text{Th}$ ) undergo fission at such low rates that spontaneous track formation can be disregarded, however, bombardment with thermal neutrons can induce  $^{235}\text{U}$  (and other fissile nuclides) to fission. Induced fission tracks are utilised in the external detector method of fission track dating, to determine the U content of the crystal (Section 2.2.3).

The number of spontaneous fission tracks produced in a unit volume, defined as  $F_S$ , is proportional to the concentration of  $^{238}\text{U}$  in that volume and the time,  $t$ , over which damage has been accumulating [Donelick *et al.*, 1990; Gallagher *et al.*, 1998 and refs therein]. With an accurate knowledge of the rate of fission track production ( $\lambda_{\text{fission}}$ ), and the total rate of  $^{238}\text{U}$  decay ( $\lambda$ ),  $F_S$  is described by Equation 1 [Gleadow & Duddy, 1981].

$$F_S = \frac{\lambda_{\text{fission}}}{\lambda} {}^{238}\text{U} (e^{\lambda t} - 1)$$

Equation 1

### 2.2.2 Fission track annealing

Annealing repairs the damage to the crystal structure caused by fission. Fission track annealing is a dominantly thermally-activated diffusive process and causes a progressive reduction in the etchable track length with increasing temperature and time [Gleadow & Duddy, 1981]. Laboratory experiments and studies of borehole samples have shown that over geological time (Myr), temperatures above 120°C allows highly efficient annealing and repair of all tracks as they form [Naeser & Faul, 1969; Gleadow & Duddy, 1981; Green *et al.*, 1986]. 10 - 90 % of track shortening occurs between 120°C and 60°C, and this is defined as the “partial annealing zone” (PAZ) [Gleadow *et al.*, 1993]. Fission track annealing is not a linear function of temperature or time, and contours of equal track shortening for different time-temperature conditions plot as linear or

curvilinear arrays on Arrhenius plots [Green *et al.*, 1985; Laslett *et al.*, 1987]. Extensive laboratory experiments have led to the development of annealing models that can be used to extrapolate from the laboratory to the geological timescale [Naeser & Faul, 1969; Green *et al.*, 1986; Laslett *et al.*, 1987; Duddy *et al.*, 1988; Green *et al.*, 1989; Ketcham *et al.*, 1999], and allow the interpretation of the annealing observed in geological samples [Laslett *et al.*, 1987; Crowley *et al.*, 1991; Ketcham *et al.*, 1999]. Existing annealing algorithms fit much of data from laboratory annealing experiments and natural samples, but they remain incomplete.

Induced tracks in apatite are  $16.3 \pm 0.9 \mu\text{m}$  long [Fleischer *et al.*, 1975], however even in very rapidly cooled volcanic samples spontaneous tracks rarely exceed 14 - 15  $\mu\text{m}$ . This discrepancy is poorly understood, but could be because of a fundamental difference in the energies of induced and spontaneous fission fragments [Wagner & Van der Haute, 1992]. The amount of track shortening that occurs below 60°C is difficult to measure over  $10^6$  -  $10^8$  Myr, and annealing is therefore assumed to be negligible in the annealing algorithms. However, annealing of spontaneous tracks has been observed at room temperatures, and Donelick *et al.* (1991) therefore suggest that the discrepancy between induced and natural track lengths is caused by annealing at temperatures well below the PAZ. This low temperature annealing is suggested to be a result of radiation damage, where  $\alpha$ -decay promotes annealing of fission tracks, and therefore current annealing algorithms do not accurately describe annealing in samples that have experienced very long low temperature histories (e.g. cratonic complexes) [Fleischer *et al.*, 1975].

Annealing of fission tracks is also strongly controlled by chemical composition. Chlorine-rich apatite being more resistant to annealing than fluorine-rich apatite. The Cl/(F+Cl) of a crystal is the dominant chemical control on annealing kinetics [Gleadow *et al.*, 1986a], however OH, REE, Mn and Sr can also have an effect [Crowley *et al.*, 1991; Brown *et al.*, 1994; O'Sullivan & Parrish, 1995; Barbarand & Pagel, 2001; Barbarand *et al.*, 2003]. Chemical composition must be carefully considered, as chemically induced differences in annealing behaviour will control the temperatures defining the PAZ [Ketcham *et al.*, 1999].

The annealing algorithm presented by Laslett *et al.* (1987) remains widely used, and is based on track shortening observed in the fluorine-rich Durango apatite standard [Young *et al.*, 1969]. It does not incorporate chemical composition into the annealing model; however, it fits the observed track shortening in many natural apatites, because F-rich apatites dominate the natural population. An annealing algorithm that correctly incorporates variable apatite chemistry is required for the interpretation of AFT data from apatites that are Cl-rich, or of intermediate composition. Donelick (1995) showed that the chemical composition of the apatite effects the shape of the fission track etch pit, and that the maximum *c*-axis parallel diameter of the etch pits ( $D_{\text{par}}$ ), varies

systematically with the chemistry-controlled bulk solubility and variation in annealing. Therefore, when etching conditions are tightly controlled, Dpar can be used to estimate the variation of Cl/F between apatite crystals [Donelick, 1995; Donelick *et al.*, 2005]. Subsequently, Ketcham *et al.* (1999, 2000) developed an annealing model that uses crystal-specific measurements of Dpar to incorporate the effect of crystal chemistry on annealing. Recent studies suggest that the relationship between Dpar and bulk solubility exists only below 10 ppm  $^{238}\text{U}$  [Donelick, 1995].

Radiation damage caused by recoil of heavy nuclei during  $\alpha$ -decay, and pressure are also thought to control annealing, but the importance if these controls remains poorly constrained, and a topic of debate [Wendt *et al.*, 2002; Donelick *et al.*, 2003; Murrell, 2003; Lorencak *et al.*, 2004; Fitzgerald *et al.*, 2006; Green & Duddy, 2006].

### 2.2.3 The determination of apatite fission track ages

Equation 1 described the number of spontaneous tracks produced in a given volume. A plane drawn through that volume will intersect a proportion of these tracks,  $q$ , and the surface will therefore have a track density ( $\rho_s$ ), described by:

$$\rho_s = qF_s = \frac{\lambda_{\text{fission}}}{\lambda} {}^{238}\text{U} (e^{\lambda t} - 1)$$

Equation 2

where  $\lambda = 1.552 \times 10^{-10} \text{ y}^{-1}$ , and  $\lambda_{\text{fission}}$  is approx.  $7 \times 10^{-17} \text{ y}^{-1}$  [Hurford & Green, 1981]. The external detector method determines the  $^{238}\text{U}$  concentration from an independent measurement of  $^{235}\text{U}$ . After apatites are chemically etched, mica with a known, low, uranium content is placed in immediate contact with the polished surface of the grain mount, and both are irradiated with a known dose of thermal neutrons inducing fission of  $^{235}\text{U}$  [Hurford & Green, 1981]. A proportion,  $q$ , of the fission events that occur within the upper 16  $\mu\text{m}$  of the apatite will intersect the surface of the grain mount, and enter the mica. These can then be revealed by chemical etching. The induced track density ( $\rho_i$ ) revealed in the mica is proportional to the  $^{235}\text{U}$  concentration of the apatite, the thermal neutron flux per unit volume ( $\phi$ ) and the cross section of  $^{235}\text{U}$  for induced fission ( $\sigma$ ) [Green & Hurford, 1984]. The concentration of  $^{235}\text{U}$  can be calculated from:

$$\rho_i = q {}^{235}\text{U} \phi \sigma$$

Equation 3

This calculation can be simplified by comparison with the induced track densities in standard glasses ( $\rho_D$ ) of known  $^{235}\text{U}$  concentration, that were irradiated under the same conditions:

$${}^{235}\text{U}_{\text{sample}} = \frac{\rho_i}{\rho_D} {}^{235}\text{U}_{\text{glass}}$$

Equation 4

The natural isotopic ratio of  $^{235}\text{U}/^{238}\text{U} = 1/137.88$  can then be used to calculate the  $^{238}\text{U}$  content of the sample.

$$t = \frac{1}{\lambda} \ln \left( 1 + \frac{\lambda g \rho_D \rho_S}{\rho_i \lambda_{\text{fission}}} \left( \frac{^{235}\text{U}}{^{238}\text{U}} \right) \right)$$

Equation 5

In Equation 5 (terms as defined above),  $g$  is a geometry factor of 0.5 arising from the proportionality term ( $q$ ). Spontaneous and induced track densities are measured across the same area on the grain-mount-mica boundary, and the U concentration of the apatite samples is assumed to be homogeneous across the plane of the grain mount. Therefore the proportion of induced tracks intersecting the grain-mount-mica boundary is half that of the spontaneous tracks, as they were generated from only half the volume.

### 2.2.4 Zeta calibration

Although the value of  $\lambda$  is accurately known ( $1.552 \times 10^{-10} \text{ y}^{-1}$ ), the value of  $\lambda_{\text{fission}}$  is uncertain at approx.  $7 \times 10^{-17} \text{ y}^{-1}$  [Bigazzi, 1981; Wagner & Van der Haute, 1992]. To redress this uncertainty Hurford & Green (1982) suggested the zeta calibration procedure, which is dependant on the standard glass and the reactor used, and incorporates systematic errors introduced by individual analysts. Mineral standards of known age (usually the Durango, Fish Canyon Tuff, and Mt. Dromedary apatite), are irradiated with each batch of samples and standard glasses, and the track ratios of the standards, glasses and unknown samples are then compared. As all samples, standards and glasses have identical  $\lambda_{\text{fission}}$ , and experience the same neutron flux, the uncertainties in these factors are removed. The zeta value is defined as:

$$\zeta = \frac{(e^{\lambda_{\text{ind}}} - 1)}{\lambda (\rho_S / \rho_i)_{\text{std}} g}$$

Equation 6

and allows Equation 5 to be rewritten and solved for  $t$ .

$$\text{Fission track age} = t = \frac{1}{\lambda} \left[ 1 + \lambda \zeta \left( \frac{\rho_S}{\rho_i} \right) g \rho_D \right]$$

Equation 7

#### 2.2.4.1 Annealing and AFT ages

Annealing acts to shorten track lengths, reducing the probability that any track will intersect the polished surface and that it can be counted. Samples that have spent extended periods in the PAZ will have experienced greater degrees of annealing and will have a lower track density (and therefore younger fission track age) than equivalent rapidly cooled samples. The reduction in track

density ( $\rho/\rho_0$ ) is directly proportional to the reduction in mean track length ( $l/l_0$ ), where  $l/l_0 > 0.65$  [Donelick & Miller, 1991], and  $l/l_0$  is rarely less than this critical value. The ratio of the AFT age to  $l/l_0$  gives an indication of when a sample entered the PAZ.

## 2.2.5 Fission track length distributions

The formation of fission tracks occurs at a constant rate, therefore the amount of annealing that each track in any crystal experiences will be controlled by when that track formed, and the fission track length distribution within a sample can be used to extract information about the rate of cooling [Gleadow *et al.*, 1986b; Corrigan, 1991; Gallagher, 1995; Gallagher *et al.*, 1998]. The chemical etchant used to reveal tracks passes along tracks and cracks that intersect the free surface and may intersect, and etch tracks that are completely confined within the crystal [Donelick, 1995]. Two types of confined track are formed; tracks etched by intersection with other fission tracks are known as Tracks-IN-Tracks (TINTs), whereas those intersected by a crack are Tracks-IN-CLEavage (TINCLEs). All confined tracks measured are identified as either TINT or TINCLE, as the etchant pathway can affect the degree of etching [Donelick & Miller, 1991]. To ensure accuracy, track length measurements are made on confined tracks that lie close to the horizontal ( $\pm 10^\circ$ ) that have been fully etched. Etching is carried out under tightly controlled conditions, and well etched samples have confined track widths of  $\sim 1.5 \mu\text{m}$ , and characteristic conical terminations.

In all minerals dated using the fission track technique, the crystallographic orientation of the fission track affects the annealing and etching characteristics. In apatite, tracks formed at high angles to the crystallographic *c*-axis anneal at a faster rate than those that are *c*-axis parallel [Donelick, 1991]. Anisotropic etching means that the longer *c*-axis parallel tracks are not commonly seen [Carlson *et al.*, 1999]. Statistically viable track length distributions require 100 track length measurements, and in many samples the measurement of 100 tracks with the same crystallographic orientation i.e. *c*-axis parallel ( $\pm 15^\circ$ ) is not possible. Translation of the lengths of all randomly orientated track measurements to their equivalent "projected" *c*-axis parallel length can dramatically increase the number of measurable tracks in any sample [Donelick, 1991; Donelick *et al.*, 1999; Donelick *et al.*, 2005]. This projected track length conversion has been included into the annealing algorithm of Ketcham *et al.* (1999).

Track length measurements are biased towards long track lengths, but track length distributions can still provide detailed information about the thermal history of sample [Laslett *et al.*, 1987]. Rapidly cooled samples have a characteristic unimodal distribution with a long mean track length, whereas slowly cooled samples have broad skewed distributions with many short track lengths. This means that samples that enter the PAZ at the same time, but cool at different rates can record very

different track length distributions and will have different fission track ages (e.g. Figure 2). Forward and inverse modelling of the apatite fission track ages and track length distributions using modelling packages such as HeFTy [Ketcham *et al.*, 1999; Ketcham, 2005] and MonteTrax [Gallagher, 1995] allows the extraction of information about possible thermal histories.

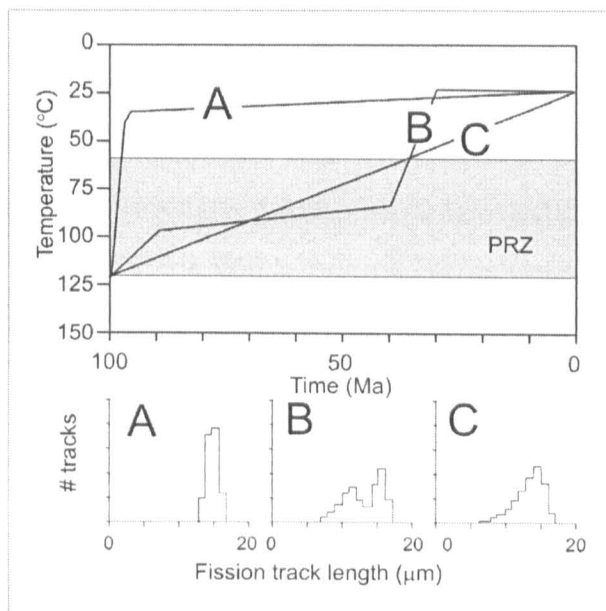


Figure 2 - The modelled track length distributions for three different thermal histories [from Gleadow & Brown, 2000].

### 2.2.5.1 Cf irradiation

A further method for improving the number of samples for which statistically valid AFT length distributions can be obtained is  $^{252}\text{Cf}$  irradiation. In young samples, or samples with very low U contents, low track densities mean that few confined tracks (TINTs) are revealed. In these cases, irradiation with  $^{252}\text{Cf}$  generated fission fragments prior to etching produces an increased number of induced semi-tracks that intersect the surface, which increases the number of TINTs intersected by an etchant pathway [Donelick & Miller, 1991].  $^{252}\text{Cf}$  irradiation can therefore be a valuable tool for determination of thermal histories.  $^{252}\text{Cf}$  irradiation has a biasing effect on the track length distribution, as it reveals a greater proportion of harder-to-detect tracks (short tracks and *c*-axis parallel tracks), however, using the procedure outlined by Donelick *et al.* (1999), to transpose all track lengths to their equivalent *c*-axis parallel length removes this bias. Track length distributions from  $^{252}\text{Cf}$  irradiated samples can only be correctly modelled by the Ketcham *et al.* (1999) annealing model.

## 2.3 Zircon fission track thermochronology

Zircon is a common accessory mineral in a wide variety of rocks, and its chemical stability and high uranium and thorium contents make it highly suitable for geochronology. Although it was

one of the first minerals to be dated using the fission track technique [Fleischer & Price, 1964], the zircon fission track (ZFT) thermochronometer has remained largely undeveloped, and many of the controls on the annealing kinetics of fission tracks in zircon remain poorly constrained.

### 2.3.1 Zircon fission track annealing

The wide range of closure temperatures and partial annealing zones used in the existing zircon fission track (ZFT) literature reflects the uncertainty associated with fission track annealing in zircon [Fleischer *et al.*, 1965; Hurford, 1985; Zaun & Wagner, 1985; Hurford, 1986 and others]. Early laboratory annealing experiments based on track density reductions suggested that the lower boundary of the zircon partial annealing zone (PAZ) was approximately 310 - 350°C [Fleischer *et al.*, 1965], in poor agreement with evidence from natural samples, where ZFT ages were consistently younger than K-Ar ages from co-existing biotite micas ( $T_C = 300^\circ\text{C}$ ) [Harrison *et al.*, 1985]. Estimates from studies based on natural samples place the ZFT closure temperature at  $240^\circ \pm 50^\circ\text{C}$  [Hurford, 1985, 1986] from cooling curves determined from other geochronometers, while down-borehole age reductions linked to thermal annealing suggested  $T_C = 195^\circ \pm 20^\circ\text{C}$ , with a PAZ of 158 - 244°C [Zaun & Wagner, 1985].

Track shortening is more sensitive to small amounts of annealing than track density reductions, and is less affected by U zonation [Tagami, 1990; Carpena, 1992; Yamada *et al.*, 1993; Hasebe *et al.*, 1994; Yamada *et al.*, 1995a; Yamada *et al.*, 1995b; Tagami *et al.*, 1998; Hasebe *et al.*, 2003]. However, annealing and etching in zircon is more strongly anisotropic than in apatite, and to prevent this introducing a bias, only tracks at high angle to the *c*-axis are chosen for measurement [Yamada *et al.*, 1995a]. These are the tracks most sensitive to small amounts of annealing, and are those most easily revealed. Using this track selection criteria, experiments have shown that fission track annealing in zircon is non-linear with respect to temperature and time, and contours of equal track shortening plot as a series of parallel, sub-parallel, or curvilinear arrays on an Arrhenius plot [Yamada *et al.*, 1995b]. The similarity in the form of the zircon and apatite Arrhenius plots has been used to suggest that the annealing processes are broadly similar [Yamada *et al.*, 1995b].

Residual plots from best fitting equations suggest that the fanning model [Laslett *et al.*, 1987] best fits the data, predicting a zircon PAZ ~ 190 - 350°C [Yamada *et al.*, 1995b], but an improved statistical treatment suggests that the data was insufficient to distinguish between the fanning and parallel models [Galbraith & Laslett, 1997]. Further annealing experiments on zircon are required. Rigorous testing of the mathematical extrapolations is prevented by the limited number of natural samples that preserve evidence of thermal resetting of the ZFT system. Data from the Kontinentale Tiefbohrung [Coyle & Wagner, 1996], Kola [Green *et al.*, 1996], Vienna [Tagami *et al.*, 1996], and the Nishikubiki and Mishima [Hasebe *et al.*, 2003] ultra deep boreholes, and metamorphic aureoles

[Tagami & Shimada, 1996] implies that on geological timescales track-shortening does not occur below 200°C, and that the extrapolation of laboratory data is reasonable.

The PAZs predicted by the Yamada *et al.* (1995a) annealing models fit much of the experimental data, but they do not correlate well with the PAZs constrained by other techniques [Hurford, 1985; Zaun & Wagner, 1985]. In the AFT system chemical composition exerts substantial control over annealing kinetics, but it is the effects of radiation damage rather than chemistry that are thought to have the greater influence on annealing in zircon [Ewing *et al.*, 2003; Rahn *et al.*, 2004; Tagami, 2005; Tagami & O'Sullivan, 2005]. However, as up to 4% of Zr in natural zircon crystals can be substituted by REEs, it is possible that minor chemical controls have yet to be recognised.

### 2.3.2 The accumulation of radiation damage in zircon

Radiation damage to the crystal lattice leads to changes in chemical reactivity, and therefore both annealing and etching response [Balan *et al.*, 2001; Ewing *et al.*, 2003; Garver, 2003; Nasdala *et al.*, 2005].

#### 2.3.2.1 Fission fragments

The formation of ZFTs causes significant localised damage on a 10 µm length scale, and large numbers of defects are generated at each fission event ( $10^5 - 10^6$ ) [Nasdala *et al.*, 2005]. However, the probability of spontaneous fission is  $\sim 10^{-6}$  that of alpha decay, and therefore although only 700 - 2000 defects are generated during each alpha decay, the fission events make a negligible contribution to the total radiation damage.

#### 2.3.2.2 Recoil of heavy nuclides

The recoil of the heavy nuclei generated during  $\alpha$ -series decay is the dominant cause of crystal lattice damage [Weber *et al.*, 1997; Ewing *et al.*, 2003]. During each alpha decay event the low-energy (0.07 - 0.17 MeV), high mass daughter nucleus recoils a short distance (30 - 40 nm) through the crystal lattice. This causes a cascade of approximately 700 - 2000 permanent atomic displacements. Each decay generates an “ $\alpha$ -damage” cluster that can have sufficient defect density to generate an amorphous volume [Meldrum *et al.*, 1998; Nasdala *et al.*, 2005]. Zircons have typically high U contents, and as eight  $\alpha$ -decays occur during the series decay of  $^{238}\text{U}$ , seven during that of  $^{235}\text{U}$  and six during that of  $^{232}\text{Th}$ , there is often overlap of defect clusters. When this occurs (between  $2 \times 10^{15}$  to  $8 \times 10^{15}$   $\alpha$ -decay events/mg), there are significant changes to the crystal density and other physical properties [Ewing *et al.*, 2003 and refs. therein]. Although the  $\alpha$ -damage can be thermally annealed (see Section 2.3.3), the overlapping of defect clusters increases the stability of the amorphous volume, therefore requiring higher temperatures for lattice recovery

[Murakami *et al.*, 1991; Jonckheere & Gogen, 2001; Ewing *et al.*, 2003; Palenik *et al.*, 2003; Nasdala *et al.*, 2005]. The accumulation of  $\alpha$ -damage eventually leads to the onset of metamictisation at  $\sim 3.5 \times 10^{15}$   $\alpha$ -decay events/mg [Ewing *et al.*, 2003; Palenik *et al.*, 2003; Bernet *et al.*, 2004]. Other authors report fully metamict zircon crystals at doses of  $\sim 10^{16}$  events per mg [Murakami *et al.*, 1991; Ewing *et al.*, 2003; Nasdala *et al.*, 2005]. The rates of U- and Th- series decay are accurately known, and so for any U and Th concentration and accumulation time, the number of decay events that have occurred can be calculated.

### 2.3.2.3 Recoil of $\alpha$ -particles

Compared to the recoil of the heavy nuclei, the  $\alpha$ -particles generated during series decay of  $^{238}\text{U}$ ,  $^{235}\text{U}$  and  $^{232}\text{Th}$  are relatively inefficient at generating defects. To conserve momentum, 98 % of the energy of the decay is lost to  $\alpha$ -particle, but the  $\alpha$ -particle generates only 15 % of the total number of  $\alpha$ -decay related defects [Nasdala *et al.*, 2005]. The high-energy (4.0 - 8.8 MeV)  $\alpha$ -particles lose most of their energy through ionisation of the crystal structure, then generate scattered point defects as they come to rest 10 - 20  $\mu\text{m}$  from the decay site. These isolated point defects appear to have long-term stability and cause small-scale complexities in the distribution of radiation damage [Nasdala *et al.*, 2005].

## 2.3.3 Annealing and radiation damage

Variation in  $\alpha$ -damage dose is thought to account for many of the discrepancies between the zircon fission track PAZs predicted from the different annealing experiments and those inferred from other techniques [Hurford, 1985; Zaun & Wagner, 1985; Hurford, 1986; Yamada *et al.*, 1995b]. Many ZFT annealing experiments are based on induced tracks in samples that were annealed at high temperatures ( $> 1000^\circ\text{C}$ ) prior to irradiation, but Rahn *et al.* (2004) re-evaluated the data from several studies describing annealing behaviour in zircons with some degree of  $\alpha$ -damage [Kasuya & Naeser, 1988; Carpena, 1992; Yamada *et al.*, 1995b] [Zaun & Wagner, 1985; Kasuya & Naeser, 1988; Tagami, 1990; Tagami *et al.*, 1998]. From this analysis, it is suggested that the laboratory experiments represent “zero  $\alpha$ -damage” annealing. This provides a possible explanation for the discrepancies between the higher temperatures of the PAZs predicted from some annealing experiments (zero damage), and the lower, and varied temperatures of the PAZs observed in boreholes and inferred from other geological constraints (highly variable amounts of  $\alpha$ -damage) (Figure 3).

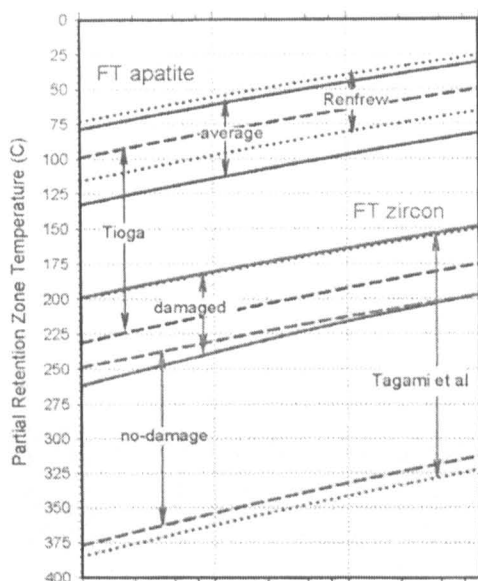


**Figure 3 - The effect of increasing alpha radiation dose on annealing, and the location of the partial annealing zone [Ehlers *et al.*, 2005].**

The ability of the zero  $\alpha$ -damage model to accurately describe the annealing of induced fission tracks in thermally annealed zircons (heated for 2hr at  $>1000^{\circ}\text{C}$ ) suggests that these heating conditions are sufficient to repair both fission tracks and  $\alpha$ -damage. It is thought that the annealing of  $\alpha$ -damage and fission tracks begins at similar temperatures ( $450 - 500^{\circ}\text{C}$  for heating of 1hr) [Rahn *et al.*, 2004], although some workers report the onset of  $\alpha$ -damage annealing at significantly higher temperatures; from  $550 - 600^{\circ}\text{C}$  [Yamada *et al.*, 1995b] to in excess of  $750^{\circ}\text{C}$  [Murakami *et al.*, 1991].  $\alpha$ -damage annealing is thought to begin at temperatures close to those of ZFT annealing in “low damage” zircons with  $\alpha$ -doses in the order  $\sim 4 \times 10^6 \text{ cm}^{-2}$  [Rahn *et al.*, 2004], and the zero damage model suggests an empirical function describing the effect of  $\alpha$ -damage on the observed fission track annealing may be determined from further annealing experiments on natural samples with variable degrees of radiation damage. The variation of U and Th in natural crystals means that every zircon crystal will anneal differently. Until the effects of radiation damage on annealing kinetics are fully understood, the crystal specific closure temperature cannot be determined.

### 2.3.3.1 Radiation damage and etching response

Zircon has highly anisotropic etching characteristics, and careful control of the etching conditions is needed to ensure the effect of preferential etching does not bias length measurements [Yamada *et al.*, 1993, 1995a; Yamada *et al.*, 1995b; Bernet *et al.*, 2004]. As radiation damage is accumulated, the break-down of crystallinity increases chemical reactivity and reduces the time and the anisotropic nature of the etching. Short etching times will reveal tracks in those grains that are old, or that have high U and Th contents, whereas excessive etching will ensure that only those young, low U and Th grains are countable. To minimise the effects of anisotropy and etching bias in any sample, only those crystals that show a pre-determined amount of etching are counted. The etching

conditions required for track density measurements are insufficient to fully reveal confined tracks. For track density measurements tracks intersecting the free surface are required to be approximately 1  $\mu\text{m}$  in diameter [Tagami, 1990; Hasebe *et al.*, 1994]. Etching is generally performed in one of two ways; either by stepwise incremental etching until the correct etch pit diameter is achieved, or by the etching of multiple grain mounts for different lengths of time. The highly variable etch times required to reveal tracks in natural samples suggests that the effects of radiation damage on etching are apparent even at low radiation doses. If crystallinity is affected at low radiation doses, there is a strong possibility that annealing is also effected. Further studies may constrain this effect and enable the extraction of additional thermochronological information [after Lovera *et al.*, 1997, 2002].

## 2.4 Apatite (U-Th)/He thermochronology

The (U-Th)/He chronometer was one of the first radiometric systems to be considered for the absolute dating of geological samples [Rutherford, 1905; Strutt, 1905], but the technique was abandoned after several workers found (U-Th)/He ages to be much younger than the age of crystallisation [Strutt, 1910a, 1910b, 1910c; Hurley, 1954; Hurley *et al.*, 1956; Fanale & Kulp, 1961; Damon & Green, 1963]. It was Strutt (1910c) who first noted that the young (U-Th)/He ages were caused by helium leakage, but the thermochronological application of this leakage was not realised until much later. In the mid 1980's renewed interest in the technique followed the publication of a series of diffusion experiments suggesting that, while retained in apatite at earth surface conditions, temperatures of  $\sim 100^\circ\text{C}$  allowed the complete diffusive loss of radiogenic helium [Zeitler *et al.*, 1987]. These results allowed the re-interpretation of the "anomalously" young data, and showed (U-Th)/He ages to be a record of cooling through very low temperatures [Zeitler *et al.*, 1987].

### 2.4.1 Helium production

The majority of  $^4\text{He}$  is produced through the radioactive decay of  $^{238}\text{U}$ ,  $^{235}\text{U}$ , and  $^{232}\text{Th}$ . Each of these parent isotope series ultimately decay to different isotopes of lead (Equation 8 to Equation 10 after Farley 2002), producing several  $^4\text{He}$  nuclei, during a series of decay events.  $^{147}\text{Sm}$  undergoes a single decay to  $^{143}\text{Nd}$  (Equation 11) producing a single alpha particle. Each decay series has a characteristic decay constant,  $\lambda^x$ , and the energies produced at each intermediate decay can be summed as  $Q_{(x)}$  (MeV).

$$^{238}\text{U} \Rightarrow \text{Pb} + 8\alpha + \beta + Q_{238} \quad \lambda^{238} = 1.552 \times 10^{-10} \text{ y}^{-1}$$

Equation 8

$$^{235}\text{U} \Rightarrow ^{207}\text{Pb} + 7\alpha + 4\beta + Q_{235} \quad \lambda^{235} = 9.848 \times 10^{-10} \text{ y}^{-1}$$

Equation 9

$$^{232}\text{Th} \Rightarrow ^{208}\text{Pb} + 6\alpha + 4\beta + Q_{232} \quad \lambda^{232} = 4.947 \times 10^{-11} \text{ y}^{-1}$$

Equation 10

$$^{147}\text{Sm} \Rightarrow ^{143}\text{Nd} + \alpha + Q_{147} \quad \lambda^{147} = 6.538 \times 10^{-12} \text{ y}^{-1}$$

Equation 11

These equations can be combined to form a single equation for the total  $^4\text{He}$  production (Equation 12), where  $^4\text{He}$ ,  $^{238}\text{U}$ ,  $^{235}\text{U}$ ,  $^{232}\text{Th}$  and  $^{147}\text{Sm}$  are the present day concentrations (numbers of atoms),  $t$  is the accumulation time, and  $\lambda^x$  the decay constants as listed above.

$$^4\text{He} = 8 ^{238}\text{U} (e^{\lambda^{238}t} - 1) + 7 ^{235}\text{U} (e^{\lambda^{235}t} - 1) + 6 ^{232}\text{Th} (e^{\lambda^{232}t} - 1) + ^{147}\text{Sm} (e^{\lambda^{147}t} - 1)$$

Equation 12

This equation can be simplified using the constant natural  $^{235}\text{U}/^{238}\text{U}$  of 1/137.88, therefore removing the need for direct measurement of both isotopes. The  $^{147}\text{Sm}$  term can be disregarded in many samples, as  $^{147}\text{Sm}$  makes up only 15 % of the Sm, and although  $^{147}\text{Sm}$  is not routinely measured by many laboratories, bulk ppm is typically low and is generally insignificant unless U and Th contents are very low [Farley, 2002]. Thus Equation 12 becomes:

$$^4\text{He} = \left[ 8 ^{238}\text{U} (e^{\lambda^{238}t} - 1) + 7 \left[ \frac{1}{137.88} \right] ^{238}\text{U} (e^{\lambda^{238}t} - 1) \right] + 6 ^{232}\text{Th} (e^{\lambda^{232}t} - 1)$$

Equation 13

where  $^4\text{He}$ ,  $^{238}\text{U}$ , and  $^{232}\text{Th}$  are the present day concentrations (atoms), and  $t$  is the accumulation time. After measurement of  $^4\text{He}$ ,  $^{238}\text{U}$ , and  $^{232}\text{Th}$ , this equation can be solved iteratively to determine the accumulation time.

As with all radiometric systems, the correct calculation of  $t$  is only possible when certain criteria are met.

(i) The initial concentration of  $^4\text{He}$  must be known. In apatite, this initial  $^4\text{He}$  concentration is assumed to be zero, as the low atmospheric  $^4\text{He}$  content (5 ppm) and fast diffusion of  $^4\text{He}$  in apatite (discussed in Section 2.4.2) makes trapped atmospheric  $^4\text{He}$  unlikely. The high rate of diffusion also makes the  $^4\text{He}$  inheritance improbable [Farley, 2002]. When this assumption fails, it generally does so through the presence of fluid inclusions trapped within the crystal. These can contain variable and often large amounts of  $^4\text{He}$  from mantle or crustal sources, and this excess  $^4\text{He}$

component has no measurable parent U and Th, and so generates excessively old and poorly reproducing ages [Farley, 2002; Persano *et al.*, 2002]. To avoid these problems every effort is made during crystal selection (Section 3.6.1), to discard crystals containing fluid inclusions, however small inclusions may be overlooked. Initial  $^4\text{He}$  concentrations can also be affected by the implantation of helium from U-Th-rich minerals adjacent to, or present as inclusions in the apatite (see Section 2.4.3.1).

(ii) Secular equilibrium must be established between all intermediate actinides prior to the onset of  $^4\text{He}$  accumulation. This steady state decay is reached when the rates of production and decay of each intermediate actinide are equal. From any initial starting condition, this is established after five half-lives of the longest-lived intermediate daughter actinide. Within the  $^{238}\text{U}$ ,  $^{235}\text{U}$  and  $^{232}\text{Th}$  decay chains  $^{234}\text{U}$  is the longest-lived intermediate decay product, and has a half-life of 248 kyr. This limits the application of the (U-Th)/He thermochronometer to cases where crystallization occurred  $> 1$  Myr before the onset of helium accumulation [Farley, 2002].

(iii) Once accumulation has begun, the concentration of U and Th within the crystal must only be altered by radioactive decay. The introduction or removal of U, Th or any intermediate daughter actinide by non radiogenic processes will alter parent-daughter ratios, temporarily disrupt the equilibrium, and change the rate of  $\alpha$ -particle production. The use of Equation 13 then leads to inaccuracies in the calculated ages.

U and Th can be mobilised in fluids, and Th mobilisation can trigger the exsolution of small monazite crystals within the apatite grain [Harlov & Forster, 2003]. Although mobilisation is thought to occur at temperatures of  $\sim 300^\circ\text{C}$  [Harlov *et al.*, 2002; Harlov & Forster, 2003], well above the  $T_c$  of the (U-Th)/He system, care should be taken in sample and grain selection to minimise any potential fluid-rock interaction.

Studies have modelled the U and Th decay series in disequilibria [Bender, 1973; Farley *et al.*, 2002], in an attempt to determine (U-Th)/He formation ages from very young samples ( $< 1$  Ma). These show that the typical U and Th content of apatite is insufficient to generate measurable concentrations of daughter nuclides, and large uncertainties are introduced when measuring the low concentrations of  $^4\text{He}$  [Farley *et al.*, 2002]. Minerals such as zircon and monazite hold more potential for the (U-Th)/He dating of formation ages for young samples.

## 2.4.2 Helium diffusion in apatite

The step-heating diffusion experiments performed by Zeitler *et al.* (1987) first determined the low closure temperature of the apatite (U-Th)/He system. Subsequent laboratory heating experiments [Zeitler *et al.*, 1987; Lippolt *et al.*, 1994; Wolf *et al.*, 1996; Warnock *et al.*, 1997; Farley, 2000;

Reiners & Farley, 2001; Farley, 2002] have shown that below  $\sim 400^\circ\text{C}$  diffusion in apatite occurs by single mechanism thermally-activated volume diffusion, and obeys the Arrhenius relationship:

$$\frac{D}{a^2} = \frac{D_0}{a^2} e^{-E_a/RT}$$

Equation 14

where  $D$  is the rate of diffusion,  $D_0$  diffusivity at infinite temperature,  $a$  the diffusion domain radius,  $E_a$  the activation energy,  $R$  the gas constant, and  $T$  the Kelvin temperature. Measurements of  $\ln(D/a^2)$  plot as a linear function of  $1/T$  on the Arrhenius plot, with a y intercept of  $\ln(D_0/a^2)$  and a gradient of  $-E_a/R$  (Figure 4). Above  $\sim 400^\circ\text{C}$  the Arrhenius plot becomes curved, implying more complex diffusion behaviour [Wolf *et al.*, 1996; Warnock *et al.*, 1997].

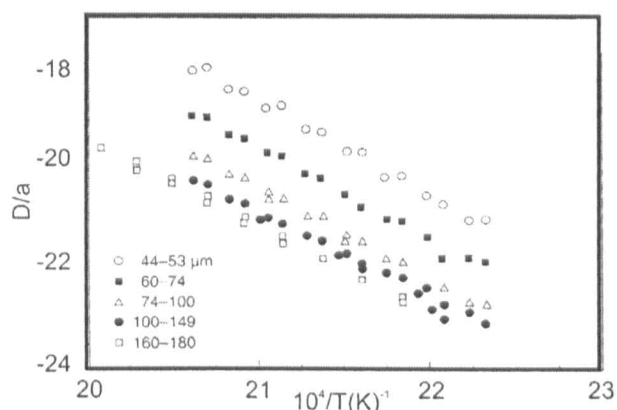
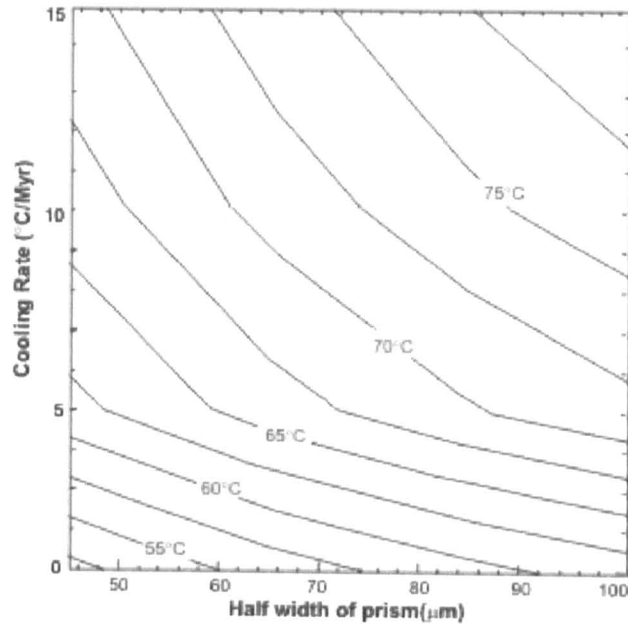


Figure 4 - The Arrhenius plot for helium diffusion in apatite [Farley, 2000]. The plot shows the relationship between diffusivity and  $1/T$ . The constant gradient with increasing grain size indicates that the diffusion domain is the crystal.

Heating experiments carried out on fragments of Durango apatite showed that the parameter  $D/a^2$  varies with grain size, and that the diffusion domain radius is the minimum grain dimension (usually grain radius or crystal half width in typically elongate apatite crystals) [Warnock *et al.*, 1997; Farley, 2000; Farley & Stockli, 2002]. This has been corroborated by studies of diffusion in a number of other apatites [Reiners & Farley, 2001].  $T_C$  can be computed from Equation 14 for individual crystal dimensions [Dodson, 1973]. For typical grains (between 50 and 150  $\mu\text{m}$ )  $T_C$  lies between  $63^\circ\text{C}$  and  $72^\circ\text{C}$ , for cooling rates of  $10^\circ\text{C}/\text{Myr}$  (Figure 5).

Apparent ages for crystals held at constant temperature, presented by Wolf *et al.* (1998), demonstrated that for typically-sized apatite crystals (30 - 100  $\mu\text{m}$  radius) retention begins as the temperature of the sample falls below *c.*  $80^\circ\text{C}$ , and diffusion effectively ceases at *c.*  $40^\circ\text{C}$ . The rapid increase in helium retention over this temperature interval has led to the definition of a helium partial retention zone (PRZ). The boundaries of the PRZ are defined as the temperatures at which diffusion causes 5 % and 95 % He loss [Wolf *et al.*, 1998]. The precise location of the PRZ is therefore dependant on crystal size.



**Figure 5 - The variation of the apatite (U-Th)/He closure temperature.**

The relationship between the closure temperature (shown in red), grain size and the cooling rate, based on diffusion from spherical geometries [from Farley, 2002].

There is a slight preferential diffusion along the apatite crystallographic *c*-axis, and so crystal geometry will affect diffusion [Warnock *et al.*, 1997]. Apatite typically forms elongate hexagonal crystals, and although sub-rounded and rounded detrital apatites are also dated using (U-Th)/He, diffusion models that consider finite cylindrical or hexagonal prism geometries will be more appropriate than spherical models [Farley, 2002; Meesters & Dunai, 2002a]. Meesters & Dunai (2002a) showed the importance of crystal geometry of the diffusion domain, but more crucially showed that preferential diffusion is controlled by the surface area-to-volume ratio of the crystal. For crystals of different geometries, but identical surface area-to-volume ratios, differences in diffusive behaviour are negligible [Meesters & Dunai, 2002a].

### 2.4.3 Alpha particle ejection ( $\alpha$ -recoil)

To conserve energy and momentum, the energy generated at each  $\alpha$ -decay is imparted to the daughter products as kinetic energy. The high-mass radiogenic daughter nuclide travels approximately 30 nm through the apatite lattice before coming to rest, whereas the low-mass  $\alpha$ -particle moves 10 - 20  $\mu\text{m}$  away from the decay site. The distance each  $\alpha$ -particle travels before coming to rest is controlled by the kinetic energy of the  $\alpha$ -particle and the density of the mineral through which it is moving, and is known as the “stopping distance”, *S*. The stopping distances of  $\alpha$ -particles produced by each stage of the U and Th decay series are well established for apatite and other accessory minerals [Zeigler, 1977]. Monte Carlo modeling has showed that although each decay has a unique stopping distance, using the series averaged stopping distances of each

decay series (Table 1) introduces minimal error into the calculation of the spatial distribution of helium [Farley, 2002].

	Apatite	Titanite	Zircon
$^{238}\text{U}$ series averaged ( $\mu\text{m}$ )	19.68	17.78	16.65
$^{235}\text{U}$ series averaged ( $\mu\text{m}$ )	22.83	21.01	19.64
$^{232}\text{Th}$ series averaged ( $\mu\text{m}$ )	22.46	20.88	19.32

**Table 1 - The series averaged alpha particle stopping distances in common accessory minerals [after Farley, 2002].**

Each  $\alpha$ -particle moves through the crystal lattice, away from the decay site in a random radial direction, and will come to rest on the surface of sphere, of radius  $S$ , causing a spatial separation of the radiogenic products (Figure 6 A). When decay events occur less than one stopping distance ( $\sim 20 \mu\text{m}$ ) from the surface of the crystal a proportion of the  $\alpha$ -particles generated at the decay site will come to rest outside the crystal (Figure 6), and are lost from the crystal. The fraction of  $\alpha$ -particles retained within any apatite is defined as  $F_T$ . If the generation of  $\alpha$ -particles is assumed to be homogeneous and ejection is the only mechanism by which  $\alpha$ -particles are lost, then the fraction of  $\alpha$ -particles retained will decrease from 100 % (decay sites more than  $\sim 20 \mu\text{m}$  from the crystal surface) to 50 % (decay sites on the crystal surface) as shown in Figure 6 B)

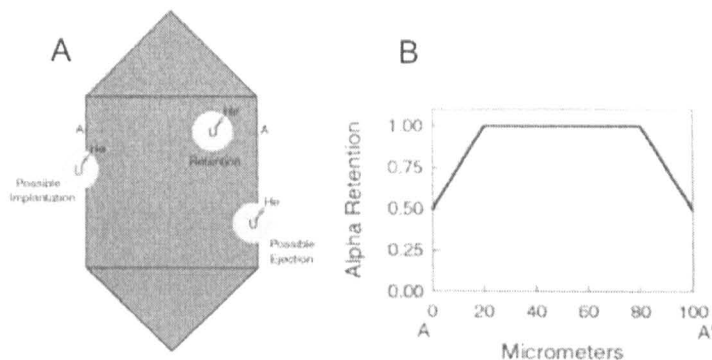


**Figure 6 - A schematic representation of  $\alpha$ -recoil from apatite crystals.**

**A)** The movement of the  $\alpha$ -particle through the apatite lattice from the site of the U nucleus [from Farley, 2000].

**B)** The fraction of  $\alpha$ -particles retained across the profile A-A' shown in A for a 100  $\mu\text{m}$  wide crystal. This profile is correct when there is a homogeneous distribution of parent nuclide, and ejection is the only mechanism for the redistribution of  $\alpha$ -particles.

With a homogeneous distribution of U and Th,  $F_T$  is dependent on the crystal geometry and the stopping distance and can be calculated for different geometries.  $^4\text{He}$  measurements cannot include the ejected  $\alpha$ -particles, but the accurate calculation of  $F_T$  allows correction for the proportion of  $\alpha$ -particles lost if all crystal dimensions are carefully measured prior to analysis. For simple spherical geometries,  $F_T$  can be easily computed by Equation 15:

$$F_T = 1 - \frac{3S}{4R} + \frac{S^3}{16R^3}$$

**Equation 15**

where  $S$  is the average stopping distance of the  $\alpha$ -particles and  $R$  is the grain radius [Farley *et al.*, 1996]. For most apatites the grain radius is much larger than the stopping distance, thus the  $S^3$  term tends to zero and Equation 15 becomes:

$$F_T = 1 - \frac{3S}{4R}$$

Equation 16

Monte Carlo modelling has shown that using the average stopping distance of each decay series (Table 1) introduces minimal errors into the calculation, and significantly reduced computing time [Farley *et al.*, 1996]. Spherical crystal geometry is uncommon in apatite, and therefore incorrectly modelling elongate cylindrical or hexagonal grains as perfect spheres is a source of error. Monte Carlo modelling is required to determine  $F_T$  values for more realistic, finite cylindrical and finite hexagonal geometries [Farley *et al.*, 1996; Farley, 2002], and the results show that for typical geometries, the  $F_T$  can be described by the second order polynomial;

$$F_T = 1 + a\beta + b\beta^2$$

Equation 17

where  $a$  and  $b$  are fitting parameters incorporating the average mineral density and decay specific stopping distance, and  $\beta$  is the surface to volume ratio calculated from length  $L$ , and radius  $R$  or half-width of the crystal. The similarity of the mean stopping distances in the  $^{235}\text{U}$  and  $^{232}\text{Th}$  series (Table 1), allows further simplification as both are fitted by essentially the same polynomial curve, hence in all subsequent modelling only two sets of fitting parameters are reported [Farley *et al.*, 1996; Farley, 2002]. Farley (2002) determined that for a finite hexagonal prism these parameters are  $a = -5.31$  and  $b = 6.78$  for  $^{238}\text{U}$  and  $a = -5.90$  and  $b = 8.99$  for  $^{235}\text{U}$  and  $^{232}\text{Th}$ . It should be noted that the modelling presented by Farley *et al.* (1996) and Farley (2002) does not take into account the effect of crystal terminations. Several workers have also investigated  $\alpha$ -particle recoil for tetragonal geometries such as zircon, which is discussed in Section 2.5.3. Comparing the results of the Monte Carlo simulations with those of the spherical model shows that for very large crystals the assumption of spherical geometry introduces minimal errors, but that at typical crystal sizes (30 - 100  $\mu\text{m}$  radius) the difference between the spherical and hexagonal  $F_T$  is approximately 13 %.

$\alpha$ -particles generated by  $^{238}\text{U}$  decay have a shorter stopping distance than those generated by  $^{235}\text{U}$  and  $^{232}\text{Th}$  (Table 1), and a greater proportion of  $^{238}\text{U}$  generated  $\alpha$ -particles are retained. Calculation of the mean  $F_T$  therefore requires a weighting factor,  $a_{238}$  to account for the relative proportion of the parent isotopes [Farley, 2002]. The mean  $F_T$  is calculated from Equation 18.

$$\text{mean } F_T = a_{238} \cdot [^{238}\text{U}] F_T + (1 - a_{238}) \cdot [^{232}\text{Th}] F_T$$

Equation 18

where  $a_{238}$  can be determined directly from measured values and Equation 13 [Farley, 2002], or can be approximated using:

$$a_{238} = \left( 1.04 + 0.245 \left( \frac{Th}{U} \right) \right)^{-1}$$

Equation 19

This mean  $F_T$  value is then used to correct the measured ages:

$$\text{Measured age} = \text{mean } F_T \times \text{Corrected age}$$

Equation 20

The dependence of  $F_T$  on  $\beta$  means that  $\alpha$ -particle recoil from finite cylindrical and hexagonal geometries can be accurately described by the spherical model, provided the crystal radius is correctly scaled. Apatite crystals and model spheres of the same surface area-to-volume ratio will have the same  $F_T$  [Meesters & Dunai, 2002a].

### 2.4.3.1 Alpha Implantation

When using Equation 13 to generate (U-Th)/He ages, it is assumed that all  $\alpha$ -particles are generated from U and Th decay within the apatite lattice. The large separation between the decay site and the resultant  $\alpha$ -particle introduces two sources for non-lattice generated  $\alpha$ -particles. Firstly, helium can be implanted from U-, Th-, and Sm-rich phases bounding the apatite. In most sedimentary and metamorphic rocks, the surrounding matrix contains negligible amounts of U and Th, making implantation insignificant, but in some igneous rocks apatite is commonly found in contact with apatite, zircon, monazite, and other high U and Th minerals. In most cases, the fraction of  $\alpha$ -particles implanted will be negligible, but it is necessary to characterise mineral assemblages in samples from inspection of thin sections to determine the probability of implantation.

$\alpha$ -particles can also be implanted from U-, Th-, and Sm-rich mineral inclusions within the apatite crystal. Mineral inclusions in apatite are common, and although standard selection procedures (Section 3.6.1) ensure crystals hosting inclusions are discarded, it is still possible for small (few  $\mu\text{m}$ ) inclusions to be missed, especially when they are obscured by diffraction close to the crystal faces. Zircon and monazite are two of the most common mineral inclusions in apatite, and both typically contain sufficient U, Th and Sm (from 100's ppm to several wt %) to eject large quantities of radiogenic helium from very small inclusions. Once inclusion generated  $\alpha$ -particles are implanted into the surrounding apatite, they are indistinguishable from the apatite generated component.

When the mineral inclusions are small ( $< \sim 20 \mu\text{m}$ ), all inclusion-generated  $\alpha$ -particles are ejected from the inclusion. Because of the relatively low U and Th content of the apatite, and the higher densities and lower diffusivities of the mineral inclusions,  $\alpha$ -particle implantation into inclusions is negligible. Complete  $^4\text{He}$  extraction is therefore usually obtained by standard outgassing techniques, but routine apatite dissolution methods are insufficient to recover the U, Th and Sm from the inclusions. The inclusion-generated helium is therefore parentless and (U-Th)/He ages will be excessively old and poorly reproducible. When large inclusions ( $> \sim 20 \mu\text{m}$ ) are overlooked during crystal selection, a proportion of  $^4\text{He}$  will be retained within the inclusion. In these cases the temperature and duration of the standard apatite helium extraction may be insufficient to ensure complete  $^4\text{He}$  extraction, and the differing diffusion kinetics of the apatite and the inclusion can lead to significant  $^4\text{He}$  extraction during subsequent heating cycles.

#### 2.4.4 Modelling diffusion and ejection

Much of the modelling of both diffusion [Wolf *et al.*, 1998] and ejection [Farley *et al.*, 1996] discussed in the previous sections considers diffusion and  $\alpha$ -ejection as two entirely independent processes. As  $\alpha$ -ejection operates at all temperatures and decreases the concentration of helium close to the crystal surface, the diffusion experiments performed on internal fragments of larger crystals do not incorporate the effect of this helium concentration gradient.

The assumption that the processes are independent is only valid when diffusion effectively ceases at the onset of helium accumulation, i.e. for samples that pass rapidly through the PRZ. In these samples, essentially all  $^4\text{He}$  loss is through  $\alpha$ -particle ejection, and the (U-Th)/He ages of rapidly cooled samples will represent the age of the cooling event. In samples that have cooled more slowly, both loss mechanisms will operate simultaneously, with  $\alpha$ -ejection maintaining a helium concentration gradient close to the surface of the crystal, thereby reducing the rate of diffusion at any given temperature. For samples with complex cooling histories, the combined effects of diffusion and  $\alpha$ -particle ejection make it possible for several time-temperature paths to yield the same (U-Th)/He age.

The combined effects of both loss mechanisms to be investigated using the DECOMP software program [Meesters & Dunai, 2002a], and this now enables detailed data driven consideration of the geological significance of (U-Th)/He ages from a range of cooling histories. DECOMP uses a spherical crystal geometry to forward model the raw, uncorrected ages that would result from different time-temperature paths, and for different grain sizes and apatite U/Th. Multiple time-temperature paths can lead to the same (U-Th)/He age, but the dependence of closure temperature on grain radius, the (U-Th)/He ages obtained from different size fractions can often refine the thermal history. However, sometimes further constraint (such as stratigraphy or AFT data) is

required before it is possible to determine the correct T-t path from the envelope of possible histories identified by the forward modelling.

### 2.4.5 Zonation

Initial studies concluded that unless the U and Th zonation is extreme, it has little effect on calculated (U-Th)/He ages [Farley *et al.*, 1996; Wolf *et al.*, 1998], and until recently the effect of zonation on apatite (U-Th)/He ages has been considered negligible. However, although U and Th zonation in apatite may be less extreme than in other accessory minerals, it is still common [Dempster *et al.*, 2003; Boyce & Hodges, 2005]. The enhanced diffusivity, and  $\alpha$ -ejection loss caused by the concentration of U and Th close to the crystal rims can clearly lead to significant underestimation of the (U-Th)/He ages.

The assumption of U-Th homogeneity can introduce errors into the calculation of the recoil correction  $F_T$  (see Section 2.4.3) For crystals with a surface area-to-volume ratio of  $0.03 \mu\text{m}^{-1}$ , the assumption of homogeneity underestimates the actual loss by 53 % ( $^{uniform}F_T = 0.85$ ,  $^{zoned}F_T = 0.45$ ). Alternatively, if all the U and Th is more than one stopping distance from the crystal surface then there is no recoil loss and  $^{zoned}F_T = 1$ . Heterogeneous U and Th distributions will also change the  $^4\text{He}$  concentration gradient and will therefore affect diffusion. For samples that have resided in the PRZ for considerable amounts of time zonation will alter the  $^4\text{He}$  concentration gradients within the crystal, and alter diffusive loss. Where the U and Th is in the crystal rim, diffusive loss will be greater than in crystals with homogeneous U and Th, or with enriched cores. Simple U and Th zonation in apatite can be modelled using the DECOMP software [Meesters & Dunai, 2002b], if the measured zonation patterns are correctly transposed into the spherical model.

#### 2.4.5.1 Zonation in mineral standards

Apatite (U-Th)/He ages are usually published with an uncertainty derived from the reproducibility of mineral standards. The apatite mineral standard, the Cerro de Mercado fluorapatite, from Durango, Mexico, has an accepted crystallisation age of  $31.44 \pm 0.18 \text{ Ma}$  (Ar-Ar) [Dempster *et al.*, 2003]. All (U-Th)/He laboratories report ages for Durango apatite that are within error of the accepted age, but the reproducibility of (U-Th)/He analyses are in the order of 6 - 8 %, significantly above the total analytical uncertainties of the technique (2 - 3%). (U-Th)/He analysis of Durango apatite is carried out on internal fragments of much larger gem quality apatite crystals, therefore the poor reproducibility cannot arise from poor crystal measurement or incorrect application of the  $F_T$  correction, as none is required. Recent laser ablation ICP-MS analysis performed by Boyce & Hodges (2005) suggests that poor reproducibility can be explained by observed differences in the U and Th zonation between crystal fragments.

Boyce & Hodges (2005) show that fragments of Durango apatite exhibit significant bulk U (10.1 - 15.0 ppm) and Th (203 - 329 ppm) variation, as has been shown in previous studies (9.7 - 12.3 ppm U and 167 - 238 ppm Th) [Young *et al.*, 1969]. Of more importance, the study showed significant variation in the U and Th content both within and between fragments. The U content varied between 10 - 15 ppm, and the Th between 203 - 329 ppm [Boyce & Hodges, 2005]. Two-dimensional numerical models show that the variable U and Th zonation can account for the several percent variation observed in the calculated age [Boyce & Hodges, 2005], and highlights the need to characterise zonation in (U-Th)/He mineral standards. Boyce & Hodges (2005) argue that the use of multiple internal fragments in aliquots, may lead to some averaging of the effects of zonation, as each aliquot should exhibit a variety of U and Th concentrations. However, the continuing trend for smaller aliquot sizes and single fragment analyses increasingly negates this averaging effect.

## 2.5 Zircon (U-Th)/He thermochronology

Other common U- and Th-rich accessory minerals (zircon, titanite, monazite and xenotime) are known to retain helium at earth surface temperatures, and have been considered as potential (U-Th)/He thermochronometers [Reiners & Farley, 1999; House *et al.*, 2000; Farley & Stockli, 2002; Reiners *et al.*, 2002]. The variations in diffusion kinetics between phases suggest that (U-Th)/He thermochronometry may be able to constrain large portions of thermal histories in a variety of geological settings [Reiners & Farley, 1999; House *et al.*, 2000; Farley & Stockli, 2002; Reiners *et al.*, 2002]. The limited number of studies highlight several additional factors that must be considered when undertaking zircon (U-Th)/He analysis, but they also show the great potential of the zircon (U-Th)/He system [Reiners *et al.*, 2002; Mitchell & Reiners, 2003; Tagami *et al.*, 2003; Reiners *et al.*, 2004; Hourigan *et al.*, 2005; Reiners, 2005; Reiners *et al.*, 2005].

### 2.5.1 Helium diffusion in zircon

Arrhenius plots from step heating diffusion experiments show a generally linear relationship between  $\ln(D/a^2)$  and  $1/T$ , and show a clear scaling of diffusion domain with grain size (Figure 7), indicating helium diffusion in zircon is dominantly a thermally activated volume diffusion process [Reiners *et al.*, 2002; Reiners *et al.*, 2004; Reiners, 2005]. However, significant discrepancy observed between the up- and down-temperature heating steps shows that the diffusive process is more complex during the early stages, and that for a given temperature the rate of diffusion is higher and more erratic during the early stages of the experiments. This anomalously high diffusion during the early stages of diffusion experiments is not unique to zircon, and has also been reported in monazite, titanite, xenotime and apatite [Farley & Stockli, 2002].

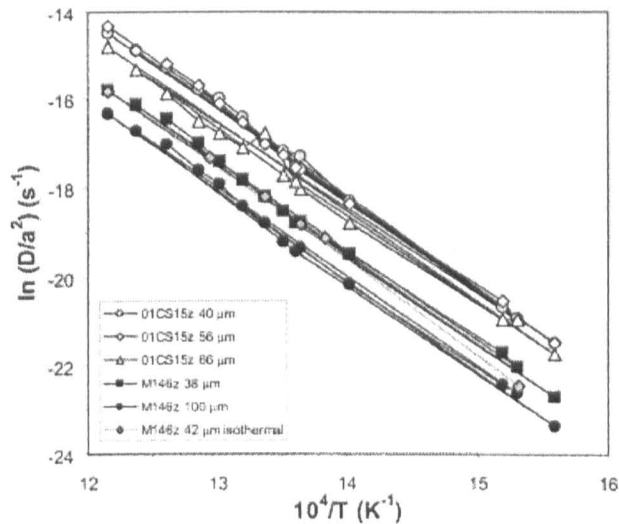


Figure 7 - The Arrhenius plot for helium diffusion in zircon [from Reiners *et al.*, 2004; Reiners, 2005]

The plot shows the linear relationship between  $\ln(D/a^2)$  and  $1/T$  which implies thermally activated volume diffusion. The relationship between the y intercept and crystal size suggests that the diffusion domain is the crystal itself.

Two mechanisms suggested for the origin of this variable behaviour are; the recovery of crystal structure through annealing of radiation damage during the high temperature stages [Reiners *et al.*, 2002; Reiners *et al.*, 2004], and differential diffusion from multiple domains during the early stages of the experiment [Reiners *et al.*, 2002; Reiners *et al.*, 2004]. Reiners *et al.* (2004) argue for the latter mechanism, showing that experiments with multiple low temperature isothermal heating steps that show the same reduction in diffusion over the length of the experiment (Figure 7), inferring no high temperature annealing control. The authors show that if diffusion remains constant throughout the experiment, as for Ar in K-feldspar, then the observed deviations from the Arrhenius trend are negligible after 5 - 10 % degassing. Reiners *et al.* (2004) use a comparison of the zircon data with forward modelling of multiple Ar-Ar diffusion domains, to suggest that the initial variable diffusion behaviour is caused by the degassing of a series of increasingly small, high diffusion domains (all  $< 2 \mu\text{m}$ ) containing a small proportion of the total helium budget (less than 3 %) [Lovera *et al.*, 1997, 2002; Reiners *et al.*, 2004]. Such small diffusion domains would have negligible effect on bulk crystal diffusivity and closure temperatures. Reiners *et al.* (2004) suggest that  $\alpha$ -radiation damage (as described in Section 2.3.2), anisotropy or multi-path diffusion may be possible mechanisms for the formation of these small diffusion domains [Reiners *et al.*, 2004].

The linear portions of the Arrhenius plots (as shown in Figure 7) indicate  $E_a = 163 - 173 \text{ kJ/mol}$  (39 - 41 kcal/mol),  $\log(D_0/a^2) = 3.7 - 4.7 \text{ s}^{-1}$ , and  $D_0 = 0.09 - 1.5 \text{ cm}^2/\text{s}$  [Reiners *et al.*, 2004; Reiners, 2005]. These ranges correspond to a closure temperature of 171 - 196°C for a crystal of 60  $\mu\text{m}$  radius at a cooling rate of 10°C/Myr. The average values of  $E_a = 169 \pm 3.8 \text{ kJ/mol}$  ( $40.4 \pm 0.9$

kcal/mol) and  $D_0 = 0.46^{+0.87}_{-0.30}$  cm<sup>2</sup>/s. The location of the zircon HePRZ, and its position relative to the apatite HePRZ is shown in Figure 8.

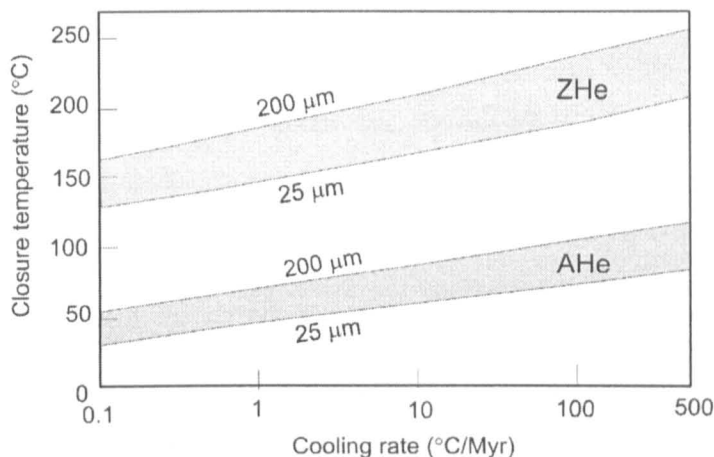


Figure 8 - The helium partial retention zone for apatite and zircon [from Farley *et al.*, 1996], for crystals between 25  $\mu\text{m}$  and 200  $\mu\text{m}$  in radius.

## 2.5.2 Radiation damage

In contrast to the complex controls seen in the ZFT system, the effect of radiation damage on helium diffusion in zircon is thought to be minimal. Reiners *et al.* (2004) and Nasdala *et al.* (2001, 2004) show that helium diffusion is identical in both young low U (120 Ma, 100 ppm) and old high U (440 Ma, 900 ppm) zircon, and that diffusion remains unchanged until total radiation doses exceed  $\sim 2 \times 10^{15}$   $\alpha$ -decay events/mg, which corresponds to the onset of double overlapping of  $\alpha$ -recoil damage zones [Nasdala *et al.*, 2001]. This radiation damage dose is equivalent to full damage retention over 0.6 - 4 Gyr for zircons with 100 - 1000 ppm U. Above this critical  $\alpha$ -dose there is a increase in the diffusivity, and Reiners (2005) reports extraction rates of 0.2 nmol/min from metamict zircon with  $\sim 5000$  ppm U, under vacuum at room temperature. The increase in diffusivity that is observed in zircons that have accumulated high doses of radiation damage is not observed in apatite. In apatite, recent studies have suggested that the increase in radiation damage actually reduced the rate of diffusion [Shuster *et al.*, 2006]. The origin of this very different diffusive behaviour is not yet understood.

Radiation damage is annealed at high temperatures, but as discussed above (Section 2.3.3), the kinetics of the process are poorly understood. Further characterisation of the effects of radiation damage at levels below the  $2 \times 10^{18}$   $\alpha$ /g cut off over long geological timescales is required, as U zonation may cause radiation damage to effect localised diffusion over the timeframes of some (U-Th)/He studies.

### 2.5.3 Alpha particle ejection ( $\alpha$ -recoil)

The higher density of zircon causes the  $\alpha$ -particle stopping distance of each decay to be shorter than in apatite (Table 1). Although Monte Carlo modelling of tetragonal pinacoidal prisms (tip height = 0) [Farley *et al.*, 1996; Farley, 2002] does not fully account for the decreased retention of He in the crystal terminations, it demonstrates that the empirical relationship between  $\beta$  and  $F_T$  (Equation 17) holds for tetragonal geometries. For pinacoidal tetragonal geometries the fitting parameters are :  $a = - 4.31$  and  $b = 4.92$  for  $^{238}\text{U}$ , and  $a = - 5.00$  and  $b = 6.80$  for  $^{235}\text{U}$  and  $^{232}\text{Th}$  [Farley, 2002]. When more realistic bi-pyramidal-terminated tetragonal prisms are considered, the relationship between  $\beta$  and  $F_T$  is maintained with the slightly modified fitting parameters of:  $a = - 4.281$   $b = 4.372$  for  $^{238}\text{U}$ , and  $a = - 4.869$  and  $b = 5.605$  for  $^{235}\text{U}$  and  $^{232}\text{Th}$  [Hourigan *et al.*, 2005]. A full discussion of the uncertainties introduced by the incorrect consideration of crystal geometry, and the available methods and models used for calculating  $\alpha$ -particle loss in zircon are presented in Chapter 4.

### 2.5.4 U and Th zonation in zircon

High bulk U and Th concentrations and highly variable U and Th zonation are common in many zircon samples [Hanchar & Hoskin, 2003]. Boyce & Hodges (2005) have shown that zonation of U and Th in Durango apatite can lead to significant scatter in the calculated ages, and so the U and Th zonation seen in zircons must be carefully considered. The only quantification of the distribution of U and Th in zircon to be reported in a (U-Th)/He study has used laser ablation ICP-MS to measure the concentration profiles [Hourigan *et al.*, 2005]. The limited availability of this technique has prompted the investigation of other, potentially routine microscopic methods for the determination of U- and Th-zonation in zircon. The Hourigan *et al.*, (2005) model allows the calculation of zonation specific  $\alpha$ -recoil corrections for rapidly cooled samples, but has limitations which are discussed in Chapter 4, together with a consideration of the combined effects of zonation, diffusive loss, and  $\alpha$ -recoil.

### 2.5.5 Mineral standards

Zircon (U-Th)/He ages are published with uncertainties derived from the  $2\sigma$  reproducibility of mineral standards. The Fish Canyon Tuff (FCT) is the only mineral standard that has been extensively analysed using the (U-Th)/He system. The FCT is widely used for technique intercalibrations, and is the dominant mineral standard used by the ZFT community. Fission track ages of  $26.8 \pm 4.2$  Ma ( $1\sigma$ ) (apatite) and  $27.9 \pm 2.2$  Ma ( $1\sigma$ ) (zircon) [Carpéna & Mailhé, 1987], show good agreement with the  $^{40}\text{Ar}/^{39}\text{Ar}$  ages of  $27.8 \pm 0.4$  Ma ( $2\sigma$ ) (biotite) [Hurford & Hammerschmidt, 1985] and  $28.03 \pm 0.36$  Ma ( $2\sigma$ ) (K-feldspar) [Renne *et al.*, 1994] and the zircon

U-Pb age of  $28.50 \pm 0.07$  Ma ( $2\sigma$ ) [Schmitz & Bowring]. Titanite (U-Th)/He ages of  $27.9 \pm 1.1$  Ma have been reported [House *et al.*, 2000]. The zircon (U-Th)/He ages reported from the laboratories making routine determinations are shown in Table 2.

Laboratory	Age	% Uncertainty
Yale [Reiners, 2005]	$28.3 \pm 2.6$ Ma ( $2\sigma$ , n = 83)	9.1 %
CalTech [Tagami <i>et al.</i> , 2003]	$28.6 \pm 2.8$ Ma ( $2\sigma$ , n = 12)	9.7 %
CPRG, [Pik pers com]	$28.7 \pm 5.1$ Ma ( $2\sigma$ , n = 16)	17.8 %

**Table 2 - The (U-Th)/He ages of the Fish Canyon Tuff zircon standard reported by the laboratories performing routine determination of zircon (U-Th)/He ages.**

The age reproducibility of the standard (more than  $\pm 9$  %) is significantly higher than analytical uncertainties (1 - 3 %). Mineral and fluid inclusions are thought to have a minimal effect on (U-Th)/He ages (see Section 3.7.1.2) so it is probable that the poor reproducibility of the FCT zircon (U-Th)/He ages is a result of U and Th zonation. U and Th zonation in zircon is common, and so the selection and characterisation of mineral standards is important for accurate age determinations and inter-laboratory calibration. The results of a complete and detailed characterisation of the Fish Canyon Tuff is presented in Chapter 5, together with a discussion on its suitability for use as a zircon (U-Th)/He standard.

## 2.6 Summary

The recent development of the apatite and zircon (U-Th)/He systems has provided two thermochronometric techniques to complement existing fission track methodologies. Combined application of multiple thermochronometers can now give better resolution of geological events, through the combination of inverse and forward modelling. With suitably rigorous analytical and interpretive techniques, new insight can be gained to a wide variety of geological processes, including the late stage cooling and denudation of igneous provinces under investigation here.

# 3

## Analytical techniques

### 3.1 Introduction

The first part of this chapter contains a description of sample preparation, analytical conditions and protocols of the established low temperature thermochronometer methodologies (apatite fission-track and (U-Th)/He) used during this study (Sections 3.2 to 3.5), following the principles outlined in Chapter 2. This is followed by a more substantial section (3.6) outlining the developmental work undertaken to establish a routine procedure for the determination of zircon (U-Th)/He ages at S.U.E.R.C..

### 3.2 Mineral separation

Samples were collected from a number of lithologies in the study area (see Chapter 6). Polished thin sections were then prepared from all samples. Between 2 and 10 kg of each rock sample was then disaggregated using a jaw crusher. The crushed material was passed through a 500  $\mu\text{m}$  mesh, and the fine fraction removed from further crushing. Once ~ 95 % of all ground material was < 500  $\mu\text{m}$ , the fine fraction was passed through a 355  $\mu\text{m}$  mesh. The coarse fraction (> 355  $\mu\text{m}$ ) was then passed through the crusher and sieved (355  $\mu\text{m}$  mesh) a final time. The < 355  $\mu\text{m}$  fraction was then washed in  $\text{H}_2\text{O}$ , and dried at room temperature under an extraction hood, before being passed through a 64  $\mu\text{m}$  mesh sieve to remove the remaining fines.

Two mineral separation procedures were used. For the majority of samples apatite (and zircon) recovery from the 355 - 64  $\mu\text{m}$  fraction was achieved using a Frantz LB-1 magnetic separator, followed by heavy liquid separation using either LST fast float<sup>TM</sup> (2.8  $\text{g}/\text{cm}^3$ ), or sodium polytungstate (2.9  $\text{g}/\text{cm}^3$ ). The dense fractions contained apatite, titanite and zircon. If zircon was abundant, it was separated using di-iodomethane (3.3  $\text{g}/\text{cm}^3$ ). A few samples with large-volume non-magnetic fractions were separated by a froth-flotation technique using sodium oleate ( $\text{C}_{18}\text{H}_{33}\text{NaO}_2$ ). Approximately 1 kg of sample was agitated with 5 ml of sodium oleate in 4 litres of de-ionised water. The sodium oleate preferentially coats the calcium-rich apatite grains, causing them to float, and become trapped in the foam at the surface. The foam was skimmed off and the

sodium oleate removed from the crystals by repeated ultrasonic baths in water and acetone, before density separation using sodium polytungstate if required. Although this process significantly reduced the volume of sample entering heavy liquid separation, and improved the quality of the apatite concentrate, the removal of the detergent from the crystals was a lengthy process requiring multiple rinses. Although some samples yielded very pure (> 95%) apatite separates from froth-floatation, the sample rinsing is very time consuming; this separation technique should therefore be restricted to samples with large-volume non-magnetic fractions with a high proportion of apatite. This method cannot be used for samples containing large volumes of calcium-bearing minerals as the oleate adheres to all Ca-rich crystals preventing the clean separation of the apatite.

In many samples the small volume and poor quality of apatite recovered meant that crystals were selected for (U-Th)/He before further processing for AFT analysis. Apatite crystals were hand picked to remove contaminant mineral grains (especially zircon) and apatites with large inclusions.

### 3.3 Sample characterisation

Initial microscopic inspection was performed on polished thin sections and grain mounts using cathodoluminescence (CL) illumination. Apatite and zircon are very distinctive under CL, with apatite typically emitting strongly in the orange and zircon in the blue-green, thus making assessment of mineral abundance possible at low-magnification. The quantity and quality of the apatite and zircon were assessed on a Zeiss Axioplan petrographic microscope fitted with CITL Technosyn 8200 Mk 4 CL system. In those thin sections where apatite and/or zircon were found, a more detailed study of the sample mineralogy, abundance of mineral and fluid inclusions, and determination of the common spatial mineral associations was performed on a Zeiss Axioplan petrographic microscope. Both microscopes were fitted with a Nikon DN100 Digital Net camera for image capture. The quality of the crystals and the possibility of helium implantation was assessed in all samples (see Section 2.4.3.1).

### 3.4 Apatite fission track analytical procedures

The grains were mounted in epoxy resin, polished, and etched in 5 M HNO<sub>3</sub> for 15 seconds (20°C). The etched samples were then shrink-wrapped in immediate contact with the mica external detectors, and then irradiated with  $1.0 \times 10^{16}$  ncm<sup>-2</sup> thermal neutrons at the High Flux Australian Reactor (HIFAR), Sydney. The neutron dose was monitored using the CN5 uranium glass dosimeter. After irradiation the micas were separated from the mounts and etched in 40 % HF for 40 minutes (20°C) to reveal the induced tracks. AFT ages were then determined using the external detector method [Hurford & Green, 1982], outlined in Chapter 2. Fission track ages, track length,

and  $d_{par}$  values were measured by Dr. Cristina Persano. All measurements were made on a Zeiss Axioplan Fission Track microscope, following Persano *et al.* (2005).

Low track densities meant track length distributions could not be determined on most samples. To increase the number of confined tracks revealed, additional polished grain mounts were irradiated using a  $^{252}\text{Cf}$  source by R. & M. Donelick, A to Z Inc. The irradiated grain mounts were etched for 15 seconds in 5 M  $\text{HNO}_3$  and the confined tracks measured using the procedures of Donelick *et al.* (1991). All modelling of AFT ages, and track length distributions were performed using AFTSolve and HeFTy [Ketcham *et al.*, 2000; Ketcham, 2005].

### 3.5 Apatite (U-Th)/He analytical procedure

The apatite (U-Th)/He analytical procedure follows that of Persano *et al.* (2005), with only minor variation, with initial helium extraction and measurement followed by second stage U and Th recovery. Two methods of helium extraction were used during this study. The majority of samples were degassed using a resistance furnace, but during the later stages of the project an 808 nm diode laser extraction system was installed. This led to adoption of modified He and U and Th analytical protocols [Foeken *et al.*, 2006]. Both analytical procedures and operating parameters are outlined below.

#### 3.5.1 Crystal selection and encapsulation

Inclusion- and crack- free apatites were selected under high magnification (up to 500 x) binocular polarising microscope (see Section 2.4.3.1). In apatite, small ( $< 1 \mu\text{m}$ ) fluid inclusions are easy to observe when the mineral is orientated in an extinction position, however mineral inclusions are less easily observed. Monazite and zircon inclusions are typically very small ( $< 5 \mu\text{m}$  in length,  $< 1 \mu\text{m}$  diameter) and acicular, and are easily missed when their crystallographic orientation is close to that of the host apatite, or if they are located close to the apatite crystal faces. To minimise the potential for inclusions being overlooked, all apatite crystals selected for (U-Th)/He analysis were double-checked by a second experienced analyst, before being sketched and measured using a  $10 \times 10 \mu\text{m}$  graticule. Only inclusion-free crystals  $\geq 40 \mu\text{m}$  in diameter and good crystal morphology were selected for analysis, as the uncertainties on measurements smaller than  $40 \mu\text{m}$  exceed 5 % (see discussion in Chapter 5). Where multiple crystals were analysed in each aliquot, they were selected for consistent diameter to ensure constant diffusion and ejection characteristics.

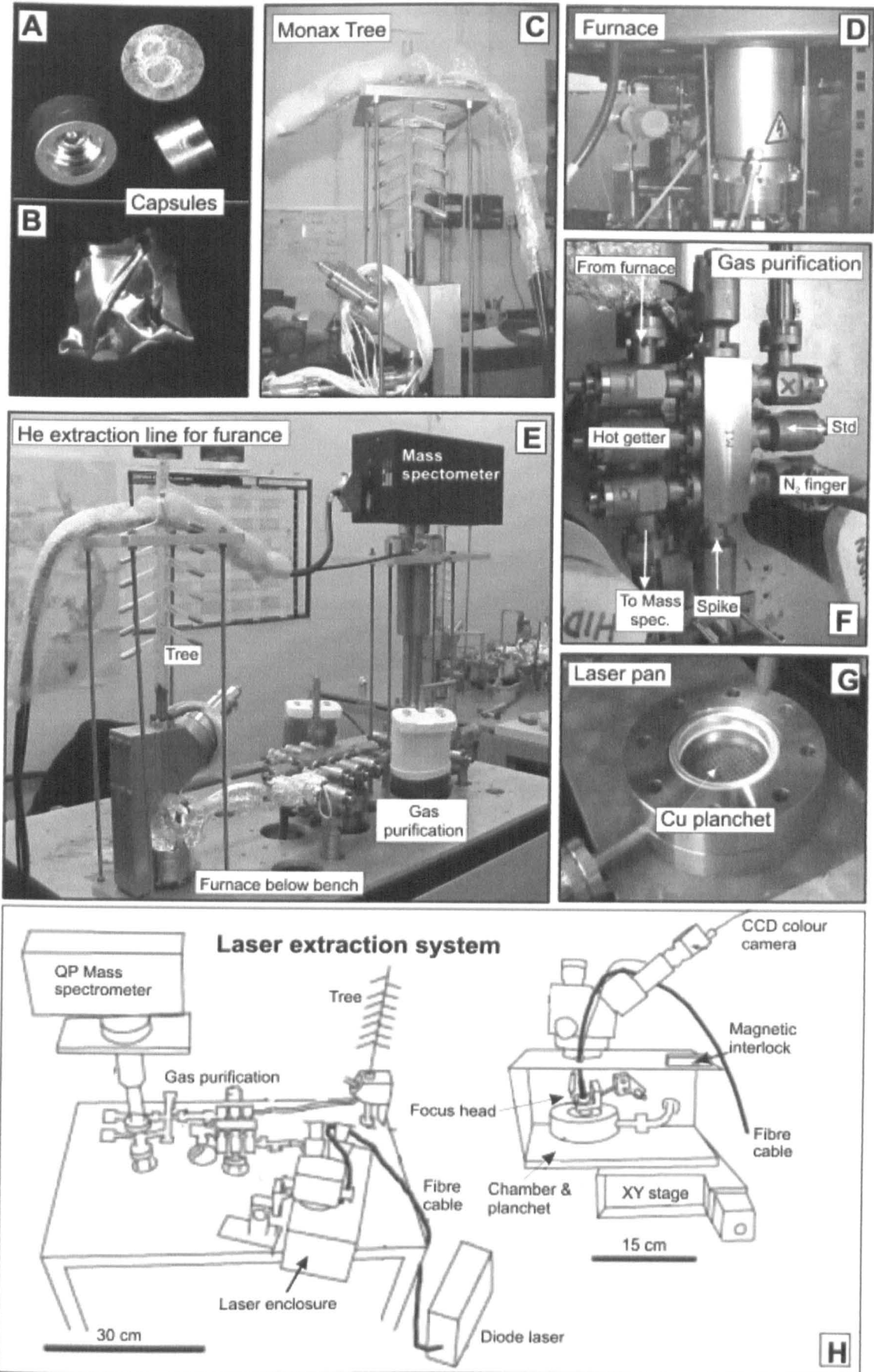


**Figure 9 - The helium extraction line used for apatite and zircon (U-Th)/He analysis.**

**The system allows for both furnace and laser extraction techniques. See text for details.**

Crystals that were to be heated in the furnace were loaded into re-usable stainless steel capsules (Figure 9 A) and wrapped in pre-heated, degassed copper foil (Figure 9 B). Up to 24 capsules were loaded into a 12-arm Monax glass “Christmas tree” (Figure 9 C), mounted above the furnace (Figure 9 D & E). For laser extraction system the crystals were placed into 0.5 mm Pt foil packets (Section 3.6.2) and around 10 Pt foil packets were loaded into 1.5 mm deep x 2 mm diameter holes in a high purity copper planchet. The planchet was then loaded into the laser chamber [Foeken *et al.*, 2006] (Figure 9 G-H).

### 3.5.2 Furnace extraction and He analysis

Once mounted the furnace and tree were pumped for 30 minutes using a turbo pump, before the tree was isolated, and the furnace degassed for 40 minutes at 1200°C. Ultra-vacuum (approximately  $10^{-9}$  torr) conditions were then achieved using a 301/second triode ion pump for approximately 2 hours.

Individual samples were dropped sequentially into a double-walled resistance furnace with a Mo crucible and liner (Figure 9 D). Helium extraction was achieved by heating at 950°C for 40 minutes; a heating schedule has been shown to be sufficient for complete helium extraction without volatilisation of U and Th [Persano *et al.*, 2002]. The evolved gases were purified using hot and cold SAES<sup>®</sup> TiZr getters and two liquid N<sub>2</sub>-cooled traps (Figure 9 E & F). <sup>4</sup>He analysis was carried out by isotopic dilution with a <sup>3</sup>He spike, using a Hiden HAL3F quadrupole mass spectrometer. (Figure 9E). Furnace blank analyses were performed before each sample to establish the blank <sup>4</sup>He, and a repeat heating cycle is performed to ensure complete <sup>4</sup>He extraction. Incomplete <sup>4</sup>He extraction required additional heating cycles until the measured <sup>4</sup>He had returned to blank levels, which were typically  $\leq 0.5$  % of the total <sup>4</sup>He extracted from the sample. In each batch of 24 samples, three aliquots of Durango apatite were analysed at intervals within the sample sequence as an internal procedural standard (Section 4.6.5).

Reproducibility of the <sup>3</sup>He-spike and system sensitivity was calibrated against twice-daily measurement of the <sup>3</sup>He/<sup>4</sup>He of a spiked-standard, using a manometrically determined <sup>4</sup>He gas standard. Over the period of all (U-Th)/He analyses performed during this study, measurement of the <sup>4</sup>He in the spiked-standard was  $\pm 0.1$  % ( $1\sigma$ ) within each analysis. The difference between the abundances in the twice-daily measurements was less than  $\pm 0.1$  % ( $1\sigma$ ), and variation of <sup>3</sup>He/<sup>4</sup>He was  $\pm 0.37$  % ( $1\sigma$ ) for all spiked-standards. Background measurements (unspiked) were  $\sim 8.0 \times 10^{12}$  torr  $\pm 3.7$  % ( $1\sigma$ ) <sup>4</sup>He. Spiked background “hot blanks” were measured at the start of each day of analysis, and yielded <sup>3</sup>He/<sup>4</sup>He with an average value of  $409 \pm 14.6$  % ( $1\sigma$ ) for a 40 minute heating cycle. The <sup>4</sup>He in the hot blank ( $\sim 1.88 \times 10^{11}$  cc  $\pm 24.9$  %, ( $1\sigma$ )) is dominated by the <sup>4</sup>He in the <sup>3</sup>He-spike. Total analytical uncertainty on the <sup>4</sup>He measurement was approximately 1.5 % ( $1\sigma$ ).

### 3.5.3 Laser extraction and He analysis

Laser extraction systems have several advantages over furnace extraction techniques, including faster extraction times and lower background levels of  $^4\text{He}$  and interfering species. This allows dating of smaller crystal volumes and younger samples, as well as faster sample throughput and better replication [Foeken *et al.*, 2006]. The details of the laser extraction systems at S.U.E.R.C. can be found in Foeken *et al.* (2006). Samples were heated for 30 seconds at approximately 600°C, using a 0.5 W beam with a 2 mm spot-size. This extraction protocol is sufficient to degas the crystals without causing U and Th volatilisation, as shown by initial degassing experiments and the preservation of subtle variations in the U/Th ratios observed in non-heated fragments from different Durango apatite crystals [Foeken *et al.*, 2006]. Purification of the evolved gases was identical to that for furnace extraction. To reduce the uncertainty caused by the  $^4\text{He}$  in the  $^3\text{He}$  spike, samples were run “unspiked”, and the absolute  $^4\text{He}$  abundances were calculated by peak height comparison against a calibrated standard. This protocol allows analysis of lower  $^4\text{He}$  abundances than with the furnace. The reproducibility of the  $^4\text{He}$  standard is  $\pm 0.4\%$  ( $1\sigma$ ,  $n = 27$ ), and system background levels are  $1.5 \times 10^{-12} \pm 0.2$  cc STP, ( $n = 27$ ) [Foeken *et al.*, 2006].

### 3.5.4 U and Th analysis

After  $^4\text{He}$  analysis, the samples are retrieved from the furnace by extracting the Mo liner. The copper foil is removed, the steel capsules opened, and placed into a clean Teflon<sup>®</sup> beaker. The Pt foil packets retrieved from the laser pan were placed unopened into the pre-cleaned Teflon<sup>®</sup> beakers. All samples were then spiked with approximately 0.45 ng  $^{230}\text{Th}$  and 0.18 ng  $^{235}\text{U}$ , and the volume made up to 2 ml with 5% ultra pure  $\text{HNO}_3$ . The solutions were then equilibrated for 24 hours on a hotplate at 80°C, before being transferred to a clean 2 ml vial for ICP-MS analysis.

All U and Th analyses were performed on a VG Plasma Quad PQ2 + ICP-MS. Fractionation in the mass spectrometer was monitored using the U500 standard with a certified value of  $^{235}\text{U}/^{238}\text{U} = 0.9997$ . A 5 ppb U500 solution was measured in duplicate at the start of every analysis, and additional aliquots bracketed every three samples. Reproducibility of the U500 solution on each run was to  $\pm 0.6\%$  ( $1\sigma$ ). U and Th measurements were replicated 5 times. A 5%  $\text{HNO}_3$  wash out solution was used to purge the ICP-MS between sample solution analyses. 100 analyses of U and Th in triple distilled 5%  $\text{HNO}_3$  were well below the limit of detection of  $\sim 80$  counts per second. Analytical uncertainty in the U and Th measurements was 1.85% ( $1\sigma$ ), increasing to  $> 3\%$  when the signal falls below 700 counts per second. Background U and Th from the steel capsules was well below the limit of detection, but initial tests showed that equilibration with 5%  $\text{HNO}_3$  causes  $\sim 0.007$  ng U and  $\sim 0.02$  ng Th to be leached from the Pt foil packets [Foeken *et al.*, 2006]. This source of blank was removed by leaching the packets in 5%  $\text{HNO}_3$  on a hotplate at 80°C for 48 hrs

prior to laser heating. Total analytical uncertainty was approximately 1 - 3 % ( $1\sigma$ ), which was dominated by the uncertainties in the concentrations of the  $^{230}\text{Th}$  and  $^{235}\text{U}$  spikes.

### 3.5.5 Reproducibility of the Durango apatite standard

Total analytical uncertainties are typically in the order of 1 - 3 %, but the reproducibility of mineral standards of known age is generally poorer. It is therefore common practice for (U-Th)/He laboratories to quote the uncertainties on (U-Th)/He ages in terms of the reproducibility of the mineral standards. The ages of the Durango apatite standard that were determined during this study are shown in Table 3. The Th/U of the measured crystals showed subtle differences between the Durango apatite supplied by Vrije Universiteit, Amsterdam (VU) and California Institute of Technology (CIT), suggesting the samples originate from different crystals. Average apatite (U-Th)/He ages in this study are reported with 8 % uncertainty unless stated otherwise.

Source of Durango apatite	S.U.E.R.C. Furnace extraction	S.U.E.R.C. Laser extraction
Vrije Universiteit, Amsterdam (VU): 32 ± 1 Ma (n = 5) [Foeken, 2004]	Age = 32.8 ± 1.3 Ma (n = 11)	Age = 32.6 ± 0.7 Ma (n = 8)
	Th/U = 22.9 ± 0.4 (n=11)	Th/U = 22.9 ± 2.2 (n = 8)
California Institute of Technology (CIT) 32.1 ± 1.7 Ma (n = 11) [House <i>et al.</i> , 2000]	Age = 31.9 ± 2.0 Ma (n = 11)	Age = 33.4 ± 0.7 Ma (n = 3)
	Th/U = 18.8 ± 1.5 (n = 11)	Th/U = 18.6 ± 0.4 (n = 3)

Table 3 - The (U-Th)/He ages and Th/U of Durango apatite [Foeken *et al.*, 2006 and unpublished data] determined at S.U.E.R.C.

## 3.6 Zircon (U-Th)/He analytical procedures

As outlined in Chapter 1 the ~ 200°C closure temperature of the zircon (U-Th)/He thermochronometer makes it a system ideally suited for separating the signatures of the plutonic and denudation driven cooling. While the understanding of helium diffusion in zircon has improved (Section 2.5.1), several practical considerations prevent the routine determination of zircon (U-Th)/He ages in many laboratories. Helium extraction from zircon crystals requires temperatures that are significantly higher than used for apatite, and the recovery of U and Th requires much stronger acids and harsher conditions. A significant volume of work has been carried out during this study in order to establish a methodology suitable for routine (U-Th)/He analysis. This routine protocol is outlined in detail in the following sections.

### 3.6.1 Crystal selection

Transparent zircons with undamaged surfaces and no visible defects or inclusions were hand picked under air, at 500 x magnification using a polarising binocular microscope. Crystals

containing obvious defects and large inclusions were easily identified and discarded, however inclusions with a minimum dimension of  $< 2 \mu\text{m}$  may be overlooked during the picking procedure, as inclusions can be masked by the strong birefringence of the host crystal, and by diffractive and reflective effects at the crystal edges. Large fluid inclusions ( $> 5 \mu\text{m}$ ), or those in the central regions of crystals, were visible, but inclusions  $< 5 \mu\text{m}$ , or close to the faces were typically much harder to observe. Viewing under liquids with different refractive indices (alcohol, acetone and clove oil) did not improve the identification of small inclusions.

Euhedral crystals that were lacking in inclusions were sketched, the dimensions measured, and the surface area-to-volume ratios calculated (see detailed discussion in Chapter 4). Where multiple crystal aliquots were prepared, crystals of equal minimum dimension, morphology, and surface area-to-volume ratio ( $\beta$ ) were selected for each aliquot.

### 3.6.1.1 The impact of inclusions on zircon (U-Th)/He ages

The typically high concentrations of U and Th ( $\sim 100$ 's ppm) in zircon generate high  $^4\text{He}$  content through time, reducing the potential impact of mineral inclusion-hosted helium on (U-Th)/He ages. The majority of small inclusions will have minimal effect on the measured (U-Th)/He ages, however there are a few exceptions. For most inclusions, inherited  $^4\text{He}$  is highly unlikely because magmatic temperatures will be sufficient to degas any inclusion-hosted  $^4\text{He}$  component, prior to their inclusion in the host zircon. Furthermore, all  $^4\text{He}$  generated from decay in small inclusions will be recoiled into the surrounding zircon lattice. All diffusive processes will then be controlled by the diffusion kinetics of the host crystal, and complete helium extraction will be achieved. Inclusions within the central zones of the host crystal will have negligible effect on bulk diffusion and  $\alpha$ -recoil corrections, as there will be little perturbation of the  $^4\text{He}$  concentration gradients. The harsh dissolution procedures required to ensure recovery of U and Th from zircon (Section 3.6.4) will be sufficient to recover inclusion hosted U and Th, and therefore (U-Th)/He ages will be largely unaffected by most inclusion phases. Urananite and thorite inclusions may affect the (U-Th)/He age of the host zircon, as these may not be fully dissolved.

In the few samples where very small inclusions were unavoidable crystals were analysed in separate aliquots. Fish Canyon Tuff crystals containing small ( $< 2 \mu\text{m}$  diameter) inclusions yielded (U-Th)/He ages identical to those from inclusion-free crystals, indicating the  $^4\text{He}$  in the inclusions was negligible [Reiners, 2005]. However, as the concentration of He within fluid inclusions can be highly variable all crystals containing fluid inclusions were discarded.

### 3.6.2 Aliquot preparation

Samples were packed in small Pt-foil packets, formed by crimping one end of a Pt-foil tube (0.5 mm diameter, 1 mm long) (Figure 10A). The average mass of the Pt-foil packets was  $1.754 \pm 0.038$  mg ( $1\sigma$ ,  $n = 84$ ). The Pt-foil packets were weighed, and mounted upright into a thin sheet of Parafilm™ to assist crystal loading. Crystals were packed under low magnification, and the location of the crystals within the Pt-foil packet verified. The packets were then crimped shut and both crimps inspected to ensure that they were sufficient to prevent loss of crystal fragments during heating.

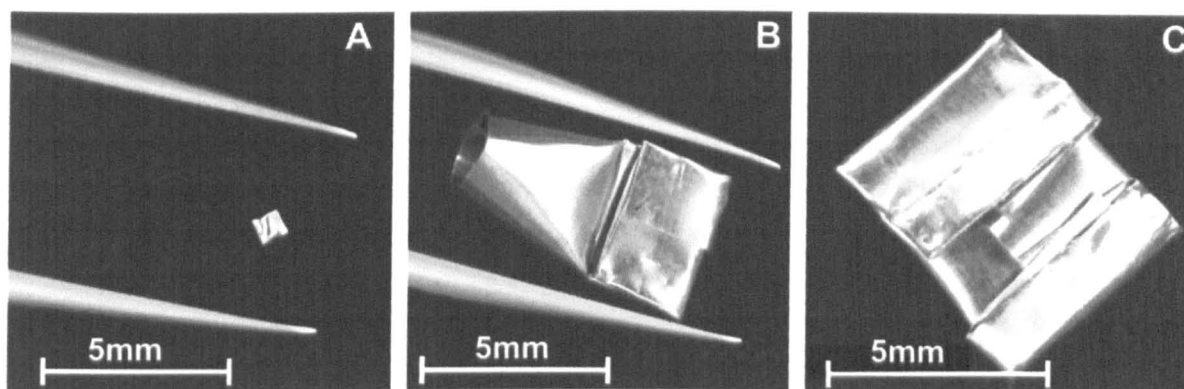


Figure 10 – The capsules used for zircon (U-Th)/He analysis.

**A) A Crimped Pt foil tube, ready to be loaded for extraction. For laser extraction these are loaded directly into the laser pan.**  
**B) Mo envelopes used to aid recovery and identification during furnace extraction.** C) Closed Mo envelope ready to be loaded.

For the majority of the samples helium was extracted using the furnace. The Pt-foil packets are too small to be marked for simple identification upon retrieval from the furnace, so they were loaded into larger molybdenum foil envelopes (Figure 10 B & C). Up to 12 envelopes were loaded into a 12-arm Monax glass “tree” mounted directly above the furnace (Figure 9). During laser helium extraction, the Pt-foil packets were loaded directly into the sample planchet and mounted in the laser pan (Figure 9)

### 3.6.3 He extraction

After the samples were loaded, the furnace was degassed at  $\sim 1300$  °C for 40 minutes directly to the turbo pump. Analytical procedures and standard calibrations were the same as for apatite. Complete helium extraction from zircon was achieved by heating for 30 minutes at  $\sim 1200$ °C, and the  $^4\text{He}$  released on reheat cycles was indistinguishable from the hot blank value. Furnace spiked blanks (30 minutes at  $\sim 1200$ °C) were run at the start of each day of analysis, and had  $^3\text{He}/^4\text{He}$  of  $466 (\pm 20 \%)$ . The blank  $^4\text{He}$  was  $1.42 \times 10^{-11}$  cc  $\pm 82 \%$  STP ( $1\sigma$ ,  $n = 68$ ). The blank is lower than that measured during apatite analysis ( $1.88 \times 10^{-11}$  cc), thought to be a result of the higher furnace temperatures during degassing. In over 98 % of helium analyses, the  $^3\text{He}/^4\text{He}$  of the re-heat was

within error of the preceding blank, and typically 99.97 % of the total  $^4\text{He}$  was released during the first extraction step. Total analytical uncertainty on the  $^4\text{He}$  measurement was approximately 1.5 % ( $1\sigma$ ).

For the laser, complete extraction required ~ 20 minutes heating using a 1.25 – 2.00 W defocused beam (~ 1200°C) [Foeken *et al.*, 2006]. The heating schedules are in good agreement with the time-temperature conditions reported by other helium laboratories [House *et al.*, 2000; Reiners *et al.*, 2002; Reiners, 2005]. Daily reproducibility of the  $^4\text{He}$  standard was better than  $\pm 0.4$  % ( $1\sigma$ ,  $n = 27$ ), with precision of  $\pm 0.8$  % over the three month period of analysis. System blank  $^4\text{He}$  from heating empty Pt-foil packets was  $1.5 \times 10^{-12} \pm 0.2$  cc STP ( $n = 33$ ).

### 3.6.4 Existing methodologies for U and Th recovery

Two techniques are routinely used in other laboratories for the dissolution of zircon for U and Th analysis. These were developed as bulk dissolution techniques for U-Pb analysis, and have potentially significant drawbacks for routine (U-Th)/He analysis.

#### 3.6.4.1 Flux Melting

Farley *et al.* (2002) and Tagami *et al.* (2003) use a flux melting procedure, in which opened Pt capsules are flux melted with lithium borate (5 mg; Farley *et al.* 2002) or lithium metaborate (7 mg Tagami *et al.* 2003) at ~ 1200°C for 2 - 3 hours. The flux lowers the melting temperature of the mixture, allowing total fusion in the furnace, and formation of a borate glass. This glass is then dissolved and equilibrated with an isotopic spike, before U and Th measurement using isotopic dilution ICP- MS.

There are two significant drawbacks to this method. Firstly, the need to open the Pt capsules after degassing introduces the potential for partial crystal loss prior to U and Th analyses, leading to incomplete U and Th recovery, and anomalously old (U-Th)/He ages. Secondly, the large volume of fluxing agent leads to the introduction of contaminant U and Th. Farley *et al.* (2002) report analytical blanks of less than a few percent, whereas Tagami *et al.* (2003) obtained procedural blanks of up to  $4 \times 10^{-13}$  mol U and  $2 \times 10^{-13}$  mol Th, even when using ultra pure Li metaborate. Tagami *et al.* (2003) report that this blank is equivalent to ~ 15 % of the U in a typical Fish Canyon Tuff zircon. The U and Th blank is likely to be variable, affected by subtle changes in bulk flux U and Th contents. This makes accurate quantification of the U and Th blank difficult.

Furthermore, few ICP-MS facilities are dedicated to U and Th measurements, and most routinely analyse a wide range of samples. Without further purification techniques, flux melting methodologies introduce large quantities of matrix elements into the ICP-MS, which has the potential to cause both peak suppression and isobaric interference. The large concentration of Li,

Na and B in the sample solutions also prevents routine trace level analyses of these elements without extensive cleaning of the ICP-MS. For these reasons flux melting procedures were not adopted at S.U.E.R.C..

### 3.6.4.2 Acid Digestion

The alternative method is that of Reiners *et al.* (2002), who adapted the U-Pb methodology outlined by Parrish (1987a, b) for (U-Th)/He analysis. After He extraction, Pt-foil capsules are opened and the degassed crystals are transferred into Teflon<sup>®</sup> micro-vials used with a Parr acid digestion bomb. The zircons are dissolved using an HF-HNO<sub>3</sub> mixture at ~ 235°C for 48 hours, followed by evaporation and rehydration with 5 % HNO<sub>3</sub> prior to ICP-MS analysis [Reiners *et al.*, 2002; Reiners *et al.*, 2004].

Opening the capsules to recover the zircons may result in the partial or complete crystal loss between the two phases of analysis, resulting in anomalously old (U-Th)/He ages. Reiners *et al.* (2005) addressed this by using a complete dissolution of both zircon and capsule. It was found that production of PtAr<sup>+</sup> in the ICP-MS caused isobaric interferences at U isotopic masses [Reiners, 2005], and so the Pt-foil was replaced by Nb-foil. Reiners *et al.* (2005) analysed the U and Th of the resultant solution using standard isotopic dilution ICP-MS, and report procedural blanks 4 - 25 times lower than those of Tagami *et al.* (2003). However although removing the issue of PtAr<sup>+</sup> interference, the large volumes of contaminant material typically causes a 40 % decrease in ICP-MS sensitivity [Reiners, pers. com.], and additional higher suppression effects are also recorded on some ICP-MS. For these reasons, the acid digestion methodology of Reiners *et al.* (2005) was not adopted at S.U.E.R.C..

### 3.6.5 A routine methodology for U and Th recovery

As the flux melting and bulk dissolution techniques described above are not possible at S.U.E.R.C., development of a new methodology was undertaken. In this study, the acid digestion technique was coupled to a simple cation exchange column chemistry to achieve recovery and purification of U and Th from the matrix elements. The technique can be applied in the majority of (U-Th)/He laboratories, and through-put of samples is limited only by the acid dissolution step.

#### 3.6.5.1 Zircon dissolution

Unopened, degassed Pt-foil packets were loaded into individual pre-cleaned Parrish-type Teflon<sup>®</sup> microcapsules. 30 µl of Ultra Pure 11.2 M HCl was added to each sample, along with 300 µl of dilute spike solution (in 5 % HNO<sub>3</sub>) equivalent to ~ 2.28 ng <sup>230</sup>Th and ~ 0.93 ng <sup>235</sup>U. The microcapsules were then placed on a hotplate at 80°C for two hours, reducing the volume of the solution by approximately 50 %. The microcapsules were then sealed and left to equilibrate on the

hotplate overnight, during which time the formation of aqua regia causes dissolution of the Pt capsule. The solutions were then evaporated to dryness, and rehydrated with 15  $\mu\text{l}$  of 16 M  $\text{HNO}_3$  and 180  $\mu\text{l}$  of 27.6 M HF. The microcapsules were sealed and loaded into the PTFE liner of a 125 ml capacity Parr™ acid digestion bomb (Figure 11), with 180  $\mu\text{l}$  16 M  $\text{HNO}_3$  and 9 ml 27.6 M HF.

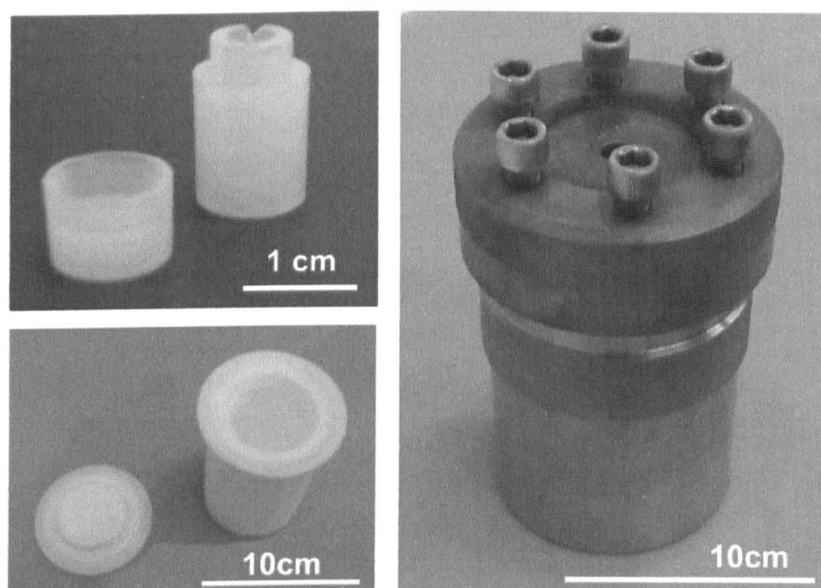


Figure 11- The Parr bomb, PTFE liner and Parrish-type Teflon<sup>®</sup> microcapsules used for zircon dissolution.

The assembled bomb was heated in an oven at  $230 (\pm 1^\circ\text{C})$  for 48 hours. When cooled the microcapsules were removed, and rinsed with MilliQ  $\text{H}_2\text{O}$  to remove all traces of HF. The PTFE liner was rinsed with MilliQ  $\text{H}_2\text{O}$  and dried. The open microcapsules were placed on a hotplate at  $80^\circ\text{C}$  for 2 hours. After evaporation to dryness, the samples were rehydrated in 195  $\mu\text{l}$  3M Ultra pure HCl, sealed, and re-loaded into the bomb with 9 ml 3 M Ultra pure HCl. The bomb was then heated for 14 hours at  $230 \pm 1^\circ\text{C}$  to ensure the dissolution of any fluoride salts.

After cooling, the micro-capsules were recovered from the bomb and rinsed as before, and the contents transferred to 2 ml pre-cleaned Teflon<sup>®</sup> beakers. The micro-capsules were equilibrated with an additional 195  $\mu\text{l}$  3 M Ultra pure HCl on a hot plate at  $80^\circ\text{C}$  for 2 hours to ensure complete U and Th recovery. These solutions were then added to the 2 ml beakers. The samples were evaporated to dryness (hotplate at  $80^\circ\text{C}$ ), and re-equilibrated with 1 ml 1.5 M  $\text{HNO}_3$  on the hotplate overnight.

### 3.6.5.2 U-Th purification and ICP-MS analysis

Purification of the U and Th was achieved using a procedure modified from Luo *et al.* (1997). Clean Teflon<sup>®</sup> columns were loaded with 1 ml Eichrom TRU Resin (Blue), then rinsed with 9 ml 0.2 M HCl and 9 ml 0.1 M HCl & 0.3 M HF to remove any contaminant Th and U. The resin was pre-conditioned using 9 ml 1.5 M  $\text{HNO}_3$ , before the equilibrated sample was introduced in 1 ml 1.5

M HNO<sub>3</sub>. The column was then rinsed with 12 ml 1.5 M HNO<sub>3</sub> and 2.5 ml 3 M HCl to remove Pt and other contaminants, before the elution of both U and Th was achieved using 12 ml 0.1 M HCl & 0.3 M HF (see Appendix A). This procedure allows the recovery of the U and Th in the same elution fraction. The final elutes were evaporated to dryness on a hotplate, at 80°C, then set to reflux with 2 ml 5% HNO<sub>3</sub> and trace HF, for 24 hours before ICP-MS analysis.

U and Th measurements were made following the procedure for apatite (Section 3.5.4). U and Th measurements were replicated 5 times, and cross contamination was avoided by using a 5 % HNO<sub>3</sub> rinse between samples wash out solution. Machine background measurements in counts per second (cps) were averaged from 100 analyses of triple distilled 5 % HNO<sub>3</sub>, and the raw cps measured in the wash out solutions was generally within error of this machine background. This was well below the limit of detection. Cross contamination during dissolution did not occur, as regular bomb blanks were indistinguishable from background.

### 3.6.5.3 The U and Th blank

The Pt-foil packets used at S.U.E.R.C. had measurable blank U and Th content that was not reduced by the pre-analysis leaching step used in the apatite procedure (Section 3.5.4). Procedural U and Th blanks were 0.1067 ng U ( $\pm 14$  %, n = 11) and 0.0997 ng Th ( $\pm 11$  % n = 11). Total analytical uncertainty is therefore dominated by the uncertainty in the U and Th blanks. Negligible U and Th blank in the Pt (100 pg per 2 mg) have been reported by other laboratories for the zircon dissolution procedures [Reiners pers. com.] and a U and Th blank using the apatite dissolution procedure has not been measured [Leighton pers. com.].

### 3.6.5.4 U and Th uptake into the sample solution

During the initial stages of this project the final U and Th bearing column elutes were evaporated to dryness and then re-equilibrated with 2 ml HNO<sub>3</sub> prior to ICP-MS analysis. The U and Th yields from the calibration solutions run using this procedure were good (see Appendix A), however, the initial zircon samples had lower, and highly variable yields of U and especially Th. More importantly, in some samples, the Th (spike and sample) was not present. Repeated refluxes (using 2 ml fresh 5 % HNO<sub>3</sub>), showed that the low yields, and lack of Th, were because of poor take-up from the surface of the Teflon<sup>®</sup> beaker into the carrier solution. The first and second reflux released the majority of U, and in the solution with the greatest U yield ~ 40 % of the <sup>235</sup>U spike was measured. Yields were sufficient to calculate the U<sup>235</sup>/U<sup>238</sup> to less than  $\pm 2$  %. Incomplete Th release occurred during the second or third refluxes, with between 20 - 50 % of the <sup>230</sup>Th spike recovered in most samples. The uncertainty in Th<sup>230</sup>/Th<sup>232</sup> is therefore much larger than for the U<sup>235</sup>/U<sup>238</sup>, typically greater than  $\pm 10 - 20$  %. A few samples yielded ~ 80 % of the <sup>230</sup>Th spike during the second reflux, and on these samples Th<sup>230</sup>/Th<sup>232</sup> was determined to  $\pm 5$  %.

For all samples the  $U^{235}/U^{238}$  and  $Th^{230}/Th^{232}$  of the two refluxes were the same within the uncertainty of the ratios, and so fractionation did not occur. As there was no fractionation the (U-Th)/He ages of these samples could be calculated. These (U-Th)/He ages will have large analytical uncertainties associated with them. Addition of the trace HF to the sample carrier solution yielded both the U and Th during the initial reflux, with spike yields of > 80 %. The concentration of HF within the sample carrier solution (5 % HNO<sub>3</sub> & trace HF (0.01 %)) was insufficient to strip any contaminant U and Th from the within ICP-MS.

### 3.6.6 The (U-Th)/He age of the Fish Canyon Tuff zircon

The Fish Canyon Tuff zircon fission track standard has been adopted by the (U-Th)/He community as a suitable standard. Table 4 shows the data from 16 (U-Th)/He analyses of the FCT zircon performed during this study using the furnace extraction technique. Table 5 shows the (U-Th)/He ages from three aliquots (3 crystals in each aliquot) which were analysed using the laser extraction, towards the end of this work.

The majority of unknown zircons analysed during this study underwent furnace extraction. Samples FCT 1 to FCT 5 were analysed prior to the addition of HF to the sample solution. Although these samples had low U and Th yields, the repetition of the refluxing step released sufficient U and Th for measurement in the same solution. The  $^{230}Th/^{232}Th$  and  $^{235}U/^{238}U$  in both the low yield and high yield solutions were within error (indicating no fractionation), and so (U-Th)/He ages could be calculated. In aliquots FCT 3 and FCT 4 the second reflux step failed to recover the majority of the U and Th spikes (~ 50 % U, < 10 % Th), and although these data are included in the table, they are not considered reliable age determinations, and are not considered further. All data are corrected for  $\alpha$ -recoil using Equation 17, using the fitting parameters of Hourigan *et al.* (2005) (see Section 2.5.3).

The average (U-Th)/He age for the Fish Canyon Tuff analyses performed using furnace extraction at S.U.E.R.C. is  $26.6 \pm 6.6$  Ma (25 %,  $2\sigma$  stdev,  $n = 14$ ). This value includes the age of 16.6 Ma obtained from FCT 14. This single crystal analysis falls well outside the range of the other aliquots (24.4 - 29.4 Ma), and if this is considered an outlier and removed from the dataset, the mean (U-Th)/He age of the FCT zircon measured during this study becomes  $27.4 \pm 3.5$  Ma (11.2 %,  $2\sigma$  stdev,  $n = 13$ ). The average age obtained from the laser extraction system is  $29.2 \pm 1.1$  Ma ( $2\sigma$  stdev, 4.0 %,  $n = 3$ ).

Sample	No. xls.	$^{238}\text{U}$ (ng)	$^{232}\text{Th}$ (ng)	$^4\text{He}$ (cc)	Th/U	Total An. Uncert.	Raw age (Ma)	$F_T$	Corrected age (Ma)
FCT 1	1	6.68	3.37	2.12E-08	0.50	3.86%	23.2	0.849	27.4
FCT 2	2	1.58	1.04	4.59E-09	0.66	2.67%	19.8	0.747	26.5
FCT 3	1	0.85	0.41	2.60E-09	0.48	12.7%	25.1	0.769	* 32.9
FCT 4	2	1.17	0.70	2.17E-09	0.60	8.55%	13.4	0.700	* 19.1
FCT 5	2	1.62	2.44	4.96E-09	1.50	2.79%	18.5	0.701	26.4
FCT 6	1	1.51	0.83	4.69E-09	0.55	2.41%	22.6	0.797	28.3
FCT 7	2	0.47	0.22	1.10E-09	0.46	6.16%	17.1	0.703	24.4
FCT 8	2	0.66	0.30	1.84E-09	0.46	8.64%	20.6	0.702	29.3
FCT 9	2	0.53	0.23	1.33E-09	0.43	6.89%	18.6	0.693	27.2
FCT 10	1	0.66	0.39	2.11E-09	0.59	4.20%	23.0	0.844	27.3
FCT 11	1	0.69	0.32	1.89E-09	0.47	4.50%	20.3	0.689	29.5
FCT 12	1	0.41	0.25	1.31E-09	0.61	6.58%	22.9	0.820	27.9
FCT 13	1	0.40	0.23	7.79E-10	0.58	6.57%	14.1	0.579	24.4
FCT 14	1	0.60	0.52	9.70E-10	0.86	4.01%	11.0	0.662	16.6
FCT 15	3	1.68	1.23	5.12E-09	0.73	1.88%	21.3	0.760	28.1
FCT 16	3	1.44	0.89	4.19E-09	0.61	2.26%	20.8	0.720	28.9

Table 4 - The (U-Th)/He age of the Fish Canyon Tuff zircons by furnace extraction. \* - ages not included in the calculation of the average (U-Th)/He age. See Section 3.6.6 for discussion. Uncertainties on all U and Th measurements in  $\pm 0.1$  ng.

Sample	$^{238}\text{U}$ (ng)	$^{232}\text{Th}$ (ng)	$^4\text{He}$ (cc)	Th/U	Total An. Uncert.	Raw age (Ma)	$F_T$	Corrected age (Ma)
FCT L1	4.08	2.38	1.15E-08	0.58	2.2 %	20.2	0.71	28.59
FCT L2	3.32	1.82	9.50E-09	0.55	2.2 %	20.6	0.70	29.27
FCT L3	1.62	1.12	4.43E-09	0.69	2.4 %	19.3	0.65	29.68

Table 5 - The (U-Th)/He age of the FCT by laser extraction.

### 3.6.6.1 Comparison with the existing (U-Th)/He age dataset

The FCT zircon (U-Th)/He ages determined during this study fall within the range of ages reported by other laboratories performing routine analyses. The data from Reiners (2005) and Tagami *et al.* (2003) are presented in Figure 12, along with the FCT zircon (U-Th)/He ages determined at CPRG [Pik, pers. com.] and the ages shown in Table 5 and Table 4. Figure 12 A shows all the reported (U-Th)/He ages, including a data point discarded by Tagami *et al.* (2003) as being anomalous ((U-Th)/He age = 16.6 Ma), together with the calculated mean age for all the analyses. Figure 12B shows the filtered dataset, from which those values deemed as analytically unreliable analyses (FCT 3 and FCT 4), and those classed as outliers (FCT 14 and Tagami *et al.* 2003), have been removed (see below).

### 3.6.6.2 The origin of the anomalously young FCT zircon (U-Th)/He ages

The two anomalously young ( $F_T$  corrected age of ~ 17 Ma) (U-Th)/He ages within the FCT zircon dataset lie well outside the range of the other analyses. These analyses are analytically robust (no apparent U or Th contamination, or other issues), and require explanation. The most probable cause of these “young” ages is an extreme form of zonation. This would enable the generation of excess He by an inaccurate  $\alpha$ -recoil correction. This implies that the two crystals which yield young ages have strongly U- and Th-enriched rims, and so the assumption of homogeneity underestimates the fractional loss of He.

If the U and Th is located very close ( $< 1\ \mu\text{m}$ ) to the crystal rim, then ~ 50 % of the  $\alpha$ -particles will be ejected through the planar surfaces of the crystal [Farley, 2002], and close to the intersection of crystal faces the % lost will increase. If the enriched rim is very narrow, then the fraction of  $\alpha$ -particles lost will be largely insensitive to crystal size, and the estimated fractional loss will be ~ 50 %. Consequently, if this crystal is assumed to be homogeneous, then the  $F_T$  corrected ages will be between 20 % ( $F_T = 0.60$ , small crystals) and 60 % ( $F_T = 0.8$ , large crystals) too young. The ~ 50 % increase in age that is required to reconcile these young ages with the majority of the data set implies that if this is as a result of zonation, the rims must be narrow, and strongly enriched. The nature of the zonation in the FCT zircons is investigated further in Chapter 5.

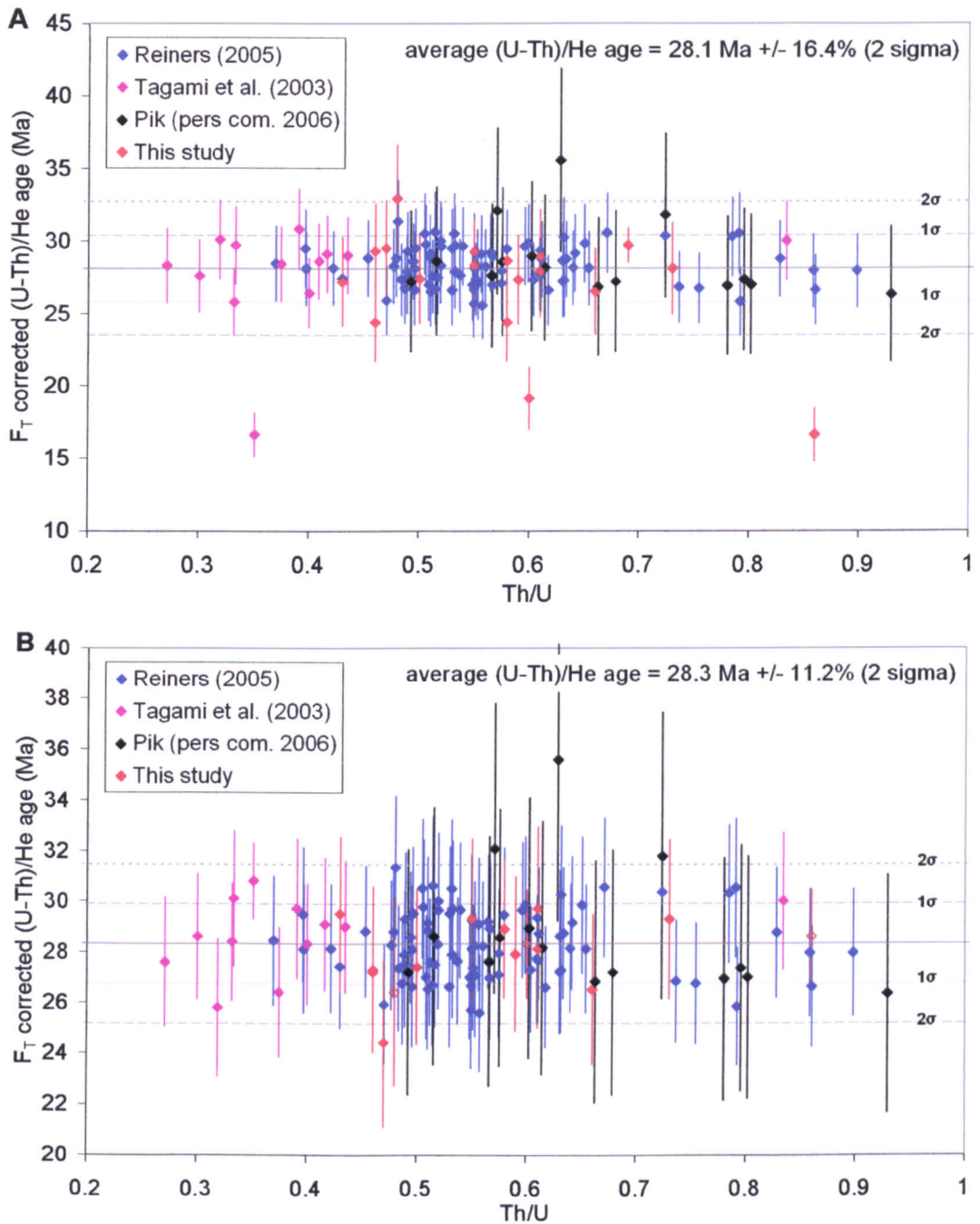


Figure 12 - The (U-Th)/He data set for the FCT zircon.

**A)** The full data set. Mean age is calculated using all values. Error bars shown for  $2\sigma$  reproducibility for each dataset. Horizontal lines (solid, short and long dashed) are the average,  $1\sigma$ , and  $2\sigma$  reproducibility for the combined data set.

**B)** The filtered dataset. This plot does not include the FCT 3 and FCT 4 analysed during this study (see Section 3.6.6) nor the two single crystal analyses that yielded ages of 16.6 Ma (Tagami *et al.* (2003) and FCT 14 this study). Error bars and horizontal lines as before.

### 3.6.6.3 The poor reproducibility of the FCT zircon (U-Th)/He ages

The (U-Th)/He age reproducibility of the FCT zircon analyses performed during this study is  $27.6 \pm 3.3$  Ma ( $2\sigma$  stdev, 11.9%,  $n = 16$ , furnace and laser). This mean age is within error of other published analyses for the FCT (Table 2). The age reproducibility of this, and the other datasets listed in Table 2 are significantly higher than typical analytical uncertainties (2 - 3 %), and can be as high as ~ 17 % [Pik, pers. com.]. If the filtered dataset is considered as a whole, the mean (U-Th)/He age of the FCT zircon is  $28.3 \pm 3.1$  Ma ( $2\sigma$  stdev, 11.2 %,  $n = 127$ ).

Such poor reproducibility has direct implications for the precision of the ages of unknown samples. It has been suggested that the origin of the  $\pm \sim 11$  % reproducibility observed in this sample is because of (subtle) zonation. There has been little investigation into the age variation that can be introduced by variable inter-crystalline zonation. A theoretical investigation of this effect of U and Th zonation within a zircon population, and a quantitative investigation of the nature and impact of U and Th zonation in the FCT zircons are presented in the following chapters.

## 3.7 Summary

The developmental work carried out during this study has established a routine methodology for the determination of zircon (U-Th)/He ages at S.U.E.R.C. Furthermore, this methodology can be used in any (U-Th)/He laboratory in which helium extraction from zircon can be achieved (see discussion in Section 3.6.4). The existence of a routine methodology for zircon (U-Th)/He analysis now enables the application of this chronometer to complement existing thermochronological techniques, and to constrain cooling at ~ 180 - 200°C. Although many of the analytical difficulties have been overcome, the techniques for the treatment and interpretation of zircon (U-Th)/He data remain poorly developed. Most notably the effect of crystal geometry on the  $\alpha$ -recoil correction and the effect of U and Th zonation on helium diffusion and  $\alpha$ -ejection are largely unconstrained. These issues were the basis for the investigations presented in Chapters 4 and 5, as they must be understood before it is possible to interpret (U-Th)/He ages of unknown samples.

# 4

## The treatment of zircon (U-Th)/He data

### 4.1 Introduction

Previous investigations using the zircon (U-Th)/He thermochronometer have calculated ages that are in agreement with the time-temperature curves predicted from other radiometric techniques [Kirby *et al.*, 2002; Reiners *et al.*, 2002; Tagami *et al.*, 2003; Reiners *et al.*, 2004]. However, the age reproducibility of even the rapidly cooled Fish Canyon Tuff standard is poor, ~ 11 - 12 %, and significantly higher than analytical uncertainties (2 - 3 %). The cause of this poor reproducibility is likely to be dominated by the three key factors: the effect of crystal geometry on the  $\alpha$ -recoil correction, the effect of U and Th zonation on the  $\alpha$ -recoil correction, and the effect of U and Th zonation on diffusive He loss. The errors that are introduced when analysts make assumptions about these issues are poorly understood. This chapter presents a discussion of these issues and a quantitative assessment of the associated effects.

### 4.2 Current techniques and sources of error

For age determinations, zircon (U-Th)/He analyses of zircons are generally recoil corrected, following the technique outlined in Section 2.4.3. Crystal dimensions are measured at high magnification using a graticule, and surface area-to-volume ratios ( $\beta$ ) is calculated. After analysis, zircon (U-Th)/He ages are corrected using an empirical second order polynomial (Equation 17) that relates the fraction of  $\alpha$ -particles retained in the crystal ( $F_T$ ) to the surface area-to-volume ratio ( $\beta$ ) where  $a$  and  $b$  are fitting parameters that incorporate the mineral density and stopping distance of the  $\alpha$ -particles [Farley, 2002].

In all but the most recent studies [Hourigan *et al.*, 2005; Reiners, 2005], Equation 17 has been applied using the fitting parameters presented in Farley (2002). These were determined from Monte Carlo simulation of the  $\alpha$ -particle loss from finite tetragonal pinacoidal (termination height = 0) crystals with homogeneous U and Th distributions. This methodology introduces several potential sources of uncertainty into the zircon (U-Th)/He ages.

Zircon used in (U-Th)/He studies are generally either well rounded detrital grains, or have prismatic crystal geometries. The following discussion considers only the measurement and modelling of  $\alpha$ -recoil and diffusion from prismatic crystals as no detrital crystals were analysed during this study. For a full discussion of the treatment and modelling of detrital zircon (U-Th)/He data, the reader is directed to Rahl *et al.* (2003).

## 4.3 Crystal measurement

$\beta$  is calculated directly from the crystal measurements, and the propagation of the errors in the measurements through the subsequent calculations must be quantified if the uncertainties associated with the recoil-corrected data are to be understood.

### 4.3.1 Unbroken crystals

In crystalline rocks zircon separates are dominated by unbroken crystals, which have a geometric uniformity that minimises the uncertainties in the measurements. This enables measurements of zircon crystal dimensions to be made more precisely than for apatite, where breakages and abrasion during processing, or undulating and uneven crystal faces cause greater uncertainty in the measurements.

Zircon has a variety of crystal geometries, with a wide range of termination styles superimposed upon basic tetragonal or octahedral crystal forms (Figure 13). Zircon geometry will depend on the magmatic and metamorphic history of the host rock, and is thought to be controlled by the rate of crystal growth, the composition and temperature of the crystallisation medium, and the presence of fluid phases [Corfu *et al.*, 2003]. A number of geometries can often be found in any one sample.

#### 4.3.1.1 Crystal geometries observed during this study

The distribution and range of zircon geometries in the samples from the HIP reflects the variation seen in many igneous rocks. They are dominated by zircons that can be described as Type A & B zircons (Figure 13). The orthorhombic form (Type B) dominates the populations in the majority of samples. Right-pyramidal terminations (where the termination apex is above the centre of the tetragonal base of the termination) are common; however more complex termination geometries are seen in all samples (Types i - vi, Figure 13). In the granitic, tholeiitic and pegmatitic samples analysed during this study, crystals with octagonal cross sections (Types C & D) are generally less common than their tetragonal equivalents (Types A and B), but can dominate the populations from other lithologies [see discussion in Corfu *et al.*, 2003].

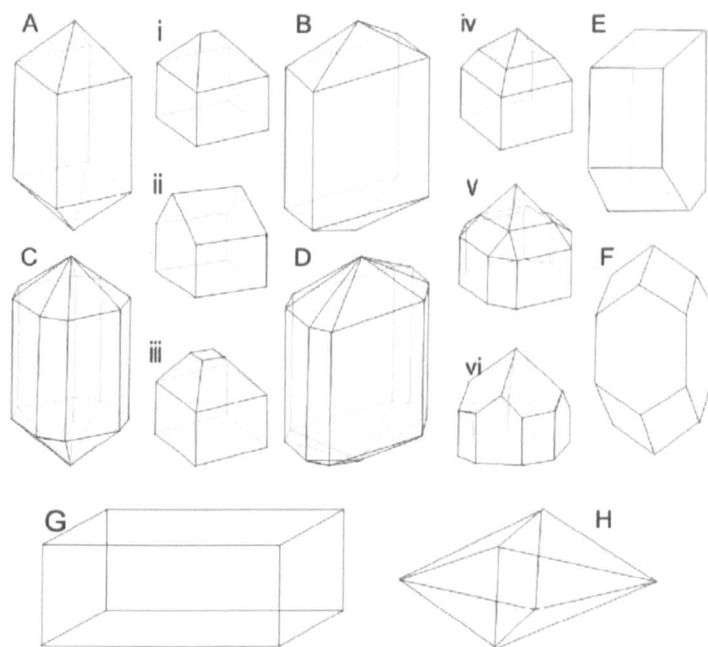


**Figure 13 - A schematic representation of the typical geometries seen in primary magmatic zircon.**

**A - H) The general forms of crystal geometry. i - vi) The termination forms superimposed on basic crystal geometries A-F.**

The full description of all measurements and equations required to accurately determine surface area-to-volume ratios for all crystal geometries shown in Figure 13 are described in Appendix B. The relatively simple Type A and B geometries, with pure pyramidal terminations can be described using five measurements: the length of the prismatic section ( $L_R$ ), the perpendicular crystal widths ( $W_1$  and  $W_2$ ), and the two termination lengths ( $T_1$  &  $T_2$ ), as shown in Figure 14. All crystal dimensions measured during this work were accurate to  $\pm 2 \mu\text{m}$ . Crystal widths were recorded such that  $W_1/W_2 \geq 1.0$  in all cases, and repeated measurements along the crystal showed no variation in width. Length and width measurements were taken perpendicular to the  $c$ -axis and  $L_R$ , and the termination lengths were measured parallel to the  $c$ -axis.

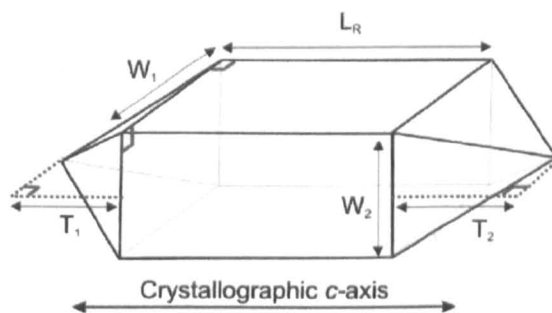


**Figure 14 - The measurements required to calculate surface area and volume for typical zircon crystals with two quadrilateral based pyramidal terminations.**

$W_1$  and  $W_2$  are the mutually perpendicular crystal widths. The maximum termination lengths,  $T_1$  and  $T_2$  are measured parallel to  $L_R$  which is parallel to the crystallographic  $c$ -axis.

### 4.3.2 Broken crystals

Comparison of zircons in mineral separates and thin sections of the rock specimens suggests that most crystal breakages occur during crushing. In many samples comparison of the lengths of complete and broken crystals suggests that the crystals typically break cleanly, perpendicular to the *c*-axis and away from the terminations; broken crystals can therefore be analysed with confidence, as no  $\alpha$ -recoil will have occurred through the surface of the break. However, this makes the assumption that the geometry of the zircons in the mineral separate is a true reflection of that which existed in the host rock.

Zircon overgrowths are relatively common in some rock types and can disintegrate and be removed during crushing [Dempster *et al.*, 2004]. The determination of surface area-to-volume ratios from the surviving crystal will over estimate the fraction of  $\alpha$ -particles lost by recoil. The timing of formation and the dimensions of the overgrowths will control the amount of  $\alpha$ -recoil and diffusion that has occurred from the recovered crystal. Small (< 15  $\mu\text{m}$ ) zircon overgrowths are associated with the low temperature ( $\sim 120^\circ - 300^\circ\text{C}$ ) mobilisation of zirconium following preferential dissolution of radiation damaged areas within crystals [Dempster *et al.*, 2004].

#### 4.3.2.1 Broken crystal geometries observed during this study

Although most analysed crystals were complete, a few broken crystals were analysed during this study. These were selectively chosen so that the fraction analysed was equivalent to approximately half the original crystal, by comparison with lengths of complete crystals within the separate, and therefore the surface area-to-volume ratio of a "complete crystal" can be used as a good approximation, to correct for  $\alpha$ -recoil. In these cases the "missing" half of the crystals was assumed to have the same termination length as the analysed fraction.

The existence of magmatic or late-stage overgrowths on some of the crystals analysed in this study cannot be entirely discounted, but none were seen in thin section, and no partial dissolution of crystals was observed. Overgrowths previously surrounding the crystals were therefore likely to be small, and limited to small discrete regions. In samples that are old, that have very high U-Th, or that show evidence of partial dissolution or precipitation of zirconium, the nature and extent of overgrowth formation should be considered carefully before (U-Th)/He ages are corrected for  $\alpha$ -recoil.

## 4.4 The calculation of surface area-to-volume ratio

If the surface area-to-volume ratio ( $\beta$ ), exerts a first-order control over bulk  $\alpha$ -particle retention and the use of simplified geometrical models to calculate  $\beta$  may lead to significant uncertainty. This will introduce large errors into the corrected (U-Th)/He ages. Calculating geometry specific  $\beta$  is possible, if complicated (see Appendix B), and is not routinely performed.

Equation 21 describes  $\beta$  for the only realistic crystal geometry routinely considered during (U-Th)/He analysis, that of Type A and B zircons with pure pyramidal terminations. The calculation uses the five measurements shown in Figure 14.

$$\beta^{Type\ B} = \frac{2W_1L_R + 2W_2L_R + W_1 \left[ \sqrt{\left(\frac{W_2}{2}\right)^2 + T_1^2} + \sqrt{\left(\frac{W_2}{2}\right)^2 + T_2^2} \right] + W_2 \left[ \sqrt{\left(\frac{W_1}{2}\right)^2 + T_1^2} + \sqrt{\left(\frac{W_1}{2}\right)^2 + T_2^2} \right]}{W_1W_2 \left[ L_R + \frac{(T_1 + T_2)}{3} \right]}$$

Equation 21

If both terminations are the same length,  $T_1 = T_2 = T$ , and Equation 21 simplifies to:

$$\beta^{Type\ A\ or\ B} = \frac{2W_1L_R + 2W_2L_R + 2W_1 \left[ \sqrt{\left(\frac{W_2}{2}\right)^2 + T^2} \right] + 2W_2 \left[ \sqrt{\left(\frac{W_1}{2}\right)^2 + T^2} \right]}{W_1W_2 \left[ L_R + \frac{2T}{3} \right]}$$

Equation 22

The surface area-to-volume ratio calculation simplifies still further when crystals are tetragonal (Type A) with ( $W_1 = W_2 = W$ ), and  $\beta$  is described by:

$$\beta^{Type\ A} = \frac{4 \left[ L_R + \sqrt{\left(\frac{W}{2}\right)^2 + T^2} \right]}{W \left[ L_R + \frac{2T}{3} \right]}$$

Equation 23

$\alpha$ -recoil from this crystal geometry has recently been investigated [Hourigan *et al.*, 2005]. The calculation of the surface area and volume for more complex crystal and termination geometries is discussed in Appendix B.

The  $\pm 2\ \mu\text{m}$  accuracy of all measurements made during this study introduces minimal uncertainty into the calculation of crystal volumes, but the uncertainty in the computed surface area is larger. For a small crystal ( $W_1 = W_2 = 40\ \mu\text{m}$ , total length ( $T_L$ ) =  $100\ \mu\text{m}$ ), the uncertainty in the volume increases from  $\pm 0.005\ \%$  to  $\pm 0.007\ \%$  as the termination length increases from  $0\ \mu\text{m}$  (pinacoidal,

Type G) to 50  $\mu\text{m}$  (100 % termination - bi-pyramid, Type H). Over the same change in geometry  $\beta$  increases from  $0.1400 \pm 2.2 \text{ \% } \mu\text{m}^{-1}$  to  $0.1616 \pm 3.2 \text{ \% } \mu\text{m}^{-1}$ . Measurement of crystal dimensions with an accuracy of  $\pm 1 \text{ }\mu\text{m}$  reduces the uncertainty in  $\beta$  by  $\sim 50 \text{ \%}$ , and further reduction could be achieved using higher magnification imaging using an SEM. The regularity of the crystal geometries in zircon means that the uncertainty associated with the measurement of zircons is less than that suggested for apatite (typically  $\sim 5 \text{ \%}$  [e.g. Farley, 2002])

To minimise the uncertainties associated with the calculation of  $\beta$ , crystals with short widths and long termination lengths were not selected for analysis. Selection was limited to crystals with widths between 40  $\mu\text{m}$  and 150  $\mu\text{m}$ , and with terminations  $< 50 \text{ \%}$  of the total crystal length ( $T_L$ ). For the smallest crystals ( $W_1 = W_2 = 40 \text{ }\mu\text{m}$ , total lengths = 80  $\mu\text{m}$ ,  $T_1 = T_2 = 20 \text{ }\mu\text{m}$ ) the uncertainty in the calculated surface area-to-volume ratio is  $\sim \pm 2.5 \text{ \%}$ .

#### 4.4.1 Simplification to pinacoidal geometries

The initial Monte Carlo modelling of Farley *et al.* (1996) showed that Equation 17 described  $\alpha$ -particle retention in finite tetragonal, pinacoidal (Type G) prisms. Farley (1996, 2002), and Reiners (2002) have therefore used a pinacoidal geometrical analogue in the calculation of all surface area-to-volume ratios (Equation 24).

$$\beta = \frac{4LW + 2W^2}{LW^2}$$

Equation 24

However, zircons rarely have such simple geometry (Figure 13). Tagami *et al.* (2003) modified the calculation to incorporate orthorhombic crystals; defining  $W_1$  and  $W_2$  as the two mutually- and  $c$ -axis-perpendicular measurements (Equation 25), therefore allowing the more accurate modelling, but does not consider the effect of the terminations.

$$\beta^{\text{pinacoidal}} = \frac{(2LW_1 + 2LW_2 + 2W_1W_2)}{LW_1W_2}$$

Equation 25

The difference between the  $\beta$  calculated for the pinacoidal (Equation 25) and pyramid-terminated (Equation 21) models can be substantial, with the pinacoidal model underestimating the value from the idiomorphic model by  $\sim 5 \text{ \%}$  for termination lengths typically selected for (U-Th)/He analysis (0 - 50 % of  $T_L$ ). The discrepancy between the  $\beta$  values is controlled by the termination length, and increases to  $\sim 25 \text{ \%}$  for bi-pyramidal crystals for all crystal sizes. This is illustrated in Figure 15, which shows the amount by which the pinacoidal model under estimates the pyramid-terminated, or idiomorphic model for three different crystal widths.

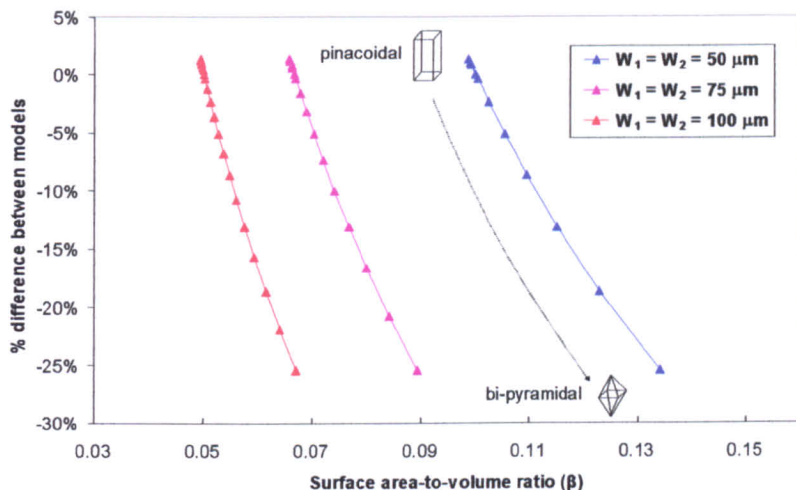


Figure 15 - The difference between the  $\beta$  values calculated using the pinacoidal and idiomorphic equations (tetragonal crystals).

The % difference increases with the increasing termination length (5  $\mu\text{m}$  increments). All crystals have total length/width = 2.0. The pinacoidal model generally under estimates the pyramid-terminated model (i.e. differences are generally negative).

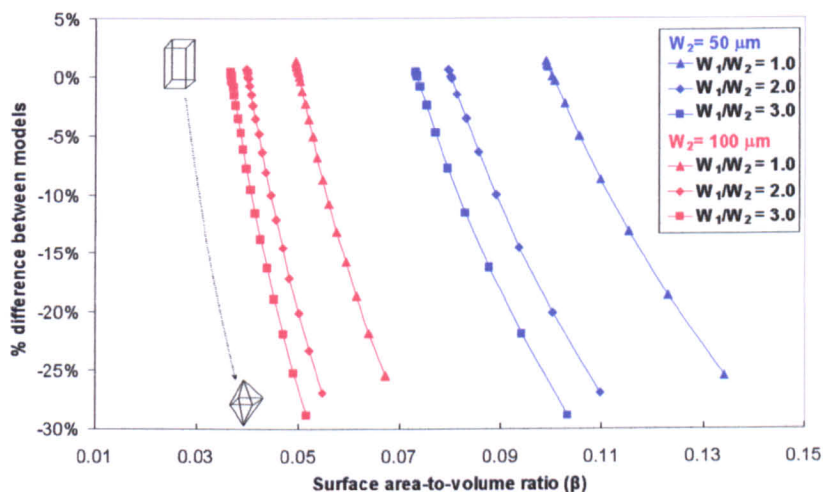


Figure 16 - The difference between the between the  $\beta$  values calculated using the pinacoidal and idiomorphic equations (orthorhombic crystals).

The % difference increases with the increasing termination length (5  $\mu\text{m}$  increments). All crystals have length/minimum width = 2.0. The pinacoidal model generally under estimates the pyramid-terminated model (i.e. differences are generally negative).

Figure 16 highlights the importance of the width ratio ( $W_1/W_2$ ) on  $\beta$ , while showing an increase in the % difference between the two geometric models with increasing termination length (as in Figure 15). The decrease in  $\beta$  that is seen with increasing  $W_1/W_2$  means that two crystals can have the same surface area-to-volume ratio while having very different geometries.

If Equation 17 can be used to accurately describe the relationship between  $\beta$  and  $F_T$ , then the apparent dependence of  $\beta$  on  $W_1/W_2$ , would suggest that additional geometric factors may need to be considered in the modelling of  $\alpha$ -recoil.

## 4.4.2 Simplification of pyramid-terminated geometries

The calculation of  $\beta$  for realistic pyramid-terminated crystals has used Equation 22 [e.g. Reiners, 2005] or Equation 23 [e.g. Hourigan *et al.*, 2005], with an average termination length. This simplification introduces uncertainty into the calculation, because while the volume of the termination scales directly with the total termination length, the surface area does not. In tetragonal crystals with two right-pyramid terminations (the apex of the pyramid is above the centre of the tetragonal base of the termination), the difference between termination lengths ( $T_1 - T_2$ ) is generally 0 - 40  $\mu\text{m}$ . When the terminations ( $T_1 + T_2$ ) are 50 % of the total crystal, using  $T_1 \neq T_2$  yields  $\beta$  values between 0 - 4 % larger than those calculated using the average value ( $T_1 = T_2$ ) (Figure 17).

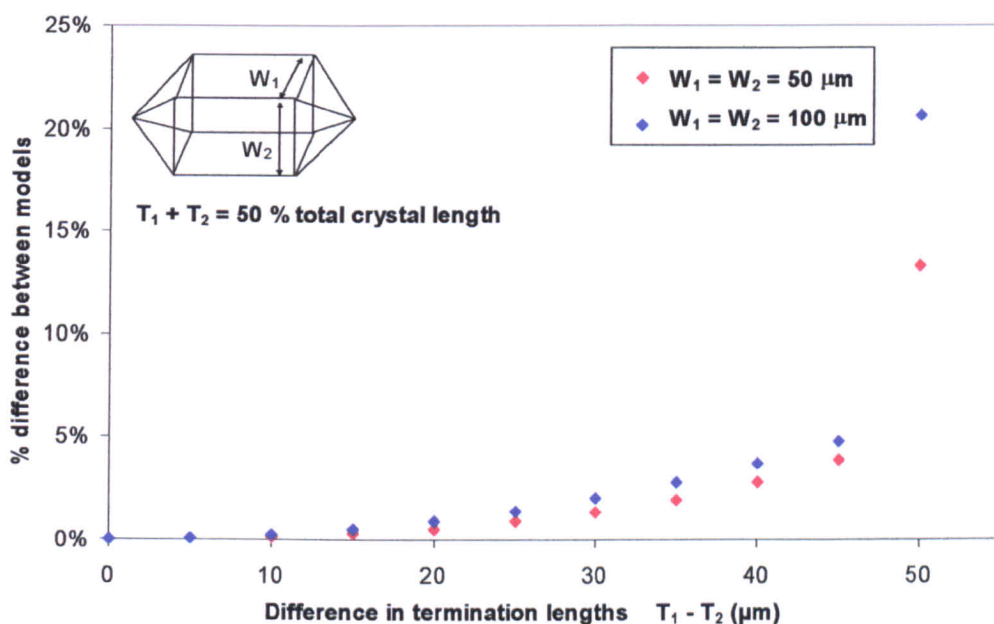


Figure 17 - The difference between  $\beta$  values calculated using the average termination length ( $T_1 = T_2$ ) and the geometry specific model ( $T_1 \neq T_2$ ). Crystals are 200  $\mu\text{m}$  in total lengths with a total termination length of 100  $\mu\text{m}$ . The differential length is calculated by  $T_1 - T_2$ . The % difference in  $\beta$  is calculated by  $\beta^{(T_1 \neq T_2)} - \beta^{(T_1 = T_2)} / \beta^{(T_1 = T_2)}$ .

### 4.4.2.1 Simplification of more complex geometries

The surface area, volume and  $\beta$  can be calculated for more complex crystal and termination geometries after the equations shown in Appendix B. Some of these crystal geometries were observed in the mineral separates used during this study, and so a methodology of calculating  $\beta$  for all common crystal forms was deduced. All crystals selected for (U-Th)/He analysis during this study were of Type A or B. Approximation of more complex crystal geometries to pinacoidal or Type A and B prisms introduces a further source of uncertainty into the calculation. The magnitude of the uncertainty will depend strongly on the geometry, and size of the natural crystal.

In many more complex crystal geometries, the precision of the additional length measurements required will introduce an uncertainty in  $\beta$  that is comparable to that introduced by the approximation of these crystals to relevant Type A or B geometry. Sample bias introduced by applying crystal size and shape selection criteria must be carefully considered during the analysis of detrital samples.

## 4.5 The $F_T$ calculation

The majority of zircon (U-Th)/He studies present data that has been  $\alpha$ -recoil corrected using Equation 17, and the fitting parameters determined from Monte Carlo modelling of pinacoidal crystal geometries [Farley, 2002]. This modelling does not incorporate the effect of the increased  $\alpha$ -recoil in the crystal terminations, and modelling of  $\alpha$ -particle retention in more realistic crystal geometries has only recently been developed.

Parent Nuclide	Farley (2002) (pinacoidal)	
	<i>a</i>	<i>b</i>
<sup>238</sup> U	- 4.31	4.92
<sup>232</sup> Th	- 5.00	6.80

Table 6 - The fitting parameters for the equation  $F_T = 1 + a \beta + b \beta^2$ , as determined by Farley (2002).

Until Hourigan *et al.* (2005) presented their combined Monte Carlo and numerical modelling technique, modelling realistic crystals was beyond the limited computational power available in many laboratories. The Hourigan *et al.* (2005) model has been used extensively during this study, and a summary of the technique is given below.

### 4.5.1 The determination of geometry specific $F_T$

The idiomorphic model developed by Hourigan *et al.* (2005) defines the zircon crystal as a right-pyramid-terminated tetragonal prism. The crystal volume can then be described within continuous Cartesian space by an isotropic three dimensional grid of discrete nodes, with the number of nodes per unit volume defined by the user. The model simplifies the calculation and reduces computing times, by fixing the origin of the co-ordinate system at the centre of the crystal. This utilizes the tetragonal symmetry of zircon so that the bulk  $F_T$  need only be calculated for nodes within the primary quadrant (Figure 18), provided ejection from all (12) crystal faces is considered.

For each node the model calculates the minimum distance to all (12) crystal faces, and determines the number of faces through which  $\alpha$ -ejection occurs. The fraction of  $\alpha$ -particles lost through each face is then calculated in one of three ways (see Figure 18B).

- Where the node is more than one stopping distance from all crystal faces  $^{local}F_T = 1$  (Figure 18B).
- Where ejection occurs through a single crystal face  $^{local}F_T$  is calculated from the surface area of the spherical cap which extends beyond the crystal face (Figure 18B).
- Where ejection occurs through multiple crystal faces, Monte Carlo simulation is used to simulate the position at which the  $\alpha$ -particle comes to rest.

The  $^{local}F_T$  is then calculated from the fraction of  $\alpha$ -particles which lie outside the crystal volume. Approximately 2500 Monte Carlo simulations are required to estimate the  $^{local}F_T$  with errors of  $< 1$  % when compared to the analytical solutions for the spherical cap [Hourigan *et al.*, 2005] (Figure 18B).

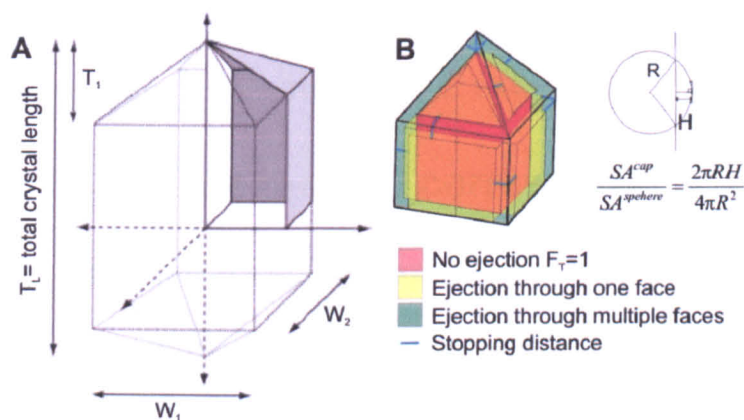


**Figure 18 - The geometrical construct of the Hourigan *et al.* (2005) model.**  
**A) The idiomorphic crystal model used to exploit the symmetry of tetragonal zircon crystals in the Hourigan *et al.* (2005) model.**  
**B) Regions within the crystal characterised by their ejection characteristics (see text for details).**

Bulk  $F_T$  is then calculated from the total number of  $\alpha$ -particles lost from all nodes, for all decay series. Although Hourigan *et al.* (2005) only present bulk  $F_T$  corrections from tetragonal crystals ( $W_1/W_2 = 1$ ), the model allows the consideration of orthorhombic geometries (Section 4.6.3), and there is potential for future developments to include more complex geometries.

The Hourigan *et al.* (2005) model does not consider the  $\alpha$ -particles generated by the  $\alpha$ -decay of  $^{235}\text{U}$  (typically 3 % total number of  $\alpha$ -particles) or  $^{147}\text{Sm}$  (typically  $\ll 1$  % total number of  $\alpha$ -

particles). This omission allows for increased computational efficiency, with minimal impact on the calculated  $F_T$  for typical concentrations (see Table 7).

	$^{238}\text{U}$	$^{235}\text{U}$	$^{232}\text{Th}$	$^{147}\text{Sm}$
Relative abundance	137.88	1.00	138.88	1.04
Relative decay rate	1.00	6.35	0.32	0.01
Number of $\alpha$ -particles produced	8	7	6	1
Proportional contribution	78.0 %	3.1 %	18.9 %	0.0007 %

**Table 7 - The typical contribution of each parent isotope to the total number of  $\alpha$ -particles generated in a crystal.**

**The values assume  $U/Th = 1.0$ , and  $Sm/U = 0.05$ , towards the high end of the range observed in natural zircons [Hoskin & Ireland, 2000]**

The average stopping distance of  $\alpha$ -particles generated during  $^{235}\text{U}$  and  $^{232}\text{Th}$  decay is almost identical (see Table 1, Chapter 2), and so the  $\alpha$ -correction factors will be approximately the same. The model outputs include the geometry specific  $F_T$  for each isotope, and so the effect of  $\alpha$ -ejection from  $^{235}\text{U}$  decay could be incorporated with minor modification of Equation 18 (Chapter 2) to incorporate the additional terms. The fraction of  $\alpha$ -particles lost through recoil following  $^{147}\text{Sm}$  decay will be minimal because of low production rates (Table 7) and very short stopping distance ( $\sim 6 \mu\text{m}$ ). If mineral chemistry indicates it is required, the model could be extended to include  $\alpha$ -particle production from these isotopes [Hourigan *et al.*, 2005].

## 4.6 Geometry and the $\alpha$ -recoil correction

### 4.6.1 $\alpha$ -recoil from tetragonal geometries

Hourigan *et al.* (2005) showed that for right-pyramid-terminated tetragonal crystals, with an aspect ratio of 2.0 ( $T_1/W_1$ ), the relationship between  $\beta$  and  $F_T$  for a range of different crystal widths can be fitted by a single polynomial curve as shown in Figure 19. Thus the polynomial relationship of Equation 17 holds, albeit with modified fitting parameters (Figure 19 & Table 6) [Hourigan *et al.*, 2005]. The plots of  $\beta$  against  $F_T$  (Figure 19 & Figure 20) also show the characteristic hooked shape caused by the slight increase in  $\alpha$ -particle retention when termination lengths are small relative to the total crystal length [Hourigan *et al.*, 2005].

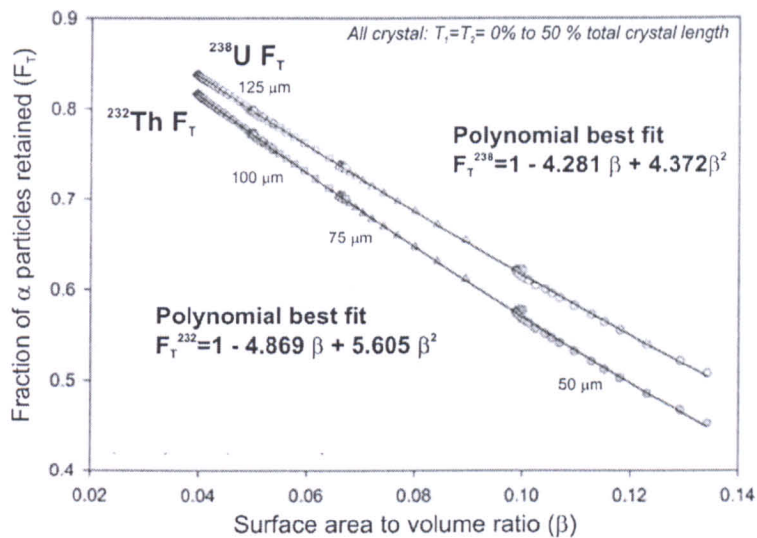


Figure 19 - The relationship between  $F_T$  and  $\beta$  for tetragonal crystals [modified from Hourigan *et al.*, 2005].

The plot shows the calculated  $F_T$  values for  $\alpha$ -recoil from U and Th decay for a range of tetragonal crystals, and the polynomial best fit curves for the data. Crystal widths are as shown on the plot and termination lengths increase from 0 % to 50 % of the total crystal length. All crystals have total length / width = 2.0.

There is a small misfit between the model outcomes and the  $F_T$  predicted by the polynomial best fit equations (see Figure 19), indicating that the  $\beta$  term does not fully capture all the geometric effects [Hourigan *et al.*, 2005]. As the difference between the model and predicted values is typically < 1 %, Hourigan *et al.* (2005) suggest that the polynomial represents a decent approximation for tetragonal crystals, proposing modification of the Farley (2002) fitting parameters to those shown in Table 8.

Parent Nuclide	Farley (2002) (pinacoidal)		Hourigan et al. (2005) (pinacoidal)		Hourigan et al. (2005) (pyramid terminations)	
	$a$	$b$	$a$	$b$	$a$	$b$
$^{238}\text{U}$	- 4.31	4.92	- 4.354	5.474	- 4.281	4.372
$^{232}\text{Th}$	- 5.00	6.80	- 4.938	6.881	- 4.869	5.605

Table 8 - The fitting parameters for the equation  $F_T = 1 + a \beta + b \beta^2$ , as determined by Farley (2002) and Hourigan et al. (2005).

The difference between the Hourigan *et al.* (2005) and Farley (2002) models introduces significant error into the calculated  $F_T$  (using Equation 17), with the Farley (2002) model over estimating the bulk  $F_T$ , by > 90 % in the most extreme cases (Figure 20). For typical crystals where  $T_1 + T_2$  is up to 50 % of the total crystal length, the differences can still be significant. The difference between the  $^{238}\text{U}$   $\alpha$ -recoil corrections ranges from ~ 0 - 6 % (125  $\mu\text{m}$  width) and 0 - 11 % (50  $\mu\text{m}$  width). The difference between the  $^{232}\text{Th}$   $\alpha$ -recoil corrections ranges from ~ 0 - 9 % (125  $\mu\text{m}$  width) and 0 - 19 % (50  $\mu\text{m}$  width). Studies using the Farley (2002) fitting parameters do not report the

termination lengths of analysed crystals, and so reappraisal of the  $F_T$  correction using new methods is not possible. Hourigan *et al.* (2005) do not investigate other geometric controls on  $\alpha$ -recoil such as aspect ratio or  $W_1/W_2$ , and do not suggest a source for the  $\sim 1\%$  discrepancy between their model and predicted  $F_T$  values.

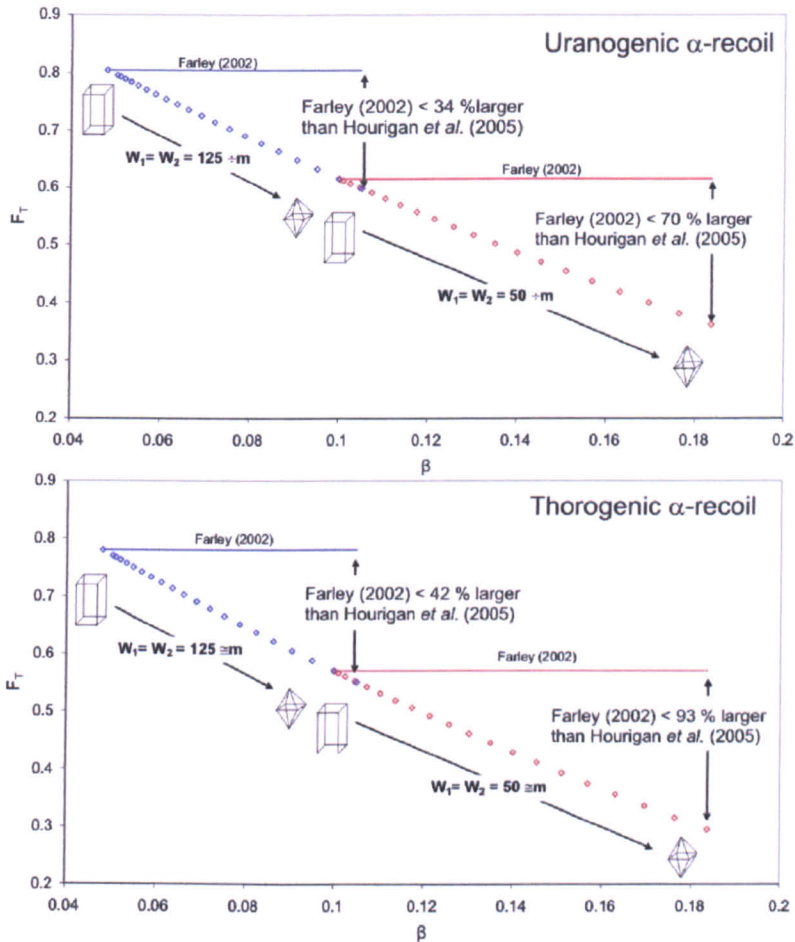


Figure 20 - The difference between the values of  $F_T$  calculated using the Hourigan *et al.* (2005) and Farley (2002) fitting parameters.

The plot shows the difference in the  $F_T$  values for a range of crystal geometries. All crystals are tetragonal, with a total length/width = 2.0. The Hourigan *et al.* (2005) model (open symbols) has  $F_T$  decreasing with increasing  $\beta$  (i.e. as the termination length increases). The Farley (2002) model will predict a single value of  $F_T$  calculated using Farley (2002) will be constant with increasing termination length, and is plotted as a horizontal line for each crystal (marked Farley (2002)).

#### 4.6.2 The effect of aspect ratio

Farley *et al.* (1996) report that although the effect of aspect ratio (total crystal length / width) on  $\alpha$ -particle retention is small, it can be seen in the models of finite cylindrical crystals with large  $\beta$  and high aspect ratios. The modelling performed by Hourigan *et al.* (2005) considered only crystals with aspect ratios of 2.0. An investigation into effect of aspect ratio on  $F_T$  showed that for both

tetragonal and orthorhombic idiomorphic geometries the effect is almost entirely captured in the  $\beta$  termination, as Farley *et al.* (1996) showed for the cylindrical case.

As crystals with aspect ratios  $> 5$  would not be selected for (U-Th)/He analysis, these were not considered in the modelling. For crystals with aspect ratios between 1 and 5 the values of  $F_T$  predicted using the Hourigan *et al.* (2005) model fall within  $\pm < 1.0\%$  of those calculated using the polynomial best fit curves (defined from crystals with aspect ratios of 2.0, i.e. the best fit curves shown in Figure 19). This was true over a range of crystal sizes, for typical values of  $\beta$  ( $0.03 \mu\text{m}^{-1} < \beta < 0.13 \mu\text{m}^{-1}$ ), with the small misfit becoming more apparent at high values of  $\beta$  ( $> \sim 0.11 \mu\text{m}^{-1}$ ), as for the cylindrical case [Farley *et al.*, 1996].

The polynomial best fit curve presented by Hourigan *et al.* (2005) was determined on crystals with a constant aspect ratio. Therefore the small misfit between the calculated and predicted values that they observe cannot be because of this effect. Although the effect of aspect ratio of  $F_T$  is almost entirely captured by the  $\beta$  term, all modelling performed during this study included crystals with a range of aspect ratios. It is possible that the misfit reported by Hourigan *et al.* (2005) is a function of insufficient simulations during the application of the Monte Carlo technique.

### 4.6.3 $\alpha$ -recoil from orthorhombic geometries

Hourigan *et al.* (2005) determined the fitting parameters  $a$  and  $b$  for tetragonal crystals. Tetragonal crystals are less common than orthorhombic geometries, and from the apparent variation of  $\beta$  with  $W_1/W_2$  (Section 4.4), further investigation of additional geometric controls is required.

#### 4.6.3.1 Correlation of modelling techniques

A series of models were run at a computational mesh density of 1 node/ $\mu\text{m}$ , with 2500 points generated during each Monte Carlo simulation. These conditions were driven by limited computing power. The Hourigan *et al.* (2005) fitting parameters were determined at mesh density of 4 nodes/ $\mu\text{m}$  and therefore, before the effects of geometry on  $\alpha$ -recoil were investigated, the uncertainties introduced by the reduced node density were investigated by a comparison of data sets from tetragonal crystals. Figure 21 shows the values of  $F_T$  calculated by the modelling performed here, for uraniumogenic (shown in blue) and thorogenic (shown in pink)  $\alpha$ -recoil. The polynomial best fit curves (and equations) for the data are shown, as are those determined by Hourigan *et al.* (2005) (shown in black).

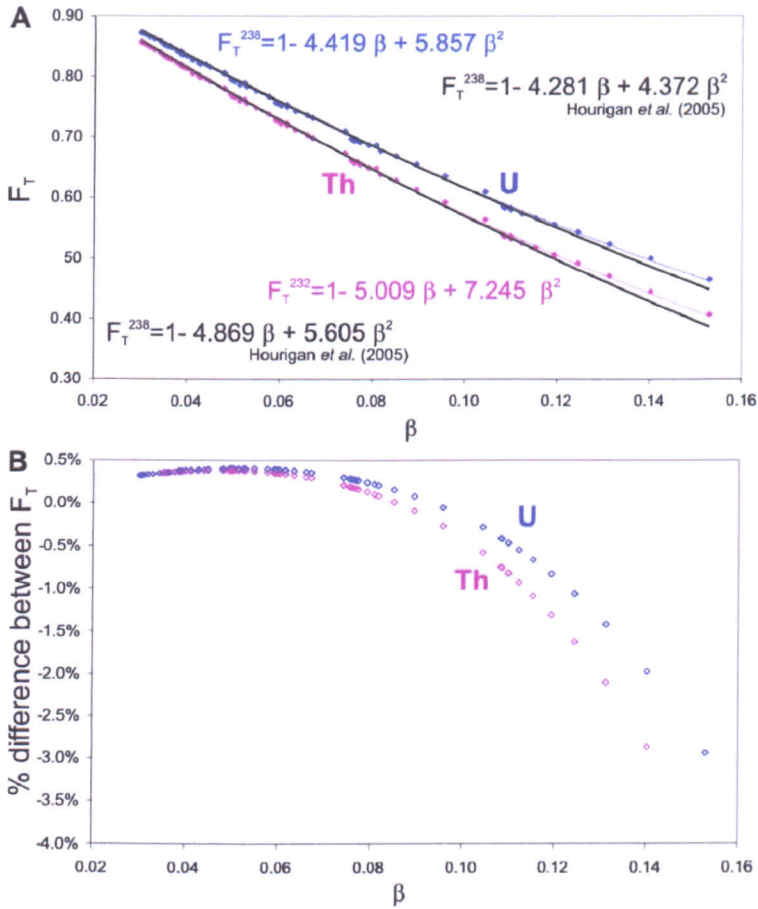


**Figure 21 - A comparison of the modelling parameters used during this study and those used by Hourigan *et al.* (2005). The subtle differences is because of the difference in the mesh density during the modelling.**

**A)** The values of  $F_T$  calculated for uranogenic (blue) and thorogenic (pink)  $\alpha$ -recoil, at a mesh density of 1 node/ $\mu\text{m}$ . The second order polynomial best fit curves and their equations are also shown. The black curves are the polynomial best fit curves calculated by Hourigan *et al.* (2005) calculated at a mesh density of 4 nodes/ $\mu\text{m}$ .

**B)** The difference between the values (%) predicted using the different fitting parameters shown in Figure 21A. The Hourigan *et al.* (2005) fitting parameters yield  $F_T$  values which are up to  $\sim 3\%$  lower than those determined here.

The values of  $F_T$  predicted from the polynomial best fit curves determined during this study are within  $\pm 1\%$  of the values obtained from the modelling outputs for  $0.03 \mu\text{m}^{-1} < \beta < 0.15 \mu\text{m}^{-1}$ . This is similar to the misfit reported by Hourigan *et al.* (2005) (see Section 4.6). Furthermore, the  $F_T$  values predicted from these best fit curves are within  $\pm 0.5\%$  of those calculated using the Hourigan *et al.* (2005) fitting parameters for  $0.03 \mu\text{m}^{-1} < \beta < 0.10 \mu\text{m}^{-1}$  (see Figure 21). The differences between the polynomial fitting parameters are through a combination of the reduced node density, and the incorporation of the effect of aspect ratio into the dataset. Hourigan *et al.* (2005) fitting parameters were determined from crystals with an aspect ratio of 2.0, whereas the data in Figure 21 have variable aspect ratios of between 1.0 and 5.0. This is thought to account for the increased discrepancy seen at high  $\beta$  (Figure 21).

In general, the two data sets are in agreement and the fitting parameters determined during this study allow a good approximation of  $F_T$  using Equation 17, when  $0.03 \mu\text{m}^{-1} < \beta < 0.12 \mu\text{m}^{-1}$ . Over this range of  $\beta$ , the fitting parameters returning  $F_T$  values within  $\pm 1.5\%$  of those calculated by Hourigan *et al.* (2005).

#### 4.6.4 The relationship between $\beta$ and $F_T$

The relationship between  $\beta$  and  $F_T$  for orthorhombic geometries was investigated using crystals with minimum widths of  $40 \mu\text{m}$  for  $W_1/W_2$  ranging from 1.0 to 5.0. Crystals of more extreme geometries were not modelled as these geometries are not usually selected for (U-Th)/He analysis. Figure 22 shows the model values of  $F_T$  against  $\beta$  for both uranogenic (A) and thorogenic (B)  $\alpha$ -recoil (open symbols), and includes the polynomial equation determined by Hourigan *et al.* (2005) for comparison (black dashed line). The data do not fit the single polynomial best fit curve determined from the tetragonal crystals ( $W_1/W_2 = 1.0$ ). The data from all crystals of a certain  $W_1/W_2$  plot as a series of arrays, each of which can be fitted by a distinct second order polynomial curve. These best fit curves are shown on Figure 22 as the solid lines. As extreme geometries were not modelled, there are a limited number of data in the arrays with high  $W_1/W_2$ .

The empirical polynomial fitting parameters for the curves in Figure 22 are shown in Table 9. The difference between the model output and the  $F_T$  predicted by the polynomial fitting parameters in Table 9 is  $< \pm 1\%$  ( $\beta < 0.12 \mu\text{m}^{-1}$ ) for  $W_1/W_2$  between 1.0 and 3.0. This is similar to that reported by Hourigan *et al.* (2005), for tetragonal crystals ( $W_1/W_2 = 1.0$ ). The limited number of model outcomes at higher  $W_1/W_2$  prevents the accurate determination of the misfit between the data and the polynomial best fit curve.

	$^{238}\text{U}$		$^{232}\text{Th}$	
	a	b	a	b
$W_1/W_2 = 1.0$ Hourigan <i>et al.</i> (2005)	- 4.281	4.372	- 4.869	5.605
$W_1/W_2 = 1.0$	- 4.415	5.826	- 5.005	7.217
$W_1/W_2 = 2.0$	-4.818	5.828	- 5.459	7.273
$W_1/W_2 = 3.0$	- 5.478	5.580	- 6.199	7.005
$W_1/W_2 = 4.0$	- 6.292	6.894	- 7.070	7.737
$W_1/W_2 = 5.0$	- 7.004	7.955	- 7.906	9.585

**Table 9 - The fitting parameters for the equation  $F_T = 1 + a\beta + b\beta^2$ . The values for orthorhombic crystals with  $W_1/W_2$  between 1 and 5, from polynomial best fit curves shown in Figure 22. The values of Hourigan *et al.* (2005) are shown for comparison.**

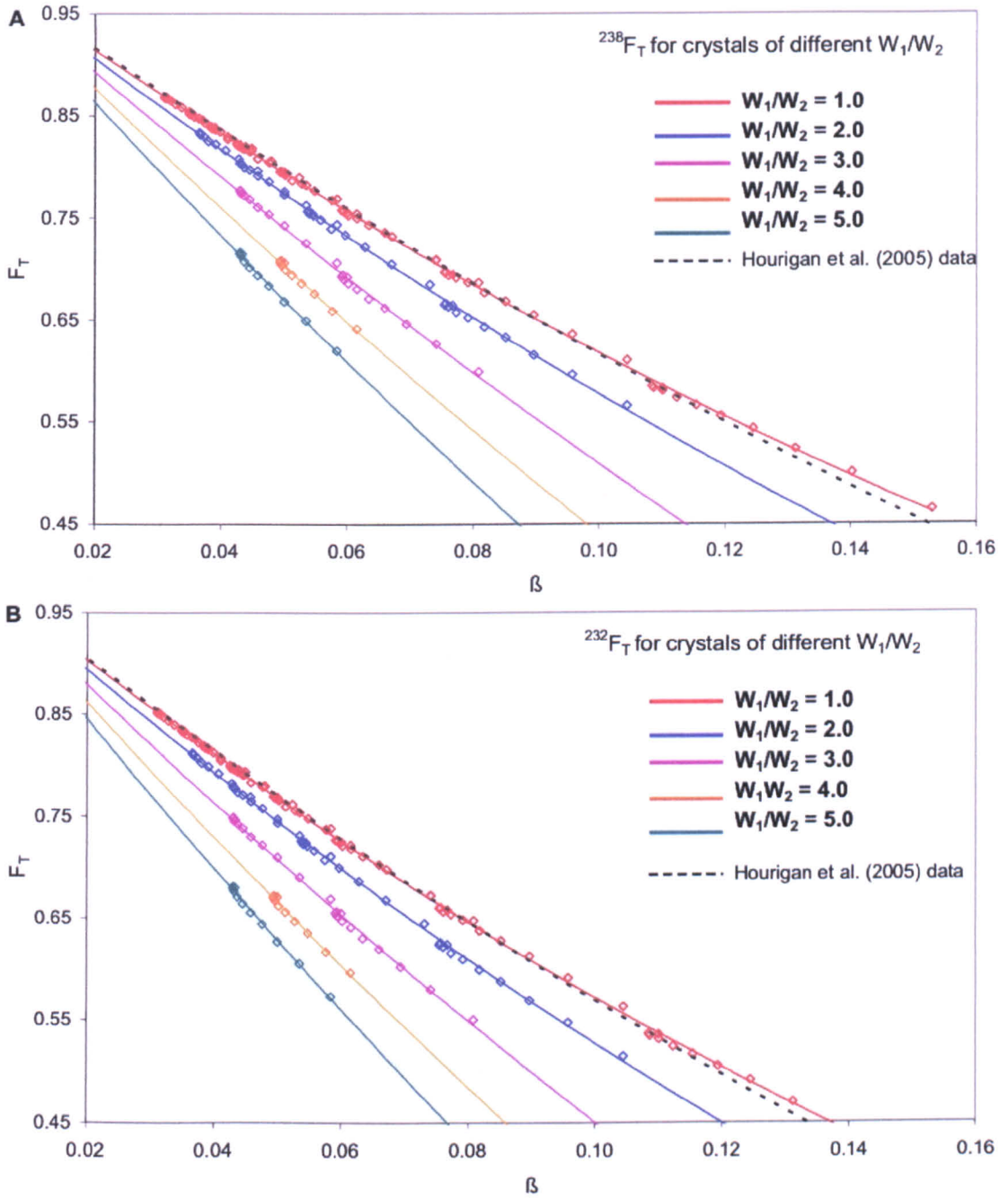


**Figure 22 -The dependence of  $F_T$  on  $\beta$  and  $W_1/W_2$ .**  
 The figure shows the  $F_T$  values calculated for A)  $\alpha$ -recoil from U decay, and B)  $\alpha$ -recoil from Th decay, using the Hourigan *et al.* (2005) model for a range of crystal geometries. The model outcomes are shown as open symbols, and the second order polynomial best fit curves are shown as solid lines. The dashed black lines shows polynomial curves derived by Hourigan *et al.* (2005).

Applying the tetragonal fitting parameters to crystals with  $W_1/W_2 < 2.0$  can generate an  $F_T$  correction that is up to  $\sim 10\%$  larger than the geometry specific values. The % difference between the tetragonal and  $W_1/W_2$ -specific  $F_T$  values can be calculated using Equation 26.

$$\frac{F_T^{(tetragonal)} - F_T^{(geometry\ specific)}}{F_T^{(geometry\ specific)}}$$

Equation 26

The % difference in the calculated values of  $F_T$  for different  $W_1/W_2$  and  $\beta$  are shown in Figure 23.

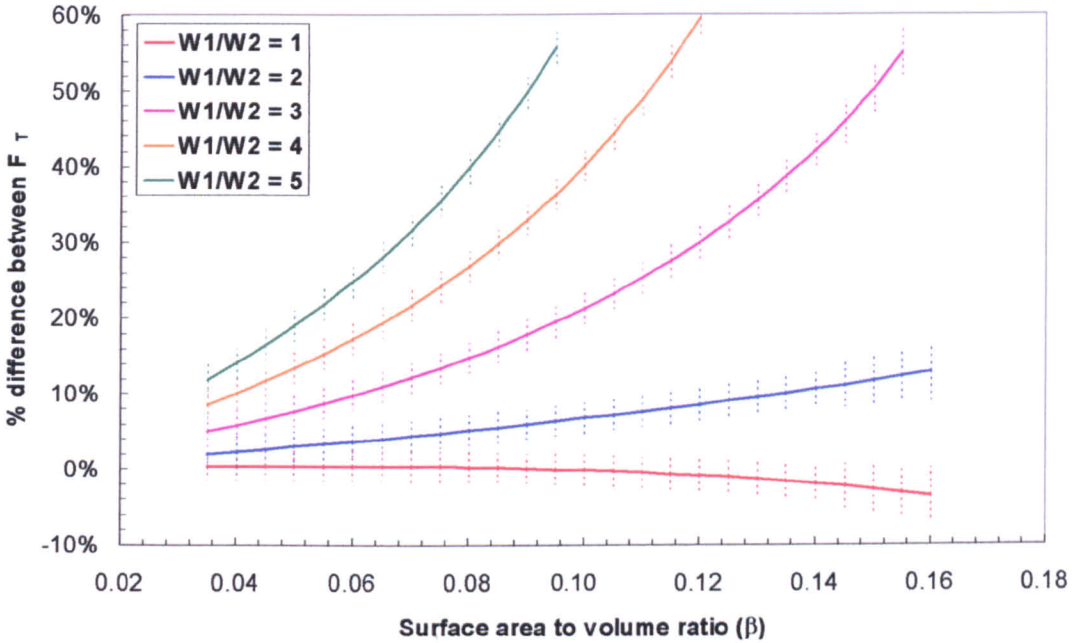


Figure 23 - The difference between the values of  $F_T$  calculated from the tetragonal and geometry-specific fitting parameters.

The plot shows the % difference between the values of  $F_T$ , and hence the % error introduced when the tetragonal fitting parameters are applied to orthorhombic crystals. Dashed error bars represent the uncertainty in the % difference. Uncertainty was calculated from the discrepancy between the outcomes from the  $W_1/W_2 = 1.0$  regressions (Figure 21).

#### 4.6.4.1 The relationship between $F_T$ and $W_1/W_2$

Zircons in many rocks exhibit a range of crystal geometries, with  $W_1/W_2$  typically between 1.0 and 4.0. The routine application of  $W_1/W_2$ -specific fitting parameters for Equation 17, would remove a large source of error (Figure 23), and reduce the uncertainty in the (U-Th)/He age calculation. Figure 24, shows a plot of the values of the fitting parameters against  $W_1/W_2$ . Both parameters for both nuclides can be fitted by second order polynomial best fit curves (as shown in Figure 24). In all cases the  $R^2$  values of these best fit polynomials is  $\geq 0.95$  (as shown).

Substitution of the Hourigan *et al.* (2005) fitting parameters for the  $W_1/W_2 = 1.0$  values causes negligible change in the relationships between  $a$  and  $W_1/W_2$ , however the polynomial relationship between  $b$  and  $W_1/W_2$  changes, and there is a reduction in the  $R^2$  value ( $\sim 0.87$  for Th). The relationship between  $F_T$  and  $W_1/W_2$  is less well defined for the fitting parameter  $b$  than it is for  $a$ ,

largely because as the value of  $\beta$  decreases, the  $b \beta^2$  term in Equation 17 tends to zero and the determination of the  $b$  cannot be as precise.

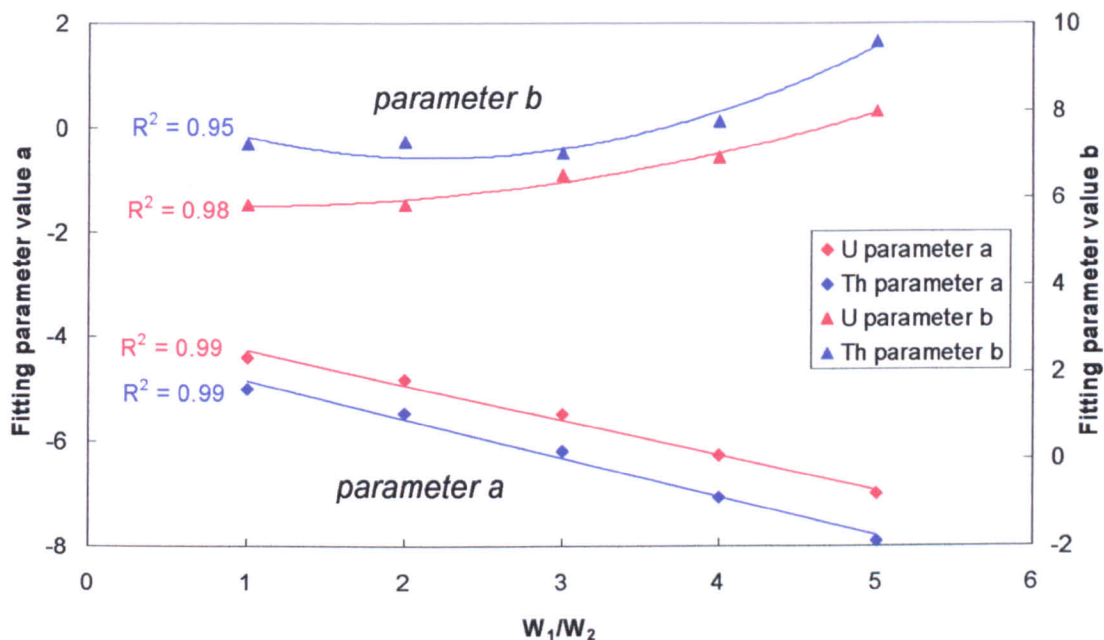


**Figure 24 - The relationship between  $W_1/W_2$  and the fitting parameters  $a$  and  $b$ .** The plot shows the fitting parameters  $a$  and  $b$  (filled symbols) plotted against  $W_1/W_2$ . The solid lines show the second order polynomial best fit curves through the data. The  $R^2$  values of each of the best fit curves are shown in the figure, and the equations are detailed below.

The relationship between  $W_1/W_2$  and the fitting parameters  $a$  and  $b$  allows the interpolation of  $W_1/W_2$ -specific fitting parameters for non integer values of  $W_1/W_2$ , which can be determined using:

$$a^{238} = -3.992 - 0.334 \left[ \frac{W_1}{W_2} \right] - 0.055 \left[ \frac{W_1}{W_2} \right]^2$$

Equation 27

$$b^{238} = 6.659 - 1.045 \left[ \frac{W_1}{W_2} \right] - 0.263 \left[ \frac{W_1}{W_2} \right]^2$$

Equation 28

$$a^{232} = -4.551 - 0.358 \left[ \frac{W_1}{W_2} \right] - 0.064 \left[ \frac{W_1}{W_2} \right]^2$$

Equation 29

$$b^{232} = 8.495 - 1.445 \left[ \frac{W_1}{W_2} \right] - 0.327 \left[ \frac{W_1}{W_2} \right]^2$$

Equation 30

Testing of this interpolation was performed against model outputs for crystals with  $W_1/W_2 = 1.5$ . The  $F_T$  values predicted using the geometry-specific fitting parameters were within  $\pm 2\%$  of the model outputs for  $0.03 \mu\text{m}^{-1} < \beta < 0.12 \mu\text{m}^{-1}$ . Equation 27 to Equation 30 can be combined to produce general forms of the polynomial equations that can be applied to all Type A and B geometries.

$${}^{238}F_T = 1 + \left[ -3.992 - 0.334 \left[ \frac{W_1}{W_2} \right] - 0.055 \left[ \frac{W_1}{W_2} \right]^2 \right] \beta + \left[ 6.659 - 1.045 \left[ \frac{W_1}{W_2} \right] - 0.263 \left[ \frac{W_1}{W_2} \right]^2 \right] \beta^2$$

Equation 31

$${}^{232}F_T = 1 + \left[ -4.551 - 0.358 \left[ \frac{W_1}{W_2} \right] - 0.064 \left[ \frac{W_1}{W_2} \right]^2 \right] \beta + \left[ 8.495 - 1.445 \left[ \frac{W_1}{W_2} \right] - 0.327 \left[ \frac{W_1}{W_2} \right]^2 \right] \beta^2$$

Equation 32

Applying geometry-specific fitting parameters during the calculation of the  $F_T$  correction can therefore keep the uncertainty associated with the calculation to a minimum. For most crystals selected for analysis, the uncertainty associated with the  $F_T$  correction will be in the order of a few %, and will be dominated by the uncertainty associated with  $\beta$ .

#### 4.6.5 $\alpha$ -recoil from more complex geometries

Many zircon crystals have different termination lengths and terminations that do not lie on the crystallographic axis. The strong dependence of  $\alpha$ -recoil on crystal geometry suggests that  $\alpha$ -recoil corrections for crystals have this asymmetry (different termination lengths and/or non axial terminations) should be calculated for each section of the crystal. In the more common case, where terminations are different lengths but have apices that lie on the c-axis, using an average termination length introduces error of up to 20 % in  $\beta$  when 50 % of the crystal is within the terminations. However, as the total crystal lengths ( $T_c$ ) are generally long relative to the  $\alpha$ -particle stopping distance, the crystal can be accurately modelled as two half crystals. The  $F_T$  for both termination lengths (Q1 & Q2) should be calculated separately, before the two values are combined as a weighted mean (by area) (Figure 25 A).

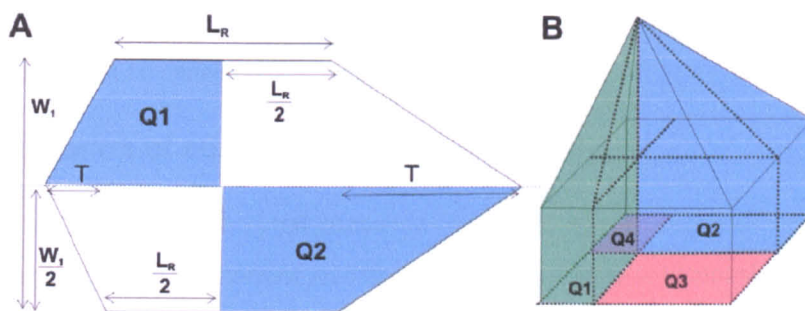


**Figure 25 - Complex crystal geometry and the  $\alpha$ -recoil correction.**

**A)** A 2D schematic of the quadrants needed to calculate  $F_T$  for a crystal with termination apices that lie along the crystallographic c-axis but with different lengths (T),  $\alpha$ -recoil from Q1 and Q2 should be calculated separately.

**B)** A 3D schematic of the quadrants needed to calculate  $F_T$  for a crystal with termination apices that do not lie along the crystallographic c-axis.

In the zircons analysed during this study, crystals with non right-pyramid terminations were rare, but modelling these geometries was considered for completeness. When the terminations cannot be described as right-pyramids; i.e. when the termination apices do not lie along the centre of the crystal (Figure 25 B) each quadrant (Q1 to Q4) of the crystal should be considered separately. Where the terminations are identical lengths and the apices fall on a single c-axis parallel line, the  $\alpha$ -recoil for the two halves of the crystal should be calculated separately, then a weighted (by surface area) average  $F_T$  for the two halves determined. For more complex crystals a full calculation of the  $\alpha$ -recoil may require the crystal to be considered as the weighted average of 8 quadrants. This complex treatment will cause minimal variation in the final  $F_T$  corrections for many samples, but does remove much of the uncertainty introduced by simplification of the complex geometries.

#### 4.6.5.1 The limitations of the current modelling techniques

The Hourigan *et al.* (2005) idiomorphic model can only be used to determine  $\alpha$ -recoil corrections for Type A and B crystals, and so the modified forms of the polynomial equations (Equation 31 and Equation 32) can only describe  $\alpha$ -recoil from these geometries. Many zircons suitable for (U-Th)/He analysis will not have these simple geometries. Crystal specific surface area-to-volume ratios (calculated from Appendix A) can be used in these equations to minimise the uncertainty introduced by the simplification, but without further development of the Hourigan *et al.* (2005) model the quantification of the effect of complex termination geometry is impossible to determine.

In octagonal crystals and in all crystals with complex termination geometries, the loss of  $\alpha$ -particles through the additional faces may increase the total fractional He loss disproportionately to the change in  $\beta$ . Small differences between  $\beta$  calculated for different complex terminations with

the same basal geometry and length, would suggest that the effect on  $F_T$  is probably in the order of a few %, but this must be considered on a crystal by crystal basis.

#### 4.6.5.2 Translation of complex geometries

It has been shown that complex crystal geometries with moderate aspect ratios can be simplified to “equivalent” spherical approximations provided the  $\beta$  of the sphere is identical to that of the crystal [Meesters & Dunai, 2002a]. From the Hourigan *et al.* (2005) study it appears that such a translation is also valid for tetragonal crystals, and therefore may allow the correct consideration of more complex crystal (and termination) geometries. The dependence of  $F_T$  on  $W_1/W_2$  shown here however, suggests that a geometric translation is not always possible, as the  $W_1/W_2$  dependence of  $F_T$  enables two different crystal geometries to have the same  $\beta$ , and equivalent spherical approximations, but dramatically different  $\alpha$ -recoil characteristics. This is discussed further in Section 4.8.

### 4.7 U and Th zonation and the $\alpha$ -recoil correction

Zonation of U and Th in zircon is widely reported [Hanchar & Hoskin, 2003], and is often extreme. yet standard (U-Th)/He procedures determine bulk U and Th in order to calculate both ages, and recoil corrections. The assumption of U and Th homogeneity can lead to significant over- and under-estimation of the fraction of  $\alpha$ -particles lost. In the most extreme cases, recoil corrected (U-Th)/He ages can underestimate recoil by over 50 %. Chemical zonation in zircons is usually highly variable both within and between samples and the identical treatment of crystals with different distributions of U and Th will lead to apparently poor age reproducibility. Quantification of the errors introduced by incorrect modelling of  $\alpha$ -recoil from zoned crystals has only recently been possible [Hourigan *et al.*, 2005]. Although investigations have tended to focus on hypothetical, simple zonation styles they highlight the need for improved understanding of the U and Th zonation in analysed crystals. In crystals where the zonation is extreme, zonation in the accumulation of radiation damage may also lead to differential diffusion kinetics between neighbouring zones. The defect density level at which radiation damage is thought to effect He diffusion will not be achieved in many samples, even where zonation is extreme [Nasdala *et al.*, 2001; Nasdala *et al.*, 2004; Reiners *et al.*, 2004]. Future investigation may show that the accumulation of  $\alpha$ -damage becomes important at lower defect densities, and the incorporation of multiple kinetic domains into the diffusion models for slowly cooled samples.

### 4.7.1 Modelling U and Th zonation

Hourigan *et al.* (2005) expanded the idiomorphic model described in Section 4.5.1 to incorporate a spatially variable U and Th concentration. The concentration specific  $\alpha$ -productivity at each computational node is determined from a user defined 1-dimensional concentration profile. The extrapolation from 1- to 3-dimensions is based on the assumption that crystal growth progressed from nucleation in a self-similar manner. All zone boundaries therefore represent isochronal surfaces, and will be located at the same relative radial positions along all face normal profiles through the centre of the crystal (Figure 26). Zonation specific  $\alpha$ -corrections ( $F_2$ ), are then calculated from the concentration specific  $\alpha$ -productivity, and the fractional loss at each node.

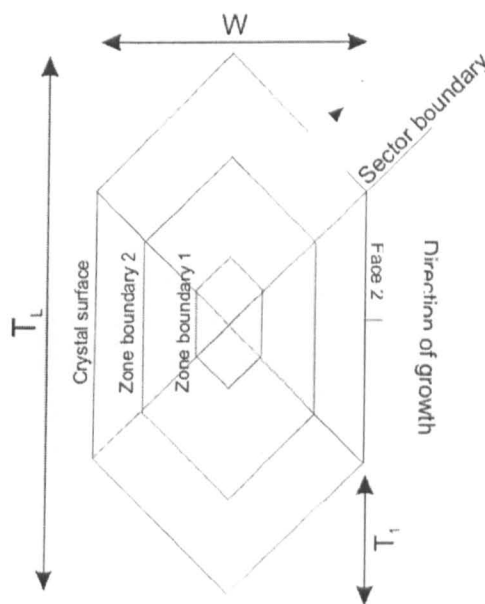


Figure 26 - The model of self similar zonation used to calculate a 3-D  $\alpha$  productivity matrix from a 1-D concentration profile [modified after Hourigan *et al.*, 2005]

#### 4.7.1.1 Simple U and Th zonation

Using a series of synthetic single-step-function zonation patterns with a range of spherical and tetragonal crystal morphologies, Hourigan *et al.* (2005) quantified the errors introduced by assuming homogeneity. Figure 27 (A - C) shows the family of curves produced by a single concentration change in a range of idiomorphic geometries. The zonation is modelled as a step-function with a concentration change of  $\Delta C$ , calculated by:

$$\Delta C = \frac{C_{RIM}}{C_{CORE}}$$

Equation 33

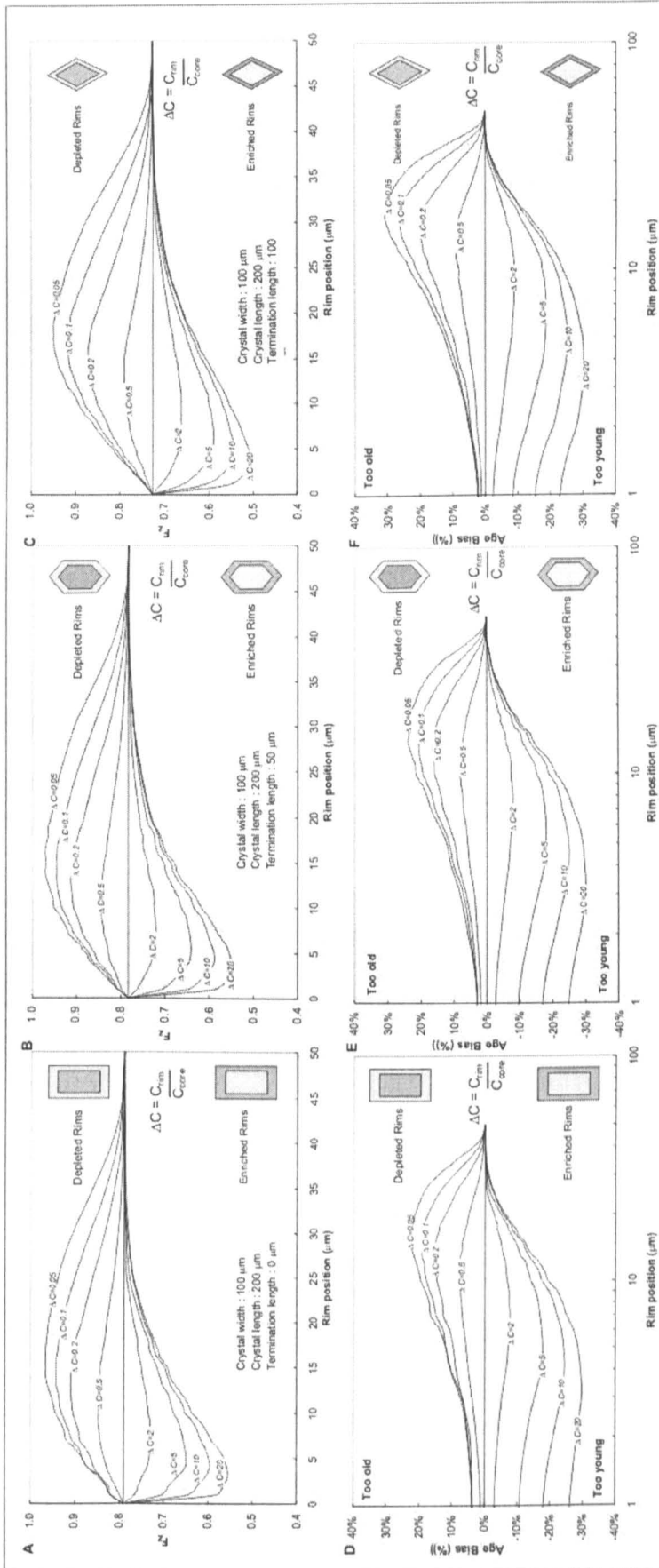


Figure 27 - The dependence of  $F_z$  on the magnitude ( $\Delta C$ ) and location (rim position) of a single zone boundary in a tetragonal crystals.

Panel A - C) The dependence of  $F_z$  on the magnitude ( $\Delta C$ ) as a function of the rim thickness for three idiomorphic tetragonal geometries (as shown in the schematic crystal representations) [Hourigan *et al.*, 2005]. The zone boundary is modelled as a step function which occurs at the interface between core and rim. The depth at which this boundary occurs is plotted as rim position ( $\mu\text{m}$ ). All curves are labelled with the concentration change that occurs across that boundary ( $\Delta C$ ) [after Hourigan *et al.*, 2005]. Panel D - F) The age bias caused by assuming homogeneity when crystals are zoned. Age biases are calculated using Equation 22 for each of the crystals and zonation patterns shown in panels A - C. The rim position (i.e. location of the zone boundary) is plotted on a logarithmic scale to emphasise the rapid changes that occur when rims are narrow.

Narrow U and Th enriched rims ( $\Delta C \gg 1.0$ ) and wide U and Th depleted ( $\Delta C \ll 1.0$ ) rims cause the greatest discrepancy between  $F_T$  and  $F_Z$ , but even relatively subtle zonation ( $0.2 < \Delta C < 5.0$ ) can mean  $F_Z$  is  $\sim 10\%$  larger (Figure 27 (A-C)). The effect that the incorrect assumption of homogeneity has on the corrected (U-Th)/He ages can be determined as an age bias,  $\gamma$ , using Equation 34 [Hourigan *et al.*, 2005].

$$\text{Age bias} = \gamma(\%) = \frac{\text{Age}_{(F_T \text{ corrected})} - \text{Age}_{(F_Z \text{ corrected})}}{\text{Age}_{(F_Z \text{ corrected})}} = \frac{\text{Age}_{(F_T \text{ corrected})}}{\text{Age}_{(F_Z \text{ corrected})}} - 1 = \frac{F_Z}{F_T} - 1$$

Equation 34

Plotting  $\gamma$  against rim position (on a logarithmic scale) for different concentration functions allows the resolution of the effect of the narrow rims on the (U-Th)/He ages (see Figure 27 (D - F), plotted using data from Hourigan *et al.* 2005). The positive age bias maxima occur when rims are large, between  $12\ \mu\text{m}$  ( $\Delta C = 0.5$ ) and  $17\ \mu\text{m}$  ( $\Delta C = 0.05$ ). Hourigan *et al.* (2005) use models of spherical crystals to show that at small radii ( $< 25 - 30\ \mu\text{m}$ ) the positive age bias maxima associated with depletion decreases significantly with increasing crystal radius, whereas the negative maxima associated with enriched rims is far less effected. This implies that in some samples it may be possible to reduce the age bias, or at least minimise the variation in the age bias introduced by the application of the  $F_T$  correction, by crystal selection from specific size aliquots.

#### 4.7.1.2 Simple zonation in idiomorphic crystals

For accurate quantification of the effect of zonation on realistic crystals, an understanding of the magnitude and variation of  $\gamma$  (age bias) is required. Modelling of a series of idiomorphic geometries was performed during this study to investigate the effects of crystal size, termination length and  $W_1/W_2$  on  $\gamma$ . The results of this modelling are shown in Figure 28 (crystal size and termination length), Figure 29 and Figure 30 ( $W_1/W_2$  and termination length).

These models show that the maximum negative bias caused by the enriched rims is relatively insensitive to changes in rim width, crystal size, and crystal geometry, remaining almost constant at  $\sim -30\%$  when rims are  $\sim 4 - 6\ \mu\text{m}$  thick (see Figure 28, Figure 29 and Figure 30). The insensitivity of  $\gamma$  to changes in geometry is because of the cubic relationship between the rim volume and crystal geometry, which causes even highly enriched rims to contain a relatively small, and similar proportion of the total crystal U and Th across all geometries [Hourigan *et al.*, 2005]. The maximum age bias associated with depleted rims is much more variable, but for all geometries rims of  $\sim 17\ \mu\text{m}$  (the  $\alpha$ -stopping distance) lead to the largest bias. The magnitude of the maximum positive bias ( $\Delta C = 0.05$ ) increases from  $\sim 20\%$  to  $\sim 40\%$  as crystal width decreases from  $150\ \mu\text{m}$

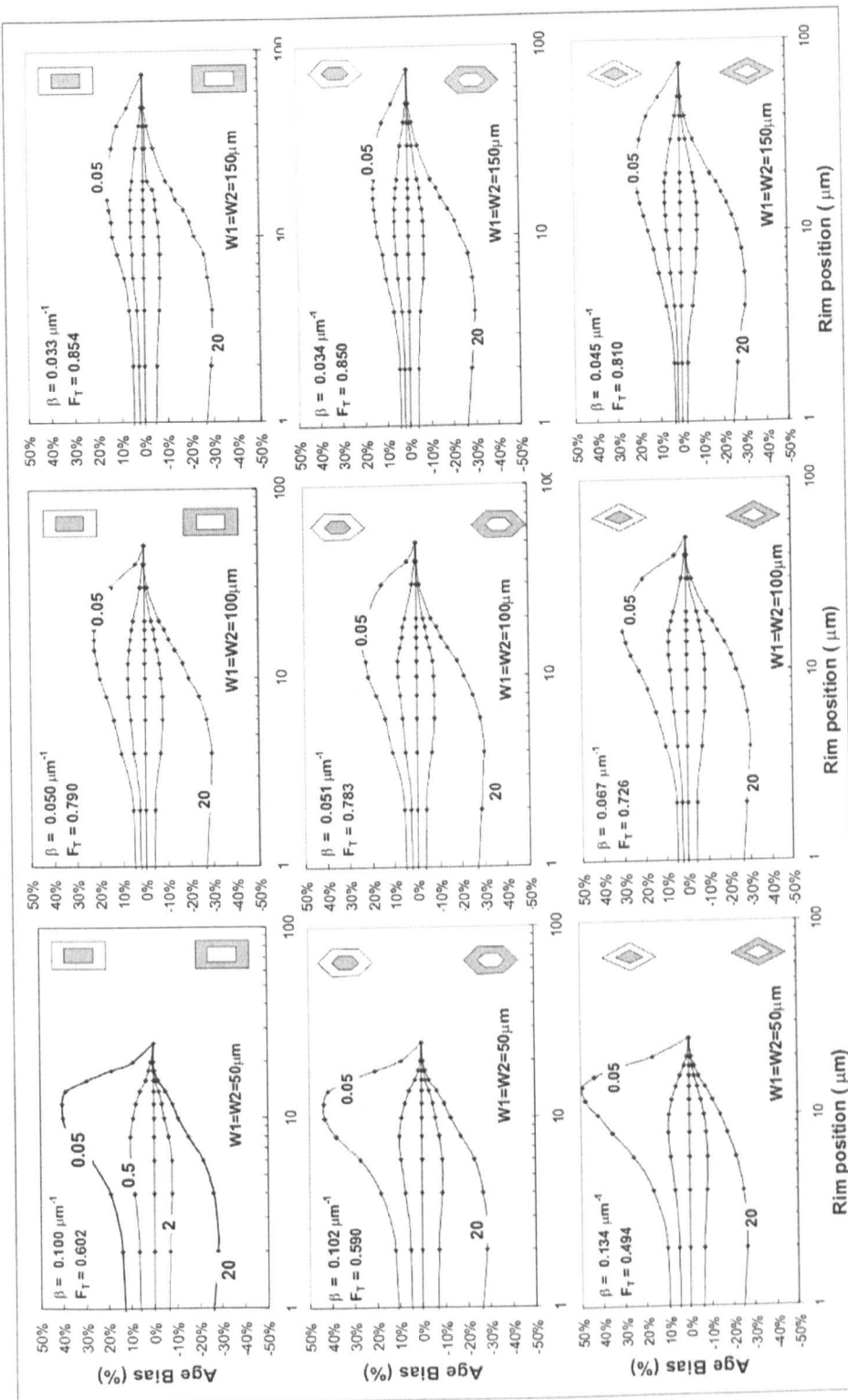
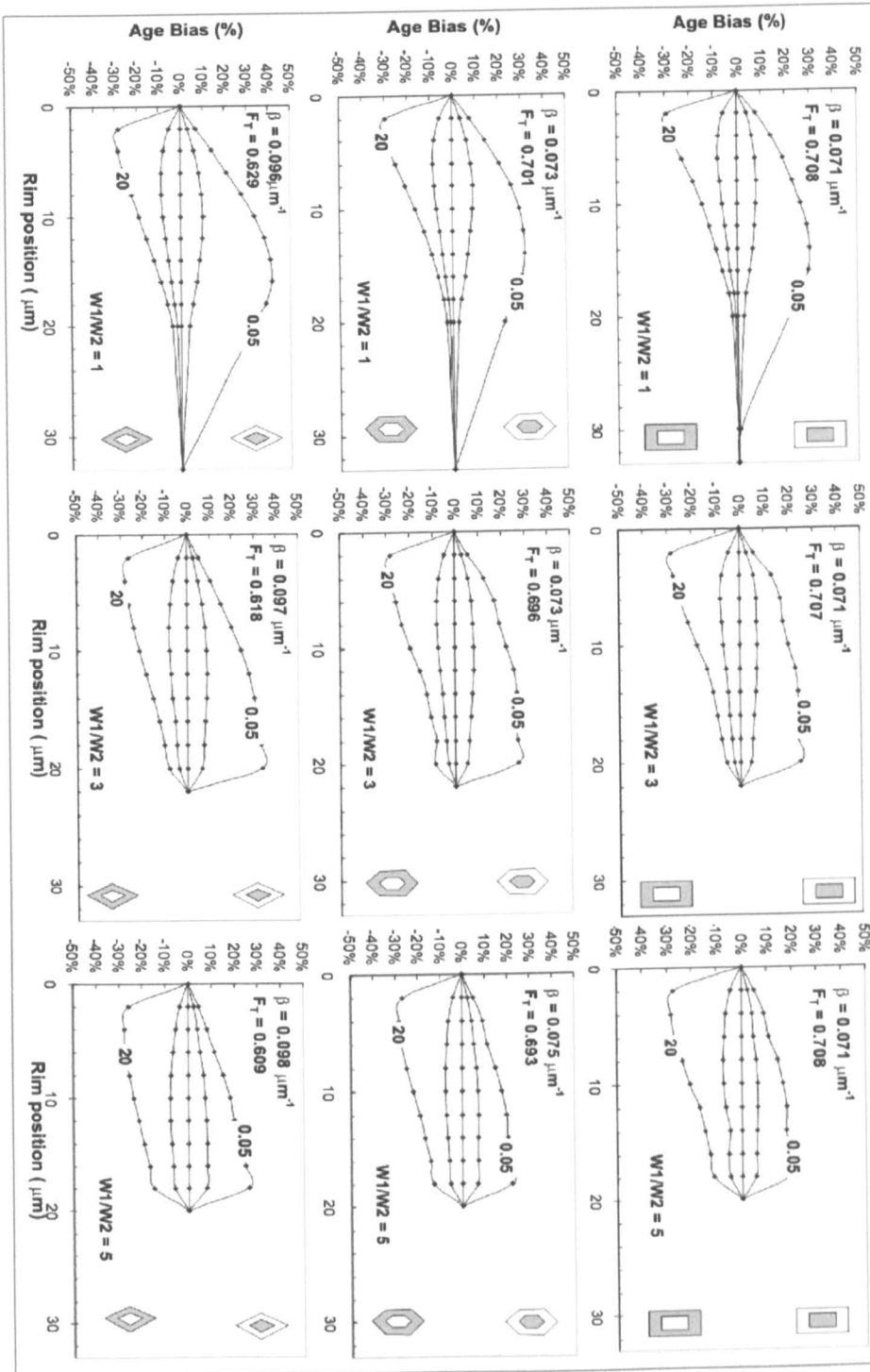


Figure 28 - The age bias introduced by assuming homogeneity in tetragonal crystals:

The relationship between ΔC, boundary location, crystal size for three idiomorphic tetragonal geometries. All crystals are tetragonal, with aspect ratio = 2.0. Panels running left to right show change in age bias with crystal size (W<sub>1</sub> = W<sub>2</sub> = constant). Panels running top to bottom show change in age bias with increasing termination length (constant crystal size). The boundary location (rim position) is plotted on a log scale to emphasise the changes when rims are narrow. Observed age bias is not proportional to the relative width of the rim, and so absolute rim positions (μm) are used in this, and subsequent plots.



(f) : The age bias introduced by assuming homogeneity in orthorhombic crystals.

The relationship between  $\beta$ , boundary location, crystal size for three idiomorphic orthorhombic geometries. Panels running left to right show the change in age bias associated with increasing the  $W_1/W_2$  for a constant  $\beta$  and termination length. When  $W_1/W_2 = 1$ ,  $T_1 = T_2 = 50\%$  of total crystal length. Top panels: Crystal is pinacoidal. Middle panels:  $T_1 + T_2 = 50\%$  of total crystal length. Bottom panels:  $T_1 + T_2 = 100\%$  of total crystal length.

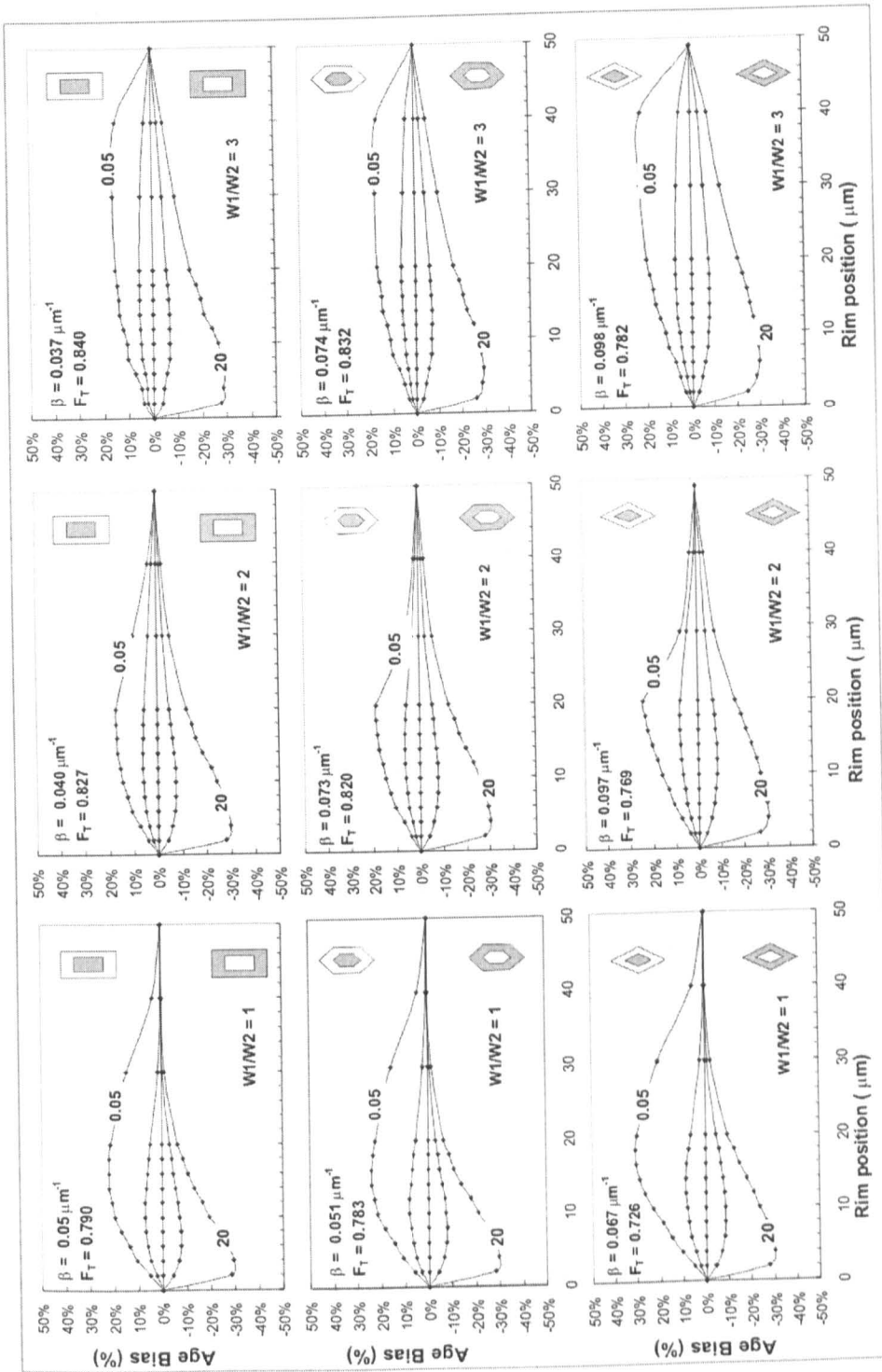


Figure 30 - The age bias introduced by assuming homogeneity in orthorhombic crystals (II)

The relationship between  $\Delta C$ , boundary location, crystal size for three idiomorphic orthorhombic geometries. Panels running left to right show the change in age bias associated with increasing the  $W1/W2$  for a constant  $\beta$  and termination length.  $W1/W2 = 1.0$  (left panel)  $W1 = W2 = 66 \mu\text{m}$ , and  $TL = 200 \mu\text{m}$ . Top panels: Crystal is pinacoidal. Middle panels:  $T1 + T2 = 50\%$  of total crystal length. Bottom panels:  $T1 + T2 = 100\%$  of total crystal length. Boundary location is plotted on a linear scale to emphasise changes when rims are broad.

to 50  $\mu\text{m}$ , and also increases by  $\sim 10\%$  increase as the fraction of the crystal within the terminations increases from 0% (pinacoidal) to 100% (by-pyramidal) (Figure 28). All three plots show the absolute position of the core-rim boundary in  $\mu\text{m}$ , and Figure 28 shows there is no correlation between the relative rim position (e.g. 10% of crystal width) and the age bias.

Figure 29 and Figure 30 show the change in the form of the curves which is associated with the increase in  $W_1/W_2$ . These plots do not show rim thickness on a logarithmic scale in order to provide better resolution at large rim thicknesses. Where the surface area-to-volume ratio and total length of the modelled crystals remains constant, while  $W_1/W_2$  increases from 1.0 to 5.0, there is a  $\sim 10\%$  decrease in the maximum magnitude of  $\gamma$ . Hourigan *et al.* (2005) suggest that a decrease in the maximum age bias seen in spherical crystals of small radii occurs because the majority of the crystal volume is affected by  $\alpha$ -recoil. In the idiomorphic crystals investigated here, the fixed value of  $\beta$  means that as  $W_1/W_2$  increases, the minimum dimension reduces, and a similar reduction in the maximum age bias is observed. In these crystals the total crystal width is 44  $\mu\text{m}$  ( $W_1/W_2 = 3.0$ ) and 40  $\mu\text{m}$  ( $W_1/W_2 = 5.0$ ) and so almost all the crystal experiences  $\alpha$ -recoil. A 10% decrease in  $\gamma$  is also observed in Figure 30, where the crystals have a constant minimum dimension of 100  $\mu\text{m}$ . As  $W_1/W_2$  increases, the surface area-to-volume ratio and the proportion of the crystal that experiences  $\alpha$ -recoil decreases, and so another geometric effect must control the observed reduction in  $\gamma$ . The exact origin of the decrease observed remains unclear, but the increasingly planar form of the crystal means that it may be associated with the proportional decrease in  $\alpha$ -recoil which occurs through the narrow  $W_2 R_L$  face as  $W_1/W_2$  increases. This may lead to the reduced  $\gamma$ , and further investigation is required.

#### 4.7.1.3 Complex U and Th zonation

Increased complexity in the zonation generally causes a reduction in age bias. Oscillatory zonation, where the concentration varies in a consistent manner (on a small length scale), has negligible effect on  $\alpha$ -particle retention. The  $\alpha$ -recoil from neighbouring zones of relative U and Th enrichment and depletion balances out, and it is the zone width and the relative concentration of the outermost zone that dominates bulk  $F_Z$ . Modelling of a fine (2.5  $\mu\text{m}$ ) oscillatory zonation where the enriched zones have twice the U and Th of the depleted zones, yields an  $F_Z$  which is  $\sim 0.01\%$  smaller than the  $F_T$  ( $F_T = 0.787$  when homogeneous,  $W_1 = W_2 = 100\ \mu\text{m}$ ,  $T_1 = T_2 = 50\ \mu\text{m}$ ,  $T_L = 200\ \mu\text{m}$ ) [Hourigan *et al.*, 2005]. The oscillatory zoned crystal has an  $F_Z$  which is comparable to that when only the outer most zone is considered ( $F_Z = 0.787$ ).

Modelling performed during this study shows that  $\gamma$  increases with zone width and the relative concentration changes across the boundary. For a 5  $\mu\text{m}$  wide oscillatory zonation pattern with enriched zones with twice the U and Th of the depleted zones,  $\gamma = 0.8\%$ . When the relative

concentration difference is increased to 20, the age bias increases to  $\gamma = 2.4\%$ . As termination lengths increase (for constant  $T_L$ ) the  $\gamma$  bias reduces by  $\sim 50\%$  because a smaller proportion of the crystal experiences no  $\alpha$ -recoil. The magnitude of the age bias will increase with increasing rim width, as the concentration profile tends towards that of a single step function.

Where the oscillatory zonation has a regular concentration change between alternating zones,  $\gamma$  is controlled by the relative concentration of the outer zone. For depleted rims  $\gamma$  is positive, and for enriched rims it is negative. No such generalisations can be made with oscillatory zonation patterns that have no regular, consistent change in the measured concentrations. The zones in the outer most regions will still dominate the calculated  $F_z$ , but the averaging effect seen with the regular zonation will be lessened, and  $F_z$  will be strongly dependant on the width, depth and concentration of individual zones.

#### 4.7.1.4 The limitations of existing modelling techniques

The method used to extrapolate a 3-D representation, limits the application of the Hourigan *et al.* (2005) model to samples with concentric zonation patterns. Zircons show a wide range of zonation styles (see Figure 31), and although the crystals in Figure 31 do not show U and Th zonation, they highlight the variety of zonation patterns that are observed. Only Crystals A and B (Figure 31) can be adequately represented by the Hourigan *et al.* (2005) model.

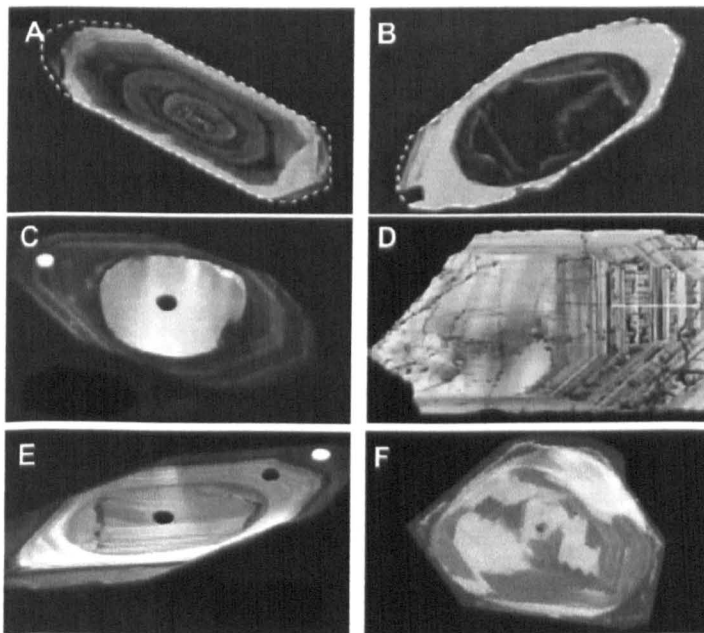


Figure 31 - Complex zonation styles in natural zircon.

A & B) Natural zonation that can be adequately modelled by the Hourigan *et al.* (2005) 3D construction CL images [both from Reiners *et al.*, 2004]. C to F) zonation patterns that cannot be modelled by the Hourigan *et al.* (2005) see text for details. C) SEM BSE image [from Poller *et al.*, 2001] D) greyscale image of birefringence [from Palenik *et al.*, 2003]. E) CL image [from Geisler *et al.*, 2003] F) CL image [from Corfu *et al.*, 2003].

Crystals C & D show faster growth parallel along the c- axis, and subsequently the self-similar model will over- or under-estimate  $\alpha$ -recoil loss from the core depending on the orientation of the concentration-depth profile. In both crystals the narrow zonation will dominate the recoil losses in the crystal terminations, and a single step function will control the  $\alpha$ -recoil through the long crystal faces. Crystal E shows a zonation pattern at an angle to the crystallographic axis, and Crystal F shows a patchy mottled zonation (typical of some metamorphic samples that have seen recrystallisation). None of these crystals can be modelled by the Hourigan *et al.* (2005) 3D construction. Qualitative assessment of the style of zonation in two and three dimensions is therefore also important before the model can be applied with confidence.

## 4.8 Recoil and diffusion and zircon (U-Th)/He ages

The application of a geometry dependent  $\alpha$ -recoil correction ( $F_T$  or  $F_Z$ ) is only strictly applicable to samples that have cooled rapidly, and it is common practice to present all (U-Th)/He ages in their  $F_T$  corrected form. A number of studies have shown the effect that simultaneous diffusion and ejection can have on the measured (U-Th)/He ages of apatite when samples have spent significant lengths of time in the partial retention zone [Meesters & Dunai, 2002a; Corfu *et al.*, 2003]. As zircons may spend significant periods in the He partial retention zone, recoil and diffusion should also be considered. This section discusses the effects of recoil and diffusion on zircon (U-Th)/He ages, and considers the effect of zonation on the measured (U-Th)/He ages from a range of thermal histories.

### 4.8.1.1 Modelling diffusive loss of He in zircon

The DECOMP software presented in Meesters & Dunai (2002a), uses an eigenmode-methodology. The model uses the eigenvalue  $\mu_m$  and the dimensionless number  $\gamma_m$  to solve the production-diffusion equation for a range of crystal geometries. These values are related to geometry, and the cooling of a body from an initial temperature, and Meesters & Dunai (2002a) present the form of  $\mu_m$  and  $\gamma_m$  for typical geometries of interest to (U-Th)/He applications (sphere, finite rectangular block, finite cylindrical block). By modelling the accumulation of helium in different crystal geometries (a cube, a sphere, finite cylinder, infinite cylinder and rectangular block) of the same surface area-to-volume ratio ( $\beta$ ), Meesters & Dunai (2002a) show that  $\beta$  is the dominant control on the recoil and diffusion process. This treatment considers a rectangular block with widths of  $160 \mu\text{m}$  ( $W_1 = W_2$ ), and a height of  $80 \mu\text{m}$  ( $\beta = 0.05 \mu\text{m}^{-1}$ ) i.e. a tetragonal crystal. Meesters & Dunai (2002a) show that for tetragonal geometry, modelling the accumulation of helium within an equivalent sphere with the same surface area-to-volume ratio is a good approximation. DECOMP can therefore be used to forward model (U-Th)/He ages in tetragonal zircon. A preliminary investigation into the combined effect of recoil and diffusion on zircon (U-Th)/He He ages

(tetragonal geometry) was performed using the diffusion parameters  $D_0 = 0.46$  cm/s and  $E_a = 40400$  cal/mol, and an  $\alpha$ -stopping distance of  $17 \mu\text{m}$  [Reiners, 2005]. The results of this investigation are discussed in Section 4.8.2.

#### 4.8.1.2 The limitations of the DECOMP model

As the user interface of DECOMP requires the input of an appropriate spherical geometry in order to forward model (U-Th)/He ages for different thermal histories, the validity of the translation from typical crystal geometries to an equivalent sphere must be assessed. Meesters & Dunai (2002a) show that for tetragonal pinacoidal geometries, translation to an equivalent spherical geometry is acceptable. The DECOMP model has only been applied to pinacoidal geometries, and the effects of the crystal terminations have not been considered. The increased  $\alpha$ -recoil from the crystal terminations will change the He concentration gradients within the crystal. As shown by the polynomial relationship between  $\beta$  and  $F_T$  (Figure 19), the surface area-to-volume ratio can be seen to exert a strong first order control over  $\alpha$ -recoil (as seen in apatite, Section 2.4.4) for tetragonal crystals, and therefore  $\beta$  is the dominant control on the He gradient established in the crystal. Consequently, although the effect of the termination has not been considered, the translation to an equivalent spherical model is probably valid, within the uncertainties of the method and the calculation of  $\beta$ .

The DECOMP model does not allow consideration of orthorhombic crystals. The complex dependence of surface area-to-volume ratio on  $\beta$  and  $W_1/W_2$  suggests that a simple translation will not fully incorporate the geometric control. From Figure 22, the relationship between  $F_T$  and  $W_1/W_2$ , allows crystals with very different geometries and recoil characteristics, to have identical surface area-to-volume ratios. Indeed, if the effect of the terminations is ignored, and the  $\beta$  is calculated using Equation 25 (pinacoidal), the same surface area-to-volume ratio can be obtained from an infinite number of combinations of the independent variables  $L$ ,  $W_1$  and  $W_2$ . Changing the geometry of the crystal (by increasing  $W_1/W_2$ ) will change the form of the He concentration gradient established by  $\alpha$ -recoil, and will also reduce the size of the diffusion domain for a constant  $\beta$ . This will shorten the fastest diffusion pathway, and lead to preferential diffusive loss through the  $W_1L$  crystal faces. The effect of increasing the rate of diffusion by changing  $W_1/W_2$  for a given  $\beta$  and thermal history, will be non-linear and is impossible to quantify.

The eigenmode-methodology of Meesters & Dunai (2002) allows the incorporation of fully independent non-tetragonal geometries ( $W_1 \neq W_2 \neq L$ ) into  $\mu_m$  and  $\gamma_m$ , and can therefore be used to determine the effect orthorhombic geometries. However, the DECOMP user interface only allows the input of the equivalent spherical approximations it is unclear how such a translation should be performed, and if an additional dependence on  $W_1/W_2$  should be incorporated. As the validity of

translation from orthorhombic crystals to equivalent spheres cannot be assessed, a consideration of the recoil and diffusion from spherical geometries can at present only be extrapolated to tetragonal crystals.

#### 4.8.2 The effect of recoil and diffusion on zircon (U-Th)/He ages

Published models used in the forward modelling of the accumulation of helium in apatite [Wolf *et al.*, 1996; Wolf *et al.*, 1998; Meesters & Dunai, 2002a], provide a framework for the investigation of recoil and diffusion in zircon. Uncorrected (U-Th)/He ages will exhibit a non-linear dependence on both crystal size and thermal history. The measured (U-Th)/He age will depend on crystal size, and the time and rate at which the crystal cools. Understanding the recoil-diffusive loss in a range of geological systems is important for interpretation of replicate analyses.

Modelling of the recoil and diffusion in zircon was performed using effective radii between 20  $\mu\text{m}$  and 200  $\mu\text{m}$ . This corresponds to the typical range of surface area-to-volume ratios i.e.  $0.015 \mu\text{m}^{-1}$  (effective radius = 200  $\mu\text{m}$ )  $> \beta > 0.10 \mu\text{m}^{-1}$  (effective radius = 30  $\mu\text{m}$ ). The modelled samples all pass through 220°C at the same time, then cool monotonically until 160°C, at which point the samples cool to 20°C over 1 Myr. Figure 32 A shows the results of this forward modelling, and illustrates the effect of combined recoil-diffusion, and the dependence of the predicted (U-Th)/He ages on effective crystal radius and cooling rate. The continuation of slow diffusive loss at temperatures below the PRZ will mean that samples which cool more slowly from 160°C to 20°C will have a greater variation of (U-Th)/He with effective radius.

Following the Farley (2002) protocol, and performing a standard recoil correction ( $F_T$ , Hourigan *et al.* 2005 parameters) on crystals that cooled through the PRZ at 100°C/Myr will yield a reproducible (U-Th)/He age  $236 \text{ Ma} \pm \sim 4 \% (2\sigma)$  (crystals between  $r = 30 \mu\text{m}$  and  $r = 200 \mu\text{m}$ ). As the cooling becomes slower, the  $F_T$  corrected ages begin to diverge, and at cooling rates of 0.5°C/Myr the mean age across the same range in crystal sizes would be  $155 \text{ Ma} \pm 19 \% (2\sigma)$ . At small effective radii the effect of combined recoil and diffusion may be apparent in both the uncorrected and  $F_T$  corrected (U-Th)/He ages for rapidly cooled samples (Figure 32 B). In many zircon samples effective radii will be  $< 80 \mu\text{m}$ , and it is therefore essential to consider the effects of diffusion and  $\alpha$ -ejection operating simultaneously. Where crystal size - crystal age relationships can be observed, it may be also possible to extract information about the rate of cooling, and to limit the number of thermal histories which can generate the measured ages.

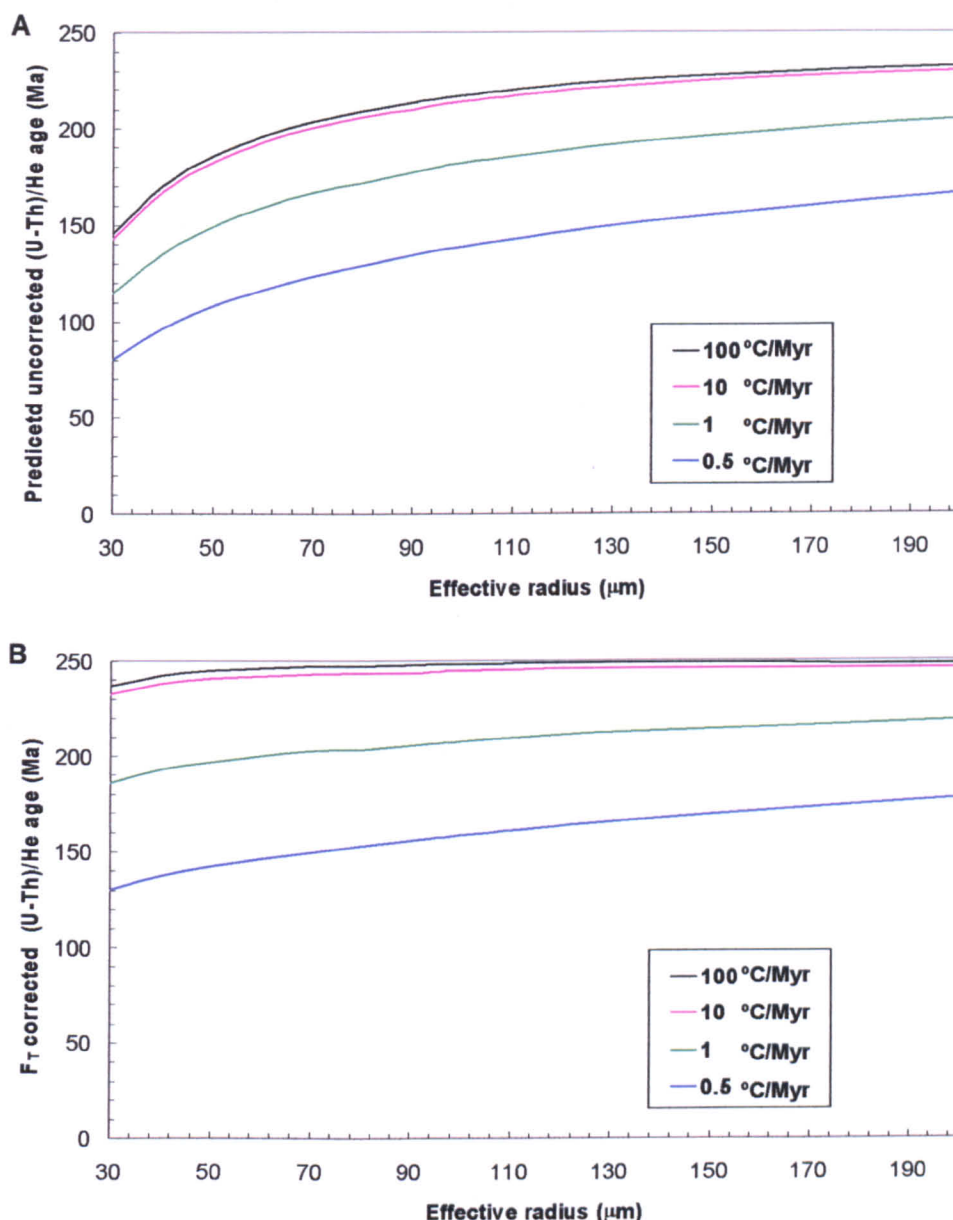


**Figure 32 - The effect of recoil and diffusion on zircon (U-Th)/He ages: Homogeneous crystals**

The dependence of the uncorrected (U-Th)/He age on cooling rate and crystal radius for homogenous crystals.

**A)** All samples pass through 220°C at 250 Ma. The uncorrected (U-Th)/He ages for a range of crystal sizes for different thermal histories. Cooling through the PRZ from 220°C to 160°C occurs at the rate shown (100°C/Myr, 10°C/Myr, 1°C/Myr, 0.5°C/My). Cooling from 160°C to 20°C occurs over 1 Myr, and then all samples remain at 20°C until the present day. All crystals have a homogeneous U and Th distribution.

**B)** The range of ages obtained following standard  $F_T$  correction procedure [Farley, 2002]. Standard  $F_T$  correction of rapidly cooled samples yields good age reproducibility. Thermal histories as for Panel A.

Full consideration of these effects may help to distinguish between a sample with poor age reproducibility which is consistent with a single thermal history, and one that may be affected by variable zonation. Given the variable U and Th zonation observed in many samples, the estimation

of cooling rates based on a strong dependence of (U-Th)/He age on crystal radius, should only be attempted when the samples is known to be homogeneous.

#### 4.8.2.1 The effect of recoil and diffusion on (U-Th)/He ages in zoned zircon

Zonation in zircon can be extreme and highly variable between individual crystals that have experienced a common thermal history. Zonation will disrupt the He concentration gradient in the crystal, and can have a significant effect on partial diffusive loss, especially during protracted cooling histories. DECOMP can currently incorporate a range of simple “all or nothing” zonation styles, in which the user can define the position of a concentration step function, where  $\Delta C = \infty$  (i.e. all the U and Th is one side of the zone boundary). The  $\Delta C = \infty$  step function that is currently available is probably more applicable to zircon than to apatite. U and Th depleted rims have the effect of reducing the concentration gradient at the crystal boundary, slowing the rate of diffusion out of the crystal. Conversely, U and Th enriched rims will increase the rate of diffusion across the grain boundary, but will also establish a more complex He concentration gradient within the crystal. The zone immediately interior to the zonation boundary will accumulate He and lead to diffusion towards the centre of the grain. Crystal specific zonation patterns will lead to a range of different diffusion profiles within a sample, and the effect on the raw (U-Th)/He age will be further controlled by the thermal history. The software cannot currently incorporate more complex zonation patterns, or  $\Delta C \neq \infty$ , however the future modification of the code to include 1-D concentration profiles should be possible [Dunai, pers com.].

The natural variability of U and Th zonation within a sample means that modelling can only allow a qualitative assessment of the effect of zonation of the zircon (U-Th)/He ages. A preliminary investigation forward modelled the different zonation profiles for the 100°C/Myr and 0.5°C/Myr thermal histories considered above. Figure 33 illustrates the range of uncorrected (U-Th)/He ages that are be expected if crystals have a constant effective radius but a variable zonation width; a form of zonation that will be common in volcanic zircons. The application of the  $F_T$  correction to this data would not change the range in ages (U-Th)/He ages as all crystals are the same size (200  $\mu\text{m}$ ,  $F_T = 0.94$  or 50  $\mu\text{m}$ ,  $F_T = 0.76$ ).

These plots are generated from a constant, infinite concentration change across a simple step function, and when samples have more moderate concentration changes the uncorrected (U-Th)/He ages will fall within the bounds defined by the “depleted” and “enriched” arrays, for a given thermal history. The range of ages that can be obtained from a given zone width is generally broader at small crystal sizes, because of the greater proportion of the crystal that has a He concentration that is modified by both diffusion and  $\alpha$ -recoil loss. In larger crystals,  $\alpha$ -recoil in the volumetrically dominant core will have little effect on the He concentration gradient, as the

majority of  $\alpha$ -particles will come to rest in the zone in which they were generated. This means that in large crystals when the core is enriched, diffusion is the dominant loss mechanism, and all crystals of the same size will yield the same age, although there will be a slight increase in the (U-Th)/He age with increasing rim depth as the diffusion pathway for the He in the crystal core increases.

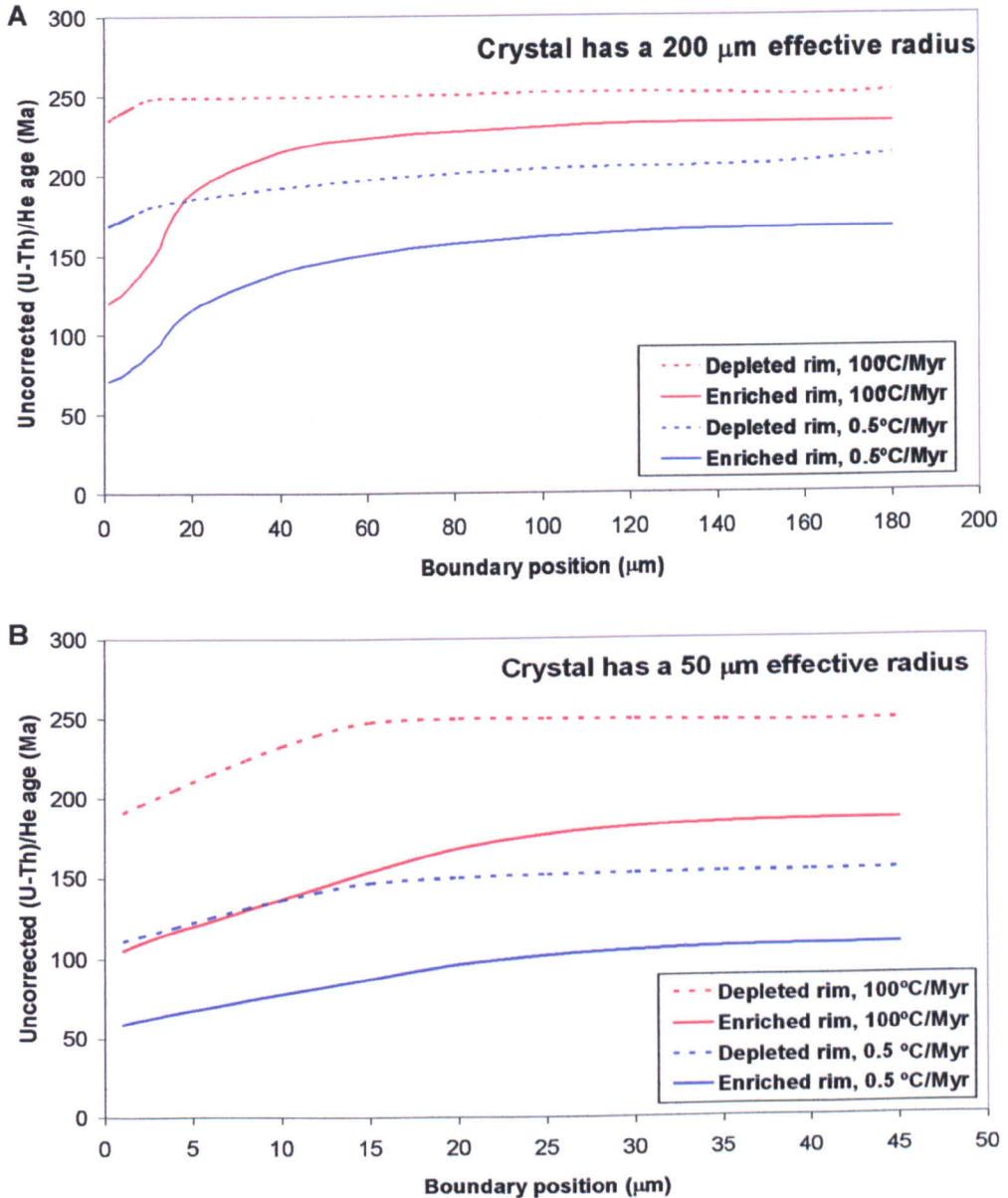


**Figure 33 - The effect of recoil and diffusion on zircon (U-Th)/He ages: Heterogeneous crystals.**

The dependence of the uncorrected (U-Th)/He age on cooling rate and zone boundary position radius for heterogeneous crystals. The plot shows the variation in the predicted (U-Th)/He ages that will be in a crystal with A) an effective radius of 200  $\mu\text{m}$  and B) an effective radius of 50  $\mu\text{m}$ . All crystals have a single step function concentration change at the boundary position shown ( $\mu\text{m}$  from crystal surface). Two cooling histories are modelled. Red: 100°C/Myr cooling through the PRZ. Blue: 0.5°C/Myr cooling through the PRZ.

It should be noted that the DECOMP models uses the effective radius for both the crystal size and the individual zones. The crystals in Figure 33 have effective radii of 200  $\mu\text{m}$  and 50  $\mu\text{m}$ . These sizes correspond to a tetragonal crystals of  $W_1 = W_2 = 300 \mu\text{m}$  and  $W_1 = W_2 = 77 \mu\text{m}$  respectively, when  $T_L = 2 W_1$ , and  $T_1 = T_2 = W_1$ . This simple theoretical application of the DECOMP modelling technique has shown the potential effect of simultaneous recoil and diffusion on the (U-Th)/He ages measured on homogenous and zoned zircons. This has revealed the substantial age variations that should be expected in heterogeneous (with respect to both crystal size and zonation) zircon populations that have experienced slow cooling. Modelling of more specific or varied U and Th zonation patterns is inappropriate because of the variable zonation patterns observed in zircon. Each crystal analysed will have a unique evolution of helium concentration dependant on the time-temperature path that it experiences, the effective radius and the U and Th zonation.

#### 4.8.2.2 Correct translation of tetragonal zonation into the spherical model

When modelling the known zonation in crystals the translation must be reversed, and the effective radius of the crystals and zones will be strongly dependant on geometry [see discussion in Hourigan *et al.*, 2005]. The translation from effective boundary position to actual rim position for tetragonal crystals is an approximately linear function, which varies with the length of the terminations as shown in Figure 34.

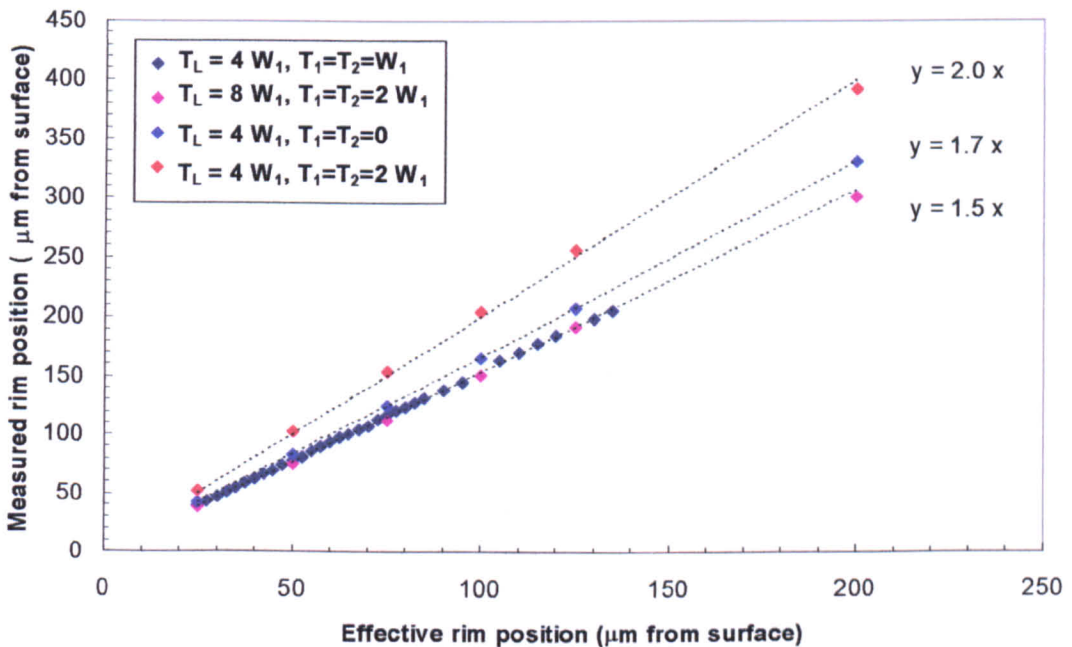


Figure 34 - The translation between effective rim position and the measured rim position in tetragonal crystals.

### 4.8.2.3 U and Th zonation and variable diffusion kinetics

The effect of U and Th zonation on the diffusion of He is poorly understood, and further diffusion experiments are required before this can be quantified. However, zones with high U and Th will have a higher density of lattice defects caused by  $\alpha$ -decay, and therefore will have different diffusion kinetics, and enhanced diffusion within highly damaged areas is to be expected. The  $\alpha$ -damage dose reported to be associated with diffusive loss under vacuum at room temperature [Reiners, 2005] is very high, and will not be routinely encountered during (U-Th)/He analysis, even in highly zoned crystals. The variations in the diffusion kinetics that will exist between zones for the majority of zircons may not be measurable using standard techniques, but further investigation of diffusion from zoned crystals with a variety of U and Th contents, zonation patterns and thermal histories is required before the impact of multi-diffusion domains can be quantitatively assessed.

### 4.8.2.4 Applied forward modelling of zircon (U-Th)/He data

While there remain several issues surrounding the routine application of DECOMP to all zircon (U-Th)/He analyses (see discussion in Section 4.8.1.2) where there is geological evidence for prolonged residence at moderate temperatures, or there is poor reproducibility in samples in which the U and Th distributions is known to be homogeneous, the effect of simultaneous recoil and diffusion on the (U-Th)/He age should not be ignored. When combined with information determined from AFT, ZFT and other chronometric or thermal indicators, the forward modelling of (U-Th)/He data can help constrain the detail of thermal histories. Selective (U-Th)/He analysis of a range of crystal sizes therefore has the potential to resolve the thermal history for the sample, and where samples have a limited grain size population it may also be possible to constrain thermal histories using crystals of the same radius, but with different U and Th distributions. For all consideration of the combined effect of diffusion and  $\alpha$ -ejection, the distribution of U and Th in the analysed crystals must be known.

## 4.9 Determining U and Th zonation in zircon

The determination of the distribution of U and Th within any crystal is crucial for the accurate consideration of the effects of geometry and zonation on  $\alpha$ -recoil and diffusion, and the correct interpretation of the (U-Th)/He data. This is rarely performed, despite the ability of several commonly used microscopic techniques to reveal the often dramatic chemical zonation. These techniques are often unsuitable for routine application required in (U-Th)/He studies, and even with recent advances, the spatial resolution and sensitivity of many techniques remains limited. This prevents the resolution of the narrow zonation patterns (few  $\mu\text{m}$ ), and subtle concentration changes that can effect (U-Th)/He ages.

## 4.9.1 Qualitative assessment of U and Th zonation

A qualitative assessment of the chemical zonation in zircons is possible using a number of imaging techniques. Perhaps most importantly, the proportion of crystals that show a certain style of zonation can be quantified. Qualitative techniques allow large numbers of crystal to be imaged, allowing the probability of a crystal having a given style of zonation to be determined. In this manner it is possible to understand how replicate (U-Th)/He ages may be affected. Although qualitative imaging techniques do not provide sufficient data to enable the detailed modelling described in Section 4.7, they can enable the analyst to preferentially select samples or size fractions that have a consistent style of zonation, and similar diffusion and ejection characteristics.

Where samples have poor age reproducibility, a statistical treatment of the zonation population may allow outlying (U-Th)/He ages to be reconciled with the data, and even where quantitative analysis is not performed, a simple qualitative assessment may allow potentially problematic samples to be avoided, or at least identified. The qualitative assessment of the different styles of zonation can also reveal any relationship between crystal size and zonation style that may exist where the zircons in a sample are from multiple generations of crystal growth within a melt, or from different source regions in the sedimentary catchment. In some samples it may be possible to determine changes in sediment supply within a catchment from a qualitative assessment of the zonation patterns alone. The following discussion, presents a summary and comparison of some of the qualitative techniques that can be routinely employed to assess the zonation of U and Th in zircon.

### 4.9.1.1 Fission-track distributions

Zircon fission track (ZFT) mounts can often be used to provide a semi-quantitative assessment on U zonation. Although the zonation styles found in a crystal population can sometimes be identified from polished, etched grain mounts, several factors must be considered before a full evaluation can be made.

Figure 35A shows an example of extreme zonation observed in the distribution of fission tracks. This shows that the application of a homogeneous  $\alpha$ -recoil correction will be incorrect, and will significantly over estimate the fraction of  $\alpha$ -particles lost. The Tardree Rhyolite (TR) zircons shown in Figure 35 exhibit major U zonation, with a U-rich, high track density core mantled by a  $\sim 25 \mu\text{m}$  thick, U-poor, low track density rim [Tagami *et al.*, 2003]. Analysis using laser ablation ICP-MS (LA-ICP-MS) depth-profiles reveal that the high U cores have  $\sim 40 \times$  the U concentration of the rims, and also confirms that the distribution of Th follows that of the U (Figure 35 B) [Hourigan *et al.*, 2005]. The uncorrected (U-Th)/He age for this sample was  $57.8 \pm 1.2 \text{ Ma}$  ( $2\sigma$ ), and using a homogeneous  $\alpha$ -recoil correction yields ages of  $\sim 81 \text{ Ma}$ , significantly older than formation age ( $58.4 \pm 0.4 \text{ Ma}$  (U-Pb); Gamble *et al.*, 1999). Modification of the  $\alpha$ -recoil correction

from  $F_T = 0.71$  (homogeneous U-Th) [Tagami *et al.*, 2003] to  $F_T = 0.94$ , incorporating the observed zonation yields corrected ages of 59.8 Ma [Hourigan *et al.*, 2005], within 2.4 % of the accepted age of formation.

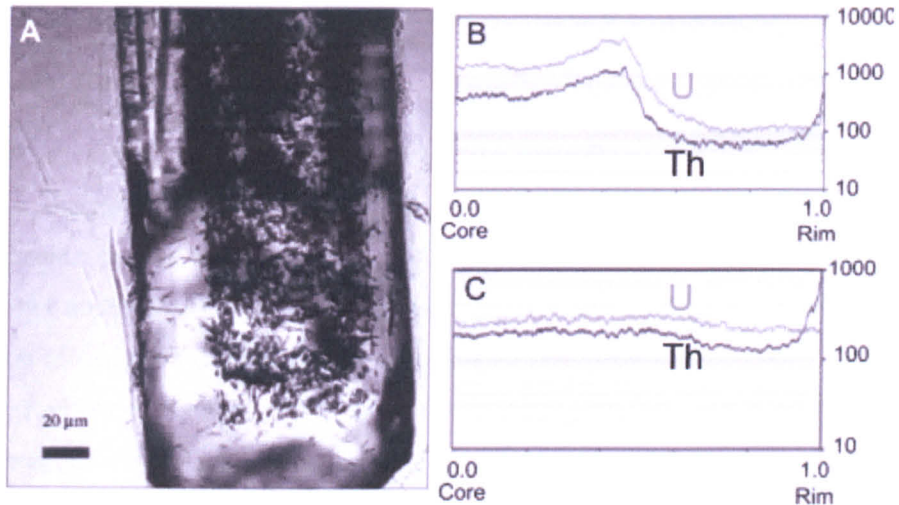


**Figure 35 - Zonation in zircons from the Tardree Rhyolite.**

**A) Zonation of spontaneous fission tracks showing relative depletion of crystal rim [Figure 2 Tagami *et al.*, 2003].**

**B & C) two laser ablation depth profiles of TR zircons showing the typical U and Th depletion in the crystal rim seen in 80 % of crystals (B), and an example of the less common zonation showing a narrow enriched rim (C) [from Hourigan *et al.*, 2005].**

Where zonation is more complex, and track lengths are long relative to the width of the zonation bands, several effects must be considered before any qualitative description of the patterns or distribution of different zonation styles within the crystal population can be performed. Tracks formed in each zone will extend beyond the zone boundaries. This will make boundaries appear more gradational and will potentially obscure narrow zones completely. The observed ZFT distribution will be further complicated by the three dimensional nature of zonation. The majority of revealed tracks will have been generated within the volume of the crystal extending to  $\sim 10 \mu\text{m}$  below the polished surface (revealed tracks intersect an unconfined track of up to  $\sim 10 \mu\text{m}$  length, or may be even deeper when confined tracks intersect a crack or other crystal defect). The ZFT distribution of both confined and unconfined tracks observed will therefore be a depth-averaged pattern.

The generation of tracks below the planar polished surface of the crystal can also lead to bias the track density seen close to crystal faces and terminations. Although the averaging effect in these marginal regions will be less, the overall track density will also be lower, and regions away from the margins will appear to have higher U concentrations. The averaging effect of the tracks produced away from the polished surface will be gradually reduced with increased amounts of thermal annealing, but in slowly cooled samples the relationship between annealing and total radiation damage may also effect the ZFT distribution. Finally, even if the zonation patterns are

clear, fission tracks do not allow the assessment of the Th concentration within the crystal. U and Th zonation is generally co-incident (with U-rich zones also having high Th contents), but absolute and relative concentrations of U and Th in each zone are highly variable [Corfu *et al.*, 2003; Nasdala *et al.*, 2003].

#### 4.9.1.2 Cathodoluminescence

Cathodoluminescence (CL) imaging allows the rapid qualitative assessment of zonation patterns in zircon. CL images are produced through the emission of energy as electron-hole pairs recombine at luminescence centres in the crystal lattice. These luminescence centres are typically sites of heterogeneity and/or dislocation of the crystal lattice. In zircon these commonly mark chemical substitution of rare earth elements (REEs) [see review by Nasdala *et al.*, 2003]. The CL emission spectrum from zircon is broadly split into blue and yellow emission bands, however the chemical substitutions that control the relative intensity of the emission spectra are poorly understood and remain the subject of debate [Hanchar & Hoskin, 2003].

The U and Th content of the zircon does not appear to have a direct control on the intensity or wavelength of CL emission, but zonation of the intensity and wavelength of CL emission has been shown to follow the distribution of REE, and U and Th [Poller *et al.*, 2001; Corfu *et al.*, 2003; Dempster *et al.*, 2003; Nasdala *et al.*, 2003]. The U and Th concentration is thought to exert a significant control over the quenching of CL because the  $\alpha$ -decay of these nuclides is the dominant source of lattice damage [Nasdala *et al.*, 2003]. Regions with high U and Th contents, and high  $\alpha$ -damage densities, and in zircons that have experienced self irradiation, CL images are related to zonation of U and Th. Thermal annealing of the radiation damage increases CL intensities and so the thermal history a sample has experienced will affect the degree of CL quenching that occurs.

Although it is not possible to use CL for quantitative analysis of U and Th distribution, CL imaging of polished grain mounts allows the variety of CL zonation patterns to be determined and the effect that the zonation will have on (U-Th)/He ages can be qualitatively assessed. Small crystal sizes and low emission intensities make capture of good quality optical CL images difficult in many cases. However, use of a CL detector attached to a scanning electron microscope (SEM-CL) can provide detailed panchromatic images of complex and narrow zonation patterns. SEM-CL allows quantitative assessment of the zonation populations within a sample as large numbers of crystals can be imaged quickly. It should be noted that the SEM-CL is more sensitive to blue-band CL emission, and so panchromatic images under represent any yellow-band zonation [Nasdala *et al.*, 2003].

CL images of the Tardree Rhyolite (TR) zircons (Figure 36) suggest that while the zircon fission tracks reveal the general pattern of zonation, much of the detail is largely obscured. The central

region of the crystal shown in Figure 35 shows a subtle concentric zonation in the distribution of fissions tracks, with small localised areas of relatively low track density away from the crystal rim. The CL images (Figure 36) show a much clearer zonation pattern. No quantitative analysis of the TR zircons was performed during this study, so direct comparison of the CL and U and Th distribution in the imaged crystals is not possible.

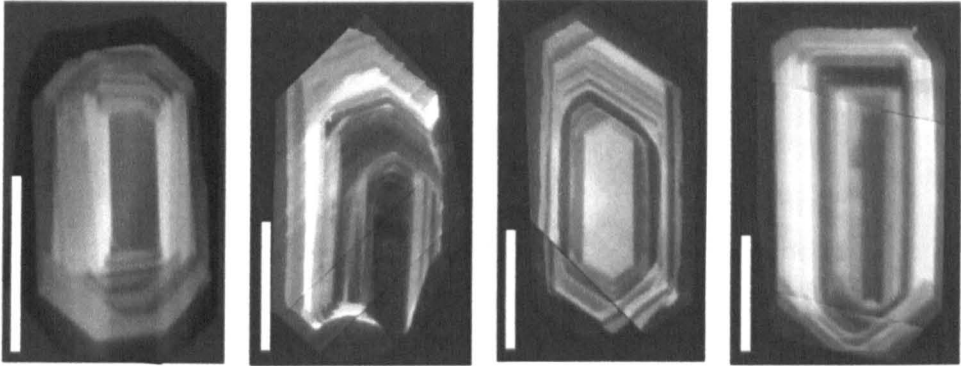


Figure 36 - CL images of Tardree Rhyolite zircon. White scale bars are 50 $\mu$ m.

The LA-ICP-MS depth profiles presented by Hourigan *et al.* (2005) show little evidence of any U and Th zonation within the crystal cores (see Figure 35). However, the beam sizes typically used for LA-ICP-MS have diameters of between 20  $\mu$ m and 100  $\mu$ m, and so even where CL zonation patterns are controlled by variable U and Th content, the large laser spot size will average the U and Th concentration of narrow adjacent bands. If the intensity of the CL emission from the TR zircons is a true reflection of the U and Th zonation, the regular variation of CL emission intensity across crystals would yield approximately constant U and Th when analysed using a 20  $\mu$ m beam LA-ICP-MS.

The region of more complex CL zonation observed in the TR zircon is in the core (more than 20  $\mu$ m from the crystal surface) and will not have a major influence in the  $\alpha$ -recoil correction calculated by Hourigan *et al.* (2005). Comparison of CL images from several TR zircons shows the variable form of the zonation patterns (Figure 36).

#### 4.9.1.3 Charge contrast imaging

Under low vacuum conditions it is possible to generate negative charge on the surface of an uncoated, ungrounded sample, when the number of secondary and back scattered electrons emitted is smaller than the number of electrons incident on the sample. The generation of this charge modifies secondary electron emission from the sample, producing contrast between areas of differing conductivity. This can be imaged on an environmental scanning electron microscope [see review in Watt *et al.*, 2000]. Charge-trapping occurs at defects, relating to luminescence centres in zircon. Charge contrast imaging (CCI) of zircon produces images that are very similar to those obtained under CL (Figure 37), but has several advantages. Zonation is often assessed using CL

before quantitative probe analyses is performed, and the high beam currents required to produce CL images of small crystals at high magnification, can damage the Au coating and the underlying sample, reducing the quality of the analysis.

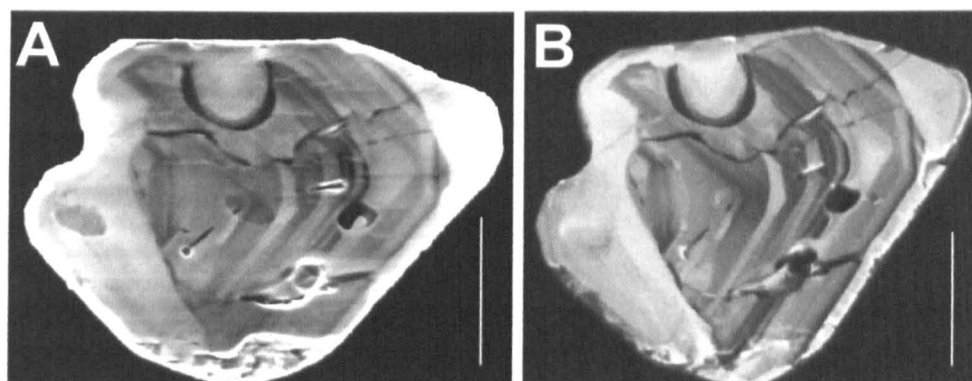


Figure 37 - A comparison of the charge contrast (a) and cathodoluminescence (b) images of a zoned zircon [from Watt *et al.*, 2000]. White scale bars are 50  $\mu\text{m}$ .

The use of uncoated samples means that CCI has the potential to be used to characterise zonation patterns in the crystals of a ZFT mount prior to etching. However, the quality and uniformity of the surface polish control the quality of the CCI, and the PFA Teflon used to mount zircons can cause difficulty as scratches and surface defects lead to charging and flaring making imaging difficult.

#### 4.9.1.4 Scanning electron microscopy

Back scattered electron (BSE) images are widely used to reveal internal structures in a range of accessory minerals. These measure variations in the average atomic number that is controlled by chemical zonation, and for zircon, the dominant control on zonation is thought to be Hf, with U only having a secondary effect [Hanchar & Miller, 1993; Corfu *et al.*, 2003]. BSE images usually show similar zonation patterns to those seen in CL, with the relative intensities reversed, and regions with high CL emissions generally correlate to regions of low BSE intensity (Figure 38 A & B). In some zircons, BSE images appear far more homogenous than the corresponding CL images, suggesting that the BSE is perhaps less sensitive to variations of U than the CL.

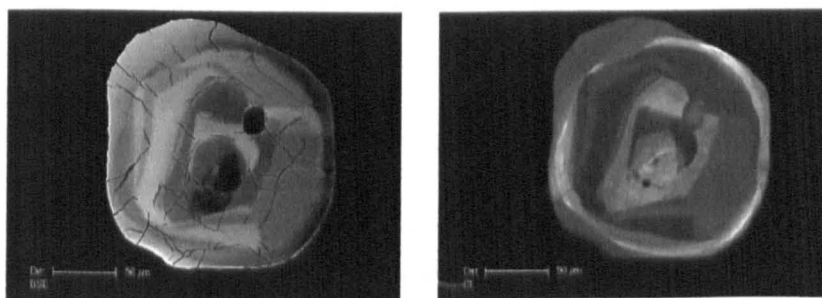


Figure 38 - A comparison of BSE (left) and CL (right) images for a single zircon crystal from Napier Complex, Antarctica [Cayzer & Hinton, 2002, unpublished data Figure 2 (unpublished data)]. White scale bars are 50  $\mu\text{m}$ .

Quantitative elemental mapping of U and Th using energy dispersive X-ray analysis (EDS) is possible, but the detection limits are too high ( $\sim 0.5$  wt %) to allow resolution of zonation in the majority of crystals.

#### 4.9.1.5 Electron back scatter diffraction

Analysis of the electron back scatter diffraction patterns (EBSD) can allow the quality of the crystal structure to be assessed [Cayzer & Hinton, 2002, unpublished data]. As the dominant mechanism that leads to the accumulation of lattice damage is  $\alpha$ -decay, zones with poor crystallinity can be used as a proxy for U (and to lesser degree Th) distribution. Unlike Raman spectroscopy (see Section 4.9.2.2), the EBSD technique cannot currently be used in a quantitative manner, but the variation in the diffraction patterns (Figure 39A & B) across the crystals is used to determine a “crystallinity map” (Figure 39), with a spatial resolution of  $< 1 \mu\text{m}$ .

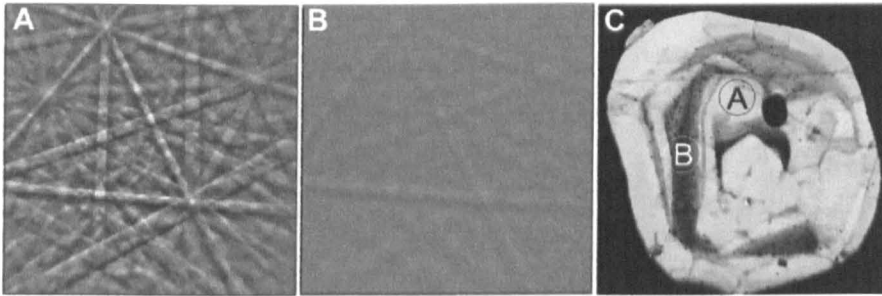


Figure 39 - Examples of the diffraction patterns obtained during EBSD analysis of zircon.

A) Good quality diffraction pattern from highly crystalline zircon.

B) Poor quality diffraction pattern from damaged crystalline structures.

C) The resultant EBSD image from the analysis of the variation in the diffraction patterns.

The crystal shown is that presented in Figure 38, the location of A and B are shown. [from Cayzer & Hinton, 2002, unpublished data (unpublished data)] Crystal is  $\sim 200 \mu\text{m}$  in diameter (see Figure 38)

#### 4.9.1.6 Other imaging techniques

Many of the other optical and SEM methods cannot readily resolve the zonation of U and Th at the concentrations seen in many zircon samples. Where techniques such as back scattered electron imaging and elemental mapping reveal major chemical or structural zonation within crystals further investigation is to be recommended.

### 4.9.2 Quantitative assessment of U and Th zonation

The selection of complete crystals, and the destructive nature of (U-Th)/He analysis prevents the application of many of the more routine techniques that can quantitatively determine the U and Th concentrations of the different zones. Performing (U-Th)/He analysis on crystals where a polished surface can allow the quantification of U and Th zonation in 2-dimensions, means reduced crystal volumes for analysis and consequently reduced precision. This also introduces the potential for He

loss during preparation or the measurement of U and Th. Quantification of the U and Th zonation after helium extraction increases the probability of crystal loss. Determining the U and Th zonation in a representative selection of crystals can be used in a manner similar the qualitative techniques outlined above, i.e. to quantify the extent and variety of zonation in a sample population.

#### 4.9.2.1 Optical microscopy

There is a linear relationship between decreasing birefringence and increasing number of  $\alpha$ -decay events, and so the U and Th content of any zone can be qualitatively and quantitatively assessed from inspection of the zonation in birefringence [Palenik *et al.*, 2003]. As both U and Th decay contribute to the total  $\alpha$ -dose, quantitative assessments require the determination of the U/Th for each zone, or the assumption that Th/U is constant. Although it is sometimes possible to identify some form of zonation in crystal structure or quality under transmitted light, polarised light often reveals a zonation in birefringence. The dramatic zonation in birefringence (e.g. Figure 40) observed in polished thin sections is not commonly seen during inspection of unpolished crystals.

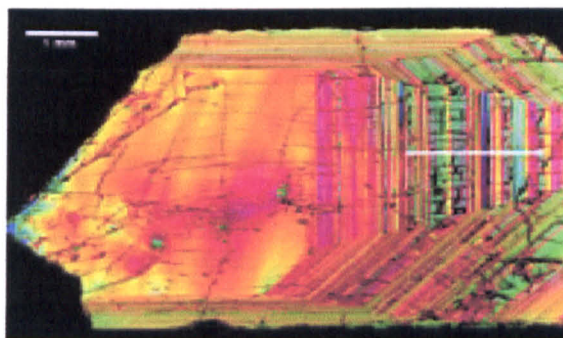


Figure 40 -Zonation in birefringence observed in Sri Lankan zircons [Palenik *et al.*, 2003 Figure 1]. White scale bar is 1 mm.

Therefore this technique cannot be directly applied to the crystals selected for (U-Th)/He analysis. During the course of this research only one zircon sample showed evidence of strong internal zonation in complete crystals. This sample was not from the HIP samples. This technique has potential applications in conjunction with ZFT analysis, where the amount of radiation damage has a direct control on annealing behaviour (see Section 2.3.1). The knowledge of total U content and total number of  $\alpha$ -decay events then allows Th to be quantitatively assessed.

#### 4.9.2.2 Raman spectroscopy

The zonation of lattice damage formed by  $\alpha$ -decay will follow the distribution of the U and Th. This allows the application Raman spectroscopy to quantify the total  $\alpha$ -dose from amount of lattice damage [see review by Nasdala *et al.*, 2003]. Raman spectroscopy is still not widely available, however cross calibration with the less sensitive EBSD technique outlined above holds some potential for quantitative assessment of U and Th zonation.

### 4.9.2.3 Electron microprobe spectroscopy

Quantitative analysis of zircon chemistry using electron microprobe (EMP) techniques is widespread, as the high spatial resolution and lower detection limits allow more detailed determinations than possible using quantitative SEM techniques. Detection limits for U and Th are typically in the order of ~ 0.01 wt %, and can be as low as 10's - 100's ppm [Hinton, pers. com] and so while EMP is sensitive enough to determine bulk concentrations of typical crystals, it will still be unable to resolve the differences in concentration that may effect the calculated (U-Th)/He ages.

### 4.9.2.4 Laser ablation ICP-MS

Laser ablation ICP-MS has several benefits for the determination of U and Th zonation in (U-Th)/He samples, and is the only technique that has been successfully applied to crystals that have been analysed for (U-Th)/He.

The determination of U and Th concentration profiles in apatite/monazite/zircon prior to He analysis would be advantageous as it could allow the preferential selection of crystals with similar zonation. However, there is evidence that the high temperatures generated in the volume surrounding the ablation pit can cause melting and the crystallisation of Si rich and ZrO regions [Kosler, pers. com; Garver, pers. com], which would suggest that some He loss will occur. LA-ICP-MS should therefore only be applied after He extraction has been achieved. LA-ICP-MS has great potential for accurate low level determinations of U and Th, but the diameter and depth of the ablation pit must be tightly controlled. Large diameter ablation spots and deep pits mean that there will be an averaging effect when multiple zones are intersected (see the discussion in Section 4.9.1.2). Large ablation volumes will enable accurate measurements, but will reduce the spatial sensitivity of the analysis. The minimum ablation volume that can be used will be governed by the U and Th concentration. Ablation volumes are not generally reported [e.g. Hourigan *et al.*, 2005].

When LA-ICP-MS is applied, the need to recover the zircons from the capsules used for He extraction introduces the possibility of crystal loss. Subsequent dissolution and analysis of the U and Th using conventional techniques may therefore be subject to reduced U and Th yields, and the (U-Th)/He ages will be too old because of the "parentless" He. When used in conjunction with a 3D self-similar model of crystal growth, the issue of crystal loss can be avoided by using the LA-ICP-MS concentration profile to calculate the bulk crystal U and Th. However, many of the images presented in this chapter show that U and Th zonation is rarely described by such a simple growth profile, and this technique can introduce large, and un-quantifiable uncertainty into the calculation of the U and Th content.

The future development of this technique to incorporate the measurement of He, U and Th during a single analysis would enable rapid acquisition of (U-Th)/He ages from individual zones within a crystal, and allow age profiles to be determined. This could be used to extract much more detailed information about the thermal history of a sample. There has also been a considerable development of LA-ICP-MS for the determination of U concentrations for zircon fission track age determinations, thereby reducing analytical time and removing the need for external irradiation [e.g. Hasebe *et al.*, 2002; Donelick *et al.*, 2005].

#### 4.9.2.5 Secondary Ion Mass Spectrometry

Secondary ion mass spectrometry (SIMS) is the most sensitive elemental and isotopic surface analysis technique [see review by Ireland & Williams, 2003]. It combines high spatial resolution (beams of 5 - 20  $\mu\text{m}$ ) with low detection limits (< 10 ppm for most heavy trace elements) and can determine both U, Th and REE contents from single analyses sites or from crystal traverses. For the U and Th concentration in typical zircon, a spot of 5  $\mu\text{m}$  diameter can be used, allowing the quantitative determination of U and Th contents from individual growth zones. The precision of the SIMS technique is typically < 2 % (at < 30 ppm Th)

#### 4.9.3 The characterisation of zircon samples

It is currently impossible to apply many of the techniques outlined above to the crystals selected for (U-Th)/He analysis, and this limits the qualitative and quantitative analysis that can be performed. When LA-ICP-MS cannot be applied a more comparative approach is required. The nature and distribution of the zonation patterns within a crystal population can be assessed using the qualitative techniques discussed above (such as CL). This can allow the zonation patterns in a large number of crystals to be characterised rapidly. Although this form of analysis cannot provide detailed information about the distribution of U and Th within a selected crystal, it is the most robust method that can be routinely applied to (U-Th)/He samples.

### 4.10 Conclusions

This study shows the need for careful consideration of the effect of geometry and zonation on (U-Th)/He ages. As many samples exhibit variable geometry and zonation within a population of zircon crystals, many samples will be affected by these issues. Consideration of the effects of geometry and zonation on (U-Th)/He ages can lead to improved age reproducibility; or allow age distributions to be more accurately interpreted. This section aims to provide a summary of the key issues that should be considered to improve the understanding of zircon (U-Th)/He data.

### 4.10.1 Improved treatment of zircon (U-Th)/He data

If samples have cooled rapidly, and the application of the  $F_T$  correction is justified, this study has shown that crystal geometry can have a significant effect on the value of the  $\alpha$ -recoil correction. The inaccurate application of the  $\alpha$ -recoil correction will introduce a large uncertainty into the corrected (U-Th)/He age. Many apatite (U-Th)/He studies present the interpretation and discussion of the data using the  $F_T$  corrected (U-Th)/He ages. Geological interpretation of  $F_T$  corrected zircon (U-Th)/He ages cannot be accurately performed without knowledge of the zonation in the sample.

#### 4.10.1.1 Improving the uncertainty associated with the $F_T$ correction

As the relationship between  $F_T$  and crystal geometry was determined from hypothetical crystals, there is no uncertainty associated with the crystal measurements, and the uncertainty in the observed relationships ( $\pm 1$  % for typical values of  $\beta$ ) is generated by the number of simulations in the Monte Carlo computational technique. Using the Hourigan et al. (2005) model at a 4 nodes/ $\mu\text{m}$  mesh density is beyond the computational capacity of many laboratories, and using a model with 1 node/ $\mu\text{m}$  introduces an additional  $\sim \pm 0.5$  % uncertainty into the calculated  $F_T$ . Crystal specific modelling using the Hourigan et al. (2005) computational technique is unlikely to become routine in many laboratories, and therefore analysts will continue to use Equation 17 to calculate  $F_T$ . For most samples, only zircons of Type A or B geometries (Figure 13) are routinely selected and therefore the geometry-specific  $\alpha$ -recoil correction can be confidently calculated using Equation 31 and Equation 32.

However, the application of Equation 17 using the tetragonal fitting parameters will over estimate the value of  $F_T$  by between 2 - 30 % depending on the geometry of the crystal (Figure 23). The uncertainty associated with the value of  $F_T$  can be reduced to  $\sim \pm 2 - 3$  % for all crystals upon the application of the geometry specific parameters. In some samples it is possible to preferentially select only those zircons with Type A geometries, thereby allowing the more precise Hourigan et al. (2005) parameters to be applied. However few zircons analysed for (U-Th)/He are tetragonal, and so to allow rigorous inter-sample and inter-laboratory comparison, the full geometric dependence of the  $\alpha$ -recoil correction should be considered for all crystals.

The geometric regularity of most zircon crystals means that the uncertainty associated with the calculation of the surface area-to-volume ratio is generally  $\sim 2$  %, and so the formal uncertainty in the (U-Th)/He age for rapidly cooled homogeneous zircons is approximately  $\pm 4$  %. This is controlled almost equally by the analytical precision and the error associated with the calculation of  $F_T$ .

### 4.10.1.2 Improving the uncertainty by applying the $F_z$ correction

Modelling of realistic 3-D zonation patterns to determine crystal and zonation specific  $\alpha$ -recoil is possible, but for the accurate determination of crystal-specific values of  $F_z$ , crystal size, crystal geometry, the relative concentration changes, zone width, and the style of zonation must all be known. Where the zonation in a sample can be characterised by other techniques (ZFT, SIMS etc.), modelling the range of probable zonation patterns will enable  $F_z$  to be estimated, and can allow poorly reproducing (U-Th)/He ages to be interpreted. Tagami *et al.* (2003) applied this approach in order to estimate  $F_z$  for the Tardree Rhyolite zircons from the FZT distribution. This estimation was corroborated by later quantitative LA-ICP-MS and crystal specific modelling [Hourigan *et al.*, 2005] (see Section 4.9.1.1). This technique is most accurately applied when zircons are strongly zoned, and estimation of  $F_z$  from the probable zonation patterns can significantly reduce the age bias in the recoil-corrected data. Estimation of  $F_z$  for samples containing a number of different zonation patterns is difficult without extensive quantitative analysis of the U and Th distribution associated with the different styles of zonation.

### 4.10.2 Interpretation of zircon (U-Th)/He ages in unknowns

In general zircon (U-Th)/He analyses of single crystal aliquots should not be expected to reproduce well, because of the large variety of zonation profiles that are typically seen with a sample. However, the reproducibility of a sample should generally reflect the lithology. Zircons from gabbroic samples will generally have a far more consistent and less complex zonation patterns that will be observed in those from granitic or high grade metamorphic samples. It should also be noted that while this study has been limited to the interpretation of (U-Th)/He ages in crystalline rocks, when considering sedimentary samples a wide variety of zonation patterns is to be expected. Different U and Th concentration profiles will lead to different amounts of helium loss, and consequently even the uncorrected ages from the same size fraction will not reproduce. Where it is possible to characterise the zonation within a crystal population, but not that of any individual crystal selected for (U-Th)/He analysis, it may be possible to reduce age reproducibility using a pooling technique.

The modelling presented here shows that for an individual crystal, the  $F_T$  corrected age can be inaccurate by 10 - 40 %, and, conversely the uncorrected (U-Th)/He ages may vary by the same amount. This is best illustrated using an extreme example: Three crystals have experienced the same thermal history and have identical geometries but very different zonation patterns: Crystal 1 has a narrow U and Th enriched rim ( $\Delta C = 20$ ), Crystal 2 is homogeneous, and Crystal 3 has broad depleted rim ( $\Delta C = 0.05$ ). For most typical crystal sizes Crystal 1 will have an uncorrected (U-Th)/He ages that is ~ 30 % smaller than that determined from Crystal 2, whereas Crystal 3 will

have a raw age  $\sim 30\%$  older. The  $1\sigma$  reproducibility of this sample is therefore  $\sim \pm 25\%$ . After a standard recoil correction, the differences will remain as all three crystals have the same geometry. With the application of crystal specific  $F_z$ , the ages will reproduce to within a few %. Where samples do not have good age reproducibility assessment of the U and Th zonation is required before the “correct” age for the sample can be determined. Calculating the average (U-Th)/He age will not include the full effect of variable zonation, and may introduce significant net age bias.

When interpreting unknown (U-Th)/He ages in apatites, a relationship between increasing crystal age and increasing crystal radius is often used to infer that the sample experienced slow cooling, and such an age-size relationship is a result of synchronous recoil and diffusion during residence in the PRZ. For zircon samples, care must be taken before a similar interpretation is made. Zircon (U-Th)/He ages should also increase with crystal half width if there has been prolonged residence in the PRZ (see Section 4.8.2), however the crystal size population in zircon often reflects multiple phases of crystal growth. Different size fractions may therefore have very different zonation profiles. Small zircons often have the same chemical composition as overgrowths on larger crystals. It is therefore possible that while the small crystals are homogenous, the larger ones are zoned. The nature of the zonation (rim-depleted or rim-enriched), and the width of the zonation will determine the nature of the age-size relationship, but a trend of increasing age with increasing grain size could also be because the outermost zone is relatively U and Th depleted.

Care must be taken with all samples however, as even where age reproducibility is observed between replicate analyses; the effects of zonation cannot be discounted. Here the effect of inter-crystalline variation on the (U-Th)/He age is minimal, but age biases must still be considered. Uncorrected (U-Th)/He ages that reproduce cannot be considered as analyses of “un-zoned” crystals. Crystals with sector zonation, or narrow and regular oscillatory zonation, will generally have good age reproducibility, and in many cases applying the  $F_T$  correction will be a good approximation to the true  $\alpha$ -recoil correction. However, a small net age bias can still be introduced (typically  $< 5\%$  positive or negative, see Section 4.7.1.3). More extreme zonation can also generate (U-Th)/He ages that reproduce. If crystals have narrow enriched rims, the age bias introduced by assuming homogeneity is largely independent of crystal size and geometry (see Figure 28). In extreme cases this can introduce a negative age bias of up to 30%. The magnitude of the age bias will be controlled by the concentration change across the zone boundary, and without knowing the U and Th distribution in the samples, the age bias cannot be fully assessed.

Improving analytical techniques, and the generally high U and Th content in most zircons is leading to the routine analysis of single crystal aliquots. In most samples the majority of crystals analysed will have a certain form of zonation, but the detail will vary; with a range of zone widths and relative concentration changes. This will lead to a range of (U-Th)/He ages being determined.

With sufficient single crystal analyses, an understanding of the range and distribution of (U-Th)/He ages within a sample can enable the identification of age outliers within that distribution, or in some cases the resolution of distinct age populations within the distribution. Outliers may have significantly different (U-Th)/He ages, especially if they have a zonation style which is “opposite” to that of the main population. Once the different zonation dependant components to an age population have been identified, the average (U-Th)/He age of each component can be determined separately. The age population in a sample may also correlate to a crystal size population as outlined in the previous section. The separation of the different zonation dependant age populations within a sample would require a substantial number of single crystal analyses to be performed. The rate determining step of the (U-Th)/He methodology presented in Chapter 3 is the dissolution and U and Th recovery. Helium extraction is relatively rapid.

Crystals of the same size and zonation will have similar recoil and diffusion characteristics and therefore have the same concentration of helium within each crystal. Therefore it should be possible to assess the age distribution following He extraction and analysis. As the volumes of zircons can be determined with an accuracy of < 1 %, it should be possible to determine zonation populations within a single size aliquot directly from the He concentration. From the range of He concentrations observed the outliers can be removed from the population prior to the lengthy dissolution, and U and Th recovery process. Some of these crystals can be analysed for (U-Th)/He and others can be used to characterise the zonation in that sub-population. When all crystals entering the U and Th recovery procedure have a very limited range of He concentrations, the impact of zonation will be approximately equal, and the age reproducibility will be improved. However, the crystals will not be homogeneous, and the true (U-Th)/He age of the sample cannot be determined unless the zonation in the analysed sub-population can be assessed. In many samples a range of crystal sizes must be analysed and therefore the additional selection criteria cannot be applied.

The relationship between grain size and the effect of the zonation means that when zonation is assessed, better (U-Th)/He age reproducibility and reduced age bias may be achieved by the preferential selection of certain size fraction. This is generally applicable to crystals which exhibit rim-depletion. A sample in which the zircons exhibit narrow rim-depletion of variable  $\Delta C$  (Equation 33, Section 4.7.1.1), the sample will exhibit smaller age bias, and a smaller variation in that age bias, when large crystals are analysed (Figure 28). The variation in age bias caused by variable rim width for a constant  $\Delta C$ , will be smaller in crystals with high  $W_1/W_2$  (Figure 30). For crystals with enriched rims, the age bias is largely independent of crystal size and so all crystals with a certain rim width will exhibit similar age bias. In this example, the large variation in age

bias that will be introduced at different rim widths (Figure 28, Figure 29 and Figure 30) may mean that distinct age populations may be apparent when the zonation is extreme.

Analysis of multiple crystal aliquots effectively averages the (U-Th)/He ages of these crystals, and will generally improve the age reproducibility. This will be most apparent where samples have approximately equal proportions of each of the zonation styles. Better age reproducibility is to be expected from larger aliquot sizes, as the effect of any outliers on the age of a particular aliquot will be reduced. In many samples the average age obtained from multiple crystal aliquots will be controlled by the average zonation; however assuming that the averaging effect equates to homogeneity is incorrect.

### 4.10.3 Closing comments

This work has highlighted the importance of considering the many effects that can generate variable (U-Th)/He ages within a single population with a common thermal history. Understanding the magnitude of the U and Th zonation, and the variety of different zonation patterns within all zircon samples is crucial if the correct (U-Th)/He age of a sample is to be determined. The major issue that prevents the accurate treatment and interpretation of zircon (U-Th)/He ages is the lack of a routine methodology for the qualitative or quantitative assessment of U and Th zonation in zircon. Although quantitative assessment of the zonation is preferable, the characterisation of crystal-specific U and Th profiles within analysed zircons is beyond current analytical techniques.

The characterisation of concentration populations within a sample can enable the probability of any single crystal analysis being affected by a style of zonation to be assessed. Modelling of the probable age bias generated from the observed zonation can then be used to assess the age bias introduced across a zircon (U-Th)/He age population, and allow an estimation of the true (U-Th)/He age of the sample. The applicability and accuracy of this technique depends on the characterisation of the zonation within the sample.

The application of these principles to unknown samples will significantly improve the age reproducibility of any sample. This is especially important when thermochronology is used to resolve and differentiate between the timing of different cooling events, such as is the case in this study. For a rapidly cooled sample from the Hebridean Igneous Province an age reproducibility of  $\pm 10\%$  will not be able to distinguish between the different cooling scenarios outlined in Chapter 1.

The Fish Canyon Tuff zircon standard has been used to assess the methodologies for the determination of the U and Th zonation in a zircon population, and perform a quantitative analysis of the age biases that can be introduced in natural samples. This is the subject of the following Chapter.

# 5

## The Fish Canyon Tuff zircon

### 5.1 Introduction

Fish Canyon Tuff (FCT) minerals are widely used as U-Pb and Ar-Ar standards, and it is one of the few standards used for both apatite and zircon fission track analyses. Because of the close agreement in the ages obtained by apatite and zircon fission track dating [Carpéna & Mailhé, 1987], the FCT zircon is the only mineral standard to have been adopted for zircon (U-Th)/He dating. Although the (U-Th)/He ages of the FCT zircon from all laboratories performing analysis are within error of those obtained from other techniques, the best age reproducibility seen within any single data set is greater than  $\pm 9\%$  ( $2\sigma$ ), and for the combined data set it is  $\pm 11.2\%$  ( $2\sigma$ ,  $n = 129$ ) (see Figure 12, page 48). Age uncertainties for unknown apatite (U-Th)/He analyses are generally calculated from the  $2\sigma$  reproducibility of known mineral standards [e.g. Reiners, 2005], so applying this protocol to zircon (U-Th)/He analyses means that use of Fish Canyon Tuff zircon as a standard limits the temporal resolution that can be achieved in unknown samples.

### 5.2 Potential causes of poor reproducibility

The poor reproducibility in apatite (U-Th)/He (AHe) samples is usually attributed to one of a number of reasons: fluid inclusions, mineral inclusions, U and Th zonation, incomplete recovery of the U, Th and He, or inaccurate modelling of the diffusion and  $\alpha$ -recoil loss mechanisms (see review in Chapter 2). For zircons, many of these reasons can be discounted (see discussion in Chapters 3 & 4), and inaccurate consideration of the effect of crystal geometry, and U and Th zonation on  $\alpha$ -recoil are the most probable sources of poor age reproducibility. Quantifying these effects in the chosen mineral standard is important for the correct interpretation of all zircon (U-Th)/He data.

In contrast to the internal fragments of the Durango apatite that are used as a standard for AHe, all FCT zircon ages must be corrected for  $\alpha$ -recoil. This introduces an additional source of uncertainty into the zircon standard dataset, which is not present in the AHe standard. The typical morphology

and dimensions of FCT zircons mean that substantial  $F_7$  corrections are required. The (U-Th)/He ages presented in Figure 12 were determined while the technique underwent refinement, and the methods used to calculate the  $\alpha$ -recoil correction are not consistent. Recalculation of the Tagami *et al.* (2003) data using termination lengths of 10 - 40 % of the total crystal length, and using the Hourigan *et al.* (2005) fitting parameters produces ages that are ~ 1 % younger, but does nothing to improve the poor reproducibility. The FCT zircon has generally euhedral form with  $W_1/W_2 \sim 1.0$  (see Section 5.3) therefore the application of the Hourigan *et al.* (2005) tetragonal fitting parameters introduces minimal uncertainty (~ 2 %) in the majority of cases (Section 4.5).

The effect of U and Th zonation on the proportional loss of  $\alpha$ -particles has been highlighted (see Chapter 4). To assess the impact of U and Th zonation on  $\alpha$ -recoil from the FCT zircons, a detailed qualitative and quantitative characterisation of the crystals has been performed. The results of this assessment are presented in the following pages, and the suitability of the FCT zircon for use as a (U-Th)/He mineral standard is discussed.

### 5.3 The Fish Canyon Tuff zircons: sample description

The FCT zircons used in this study were supplied by R. Donelick of A to Z Inc. They are generally colourless to pale pink, and while few large amber crystals were seen, no dark pink rounded crystals [as reported by Carpéna & Mailhé, 1987] were observed in this particular FCT zircon aliquot. The crystals are 50 to 250  $\mu\text{m}$  in length, with aspect ratios of 2 to 10. The zircons are typically elongate prismatic euhedral crystals with pyramidal terminations. Crystal geometries are dominated by Types A and B (as described in Figure 13, Chapter 4), but approximately ~ 30 % have Type F geometries. These were not selected for (U-Th)/He analysis. Few of those Type A and B crystals have compound terminations, and pure pyramidal and truncated pyramidal geometries dominate all size fractions. Termination lengths vary from 10 - 50  $\mu\text{m}$ , and typically account for 10 - 60 % of the total crystal length. Broken crystals are uncommon, and from comparison with complete crystals, breakage generally occurs close to the centre of the crystal, perpendicular to the crystallographic  $c$ -axis.

Crystals suitable for (U-Th)/He analysis are generally > 60  $\mu\text{m}$  in width, but range from 45 - 160  $\mu\text{m}$ , with an average of  $75 \pm 19 \mu\text{m}$  ( $1\sigma$ ,  $n = 100$ ). Larger crystals, with widths from 120 - 200  $\mu\text{m}$ , were not selected as they contained multiple, large fluid and mineral inclusions (> 20  $\mu\text{m}$  in minimum dimension). In the crystals suitable for (U-Th)/He analysis the ratio of the mutually perpendicular crystal width measurements,  $W_1/W_2$ , ranged from 1.0 to 1.8, with an average of  $1.2 \pm 0.1$  ( $1\sigma$ ,  $n = 100$ ).  $W_1/W_2$  can be as high as 2.5, but crystals with  $W_1/W_2 > 2.0$  were not selected for (U-Th)/He analysis.

Mineral and fluid inclusions are common in all size fractions and range from  $< 1 \mu\text{m}$  to a few  $10^3 \mu\text{m}$  in minimum dimension. The inclusions are dominated by elongate acicular crystals of apatite. Other mineral and fluid inclusions are also observed. Selection of crystals containing inclusions is avoided, but the presence of small ( $< \sim 17 \mu\text{m}$  maximum dimension) apatite inclusions is unlikely to effect the (U-Th)/He age (Section 3.6.1.1).

FCT zircon samples used by different laboratories have variable suites of inclusions. Reiners *et al.* (2001) report alkali feldspar and quartz as the major inclusion minerals, whereas the inclusion assemblage found during this study is closer to that reported by Lamphere & Baadsgaard (2001). No U- or Th- rich phases such as urananite and thorite have been reported as inclusions in any FCT zircon sample. The variability in the inclusion assemblage may reflect the variability in the FCT zircon observed across the outcrop, and the samples of FCT zircon in use may have been collected from different locations [Garver, pers. com.]. Variation in the REE and U and Th content and zonation in the FCT zircons may therefore also be expected, if the different localities reflect magma batches with different histories. This may prevent the direct inter-laboratory comparison of Th/U data sets.

### 5.3.1 Chemical characterisation of the FCT zircons

Chemical characterisation of the FCT zircon is extensive [Lamphere & Baadsgaard, 2001; Schmitz & Bowring, 2001], but there is only limited information on the distribution of U and Th. Bulk U is typically 200 - 850 ppm, and Th/U ratios range from 0.35 to 1.1 [Schmitz & Bowring, 2001]. Published Th measurements are less common, but both the U and Th determined during U-Th-Pb dating are in general agreement with the bulk U and Th concentrations reported in the existing (U-Th)/He studies. More importantly for the understanding of the (U-Th)/He data, the substantial variation in U and Th concentration is found between and within individual crystals (Table 10) [Lamphere & Baadsgaard, 2001] and could substantially effect  $\alpha$ -recoil (Section 4.7)

The bulk U and Th concentrations reported by (U-Th)/He laboratories are generally lower than those determined by the SHRIMP and isotopic dilution mass spectrometry U-Th-Pb techniques. U and Th concentrations are not determined during (U-Th)/He analysis, and absolute measurements (ng) are converted to concentrations using arbitrary crystal densities ( $\sim 4.6 \text{ g cm}^{-3}$ ), and crystal volumes. Published values are typically calculated using simplified pinacoidal geometries and the assumption may underestimate bulk concentrations by up to 66 % (bi-pyramid geometry). The SHRIMP data (Table 10) suggests that zonation of U and Th is seen within the FCT zircons, and that further characterisation of this standard should be performed.

	U (ppm)	Th (ppm)
Crystal 1 - A	2387	431
Crystal 1 - B	701	374
Crystal 2 - A	238	107
Crystal 2 - B	278	225
Crystal 3 - A	2316	65
Crystal 3 - B	1838	111
Crystal 3 - C	1472	121
Crystal 4 - A	419	328
Crystal 4 - B	324	222

**Table 10 - Selected SHRIMP spot analyses from the FCT zircon.**

The analyses show inter-crystalline variation of U and Th concentrations (ppm) within four FCT zircon crystals [from Schmitz & Bowring, 2001].

## 5.4 Qualitative assessment of zonation in the FCT zircon

Several zircon (U-Th)/He studies suggest variable and subtle zonation of U and Th may cause the poor reproducibility in many samples, including the FCT zircon [Reiners *et al.*, 2002; Reiners & Spell, 2002; Tagami *et al.*, 2003; Hourigan *et al.*, 2005; Reiners, 2005], yet little qualitative or quantitative characterisation has been performed. Reiners *et al.* (2002) suggest that the poor age reproducibility of the FCT zircon is due to heterogeneous U and Th distribution based on back scattered electron images (BSE) showing subtle zonation (Figure 41 A & B). These relatively homogeneous BSE images are in sharp contrast to a large number of CL images published elsewhere (Figure 41 C & D) [e.g. Schmitz & Bowring, 2001; e.g. Tagami *et al.*, 2003]. The CL images commonly show thick mantles of narrow oscillatory zonation around more homogeneous, cores with lower emission intensities [Schmitz & Bowring, 2001].

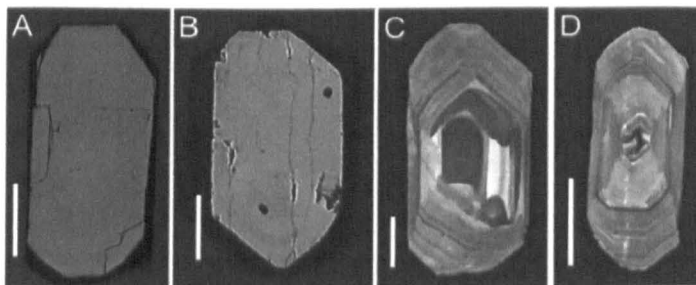


**Figure 41 - A comparison of Back Scattered Electron (BSE) and cathodoluminescence (CL) images of the Fish Canyon Tuff.**

BSE images: (A) this study (B) Reiners *et al.* (2002) CL images: (C) Lamphere & Baadsgaard (2001) (D) Schmitz & Bowring, (2001). The origin of linear feature through crystal D is unclear, but may be an annealed crack, or poor quality polish. White scale bars are 50  $\mu\text{m}$ .

The accumulation of lattice damage caused by  $\alpha$ -decay affects the quenching of CL emission in zircon (see Section 4.9.1.2), and the correlation of high U and Th concentrations with regions of CL quenching is widely reported [Corfu *et al.*, 2003; Dempster *et al.*, 2003; Nasdala *et al.*, 2003];

yet the assumption of U and Th homogeneity continues to be applied to (U-Th)/He analysis of the FCT zircons [Tagami *et al.*, 2003; Nasdala *et al.*, 2004; Reiners, 2005; Foeken *et al.*, 2006]. Qualitative characterisation of the zonation styles within the FCT zircon population was performed using a combination of techniques, in order to better assess the inter-sample variability.

### 5.4.1 Charge contrast imaging of the FCT zircon

The benefits and potential applications for the charge contrast imaging have been discussed in Section 4.9.1.3., and CCI [Watt *et al.*, 2000] was investigated here as a method for imaging the zonation in the FCT. CCI images (Figure 42A-C) taken from crystals mounted in epoxy resin show very similar zonation patterns to those observed in CL (see Figure 41). Crystals mounted in PFA Teflon (for ZFT analysis) generally yield poorer quality images (Figure 42D), as the quality of the polished surface controls the quality of the CCI image. Even though a good quality polish on the zircons is required for ZFT, the surface of the Teflon remains scratched and uneven leading to uneven charging and flaring (Figure 42D).

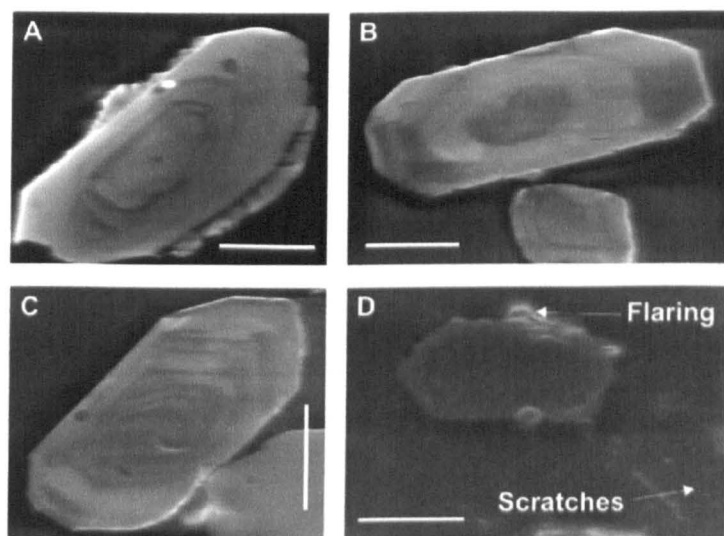


**Figure 42 - Charge contrast images of the FCT zircon.**

Crystals were mounted in PFA Teflon as for ZFT analysis. Crystals A-C mounted in epoxy resin, Crystal D mounted in PFA Teflon. The white scale bars are 50  $\mu\text{m}$

The observed CL-equivalent zonation patterns on ZFT mounts would enable semi-quantitative analyses of the U and Th distribution within the crystal, by direct comparison with fission track densities counted over specific zones. However, the quality of the Teflon surface must be improved before such comparison is possible.

### 5.4.2 EBSD imaging of the FCT zircon

Determination of the quality of the crystal structure using electron back scattered diffraction (EBSD) [Cayzer & Hinton, 2002, unpublished data] has the potential to be able to quantify the total radiation dose that a zone or crystal has experienced. Preliminary EBSD analysis suggests that the differences in the crystallinity caused by the amount of radiation damage accumulated in the FCT zircon over the ~27 Myr since formation is beyond the limits of detection (Figure 43).

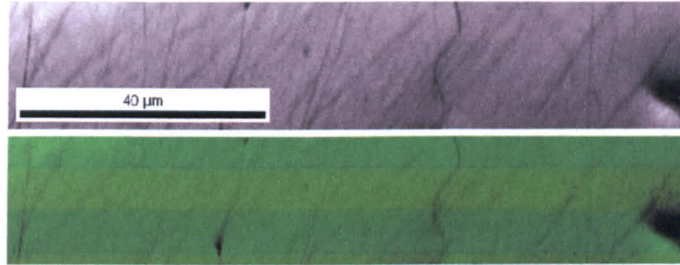


**Figure 43 - BSE (top) and false colour EBSD (bottom) image of the FCT zircon. Area of analyses was placed across area showing zonation in CL. The dark region at the far right is a speck of dust or other contaminant on the surface of the sample.**

### 5.4.3 Zircon fission track distribution

The Fish Canyon Tuff is the most widely used zircon fission track standard and, provided tracks are counted over an area within a single zone, U zonation is relatively unimportant. Comparison of the images (provided by Dr. A. Carter, University College London) of different grains suggests inter-crystal bulk U can vary considerably (Figure 44, Crystals A & B), and in some parts of the crystal it is possible to observe zonation in the track distribution. When the zonation is visible, zone boundaries are generally diffuse, and are difficult to define (Crystal C/D and E, Figure 44). Zonation can be complicated or obscured by other surface features that have also been etched during sample preparation (e.g. Crystal F, Figure 44).

From samples like the Tardree Rhyolite (TR) where U zonation in zircon appears simple and extreme (Figure 36, Chapter 4), the fission track mount can be used as a first order approximation of the U distribution [Tagami *et al.*, 2003; Hourigan *et al.*, 2005] (Section 4.9.1.1). Comparison of the fission track (Figure 44) and CL (Figure 46) images from the FCT zircons suggest that the generally subtle zonation observed in the fission track distribution broadly follows that observed in the CL.

Fission track crystal mounts can, in some cases record the heterogeneous distribution of U, but the gradational appearance of many zone boundaries (see Section 4.9.1.1) suggests that good spatial resolution on the scale that is important to  $\alpha$ -recoil is difficult to achieve when zonation is more

complex (such as for the Fish Canyon Tuff zircons). Where several zones within a single crystal have been sampled for fission track analyses, the track density can provide a semi-quantitative estimate of the U content, however defining counting areas within a single zone can be difficult, as zones can be narrow, and the zone margins are often diffuse. Determination of track densities using only those tracks which intersect the polished surface and have a certain length (i.e. all track with a length of  $\sim 6 \mu\text{m}$ ) would enable some of the 3-D effects of the zonation to be investigated. However, such detailed investigation will be unable to provide the desired spatial resolution of the zone boundaries in many cases.

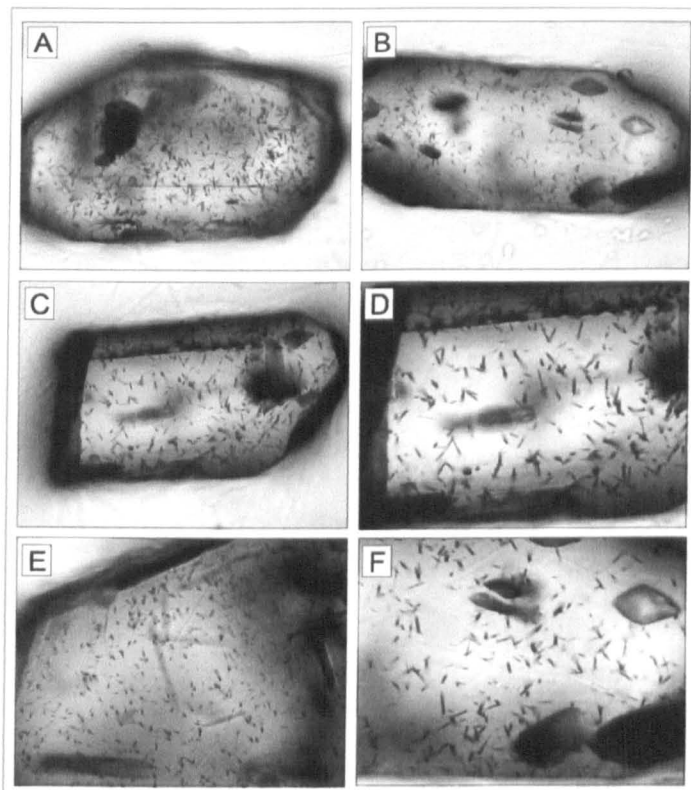


**Figure 44** - The distribution of zircon fission tracks within the Fish Canyon Tuff.

**A)** High track density FCT crystal, **B)** Low track density FCT crystal, **C & D)** apparent zonation (core with low track density) **C** = low magnification, **D** = high magnification, **E)** FCT crystal showing several apparently concentric zones but with zone boundaries that are hard to define, **F)** Clear zonation visible but boundaries obscured by other surface features. Images provided by Dr. A. Carter, UCL.

#### 5.4.4 Optical cathodoluminescence

Optical and SEM-CL were used to characterise the CL zonation, before crystals were selected for quantitative analysis using secondary ion mass spectrometry (SIMS). The initial inspection was performed on polished grain mounts using a CITL Technosyn 8200 Mk 4 CL system mounted on a Zeiss Axioplan petrographic microscope. The optical CL system has greater sensitivity to the

unique emission spectrum generated by different crystal imperfections than the SEM, and it can sometimes resolve more detailed zonation than the SEM system (Section 4.9.1.2). However it has limited magnification and this prevents detailed determination of zone widths. However the images confirm the existence of the zonation patterns observed by Schmitz & Bowring (2001). The images in Figure 45 show a representative selection of FCT zircons.

A range of magnifications were required to obtain a suitable image quality and the crystals in Figure 45 are not shown to scale, however all are 60 - 150  $\mu\text{m}$  wide. There is no relationship between crystal size and the style or intensity of the zonation pattern observed. The low emission intensity from crystals < 60  $\mu\text{m}$  prevents capture of good quality images, but zonation was visible in almost all crystals that were inspected.

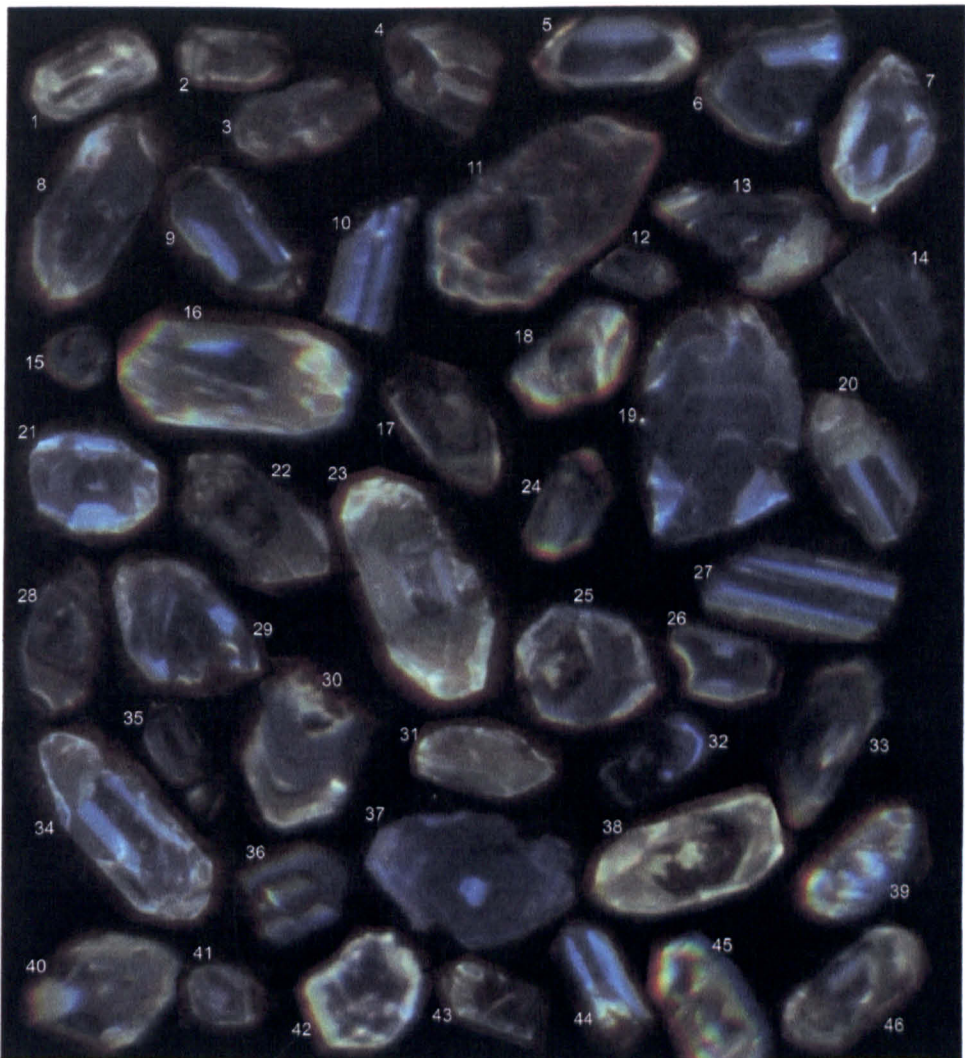


**Figure 45** - A representative selection of optical CL images of FCT zircons (see text for further discussion).

The majority of crystals (more than 90 %) have oscillatory, but not necessarily self-similar zonation, with a core of very low emission intensity mantled by a moderate to high emission rim

(Figure 45). Further complexity is often visible within the rims (e.g. Crystals 21, 23, and 25) and crystals often exhibit distinct narrow low emission zones in the outer 10 - 30  $\mu\text{m}$  of the crystal (e.g. Crystals 22, 28, & 30). Many crystals also show a zonation in the wavelength of CL emission. The CL signature of the outer-most regions of the crystals tends to be dominated by yellow broad-band emission, whereas the cores tend to have emission dominated by the blue wavelengths (e.g. Crystals 7, 30, & 34).

The mechanisms controlling the variation between blue- and yellow- emission are not understood [Ewing *et al.*, 2003; Nasdala *et al.*, 2003] (see Section 4.9.1.2). In the FCT zircons, different emission spectra show a comparable range of emission intensities, and the similarity of the zonation patterns observed in Crystals 37 & 38 (and 19 & 23), suggests that the mechanisms controlling the wavelength of the emission and the intensity of the emission are independent.

### 5.4.5 SEM Cathodoluminescence

Following the optical inspection, crystals were prepared for high magnification panchromatic CL imaging on a Quanta FEI 200F Environmental Scanning Electron Microscope. All CL images were taken under the same instrumental operating and image capture conditions.

Qualitative and quantitative assessment of the zonation patterns, and the distribution of these patterns within the crystal population, was performed using a CL map of the polished section. Only crystals sectioned parallel to the long axis, and showing complete, or near complete terminations were used for the subsequent analysis. This avoided any bias introduced when the polished surface ran parallel to the long axis, but close to a crystal face, intersecting fewer zonation bands. Crystals cut at high angles to the *c*-axis provide some insight into the third dimension (octagonal and rectangular cross sections), but were not used in the characterisation of the population, as the nature of the zonation in the terminations cannot be assessed. The random orientation of the planar interface between the polished section and the crystals means that the approximately *c*-axis parallel sections should be representative of the zonation in all orientations. This is corroborated by comparison of the styles observed in crystals that have rectangular and square geometries (e.g. Crystals J, Figure 46). These crystals show an approximately concentric zonation with similar structure and relative intensity variation as that found in the *c*-axis parallel images.

After application of these selection criteria, 400 crystals were used for the assessment of the CL zonation in the FCT zircon population. A wide variety of zonation styles were observed, and 98 % of crystals exhibit some form of CL zonation. Representative examples of each of the different zonation styles are shown in Figure 46. All crystal zonation styles were seen in all crystal size

fractions, but to allow direct comparison the crystals in Figure 46 are approximately the same width, and the white scale bars are 50  $\mu\text{m}$ . The CL images in Figure 46 do not represent the full range of zonation patterns, or the variation in zone width and relative intensity observed, but do provide an indication of the general trends.

Many of the crystals exhibit zonation that is broadly concentric (Crystals C- I, Figure 46), however only Crystal E shows a good approximation to symmetric self-similar zonation. Most crystals show preferential growth in one direction, usually perpendicular to the *c*-axis, and the locus of growth is often not at the centre of the crystal (e.g. Crystals C, D, F, & H, Figure 46). The asymmetry seen in individual zones is variable (e.g. Crystal D), and the geometry of successive zones can change (Crystals J, M, and Q, Figure 46). These differences indicate that locus of the growth changes during crystallisation in some crystals, and suggest that the crystal form (and therefore zonation) responds quickly to changes in environmental conditions. CL zonation can also reveal changes in crystal orientation and zonation style associated with the precipitation of magmatic overgrowths onto inherited cores (Crystal M & Q). Inheritance of older cores with magmatic (Crystal Q) or more rounded (Crystal M) geometries has been reported elsewhere [Schmitz & Bowring, 2001]. It should also be noted that Crystals A, F, H, Q and P exhibit narrow linear features with high CL emission similar to that seen in Figure 41. In these images the linear feature is associated with a cracks or scratches on the polished surface.

The majority of the crystal population (approximately 87 %) show complex concentric zonation patterns. The FCT zircon population can therefore be separated into several distinct styles of zonation:

#### **5.4.5.1 Type 1 zonation: complex high contrast zonation patterns**

Crystals with Type 1 zonation make up approximately 48 % of the population. Crystals have a moderate to low (dark grey-black) emission core mantled by a moderate (mid-grey) emission rim that contains several low emission zones of varying width. Within this population there is a great diversity of emission intensities, zone widths and relative changes in emission intensity across zone boundaries. However, within a crystal only a narrow bi-modal range of CL intensities are observed. Type 1 zonation is characterised by large areas with very low CL emission, e.g. Crystals C - E, G & H (Figure 46). Type 1 crystals also tend to show the largest intensity contrasts between adjacent zones, and generally broader zones (especially low CL zones) than are observed in other crystals (e.g. Crystal F). The rim-relative position of the zone boundaries can vary significantly (Crystals D, E, and H). Some crystals are relatively homogeneous in the region affected by  $\alpha$ -recoil (outermost  $\sim 17 \mu\text{m}$ ) (e.g. Crystal C), whereas others show large contrasts in emission intensity close to the crystal rims (e.g. Crystals D & E).

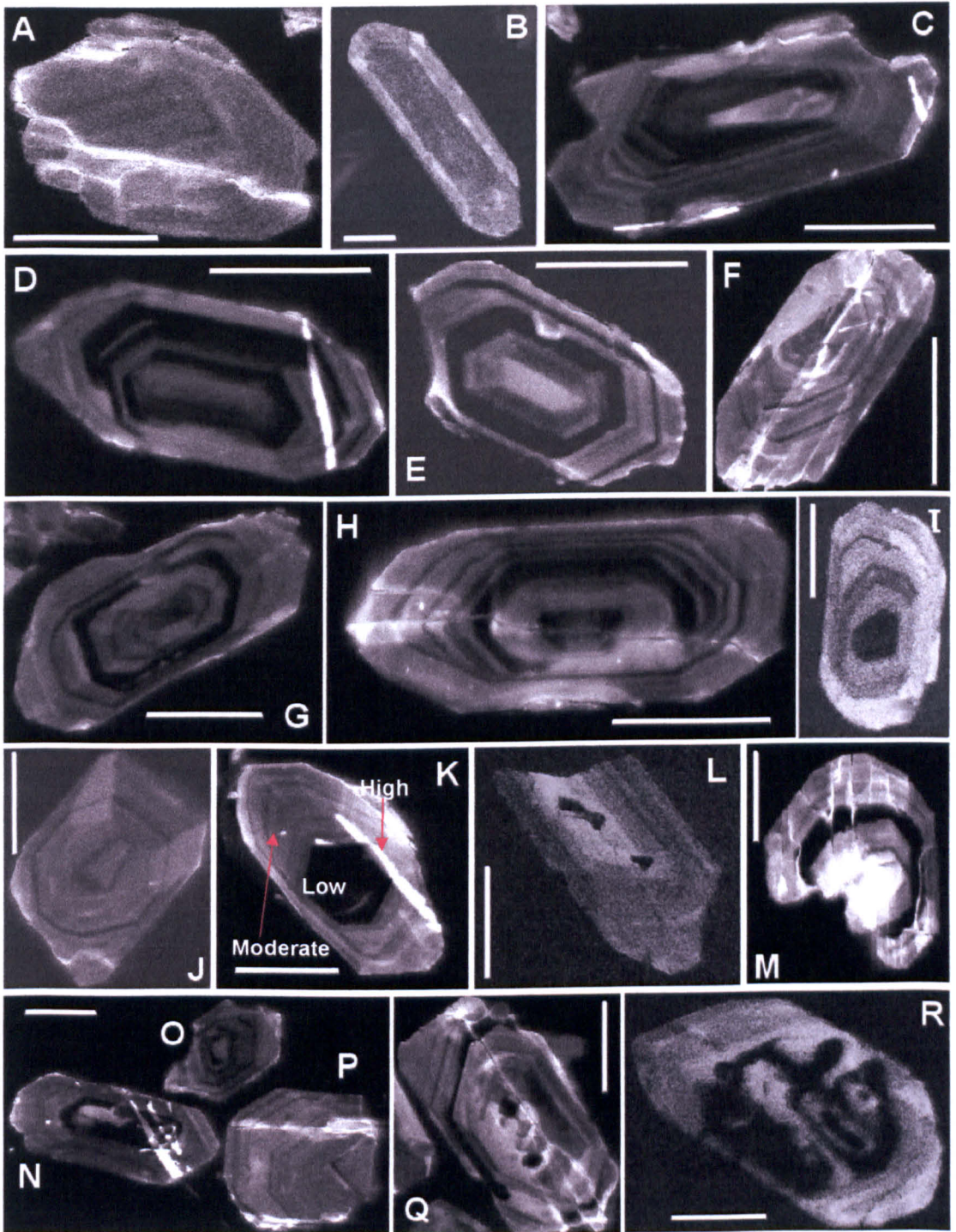


Figure 46 - Panchromatic SEM CL images of the zonation in FCT zircons.

All images are taken under the same operating conditions, and the slightly paler background to crystals B, E, I & J suggests that some charging of the resin occurred, the poorer quality of the images I and L was also because of charging on the surface. The greyscale shades typically described as low, moderate, and high intensity in the text are highlighted on crystal K. All scale bars are 50  $\mu\text{m}$ .

### **5.4.5.2 Type 2 zonation: complex moderate contrast zonation patterns**

Crystals with Type 2 zonation are the next most abundant, making up approximately 38 %, of the population. These crystals have a single dominant emission intensity, which is generally more moderate (dark-mid greys) than that observed in Type 1 crystals (e.g. Crystals F, J & O - Q, Figure 46). Type 2 zonation is characterised by moderate to high CL intensity with three or more distinct, low and generally narrow CL zones. Low CL cores are seen in some Type 2 crystals, but are generally smaller than those found in Type 1 zonation. Variation in zone width and relative intensity changes are seen both between and within crystals and the rim relative position of the low CL zones is highly variable.

### **5.4.5.3 Type 3 zonation: inclusion influenced**

Crystals with Type 3 zonation show some distortion of the internal zonation caused by large inclusions. These make up approximately 6 % of the crystal population, and would not have been selected for (U-Th)/He analysis. No mineral inclusions were identified under CL, but cavities were observed (Crystals L, Q and R, Figure 46). These cavities could represent the “plucking” of mineral inclusions during the polishing process or the presence of fluid inclusions (i.e. voids) intersected by the polished surface. Irregular shaped cavities generally cause significant disruption of the zonation pattern in the immediate area (Crystal R). Cavities with more regular shapes appear to disrupt the oscillatory zonation to a lesser degree. Inclusions are generally found in the cores of the crystals, and the zonation in the outer zones is largely unaffected (Crystals Q).

### **5.4.5.4 Type 4 zonation: high CL rims**

Crystals with Type 4 zonation make up approximately 2 %, of the population. Zonation can be described as a simple step-function zonation such as the models discussed in Section 4.7.1.1. Type 3 crystals have an almost homogeneous moderate (mid-grey) emission core mantled by an equally homogeneous rim of slightly higher intensity (mid-pale grey) (Crystal B, Figure 46). These crystals rarely show high emission intensity. The cores generally occupy between 60 - 90 % of crystal width (~ 20 - 75 % of the crystal volume is within the core) and the rim on any crystal is usually a constant thickness around the entire crystal (typically ~ 20 - 25  $\mu\text{m}$  for crystals < 120  $\mu\text{m}$  in width).

### **5.4.5.5 Type 5 zonation: high CL cores**

These crystals make up approximately 2 %, of the population, and have exhibit the same zonation structure as Type 3, but the CL intensities are reversed (Crystal L, Figure 46). Type 5 zonation is characterised by higher emission from the crystal cores, with a limited range of CL emissions.

### 5.4.5.6 Type 6 zonation: homogenous CL emission

Crystals that appear to have a homogenous CL emission at moderate magnification (Type 6), make up approximately 2 %, of the population (8 crystals). Subtle zonation was apparent in 7 crystals as the magnification was increased (e.g. Crystal A, Figure 46). These crystals generally exhibit moderate to low emission intensities, and the subtle zonation reveals an indistinct core-rim boundary, with both regions exhibiting narrow oscillatory zonation. The orientation of the zonation in the cores suggests a xenocrystic origin, with the cores forming during an earlier phase of crystal growth.

Neither CL or fission track images can be obtained from crystals used for (U-Th)/He analysis, however, if the U and Th distribution can be confidently correlated with the CL emission, the better spatial resolution and more rapid sample processing of CL images holds greater potential for the qualitative assessment of U (and Th) zonation patterns.

## 5.5 Quantifying U and Th zonation in the FCT zircon

CL emission may be controlled by many chemical substitutions [Remond *et al.*, 1995; Blanc *et al.*, 2000; Kempe *et al.*, 2000; Nasdala *et al.*, 2003], however the correlation between high U and Th contents and low CL intensity is widely reported [Hanchar & Miller, 1993; Kempe *et al.*, 2000; Ewing *et al.*, 2003; Nasdala *et al.*, 2003]. Secondary ion mass spectrometry (SIMS) analysis using the NERC Ion Microprobe facility in Edinburgh was used to quantify the distribution of U and Th in the FCT zircons. This has allowed the effect of zonation on the  $\alpha$ -recoil to be assessed (Section 5.8), and has enabled the validity of using CL as a proxy for U and Th zonation to be investigated (Section 5.6).

15 spot analyses were made using the Cameca ims 4f Ion Microprobe with a 5 - 7  $\mu\text{m}$  pit diameter. Cycles of 10 measurements were made with an energy offset of 75 V. U and Th concentrations were calculated using the NIST SRM 610 standard glass with  $\text{Th} = 28.61 \pm 0.07$  ppm and  $\text{Th}/\text{U} = 0.353$  (by weight). The three crystals selected for SIMS would have been selected for (U-Th)/He analysis, and exhibited the full range of CL intensities seen in the crystal mount. The crystals were chosen for their range in CL intensity, and for broad CL patterns which enabled the accurate determination of the U and Th concentrations on individual zones. Consequently, these crystals do not have "typical" complex oscillatory zonation (Type 1 or Type 2 zonation). CL intensities were quantified using the averaged value in greyscale colour space (Table 11) and were determined from the images using a standard image processing package (Corel Photo-paint). All images were obtained under the same SEM operational conditions (contrast, brightness, beam current etc.).

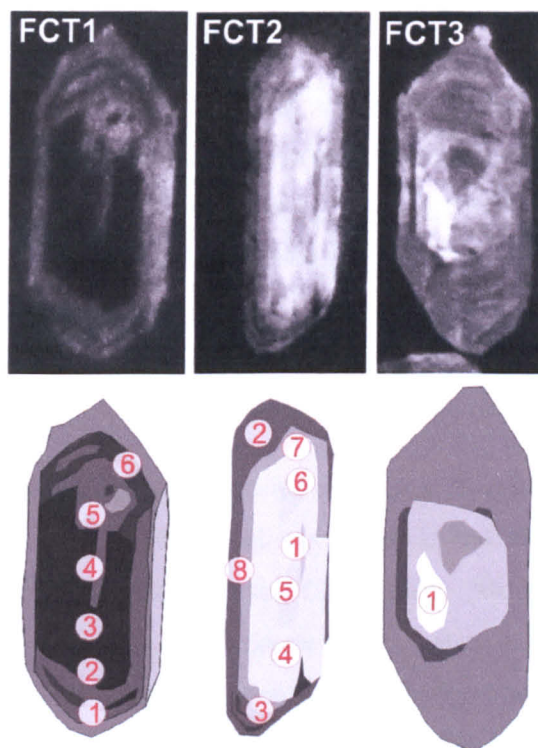


**Figure 47 - The CL images of the crystals on which SIMS analysis was performed.**

**Schematic representations show the location of the SIMS point analyses. All crystals are ~ 50  $\mu\text{m}$  in width.**

In order to minimise the lattice damage, and reduce the potential for fractionation and mobilization of U and Th, each crystal was exposed to the electron beam for a minimum length of time. Optical CL was not performed on these crystals to prevent additional lattice damage. Although variations in colour may be related to chemical substitution of U, Th, REE and trace elements into the crystal lattice, the reduced spatial resolution possible in the optical CL images would prevent direct correlation of the image with the SIMS analyses, and so this was not attempted.

The locations of the spot analyses are shown in Figure 47, and the elemental compositions for each analysis site are shown in Table 11. The images in Figure 47 are of poorer quality than those shown in Figure 46, as the time for which these crystals were exposed to the electron beam was kept to a minimum. After the SIMS analysis, re-imaging these particular crystals for illustrative purposes (under the same operational conditions) was prevented by the large amount of charging where the gold coating had been removed during the SIMS analyses. It would be possible to recoat the sample to obtain better quality images; however a different coat thickness may change the intensity of the CL emission, and prevent the accurate comparison of the data.

### 5.5.1 The distribution of U and Th

The FCT zircons show significant intra-crystalline zonation of U and Th. The analysed crystals have relatively simple CL zonation compared to other FCT zircons, and yet show significant and variable inter- and intra-zone U and Th heterogeneity. The majority of the SIMS analyses indicate U concentrations within the limits of those reported elsewhere, however at most sample sites the concentration of Th was higher than has generally been reported (see Table 10, and discussion in Section 5.3.1) [Schmitz & Bowring, 2001; Reiners *et al.*, 2002; Tagami *et al.*, 2003; Reiners *et al.*, 2004].

**FCT 1:** The distribution of the trace elements follows that of U and Th, with peaks in all trace elements at FCT 1 (2) and FCT 1 (6) (Table 11). High U and Th concentrations are found elsewhere in this crystal, in all areas with very low CL emission. Although a detailed traverse was not performed the spacing of the analyses allows an approximation to be constructed (Figure 48). In this crystal dramatic U and Th concentration differences are observed over short distances, where analyses are in adjacent zones with different CL intensities. The most extreme change in concentration between sites FCT 1 (1) and site FCT 1 (2) occurred within the outer 20  $\mu\text{m}$  of the crystal, and so recoil correction based on a homogeneous U and Th distribution will be incorrect. FCT 1 (2) has the highest U and Th content measured, and additional major and trace element analyses of this site could not identify the chemical signature of an inclusion mineral. In this crystal there also appears to be a correlation between Th/U and concentration. All analyses with U and Th concentration above 1000 ppm have a Th/U < 1.0.

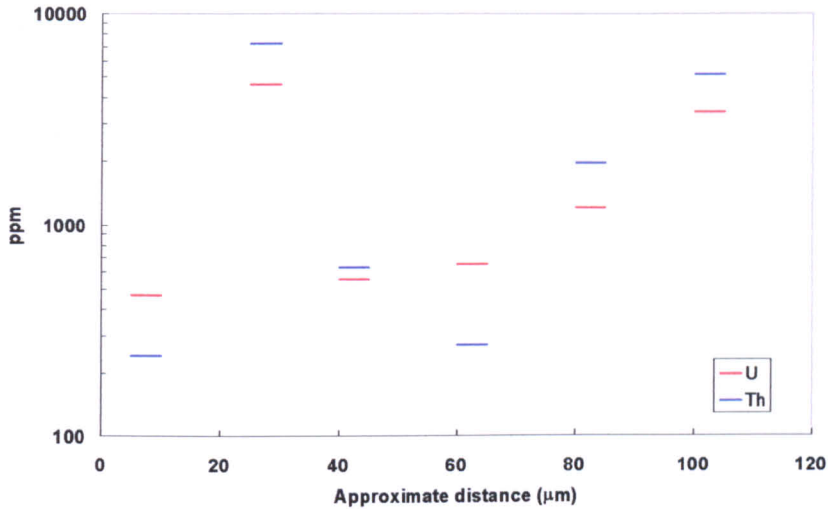
**FCT 2:** This crystal has lower concentrations than found in FCT 1, and shows less extreme CL zonation (pale-mid-greys). All analyses apart from FCT 2 (3) have low U and Th contents (< ~ 250 ppm U, Th). The distribution of trace element does not correlate closely with U and Th with peak U and Th at FCT 2 (3), and peak trace element concentration at FCT 2 (4). Again, the spacing of the analysis sites allows the construction of an approximate *c*-axis zonation profile (Figure 49).

**FCT 3:** The single analysis performed on zircon FCT 3 sampled the region of the strongest CL emission in the entire crystal mount, which was not caused by flaring from cracks or other surface imperfections. The U and Th concentration of this site is very low, at 15 ppm U and 52 ppm Th.

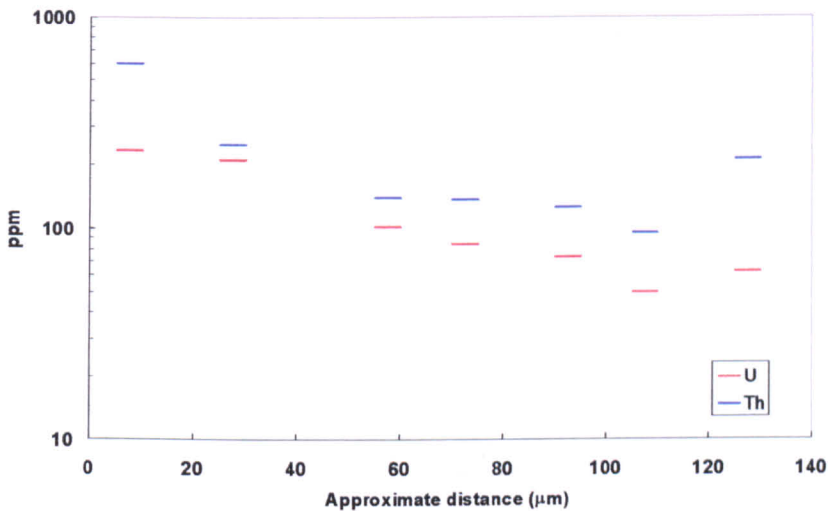
Crystal Spot #	FCT 1			FCT 1			FCT 1			FCT 2			FCT 2			FCT 2			FCT 3					
	(1)	(2)	(3)	(4)	(5)	(6)	(1)	(2)	(3)	(4)	(5)	(6)	(7)	(8)	(1)	(2)	(3)	(4)	(5)	(6)	(7)	(8)	(1)	
CL intensity	55	30	45	60	50	50	220	160	77	185	170	242	235	125	250									
U	468	4620	551	645	1193	3369	145	222	633	261	147	133	100	170	19									
error	0.9%	0.2%	0.5%	0.8%	0.3%	0.0%	1.4%	1.6%	0.9%	0.8%	1.1%	1.3%	1.6%	1.0%	3.8%									
Th	239	7207	622	269	1938	5141	119	87	328	297	143	103	70	172	73									
error	0.6%	0.2%	0.5%	0.5%	0.4%	0.1%	1.2%	0.9%	0.6%	0.8%	1.0%	1.1%	1.3%	1.0%	2.3%									
eU ([U] + .024*[Th])	526	6343	700	710	1658	4603	117	112	376	269	135	103	72	160	37									
Y	542	6672	2427	1232	1116	9248	1243	691	592	2955	1434	1256	1048	1820	369									
Ce	44	715	147	71	145	735	49	39	61	120	55	46	39	65	23									
Dy	36	698	261	136	135	1022	134	48	41	364	166	133	108	239	29									
Yb	259	2190	752	509	529	2865	419	297	350	808	457	397	322	561	126									
Hf	11801	9490	10697	9032	12148	9210	7675	9264	14200	8243	7955	7609	8132	8475	10090									
Th/U	2.63	0.86	1.19	3.21	0.83	0.88	1.63	3.40	2.58	1.18	1.38	1.72	1.90	1.33	3.36									

Table 11 - Elemental data from the SIMS analyses of zircons FCT 1, FCT 2 and FCT 3.

Crystal and spot numbers correlate with those shown in Figure 47. Determinations made from cycles of 10 measurements. Beam diameter was 5 - 7 µm for all analyses. Concentrations calculated using the NIST SRM 610 standard glass with 28.81 ± 0.07 ppm Th and Th/U = 0.353 by weight. Grey scale representations of CL intensities made using approximate (±10) average RGB values (shown in red italics) taken from spot locations on the CL images shown in Figure 47. Errors on the trace elemental determinations are ±2.0%.



**Figure 48 - An approximate U and Th concentration profile from zircon FCT 1**  
The profile is based on 6 spot analyses and does not sample all zones within the crystal. Errors in the U and Th contents as shown in Table 11. Spot analyses were 5 - 7 µm in diameter.



**Figure 49 - An approximate U and Th concentration profile for zircon FCT 2**  
The profile is orientated along the crystallographic c-axis, and is based on the rim relative positions of the 7 spot analyses and does not sample all zones within the crystal. Errors in the U and Th contents as shown in Table 11. Spot analyses were 5 - 7 µm in diameter.

### 5.5.1.1 The correlation of U, Th and CL intensity

The concentration of U and Th in all three crystals closely follows the zonation in CL emission intensity. U and Th concentrations decrease with increasing CL emission intensity, and the relationship between the radioactive content and the CL emission intensity is shown in Figure 50. The plot shows the variation of CL with U (ppm), Th (ppm) and effective U (ppm), eU, which introduces a weighting to account for the different alpha productivity of U and Th. Effective uranium content (ppm) is calculated by :  $eU = [U] + 0.24 \times [Th]$ . Direct inter-crystalline correlation

is limited, however regions of moderate CL emission - FCT 1 (4) and FCT 2 (3) - show moderate and approximately comparable U and Th concentrations ( $\sim 600$  ppm U, and  $\sim 280$  ppm Th).

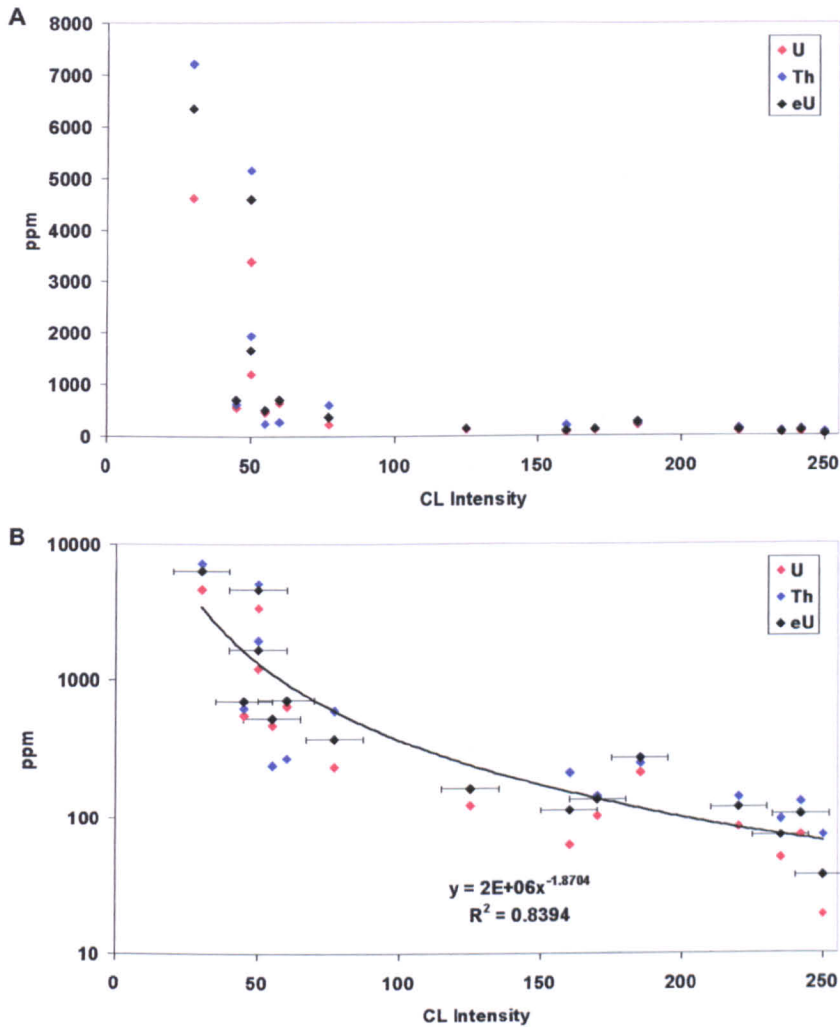


**Figure 50 - The relationship between U, Th and CL emission for the SIMS spot analyses on zircons FCT 1, FCT 2, and FCT 3.**

**A) U and Th concentrations are displayed on a linear scale. Uncertainties on all greyscale CL intensity determinations are  $\sim \pm 10$  greyscale units, errors on U and Th determinations are as in Table 11. eU = effective U concentration (ppm)  $eU = [U] + 0.24 \cdot [Th]$**

**B) U and Th concentrations are displayed on a logarithmic scale. A best fit curve is plotted for the eU data set (solid black line), and the uncertainties in both the U and Th determinations and greyscale CL intensity are shown on the values of eU only. The error in the eU effective concentration is smaller than the symbols.**

In general, zones with strong CL emission ( $> \sim 150$  greyscale units) have low eU concentrations ( $< 200$  ppm) (Figure 50 A), and zones with low CL emission (less than 40 greyscale units) have effective uranium (eU) content,  $\geq 1000$  ppm. However there is substantial scatter, and in the regions with the lowest CL, there is variation by a factor of 2 in the eU concentration while the CL emission remains largely unchanged (Figure 50 A).

A correlation of the U and Th concentration to the CL emission intensity is apparent (Figure 50 B). The relationship between eU and CL intensity is best fitted by a regression curve with the form  $y = a x^b$  ( $R^2 = 0.84$ , shown in Figure 50 B) but is also fitted well by an exponential regression ( $R^2 = 0.76$ , not shown). The physical basis for the application of either best fit curve remains unclear, but illustrates the good correlation in the data. The curve shown, and the  $R^2$  but some form of correlation between the CL emission and the eU content.

### 5.5.1.2 The correlation of trace elements and CL intensity

The amount of radiation damage within each zone may influence the quenching process (see Section 4.9.1.2), and a trend of increasing CL quenching with increasing eU may therefore be expected if the density of the CL generation sites is constant across the crystal. Homogeneity in the generation of CL is highly unlikely, as CL generation is related to the trace element concentrations and lattice defect distribution within each crystal [see review in Nasdala *et al.*, 2003 and references therein]. The total lattice defect density has not been quantified in this study, but the relationship between the trace element concentration and the CL intensity has been investigated. In the FCT zircons, the distribution of Dy, Ce, Yb and Y (Figure 51 A & B) generally follows U and Th, and the plots have a similar form to that shown in Figure 50 A. However, the correlations between CL intensity and the trace element concentrations are much less well defined than that for eU. This can be shown quantitatively by comparing the  $R^2$  values of best fit curves with those presented in Figure 50. For the trace elements the fits are significantly poorer, with  $R^2 < 0.5$  (Ce) and  $< 0.3$  (Dy, Y and Yb).

The relationship between eU and the CL intensity shown in Figure 50B is not perfect and there is considerable scatter. However, as the generation and quenching of the CL signature is most likely controlled by complex coupled substitutions [Ewing *et al.*, 2003; Nasdala *et al.*, 2003] a perfect correlation would be surprising. Dy is generally considered one of the major controls of CL generation [Corfu *et al.*, 2003; Ewing *et al.*, 2003; Nasdala *et al.*, 2003], and as the interplay between the CL generation and quenching processes will control the CL zonation observed, the relationship between Dy/U and the CL intensity was investigated. Figure 52 shows a plot of the Dy/U and Dy/Th for all the spot analyses which that although there is a general increase in the CL intensity with the Dy/U, there is no clear trend, and instead the data fall into two groups. Analyses that have Dy/U  $< 0.5$ , generally have low CL intensities, whereas high values of Dy/U (between 0.8 - 2.0) were obtained from those analysis sites with higher intensities (greyscale values  $> 100$ ). The values of Dy/Th are generally lower, but follow a similar trend.

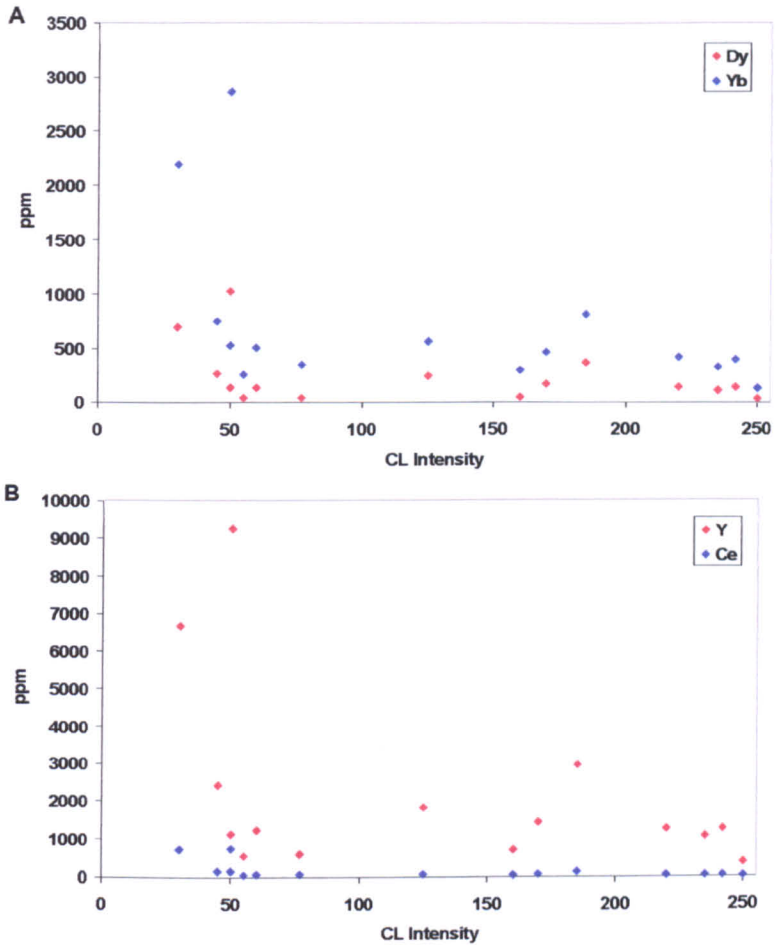


Figure 51 - The relationship between CL emission and trace element composition for the FCT zircons

A) Dy and Yb, Uncertainties on all greyscale determinations  $\sim \pm 4\%$  ( $\pm 10$  colour units), errors on elemental determinations are  $\sim \pm 2.0\%$  B) Y and Ce. Uncertainties on all greyscale determinations  $\sim \pm 4\%$  ( $\pm 10$  colour units), errors on elemental determinations are  $\sim \pm 2.0\%$

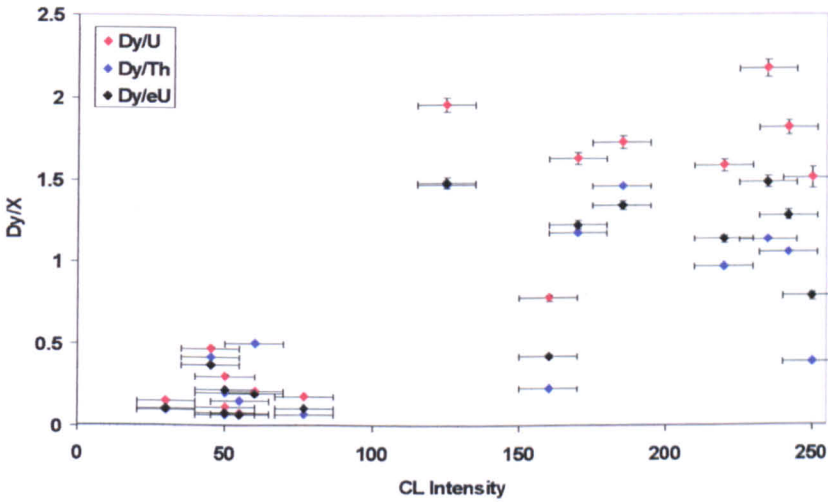


Figure 52 - The relationship between Dy/U, Dy/Th and Dy/eU with CL Intensity for each spot analyses performed on the Fish Canyon Tuff zircons. eU calculated using  $eU = [U] + 0.24*[Th]$ .

The complex coupled substitutions that introduce trace elements and U and Th into the zircon lattice, and therefore control the CL emission are poorly understood [see reviews in Hanchar & Hoskin, 2003] and have not been fully investigated here. However this study shows that in the FCT zircon, that although the distribution of trace elements generally follows the U and Th, it is the eU that appears to be the dominant control of the inter- and intra-crystalline variation in the CL emission intensity.

### 5.5.1.3 The quantification of typical zonation patterns

The spot analyses allow the determination of a general relationship between CL and U and Th concentration, however, the need to perform SIMS analyses on zircons with the full range of CL emissions meant that "atypical" crystals with broad and simple zonation were selected for the initial SIMS analysis. Crystals with more extreme intra-crystal CL zonation (e.g. Crystals D & E, Figure 46) are therefore expected to have correspondingly extreme changes in concentration across zone boundaries.

The SIMS profile of FCT 4 (Crystal I, Figure 46) allowed the U and Th distribution in a typical zoned FCT zircon to be investigated in more detail. This crystal was selected because of the relatively simple, CL zonation and the wide range of relative CL intensity changes (see Figure 53 A). U and Th concentrations were measured in 5 - 7  $\mu\text{m}$  spots along a traverse at a low angle to the *c*-axis. This allowed analysis of all major zones within the crystal (Figure 53 B). The elemental concentrations for each point on the traverse are presented in Table 12. As with FCT1 and FCT2, the distribution of Ce and Y generally follows U and Th (Figure 54), but there is a much clearer inverse correlation between the Hf and the other trace elements (and U and Th). Th/U is variable between zones and, in contrast to FCT 1 and FCT 2, is generally less than 1.0, except where U and Th concentrations are high (> 3000 ppm eU).

Figure 53 (C & D) shows the strong correlation between the U and Th concentration and the CL intensity. Furthermore, the changes in U and Th concentration correlate to the zone boundaries in the CL image. The significant variation in U and Th concentrations measured between neighbouring points on the SIMS traverse suggests that the compositional changes across zone boundaries are sharp. More accurate resolution of the zone boundaries requires smaller beam sizes (i.e. nano-SIMS). The measured increases in U and Th concentration observed over short (5  $\mu\text{m}$ ) distances, suggests that the current spatial resolution is sufficient to prevent excessive interference from multiple zones at any analysis site. To investigate this further, two additional spot analyses were performed on sites where the ion-beam interacts with zones of very different CL intensities. For analyses FCT 4 (1) and FCT 4 (2), the majority of the beam falls on a high CL emission area (predicted low eU), but a small part interacts with a narrow band (<< 5  $\mu\text{m}$ ) of lower CL intensity

(predicted high eU). The measured U and Th concentrations from these sites are higher than predicted from the dominant CL intensity, and are consistent with a SIMS signal dominated by the narrow, low CL-high U zone (see Table 12).

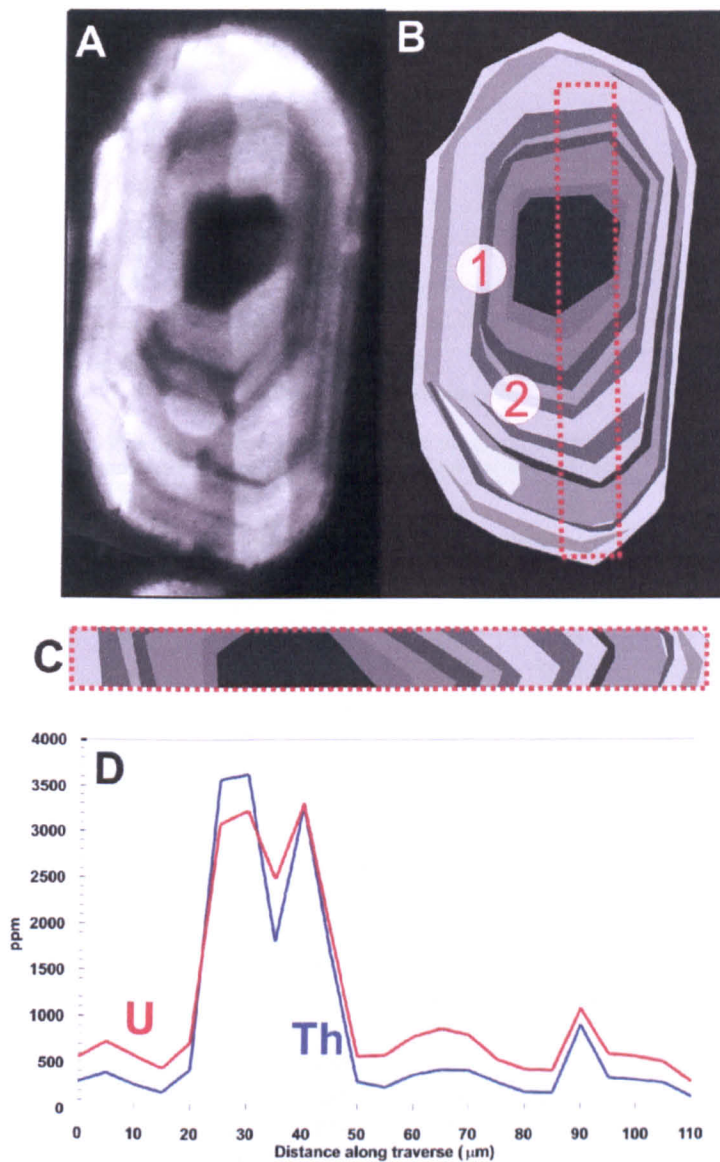


Figure 53 - A SIMS traverse along the c-axis of a FCT zircon showing typical zonation.

A) The CL image of the crystal taken after analysis, showing location of traverse and additional spot analyses.

B) A schematic representation of the zonation within the crystal showing the orientation and location of the traverse and two additional spot analyses.

C) The CL zonation along the SIMS traverse in a horizontal orientation.

D) The U and Th (ppm) measured along the traverse. Beam diameter was 5 - 7 μm.

(predicted high eU). The measured U and Th concentrations from these sites are higher than predicted from the dominant CL intensity, and are consistent with a SIMS signal dominated by the narrow, low CL-high U zone (see Table 12).

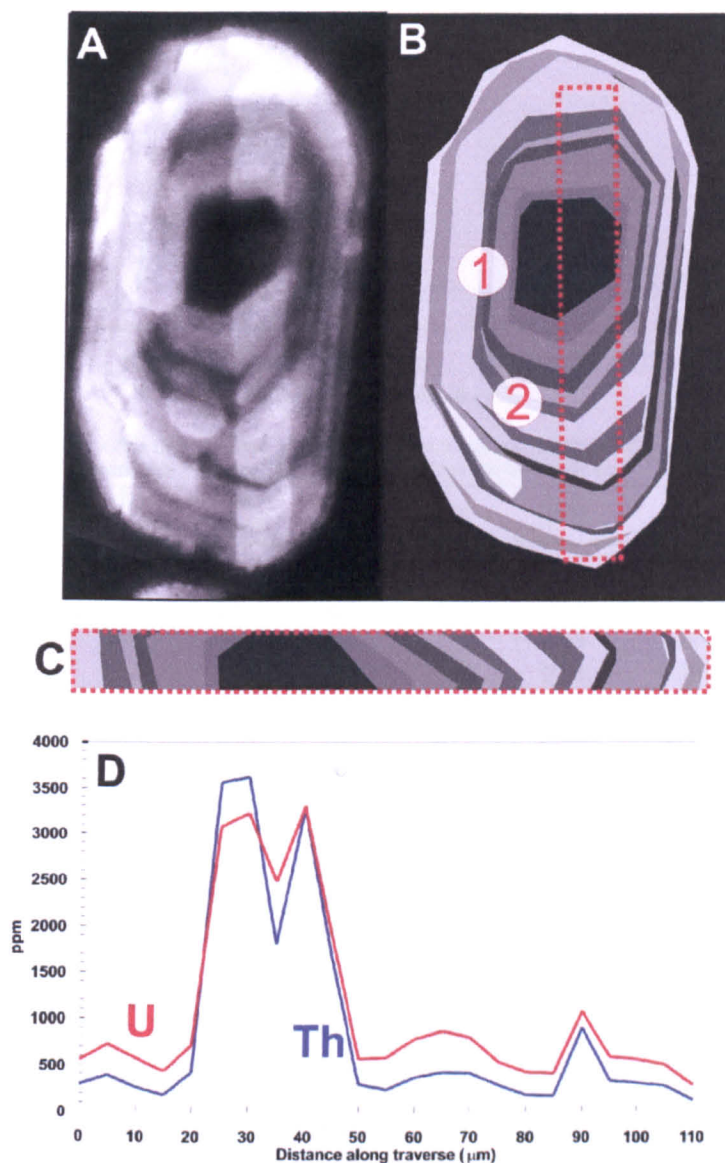


**Figure 53 - A SIMS traverse along the *c*-axis of a FCT zircon showing typical zonation.**

**A)** The CL image of the crystal taken after analysis, showing location of traverse and additional spot analyses.

**B)** A schematic representation of the zonation within the crystal showing the orientation and location of the traverse and two additional spot analyses.

**C)** The CL zonation along the SIMS traverse in a horizontal orientation.

**D)** The U and Th (ppm) measured along the traverse. Beam diameter was 5 - 7  $\mu\text{m}$ .

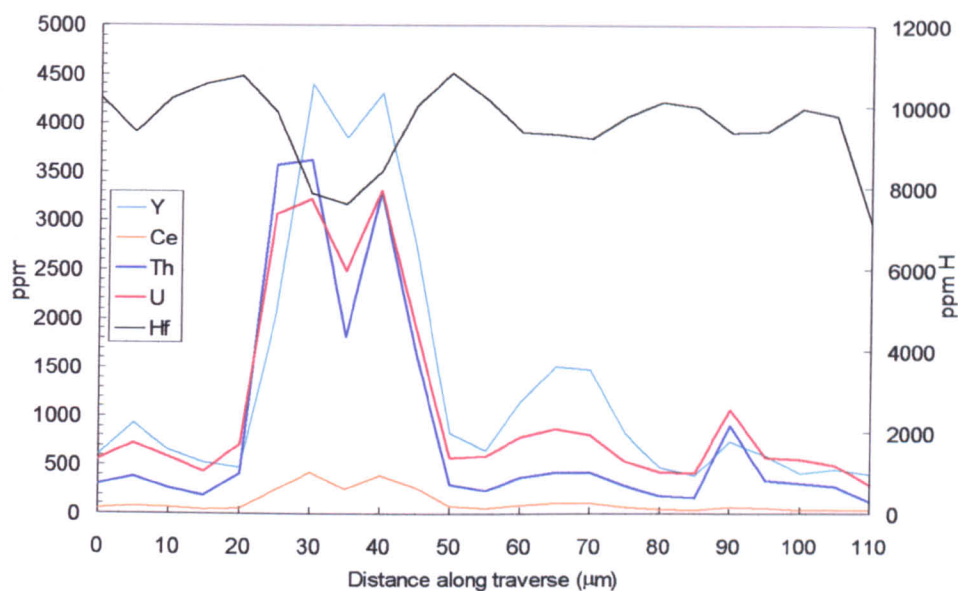


Figure 54 - The distribution of the measured trace elements in FCT4. All data shown is from the traverse. Uncertainty as detailed in Table 12.

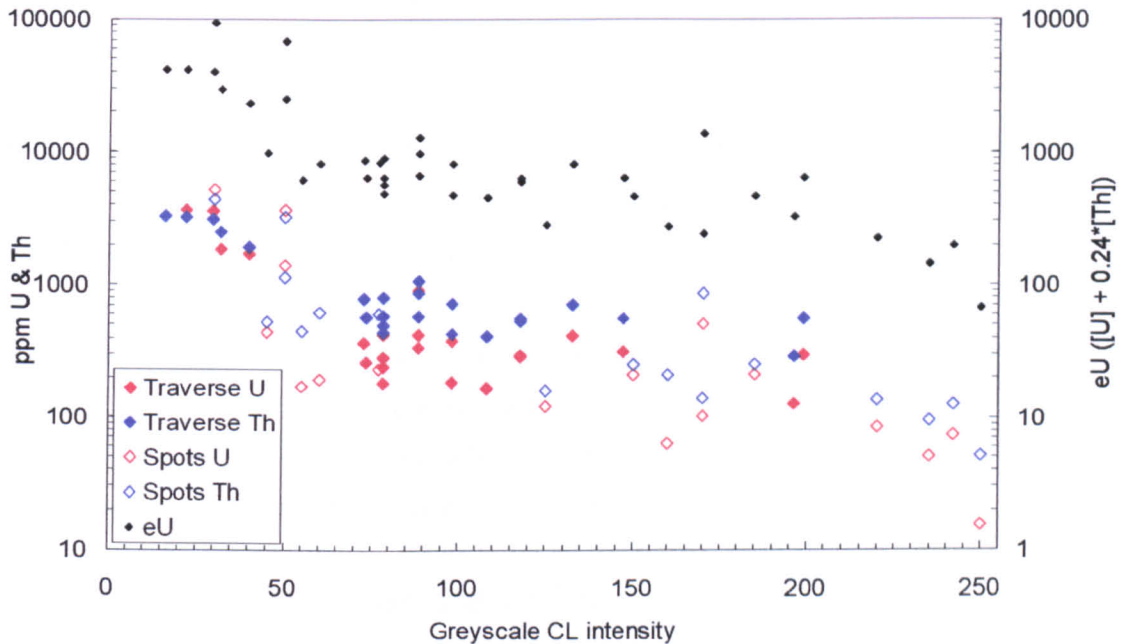
Distance (µm)	CL intensity	Th (ppm)	U (ppm)	eU	Th/U	Y	Ce	Hf
<i>Traverse data</i>								
0	199	295	559	630	0.53	606	54	10217
5	98	383	718	810	0.53	929	73	9375
10	74	261	572	634	0.46	650	58	10205
15	78	181	434	478	0.42	523	45	10565
20	132	416	712	812	0.58	471	48	10753
25	29	3567	3071	3927	1.16	2032	240	9858
30	22	3620	3221	4089	1.12	4405	426	7886
35	32	1813	2484	2919	0.73	3853	245	7593
40	16	3288	3304	4093	1.00	4302	389	8388
45	40	1676	1920	2323	0.87	2760	267	10020
50	118	296	562	633	0.53	827	72	10844
55	78	239	583	641	0.41	652	56	10180
60	73	367	778	866	0.47	1156	82	9381
65	88	424	863	965	0.49	1516	106	9334
70	78	418	798	898	0.52	1481	102	9240
75	118	286	535	604	0.53	827	57	9773
80	98	183	427	471	0.43	469	45	10112
85	108	168	410	451	0.41	395	31	9996
90	88	903	1072	1288	0.84	741	64	9375
95	88	336	579	660	0.58	592	46	9412
100	147	312	558	633	0.56	415	28	9952
105	78	282	498	566	0.57	453	35	9789
110	196	127	288	318	0.44	399	26	7135
<i>Additional spot analyses</i>								
FCT 4 (1)	87	211	569	780	2.70	817	47	11564
FCT 4 (2)	104	501	857	1358	1.71	940	75	11938

Table 12 - Elemental data from the SIMS analysis of zircon FCT 4.

Traverse and FCT4 (1) & (2) were placed as shown on Figure 53. Errors on the U and Th measurements were ~ 1.2 %, and ~ 2 % on other elements. CL greyscale values have an uncertainty of  $\pm 10$  greyscale units.

### 5.5.1.4 Extended correlation of U, Th and CL intensity

The inclusion of the data from the traverse allows correlation across the full range of CL intensities. Figure 55 shows a plot of all the FCT zircon data, except FCT 4 (1) and FCT 4 (2), and shows that on a semi-quantitative basis, the distribution of U and Th in the FCT zircons can be assessed from zonation in the CL emission intensity.



**Figure 55** - The inter-crystal correlation of CL intensity and U and Th concentration.

Both vertical scales are logarithmic. All SIMS analyses from FCT 1, FCT 2 and FCT 3, and the data from the traverse of FCT 4 are shown. Errors are as in Table 11 and Table 12.

The data in Figure 55 are best fitted by a regression curve of the form  $y = a x^b$ , and this regression has  $R^2 = 0.71$ . There are likely to be several mechanisms involved with the generation and quenching of CL in zircons, and it is perhaps surprising that the correlation is this well defined.

### 5.5.1.5 Insensitivity in the correlation

In addition to the chemical control on the CL generation, there are several possible reasons for the scatter observed in the correlation between eU and CL intensity. Greyscale values are averaged across the entire area of the analysis, and typically vary by  $\sim \pm 10$  greyscale units. Therefore at low values of CL intensity the image analysis cannot accurately quantify the greyscale value, and the relative uncertainty on these greyscale determinations is as high as  $\pm 30\%$ . The SEM operational conditions used here were selected for the best resolution of the contrasts between zones, while having a background greyscale value of approximately zero, and using the full greyscale spectrum.

Reduced uncertainty in the quantification of the greyscale values for low CL emission may be achieved by changing the SEM operational settings, but this may be at the expense of resolution at higher intensities. Alternatively, more complex image manipulation may improve the greyscale determination, but such techniques are beyond the routine application to large numbers of crystals.

The SIMS ion-beam interacts with a different volume than that involved with the generation of the CL signal, so the apparent relationship between CL intensity and U and Th concentration may fail when one technique intersects a different zonation sequence to the other. The SIMS analyses requires a spot size of  $\sim 5 \mu\text{m}$  diameter ( $\sim 5 \mu\text{m}$  deep) and the beam may therefore interact with multiple narrow zones across and into the plane of the polished surface. The CL image will have a greater 2- and 3-dimensional spatial resolution. The two techniques will therefore record information about different zonation patterns in the margins of the crystal, towards the margins of each zone, and in regions where the zonation is narrower than the width of the SIMS beam. In these regions there will be some degree of 3-D zonation. The apparent insensitivity of the CL emission to significant increases in the concentration of U and Th, which is seen in the low emission cores of FCT 1 and FCT 4, is unlikely to be caused by such a 3-dimensional margin effect, and the failure to observe a difference in the CL emission intensity is therefore probably due to the high relative uncertainty in the greyscale determination at values  $< 50$ .

## 5.6 CL as a proxy for U and Th

There is good intra- and inter-crystal correlation between the distribution of U and Th and the zonation of CL. It is therefore concluded that CL images of the FCT zircon can be used as a first order approximation for U and Th zonation in the Fish Canyon Tuff zircons. The CL images have better spatial resolution than is possible from fission track distributions (Section 5.4.3) and the collection of a large number of high resolution images can be performed quickly. The CL images appear to be more sensitive than other SEM-based qualitative methods (Sections 5.4.1 and 5.4.2), and although there are issues surrounding an apparent insensitivity at very high U and Th contents, CL imaging provides a method for the routine assessment of zonation within the FCT zircon separate.

## 5.7 Inter-sample correlation of the CL proxy

To investigate the possibility of extending the application of the CL-U-Th proxy to unknown samples, zircons from the Muck Tuff (MT) ( $60.45 \pm 0.03 \text{ Ma}$ ; Chambers *et al.*, 2005) were analysed using CL and SIMS. In the majority of the CL images, the zircons show a relatively simple zonation that has a rim with high- to moderate-CL intensity surrounding a core with much

lower emission (Figure 56). Many of these crystals show evidence of sector zonation within the cores of the crystals (e.g. Crystals F, G & I, Figure 56). Large crystals ( $> 200 \mu\text{m}$  wide) are uncommon, and typically have a strong narrow oscillatory zonation and generally contain inclusions as shown in Crystal B (Figure 56). CL images and SIMS analyses were obtained under the operating and image capture conditions used for the FCT zircon. The data obtained from the SIMS analyses of the MT zircons are shown in Table 13, and the relationship between the CL intensity and trace element concentrations are shown in Figure 57.

The CL emission intensity in the MT zircons correlates best with the U, Th, and also with Ce. The U and Th concentrations associated with a given CL intensity are much lower than the FCT zircons, and there is a larger relative reduction in U content for a given CL intensity increase. The Hf concentration is relatively constant ( $\sim 6700 \text{ ppm}$ ) and all trace element concentrations are lower than in the FCT zircons.

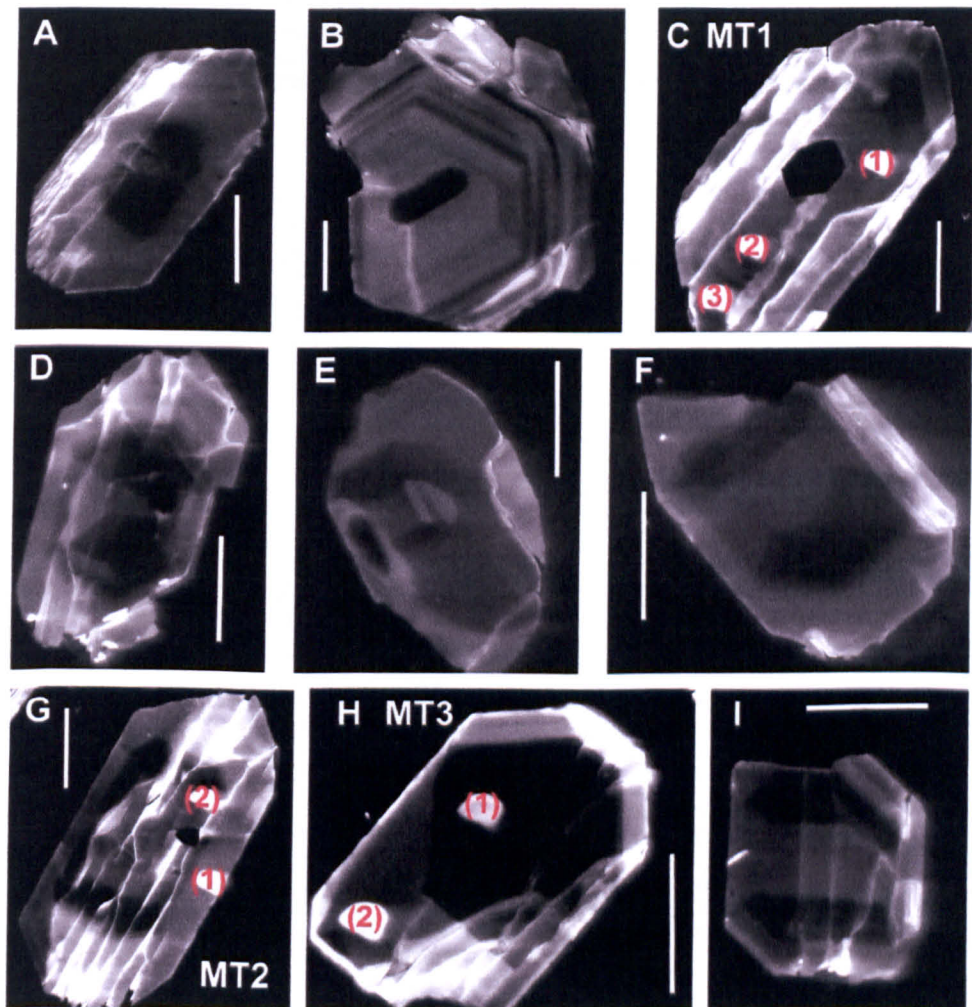
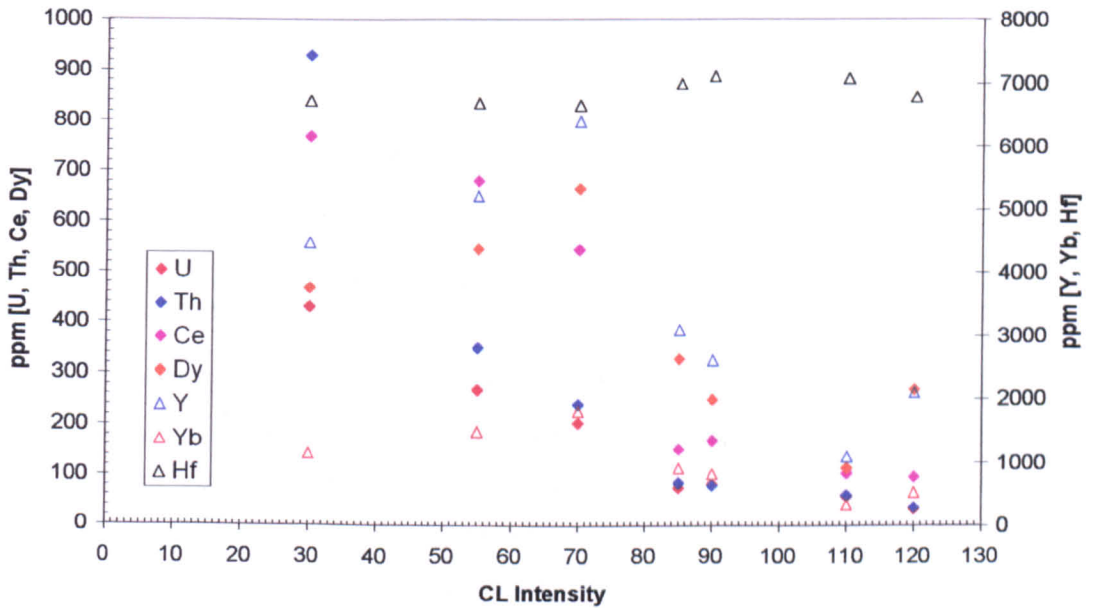


Figure 56 - Panchromatic CL images of the Muck Tuff zircons.

White scale bars are  $50 \mu\text{m}$ . White circles on crystals C & H are sites of SIMS analyses.

Crystal	MT1	MT1	MT1	MT2	MT2	MT3	MT3
Spot #	(1)	(2)	(3)	(1)	(2)	(1)	(2)
<i>CL intensity</i>	110	90	85	120	55	30	70
U (ppm)	56	81	73	31	268	432	202
Error	1.8%	1.5%	1.6%	2.4%	0.8%	0.7%	1.0%
Th (ppm)	59	79	84	35	351	931	239
Error	1.8%	1.5%	1.6%	2.4%	0.8%	0.5%	0.9%
eU ([U] + 0.24x[Th])	70	100	94	39	353	655	259
Y	1093	2605	3083	2089	5210	4471	6399
Ce	102	167	151	96	680	768	545
Dy	113	248	327	266	546	469	664
Yb	315	815	905	519	1492	1143	1801
Hf	7083	7124	6999	6786	6685	6726	6651
Th/U	1.06	0.97	1.15	1.11	1.31	2.16	1.19

**Table 13 - Elemental data from SIMS analysis of the MT zircons.**  
 Determinations made from cycles of 10 measurements. Grey scale CL intensities (shown in italics) have an uncertainty of  $\sim \pm 10$  units. Errors on the U and Th measurements are shown, and are  $\sim \pm 2\%$  for the other elemental determinations.



**Figure 57 - The relationship between CL intensity and the composition of the MT zircons.**

The limited range of greyscale values on which SIMS analysis could be performed means that the range of the greyscale axis in this plot has been reduced (0-130) compared to that shown in the FCT zircon plots above (0-255). Uncertainties on all measurements as for Table 13.

Figure 58 shows the good ( $R^2 = 0.96$ ) exponential correlation between the eU content and the CL intensity, and in addition reveals a correlation between Dy/eU and CL that is absent in the FCT

zircon dataset (see Figure 52). Six of the seven spot analyses performed on the MT zircons define a trend showing a good ( $R^2 = 0.94$ ) exponential correlation between increasing Dy/eU and increasing CL intensity (Figure 58). The single spot analysis that does not fall within the trend shown in Figure 58 has a similar composition. It is also possible that the analysis with Dy/eU  $\sim 7$  is anomalous, and the cause of these possible deviations cannot be determined without additional chemical analyses. The two correlation curves plotted in Figure 58 suggest that the generation of the CL signal in the MT may be controlled by a coupled substitution involving Dy and U and Th.

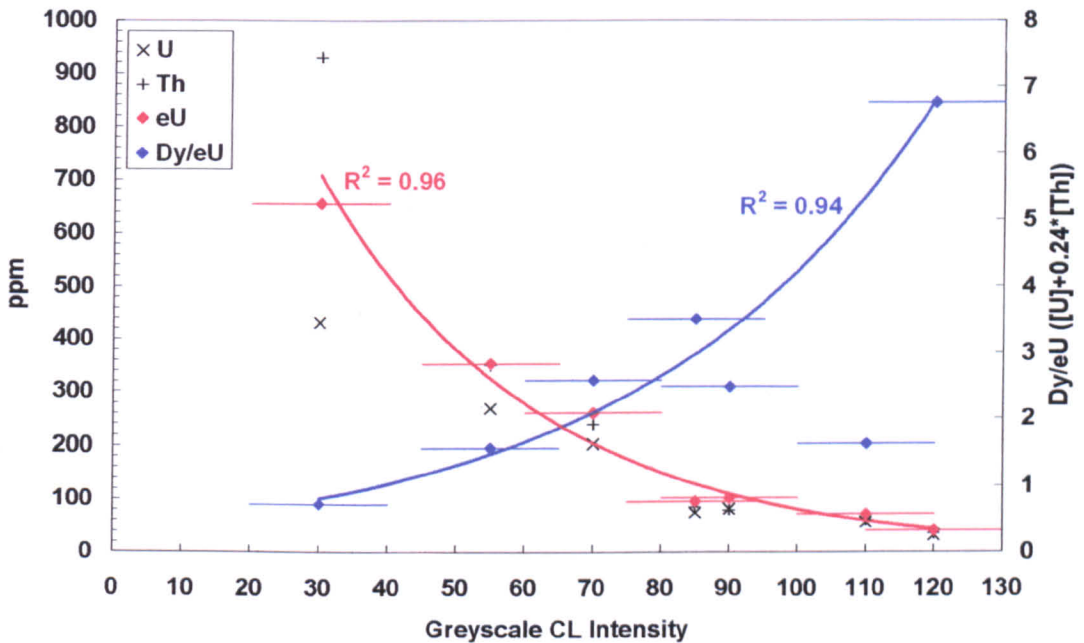


**Figure 58 - The relationship between CL intensity and the eU, and Dy/eU of the MT zircons. Uncertainties on all measurements are shown. See text for further discussion.**

Despite the uncertainty in the relationship between Dy/eU, the good correlation between the CL intensity and eU concentration suggests that using the CL emission intensity as a first order approximation of eU is also valid for the MT zircons. This correlation is determined over a limited range of CL intensities (0 - 130 greyscale units), however, this range is typical of that seen in the MT zircons. This limited study shows that although the bulk eU content of the MT zircon is much lower than in the FCT zircons, the U and Th concentrations are not homogenous, and  $F_T$  corrected ages will contain significant age bias. The implications of zonation on the (U-Th)/He age of this sample are discussed in Section 6.4.1.

Although both the CL intensity can be used as a first order approximation of the U and Th or eU concentration for both the FCT and MT zircons, plotting the two data sets together (Figure 59 A) shows that the relationship between CL emission intensity and eU is sample dependant. Across the

limited range of CL values for which comparison is possible, the MT zircons have a lower eU concentration than the FCT zircons at a given CL intensity. The best fit curves (the exponential and the  $ax^b$  regressions) for each dataset are shown in Figure 59 B.

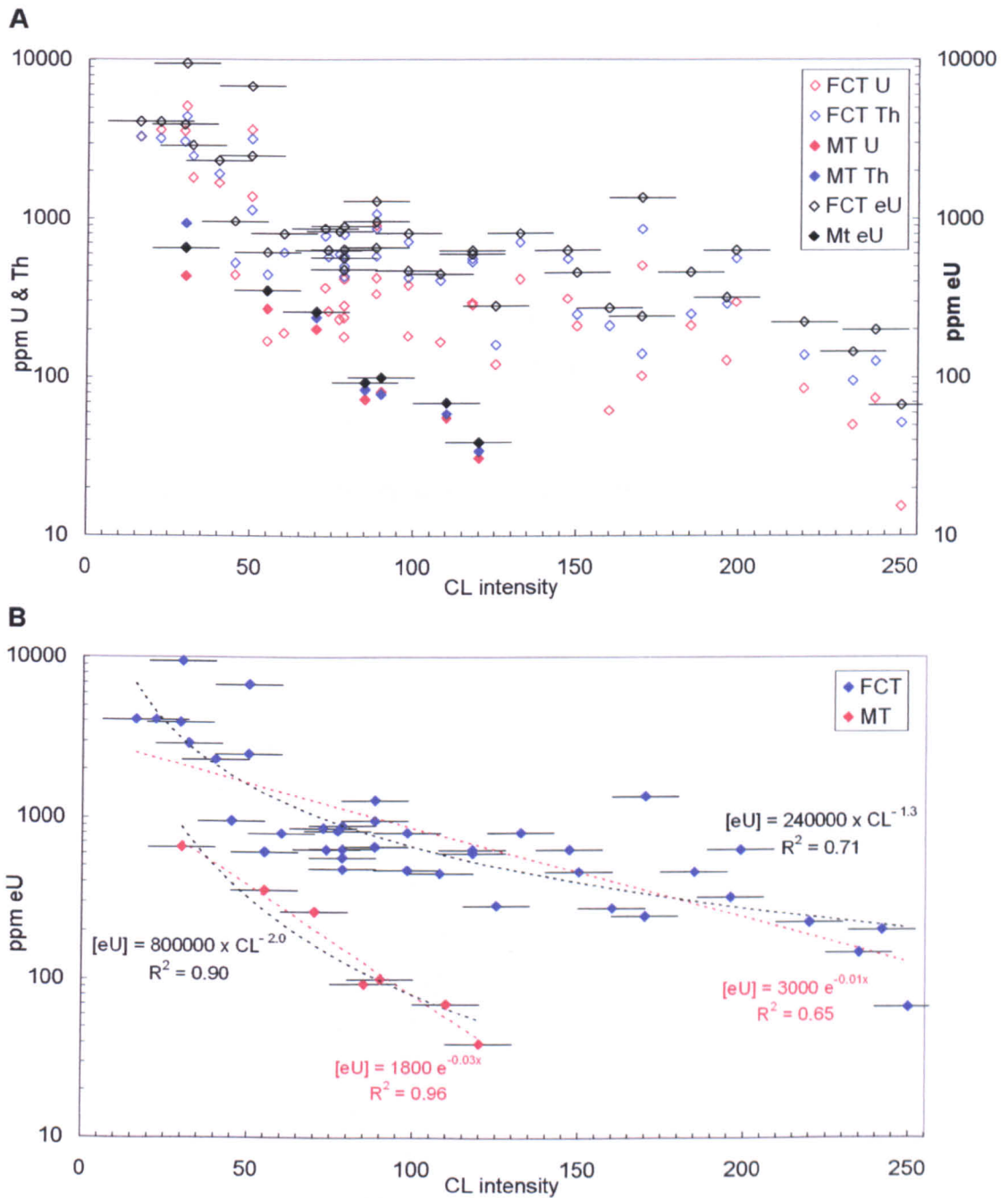


**Figure 59 - The relationship between CL intensity and eU for the MT and FCT zircons.**

**A) The U, Th and eU data sets, plotted on logarithmic axes. Uncertainties as shown.**

**B) The best fit curves for the eU data (Dashed black line = power regression, Dashed red line = exponential regression) Uncertainties as shown.**

The different trace element and REE compositions, and the different trend in Dy/eU, seen between the FCT and the MT zircons, are probable causes for the different correlation trends. However the

good correlation between the CL and the eU content suggests that eU is the dominant control in the quenching of the CL signal in both samples. Several studies into the complex chemical controls on the CL signal obtained from zircon, have been conducted on crystals with unusual compositions, or those which have been chemically doped [Blanc *et al.*, 2000; Burakov *et al.*, 2002; Finch & Hanchar, 2003; Nasdala *et al.*, 2003]. The relatively correlations observed here suggests that perhaps there are fewer dominant controls on the CL signal obtained from typical natural zircons.

The sample-dependant correlations shown in Figure 59 B imply that quantitative inter-sample comparison and eU determination, from the CL intensity in an unknown sample is not possible. However, the good correlation within a single zircon population can be used as a qualitative proxy for zonation. The probability of single analysis being affected by a U and Th zonation, and the probable style of that zonation can therefore be qualitatively assessed from SEM CL images. This assessment will allow strongly zoned samples to be identified, and the general effect of characteristic zonation patterns on the  $\alpha$ -recoil correction to be estimated.

## 5.8 Calculating $F_Z$ for the FCT zircon

The CL zonation styles observed in the FCT zircon are illustrated in Figure 46 (p 112) and the CL characteristics of each zonation style are described in Section 5.4.5. FCT zircons that have homogenous CL (Type 6, defined Section 5.4.5), and therefore homogenous U and Th distributions make up ~ 2 % of the total population, and for these samples applying the  $F_T$  correction is correct. However, crystals with a single step function zonation make up ~ 4 % of the total population (Type 3 and Type 4), and the application of  $F_T$  to these crystals will introduce substantial age bias (as Section 4.7.1.1). The effect of these step-function zonation patterns can be estimated using the theoretical treatment presented in Section 4.7. The affect of Type 1 and Type 2 zonation (defined Section 5.4.5) on  $\alpha$ -recoil is harder to quantify. The generally concentric form of Type 1 and Type 2 zonation will lead to some averaging of the effect on the  $\alpha$ -recoil (see discussion in Section 4.7.1.3), but the SIMS analysis shows that the relative concentration changes between adjacent zones are large and variable. This means that substantial and highly variable age bias will be introduced if Type 1 and Type 2 crystals are inaccurately assumed to be homogeneous. From the theoretical treatment presented in Chapter 4, the number of crystals that have an  $F_T$  corrected age that is unaffected by zonation will therefore be minimal. The correlation of CL intensity and eU suggests that the majority (~ 96 %) of the FCT zircons have rims that are depleted in U and Th relative to the cores. Therefore the assumption of homogeneity in all cases may lead to an average over-estimation of the fractional loss (as  $F_T > F_Z$ ), and a positive age bias.

Although every FCT zircon crystal has a unique U and Th distribution, CL image analysis allows the effect of zonation on  $\alpha$ -recoil corrections to be investigated. The following study was undertaken in order to determine the magnitude and variety of age biases that are introduced by assuming homogeneity in the FCT zircons, and to determine if the poor reproducibility of the S.U.E.R.C. dataset (Table 4 and Table 5, and Figure 12), and that of the full FCT (U-Th)/He zircon dataset (Figure 12), can be explained by the variety of zonation patterns observed.

The Hourigan *et al.* (2005)  $\alpha$ -recoil model (Section 4.5) can be applied to any simple idiomorphic crystal geometry, but for the purposes of this modelling, tetragonal crystals were used. As the FCT zircons generally have  $W_1/W_2 = 1.0 - 1.2$ , the use of tetragonal geometries is unlikely to introduce significant uncertainty (Figure 23). The U and Th zonation in every FCT zircon crystal will be different, and even with the correlation between CL intensity and eU, an investigation into the age bias introduced by assuming homogeneity requires several simplifications.

### 5.8.1 Model parameters

The greyscale CL intensity and zone widths were measured for all FCT zircons shown in Figure 46 that would have been selected for (U-Th)/He analysis. The widths of zones were measured across the centre of the crystals, parallel or perpendicular to the c axis, ensuring all zones were measured. Where the zonation was asymmetric across a crystal, both core-rim profiles were modelled. As the Hourigan *et al.* (2005)  $\alpha$ -recoil model assumes self-similar zonation, the measured profiles were normalised to the crystal width. All crystals modelled in the initial calculations had dimensions of  $W_1 = W_2 = 50 \mu\text{m}$ ,  $T_L = 160 \mu\text{m}$  and  $T_1 = T_2 = 30 \mu\text{m}$ , typical of the crystals imaged in Figure 46.

Across all zonation styles, image analysis of the individual zones showed that a generally limited range of CL intensities is observed within the population. The most common ranges observed were used to bin the data according to the greyscale values (Appendix C). Where narrow oscillatory zonation was too subtle to be measured accurately, (i.e. Crystal A, and the outer regions of Crystal K, Figure 46) homogeneity was assumed, as this zonation has a small impact on the value of  $F_z$  (see Section 4.7.1.3). The majority of CL determinations lie in the central region of each bin defined in Appendix C. The binned CL data was assigned U and Th contents estimated from the relationship between eU and CL intensity. The maximum U and Th concentration used was 3000 ppm U and 3000 ppm Th. The scatter in the relationship between eU and CL intensity (Figure 55) means that the U and Th content of any CL-zone can only be estimated, and this will over- and under estimate the U and Th content of individual zones. The model zonation profiles generated from this procedure are shown in Figure 101 (Appendix C), and were input into the Hourigan *et al.* (2005) model as 1D profiles running from core to rim. The asymmetric zonation determined from the SIMS traverse of FCT 4 was also modelled as two separate profiles (Figure 102).

## 5.8.2 Model results

The modelled profiles are an over-simplification of the zonation in real crystals, and do not represent the full range of zonation patterns nor the range of concentration changes that will exist in the crystal population. However, they allow the investigation of the range of age biases that can be introduced if the U and Th zonation is not considered. The age biases introduced by each of the 27 modelled profiles are shown in Figure 60.

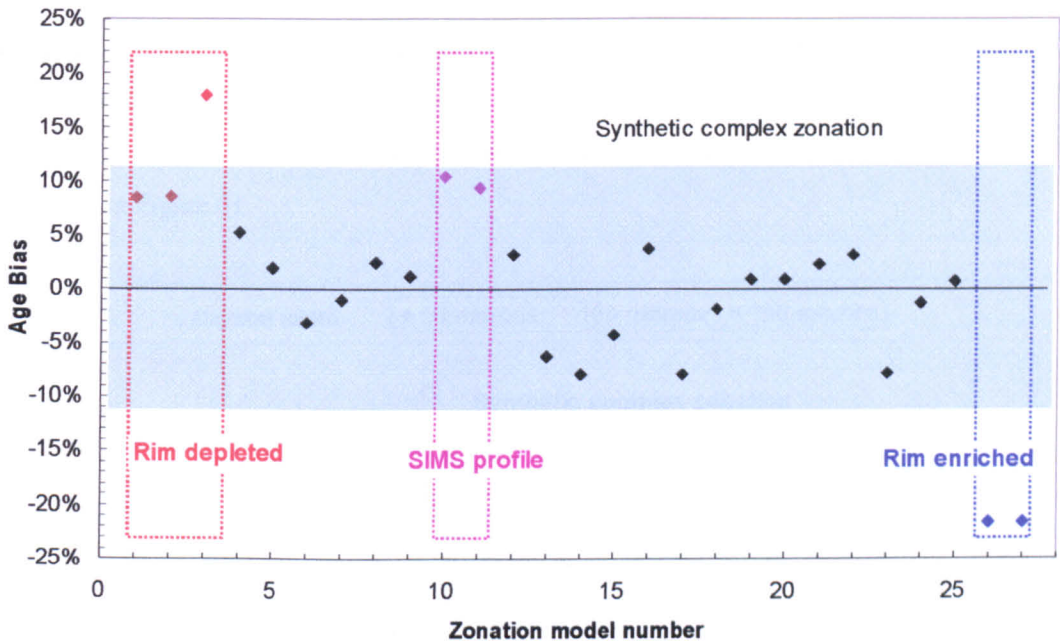


**Figure 60 - The age biases for modelled FCT zircon zonation profiles.**

All profiles are shown in Appendix E. All modelled crystals are tetragonal, with  $W_1 = W_2 = 50 \mu\text{m}$ ,  $TL = 160 \mu\text{m}$ , and  $T_1 = T_2 = 30 \mu\text{m}$ . Age biases calculated using Equation 34. The shaded region represents the age variation in the combined data set ( $11.5\%$ ,  $2\sigma$ ), assuming the mean age of this data set represents a  $0\%$  age bias.

As expected, the model concentration profiles that introduce the greatest age bias (of up to  $\pm 20\%$ ) are those associated with Type 4 and Type 5 zonation (simple single step functions). The majority of profiles generated from crystals with Type 1 and Type 2 zonation introduce a bias of between  $+5\%$  (i.e.  $F_T$  corrected ages are  $5\%$  older than that calculated using the correct  $F_Z$ ) and  $-10\%$  (i.e.  $F_T$  corrected ages are  $10\%$  younger than calculated using the correct  $F_Z$ ). The profiles with the highest negative age bias (profiles 14, 17 and 23) are generated from crystals where the zonation is essentially cyclic between two very different concentrations ( $\Delta C \approx 5$  or  $0.2$ ). These crystals have a large volume of the rim (the region affected by  $\alpha$ -recoil) that has high U and Th, and a core that is relatively depleted. The calculated  $F_Z$  for the two FCT 4 profiles generated from the SIMS traverse data have the greatest positive age bias of up to  $\sim +10\%$ . This value is similar to that calculated for Type 4 zonation (profiles 1 & 2), where the crystals have relative rim depletion. Crystal FCT 4

has a greater range of CL intensities than is seen in most of the FCT zircons, and it encompasses almost the full range of CL intensities (and eU concentrations) observed. Compared to FCT 4, approximately equal numbers of model crystals exhibit more moderate- and more extreme-CL intensity changes across the zone boundaries in the regions of the crystal. The simplifications used to generate these models are therefore concluded to be appropriate approximations.

The zonation patterns shown in Figure 46 are observed in all crystal size fractions, with no measurable change in the relative width of individual zones with increasing crystal size. Therefore the effect of zonation on larger crystals can also be investigated using the normalised zone width procedure. The FCT zircons selected for (U-Th)/He analysis generally have  $W_1 \approx W_2$ ,  $W_1 = 50 \mu\text{m}$  to  $150 \mu\text{m}$ , termination lengths between  $30 \mu\text{m}$  and  $50 \mu\text{m}$ , and total lengths of between  $160 \mu\text{m}$  and  $250 \mu\text{m}$ . The results of the modelling of crystals with widths of  $50 \mu\text{m}$ ,  $100 \mu\text{m}$  and  $150 \mu\text{m}$  are shown in Figure 61.

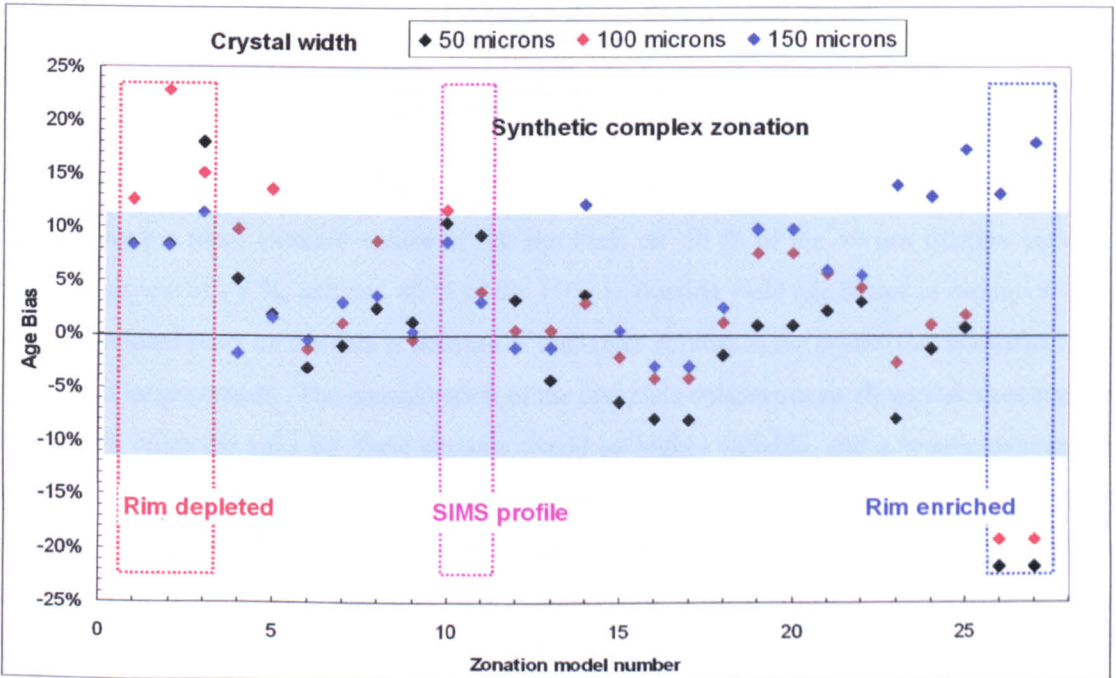


**Figure 61 - The variation of age biases from the model FCT zircon zonation profiles for different crystal sizes.**

All profiles are shown in Appendix E. All modelled crystals are tetragonal. Black filled symbols:  $W_1 = W_2 = 50 \mu\text{m}$ ,  $T_L = 160 \mu\text{m}$ , and  $T_1 = T_2 = 30 \mu\text{m}$  (Figure 60). Red filled symbols:  $W_1 = W_2 = 100 \mu\text{m}$ ,  $T_L = 200 \mu\text{m}$ , and  $T_1 = T_2 = 30 \mu\text{m}$ . Blue filled symbols:  $W_1 = W_2 = 150 \mu\text{m}$ ,  $T_L = 250 \mu\text{m}$ , and  $T_1 = T_2 = 50 \mu\text{m}$ . Age biases are calculated after Equation 34. The shaded region represents the age variation in the combined data set (11.5 %,  $2\sigma$ ), assuming that the mean age of the dataset represents a 0 % age bias.

Figure 61 shows the change in the age bias associated with increasing crystal size, for each of the 27 model profiles, and Figure 62 shows the frequency distribution of the age bias for each of the different crystal sizes, for the Type 1 and Type 2 zonation only.

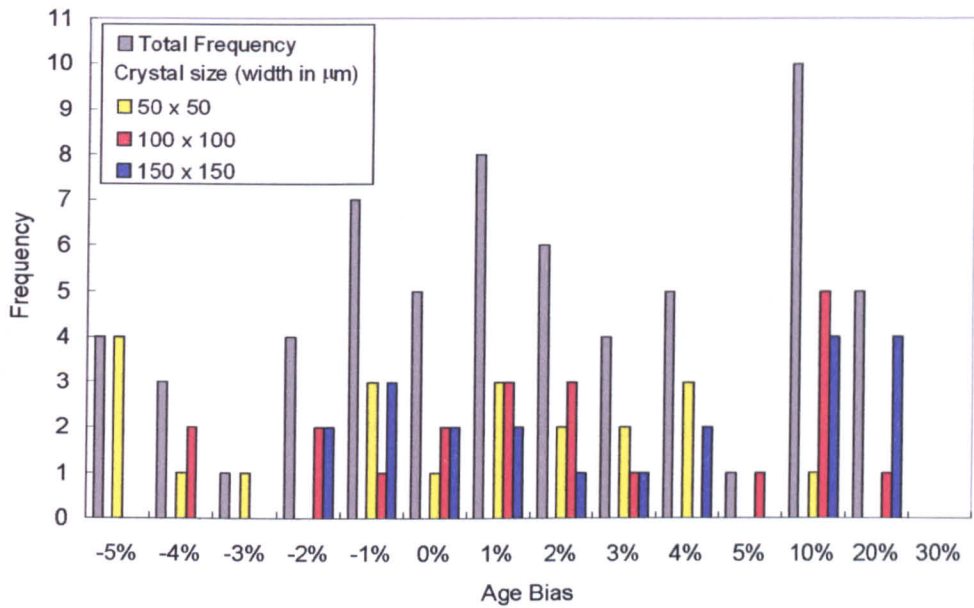


**Figure 62 - A frequency distribution plot of the age biases calculated for crystals with complex oscillatory zonation patterns.**

The data are from only those profiles with oscillatory zonation. The age biases calculated for the simple step function profiles (profiles 1, 2, 3, 26, & 27) have been removed from the data set.

All three crystal sizes show a fairly uniform frequency distribution between - 1.0 % and + 4.0 %, considering the more extreme values of the age bias, *ca.* 20 % of the 50 μm fraction yield age biases in excess of - 5 %, and *ca.* 40 % of the 150 μm fraction yield age biases in excess of + 5%. The size-related skew on the data is because of the larger volume of the crystal that is unaffected by  $\alpha$ -recoil in large crystals. The consideration of the complete dataset across all crystal sizes suggests that the  $F_T$  corrected ages for these crystals would be highly variable, and a sample average age would contain a net positive age bias ( $\sim$  1 - 3 %). The net positive age bias arises from the dominance of oscillatory zonation patterns where the outermost zone is generally depleted relative to the core of the crystal. If this modelling is appropriate, it implies that the application of the  $F_T$  correction to the (U-Th)/He ages presented in Table 4 and Table 5, will lead to an over estimation of the average age of the FCT zircon by  $\sim$  0.5 - 1.0 Myr.

### 5.8.2.1 Limitations of the modelling

There are several limitations in the modelling, which controls the accuracy with which these model profiles reflect the natural variation. Firstly the use of the CL intensities to accurately determine the U and Th concentration is not possible because of the scatter on the relationship between eU and CL intensity. The scatter in the correlation, and the need to correlate all CL intensities (0-255) to a trend defined by a limited number of CL values, means that some form of binning method is necessary (as described in Section 5.8.1). This will reduce the number of different U and Th

concentrations used in the model profiles, and will therefore over-simplify the concentration changes in natural zonation patterns. Improved resolution of CL intensity differences in the model crystals is beyond the resolution of the correlation because of the large scatter.

The use of a maximum U and Th concentration in the model profiles probably underestimates the real concentrations in the most enriched zones. The model outcomes will therefore represent moderated age biases in the overall population, as higher U and Th contents would accentuate the effects of crystal size on  $\alpha$ -recoil discussed above, and would increase the scatter in the calculated age bias. The uncertainties associated with the determination of the greyscale values at low CL intensities means that the approximation of more appropriate maximum U and Th contents is not possible.

The Hourigan *et al.* (2005)  $\alpha$ -recoil model cannot include the effects of asymmetric zonation, a form seen in many FCT zircons (Figure 46). Asymmetry in zone width and zone boundary location could lead to significantly different retention characteristics in the two halves of the crystal. In the crystals analysed here, this issue was addressed by constructing multiple profiles when asymmetry was seen, and all profiles are included in Figure 60. The scatter of age bias values should therefore be representative of  $\alpha$ -recoil from most crystals. From the SIMS analysis, the change of concentration across model zone boundaries is representative of the variation observed in the population. This is corroborated by the age biases calculated from FCT 4, which fall within the range of the model profiles (Figure 60 and Figure 61).

### 5.8.3 Discussion

The model profiles from which the age biases were calculated do not represent the proportion of each zonation style seen within the larger population. However, as the crystals in Figure 46 were selected to represent the full range of styles and CL intensity variations within the FCT, the potential impact of the U and Th zonation on the FCT zircon (U-Th)/He data can be investigated. If the crystals chosen for (U-Th)/He analysis are selected on an entirely random basis; then the age bias found within the total population should reflect each zonation style in proportion to its occurrence. The zonation population then allows the prediction of the weighted age bias distribution that should be expected across the entire population. The age bias distribution of Type 1 and Type 2 zonation was extrapolated from the model values. These were used to define the mean and standard deviation of the normal age-bias distributions (Type 1 and Type 2 as separate populations), which would be expected if the model values are representative of a randomly selected crystal population. The predicted age biases are shown in Figure 63A, for 100 crystals of each of the modelled size aliquots (300 in total), and the frequency distribution of the results shown in Figure 63B.

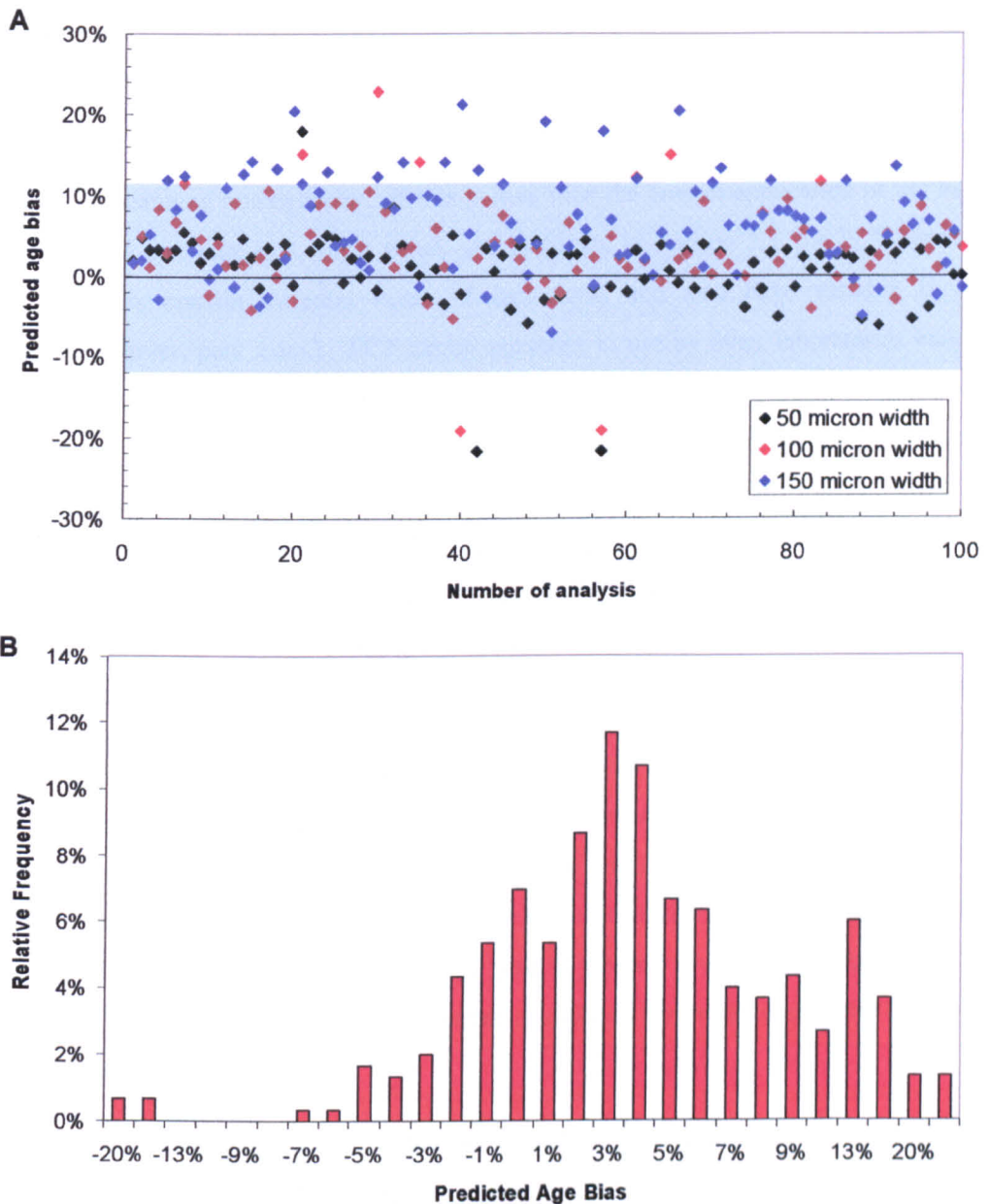


**Figure 63 - The predicted distribution of the age bias in the FCT zircon population.**

**A)** Age biases calculated using the relative abundance of each of the zonation styles outlined in Section 5.4.5, and assuming the random selection of all crystals. The age bias distribution for complex oscillatory zonation at each crystal size is assumed to be a normal distribution as described by the mean and standard deviation of the data in Figure 62. The shaded region represents the age variation in the combined data set (11.5 %,  $2\sigma$ ), assuming that the mean age of the dataset represents a 0 % age bias. **B)** The relative frequency distribution of the data.

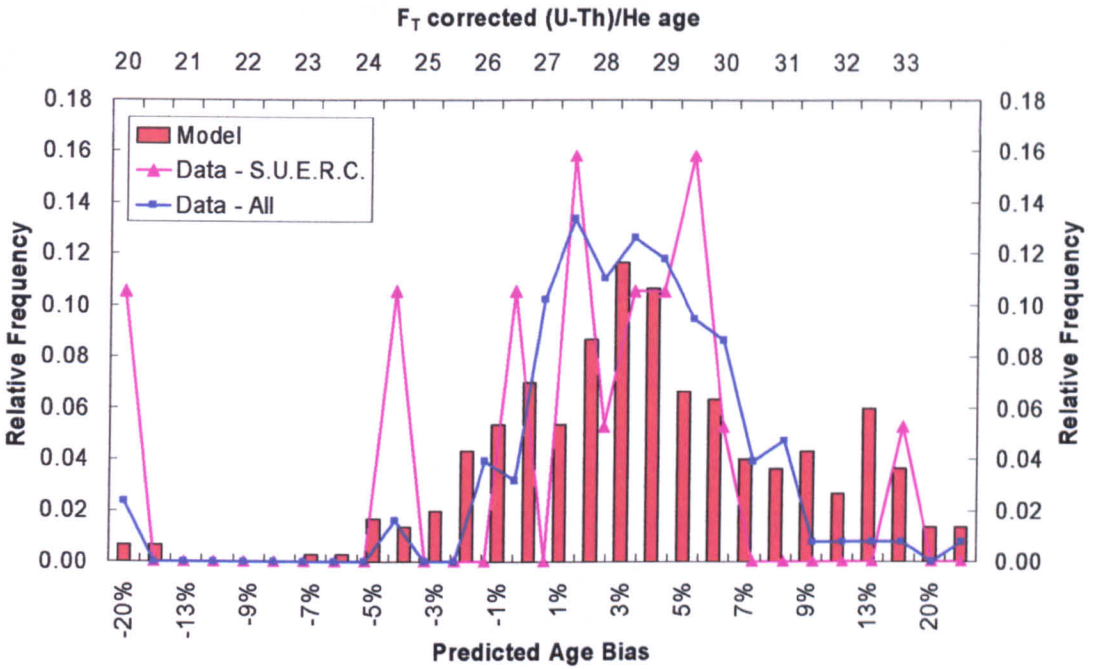
The FCT zircons that have been analysed for (U-Th)/He are known to range from 60  $\mu\text{m}$  to 150  $\mu\text{m}$  in width, but the crystal sizes used by Reiners (2005) and Pik (pers. com) are not accurately known. Reiners (2005) states that crystal widths of 75 - 150  $\mu\text{m}$  are optimal, it is assumed that the majority of the crystals analysed at Yale fall within this size range. Therefore the modelled data (50  $\mu\text{m}$ ,

100  $\mu\text{m}$  and 150  $\mu\text{m}$  crystal widths) are generally representative of the crystal size population that generated the FCT zircon dataset. The modelled age bias and the (U-Th)/He age distribution FCT zircons can therefore be compared.

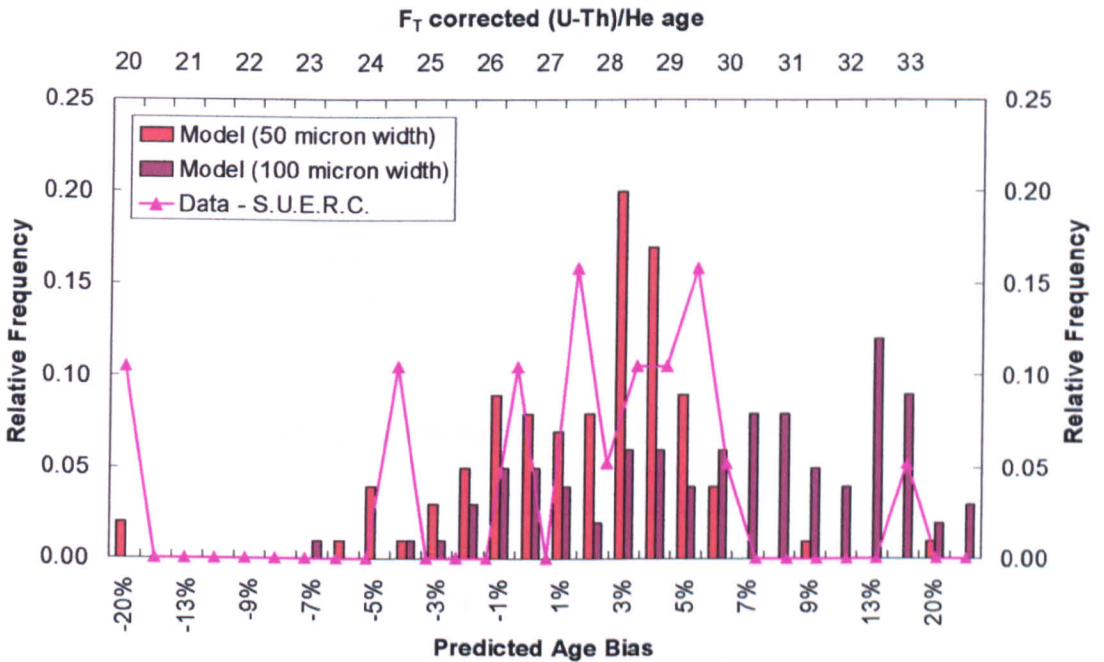
The distribution of (U-Th)/He ages in the FCT zircon dataset should reflect the age bias that was introduced by assuming homogeneity. If this is true, then the correct application of the  $F_Z$  would cause all ages to converge to a single value. As discussed in Section 5.3, the FCT zircons from different aliquots contain different suites of inclusions, and also have variable U and Th distributions [Garver, pers .com.]. FCT zircon separates in use by other laboratories may not be zoned, or may have a different zonation population to that seen in the aliquot used here. If so, then the comparison of the age bias population predicted by this study is only comparable with the  $F_T$  corrected ages presented in Table 4 and Table 5 (pages 46 and 47, Chapter 3). The model results predict a peaked age bias distribution with a mean of  $+ 3.6 \pm 11.0 \%$  ( $2\sigma$ ), and suggest that the  $F_T$  recoil correction will therefore over-estimate the actual age of the FCT zircon sample by  $\sim 3.5 - 4.0 \%$ . Furthermore, the modelling implies that the  $F_T$  corrected data should have a  $2\sigma$  age reproducibility of  $\sim \pm 11 \%$ .

Figure 64 shows the comparison between the predicted age bias distribution (shown in red), and the measured distribution of the ages determined during this study (shown in pink). The measured distribution generally follows that predicted from the modelling. Comparison of the model predictions for 50  $\mu\text{m}$  and 100  $\mu\text{m}$  crystals, shows better correlation with the data from this study (Figure 65), as would be expected given the generally small crystal sizes that were analysed (typically 60 - 80  $\mu\text{m}$  width). The limited number of analyses performed during this study will also prevent any detailed correlation.

The correlation between the model and the *combined* (U-Th)/He dataset (shown blue, Figure 65) is much more apparent. The good correlation suggests that the  $\pm 11 \%$  (U-Th)/He age reproducibility of the FCT zircon is entirely consistent with the zonation observed in this study. It also implies that all FCT zircon aliquots, that have been analysed by (U-Th)/He, contain a significant proportion of zoned crystals, and that these crystals are being selected for (U-Th)/He analysis.



**Figure 64 - The frequency distribution plots of the predicted age bias and all measured (U-Th)/He ages of the FCT zircons.**  
 The plot shows the model outcomes (red bars) in comparison with the S.U.E.R.C. (pink) and combined (blue) (U-Th)/He datasets.



**Figure 65 - The frequency distribution plots of the predicted age bias and the measured (U-Th)/He ages of the FCT zircons measured at S.U.E.R.C.**  
 The plot shows the model outcomes for the 50 µm width and 100 µm crystals separately, as these bracket the crystal size fraction typically used at S.U.E.R.C.

## 5.9 Re-evaluation of the FCT zircon as a (U-Th)/He standard

The qualitative and quantitative analysis performed during this study has allowed the application of the Hourigan *et al.* (2005)  $\alpha$ -recoil model to assess, and quantify, the effects of U and Th zonation on the (U-Th)/He age reproducibility of the FCT zircons. This work confirms the previous suggestions that the poor age reproducibility of the FCT (U-Th)/He ages is reflective of the U and Th zonation [e.g. Reiners, 2005], but has also shown that almost all FCT zircons exhibit strong zonation of U and Th.

This investigation shows that the U and Th zonation in the FCT zircon *should* generate an (U-Th)/He age reproducibility of  $\sim \pm 12\%$ . This is the observed age distribution within the  $F_T$  corrected (U-Th)/He dataset. This correlation is only clear because of the large number of single crystal (U-Th)/He analyses of the FCT zircon that have been performed. Better age reproducibility is not possible without the crystal- and zonation-specific  $\alpha$ -recoil correction. Analysis of multi-crystal aliquots should reduce the impact of the extreme zonation patterns on the age distribution, but the data suggest that the  $F_T$  corrected ages will still have a net positive age bias. The wide variety of zonation patterns observed in the FCT zircons suggests that even if large numbers of crystals are analysed in each aliquot, the FCT zircon will not show a significant improvement in the age reproducibility.

This study also suggests that the (U-Th)/He age population should contain a net  $\sim +3.5\%$  age bias. The mean (U-Th)/He age of the FCT zircon is  $28.3 \pm 3.1$  Ma ( $2\sigma$ , 11.2%,  $n = 127$ ) (see Section 3.6.6), and this work suggests that the correct (U-Th)/He age should therefore be  $27.5 \pm 3.1$  Ma. Both the mean age of the  $F_T$  corrected data set, and the revised (U-Th)/He age are within error of the AFT and ZFT ages.

### 5.9.1.1 The use of standards in zircon (U-Th)/He analysis

The age reproducibility of the FCT reflects the U and Th zonation within the crystal population, and so the established method of using standards to determine age uncertainties on unknown samples must be questioned. The FCT zircons exhibit strong U and Th zonation, and many samples will have a much simpler concentration profiles. Zircons with sector zonation and narrow, subtle oscillatory zonation will have much better age reproducibility than the FCT zircon.

As it is common practice to calculate the (U-Th)/He age uncertainty in unknown samples from the reproducibility of standards [e.g. Reiners, 2005], the use of the FCT zircon as the (U-Th)/He standard limits the temporal resolution that can be achieved in unknowns. A better understanding of the true age uncertainty associated with unknowns would be provided by a zircon standard with

an approximately homogenous U and Th distribution, or one such as the Tardree Rhyolite zircons which have a consistent and extreme zonation that negates the need for the application of the  $\alpha$ -recoil correction.

## 5.10 Implications for the (U-Th)/He analyses of unknowns

At present there is no routine method for the determination of U and Th zonation in the crystals used for (U-Th)/He analysis; as the issues of the spatial resolution, partitioning, and fractionation that are encountered during depth profiling; and the 3-D aspect to the zonation and crystal geometry that cannot be accurately constrained during 2-D surface traverses, prevents the routine application of the laser ablation techniques. The modelled profiles that can be extrapolated from the correlation between CL and U and Th represent a first order approximation of the U and Th concentration profiles within the FCT zircons, and the characterisation of the FCT zircons using CL image analysis allows the qualitative assessment of the U and Th zonation.

By attempting to characterise the population the range of probable age biases can be predicted, and the scatter in the (U-Th)/He ages following the application of the  $F_T$  correction can be assessed. In all (U-Th)/He samples the age reproducibility of the zircons will be dependant on the variety of zonation patterns within the sample. Use of CL images to assess the zonation within a population allows a qualitative assessment of the zonation, but for some samples this can be used to significantly reduce the scatter in the (U-Th)/He age distribution.

When CL images show that zonation patterns are dependant on crystal geometry, or crystal size additional crystal selection criteria can be used to optimise the reproducibility of the (U-Th)/He ages. For example: in samples where the CL imaging show complex and narrow zonation in the crystal rims, the preferential selection of small crystals will reduce the age bias as large proportions of the crystal are effected by  $\alpha$ -loss and the impact of the zonation is minimised (see discussion in Section 4.10.1.2 & Section 5.8.1.2) [e.g. Hourigan *et al.*, 2005; Reiners, 2005]. Where CL imaging reveals strongly enriched or depleted rims, then size selection may allow the effects of inter-crystal variation in rim width or variable relative concentration to be minimised (see discussion in Section 4.10).

There are samples for which representative CL images cannot be obtained because of a low zircon yield; however, consideration of the issues highlighted in this investigation can still help improve the quality of the interpretation. Where samples have good age replication from a single size fraction, it can be assumed that there is minimal variety in the U and Th zonation in the analysed crystals, however the presence of zonation cannot be discounted and a net age bias may still be

introduced by the  $\alpha$ -recoil correction. Therefore where zonation cannot be assessed, other geological constraints will be required to establish the validity of the (U-Th)/He ages.

This study has highlighted the importance of characterising the U and Th distribution in zircons prior to applying the  $\alpha$ -recoil correction, and interpreting the (U-Th)/He ages. At present there is little routine characterisation of the U and Th distribution within unknown zircons selected for (U-Th)/He analysis. This study has shown that without qualitative, and where possible quantitative investigation of all zircons analysed for (U-Th)/He, the scatter observed in  $F_T$  corrected (U-Th)/He ages will remain. Without the characterisation of the zonation, the age bias introduced by applying the geometry specific  $F_T$  cannot be assessed, and the correct  $\alpha$ -recoil correction cannot be estimated. Interpretation of (U-Th)/He ages may therefore be compromised, as net age bias may be overlooked, and many datasets will continue to be discarded because of poor sample reproducibility.

Characterisation of CL zonation and the use of the zonation population statistics, together with estimation or calculation of the associated magnitude and distribution of age bias within a population can allow the improved understanding of zircon (U-Th)/He ages. The study presented over the previous Chapters has established a routine methodology for the determination, and qualitative and quantitative assessment zircon (U-Th)/He ages. This work now allows the application of the zircon (U-Th)/He thermochronometer, and the accurate interpretation of the (U-Th)/He ages of unknown samples.

# 6

## The post-magmatic evolution of the Hebridean Igneous Province: a multi-chronometer study

### 6.1 Introduction

The North Atlantic Igneous Province (NAIP) (Figure 66) preserves a record of the complex interactions between tectonics, magmatism, uplift and denudation across a range of temporal and spatial scales. The Hebridean Igneous Province (HIP) is one of the earliest magmatic sub-provinces of the NAIP, and lies along the west coast of Scotland, covering large areas of the Inner Hebridean islands, and extending onto the mainland at Ardnamurchan and Morvern (Figure 67). The magmatic development of the HIP is generally well constrained, but despite extensive study, the post-magmatic evolution is unclear, and the timing, rate and volume of material removed from the Palaeogene volcanic sequences is poorly constrained. The application of multiple low temperature thermochronometers, and the associated forward and inverse modelling techniques, can reveal detailed information about the thermal histories of shallow crustal rocks, and has the potential to constrain the post-magmatic evolution of volcanic provinces.

Here, we re-evaluate the low temperature, post-magmatic cooling of the Hebridean region through the combination of recently reported  $^{40}\text{Ar}/^{39}\text{Ar}$  and U-Pb ages, gravity and seismic constraints, and new fission track and (U-Th)/He data from the HIP. This chapter presents a brief summary of the regional context, and the magmatic evolution of the HIP, before discussing the existing constraints on of the post-magmatic evolution. New low temperature thermochronometry is then presented, and the local and regional implications of the results are discussed.

### 6.2 Regional setting & the magmatic evolution

The distribution of the earliest phase of magmatic activity in the Palaeogene NAIP was controlled by the sub-lithospheric transfer of the anomalously hot mantle material that followed the impingement of the proto-Iceland plume beneath eastern central Greenland at approximately 62 Ma (Figure 66). This material was channelled away from the plume axis by local heterogeneities in the continental lithosphere [Hill, 1991; Thompson & Gibson, 1991; Hill *et al.*, 1993; Saunders *et al.*,

1997], and generated large volumes of mafic melts as it underwent decompression melting beneath the existing Mesozoic-Tertiary basins. The Hebridean Igneous Province (HIP) is one example of this early magmatic activity.

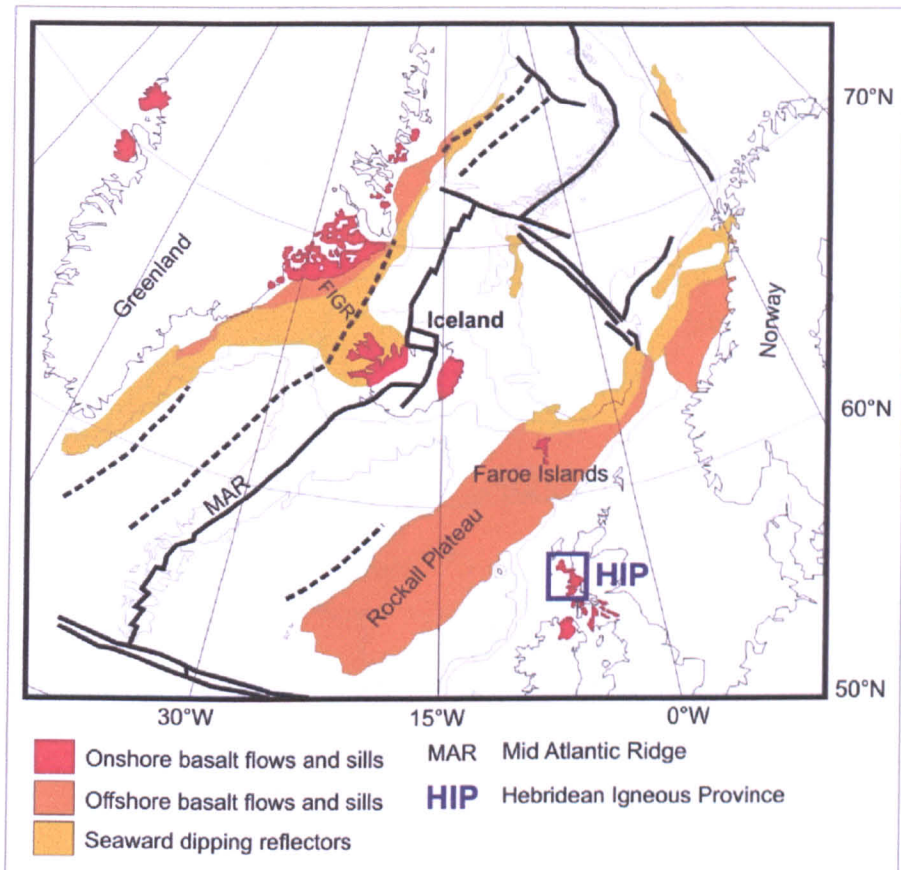


**Figure 66 - A geological map of the North Atlantic Igneous Province (NAIP), showing the location of the HIP [modified from Lawver & Müller, 1994; Saunders *et al.*, 1997]**

In the HIP the high temperature basaltic melts were erupted during three fissure-fed flood-basalt events that formed the Eigg, Mull, and Skye Lava Fields (hereafter the ELF, MLF and SLF) (Figure 67). The accumulation of the lava fields of the HIP was very rapid (< 1.5 Myr) however, volcanism in all three regions was interspersed with several hiatuses and periods of sedimentary deposition. The high-volume fissure eruptions were superseded by the development of central volcanoes, and the emplacement of the associated sub-volcanic plutonic complexes [Emeleus & Bell, 2005]. Ascending melts were trapped beneath the flood-basalt lava sequences, and large plutonic bodies were emplaced at shallow depths. Current estimates suggest emplacement was shallow, with crystallisation at depths of 1 - 3 km [Holness, 1999; Bell & Williamson, 2002]. A simplified geological map of the HIP is shown in Figure 67. More detailed maps of the individual complexes can be found in Appendix F.

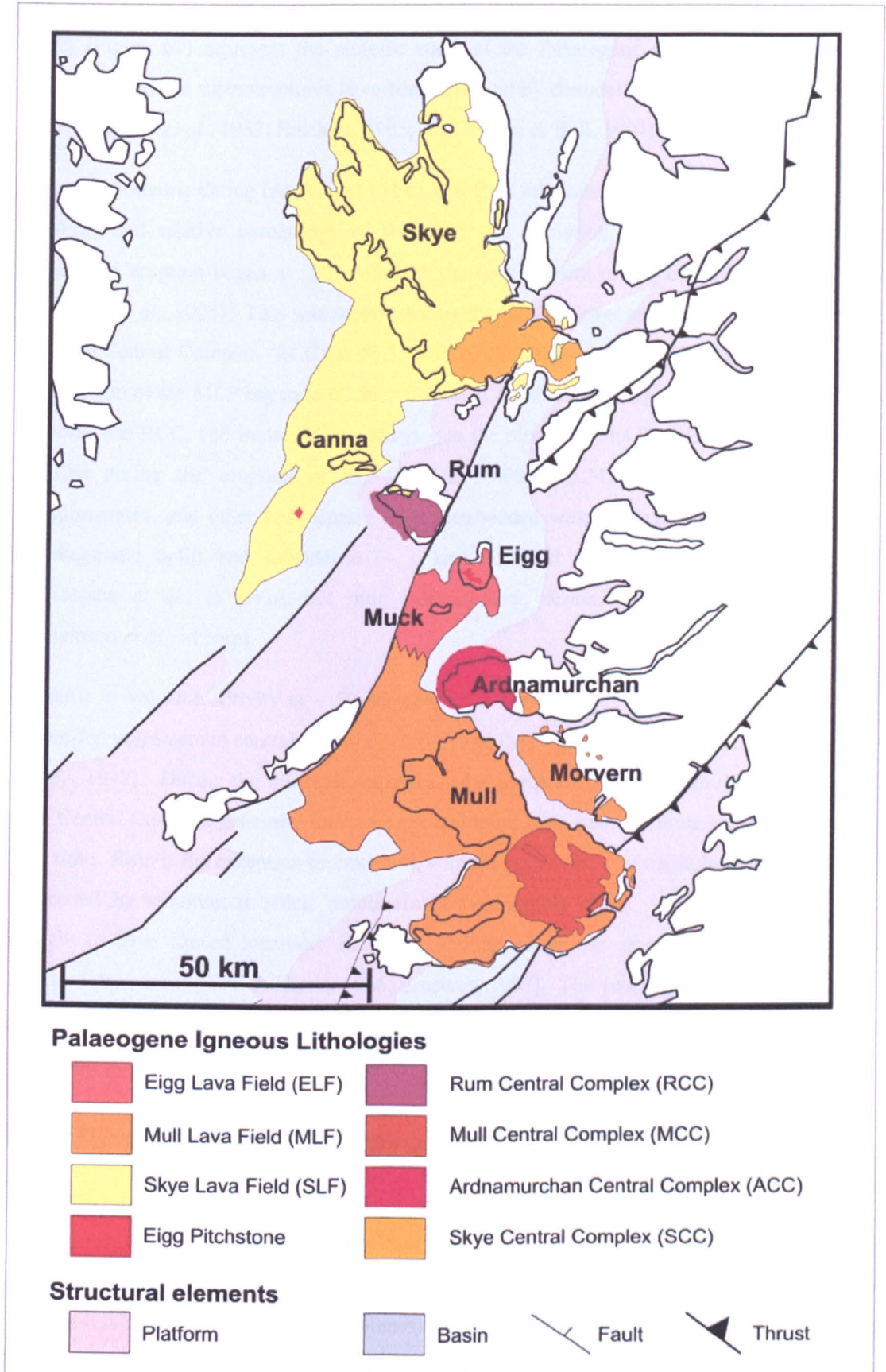


**Figure 67 - The geology of the Hebridean Igneous Province.**  
 More detailed geological maps of each of the Central Complexes can be found in Appendix F.

The Rum, Skye, Mull, & Ardnamurchan Central Complexes (hereafter the RCC, SCC, MCC and ACC) (Figure 67) represent the plutonic roots of the Palaeogene volcanoes, and much of the overlying volcanic superstructures have been removed by denudation [Judd, 1874, 1889; Emeleus, 1973; Meighan *et al.*, 1982; Emeleus, 1985; Williamson & Bell, 1994].

Recent radiometric dating (Ar-Ar and U-Pb), and field relationships provide tight constraint on the absolute, and relative chronology of the magmatic evolution (Figure 68, and Appendix D). Fissure-fed eruption began at ~ 61 Ma with the development of the ELF [Pearson *et al.*, 1996; Chambers *et al.*, 2005]. This was superseded by the shallow level emplacement (< 2 km depth) of the Rum Central Complex (RCC) at  $60.53 \pm 0.05$  Ma [Hamilton *et al.*, 1998], while to the south, the eruption of the MLF began at  $60.56 \pm 0.3$  Ma [Chambers & Pringle, 2001]. Rapid denudation unroofed the RCC, and incised deep valleys into the plutonic units [Emeleus, 1997]. These were in-filled during the eruption of the SLF, at  $59.98 \pm 0.24$  Ma [Chambers *et al.*, 2005]. Conglomerates, and other sedimentary units interbedded with the lava fields suggest significant syn-magmatic uplift and subsidence (~ 1 km) occurred during accumulation [Jolley, 1997; Williamson *et al.*, in prep], but little syn-magmatic denudation is recorded [Jolley, 1997; Williamson *et al.*, in prep].

A hiatus in volcanic activity at ~ 59 Ma marked a regional shift in the magmatic regime from fissure-fed volcanism to central volcanic activity, and the emplacement of the ACC, MCC and SCC [Jolley, 1997]. During the intrusive sequences, the composition of the individual plutons within each Central Complex generally follows a gradual trend from mafic to more evolved compositions with time. Rum is the exception to this trend, with the major phase of mafic intrusion preceded and succeeded by voluminous silicic emplacement [Williamson *et al.*, in prep]. Emplacement is thought to have caused localised uplift and doming above the ascending melts, driving rapid localised denudation [Bell & Harris, 1986; Emeleus, 1997]. The youngest intrusion in the HIP is a pitchstone dyke ( $55.89 \pm 0.18$  Ma [Hamilton, unpublished data]) which cuts the youngest pluton within the SCC (Beinn na Caillich, ~ 55.9 Ma) (Figure 68).

### 6.3 The post-magmatic evolution of the HIP

The temporal constraints on the short-lived volcanism is more detailed and complete than that of the subsequent ~ 55 Myr. Denudation has unroofed the Central Complexes, and removed the majority of the extrusive units from the overlying volcanic structures. From the remaining outcrops it is difficult to constrain the volume of material that has been removed, or the timing, and rate of its removal. Sea-cliffs of 350 - 500 m are found along the west coast of Mull, and there is ~

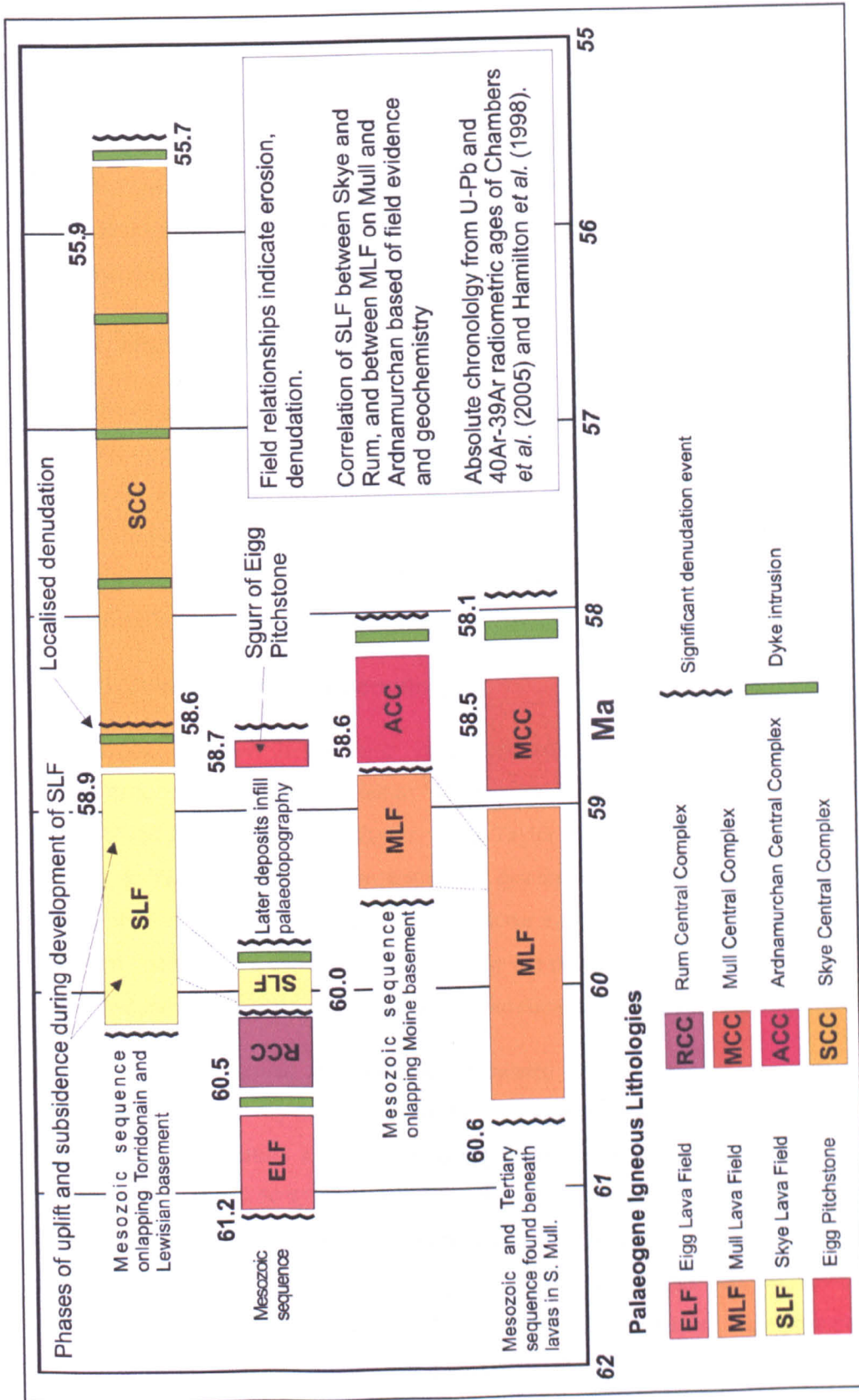


Figure 68 - The magmatic evolution of the HIP. Correlation of the MLF (Mull and Ardnamurchan) and SLF (Skye and Rum) between outcrops from correlation (indicated by dashed lines) of inter-lava sedimentary sequences. Erosion and denudation indicated by unconformable field relationships. All sedimentary units beneath the lava fields are unconformably overlain by the lavas.

30 km separation between outcrops of the Sgurr of Eigg Pitchstone Formation (Figure 67). This suggests that significant localised denudation has occurred.

It is generally believed that ~ 1 - 2 km of basaltic lavas existed above much of the current landscape [George, 1966; Walker, 1971; Emeleus, 1997; Troll *et al.*, 2000; Bell & Williamson, 2002]. These estimates are largely based on the correlation of hydrothermal mineral assemblages in the MLF, with those observed elsewhere in the NAIP. These mineral assemblages will be controlled by the local hydrothermal system, and the accuracy of this estimate is dependant on understanding the temperature and pressure conditions at the time of deposition.

### 6.3.1 The existing hypothesis

The post-magmatic evolution of the HIP is generally thought to be one of initially rapid syn- and immediately-post-magmatic denudation, followed by minimal modification. The early phase of denudation is thought to have removed the majority of the overburden, (~ 2 km), and unroofed the Central Complexes to the currently preserved level [see Bell & Williamson, 2002 and refs therein]. This hypothesis has been developed from field evidence, which suggests that the emplacement of the shallow-level intrusions triggered a dynamic response in the surrounding landscape.

#### 6.3.1.1 Evidence for rapid cooling

The emplacement of the plutonic complexes was accompanied by widespread intensive hydrothermal activity, which has led to  $^{18}\text{O}$  depletion in basalts up to ~ 8 km from the margins of the SCC and MCC [Forester & Taylor, 1976; Taylor & Forster, 1977; Valley & Graham, 1996; Monani & Valley, 2001]. The hydrothermal system attained temperatures of ~ 500°C (at the current level of exposure), and is thought to have extended to the unconformable contact with basement gneisses, at a depth of ~ 3 km (below the present surface) [Monani, 1999]. The rapid convective transfer of heat away from the plutonic complexes would lead to very rapid cooling.

The extent of the thermal anomaly that surrounded the SCC has also been constrained from biomarker carbon maturity indicators, found in the Jurassic sequence directly beneath the lava pile. These maturity indicators suggest that samples more than ~ 12 km from the complex have remained cooler than ~ 50°C since deposition [Thrasher, 1992]. For these biomarkers to record the thermal maxima requires an equilibration time of ~ 1 Myr, and it may therefore be possible that short-duration low temperature events may not be recorded. This data implies the maximum thickness of the northern SLF was little more than the approximately 1.2 km preserved sequence. The data from the maturity indicators is consistent with the extent of the hydrothermal alteration [Monani & Valley, 2001], and complements published apatite fission track analyses [Lewis *et al.*,

1992]. The AFT data from the Jurassic country rocks suggest the radial thermal overprint of the plutonic complex extends to ~ 10 km (this study is discussed in detail in Section 6.3.2.1).

### 6.3.1.2 Evidence for the timing, volume, and rate of denudation

Evidence of substantial doming above the ascending melts is preserved in some areas of the HIP [Bell & Harris, 1986; Emeleus, 1997], and correlation of Torridonian units across the major ring fault surrounding the RCC suggests the early phase of faulting accommodated movements of up to ~ 1 km during the early stages of emplacement [Smith, 1985]. Rapid removal of the 12 km diameter uplifted interior block is to be expected. Elsewhere, debris flow deposits [Brown & Bell, 2006], deeply incised valley systems [Emeleus, 1997], and sedimentary units interbedded with the lava fields preserve a record of a rapid dynamic response to the early magmatic activity [Emeleus, 1997]. However, although syn-magmatic denudation has been proposed to continue on both Skye and Mull, driven by the later intrusions, the complete removal of the younger volcanic material prevents accurate estimation of the volume, timing and rate of this process.

The estimates that ~ 2 km of volcanic material once existed above the current surface of Mull and Skye cannot be corroborated using mass balance techniques, as there has been remobilisation of the Palaeogene-derived sediments. The majority of the HIP-derived volcanoclastic material is now located in the Faroe-Shetland basin [White & Lovell, 1997; Jones *et al.*, 2002], where it is indistinguishable from the volumetrically-dominant volcanoclastic material sourced elsewhere in the NAIP. Although the remobilisation of the sediments prevents former thicknesses being constrained, the pulses of sedimentation recorded in the Palaeogene muds and sands within the North Sea, Faroe-Shetland and Porcupine basins, has been correlated with the major pulses of magmatism in the region [White & Lovell, 1997]. It has been suggested that episodic magmatic underplating and associated uplift, triggered the pulsed denudation and sedimentation events that occurred between 61.5 Ma and 58.5 Ma. The maximum sediment input to the offshore basins occurred at 59 Ma, synchronous to the acme of HIP magmatism. The two major fan sequences that developed in this period, (the Maureen and Andrew formations) represent ~ 70 % of Palaeogene marine deposition on the UK margin [White & Lovell, 1997]. A drop in the sediment supply to these fans after ~ 58 Ma suggests that the main phase(s) of denudation had occurred before this time.

Seismic and gravity studies across the UK margin have led to the development of regional scale underplating models [Al-Kindi *et al.*, 2003; Arrowsmith *et al.*, 2005], and these have been used to predict the regional denudation [Tiley *et al.*, 2004]. AFT studies from offshore wells [Clift & Turner, 1995], are generally inconsistent with the seismic models, and suggest that thicker magmatic underplating (~ 3.0 - 4.0 km) is needed to produce the reduced thermal subsidence

observed in the Rockall Trough, the West Harris Basin and the Hebridean Shelf. Recent AFT analyses from Irish Sea are also inconsistent with the seismic model [Holford *et al.*, 2005], and suggest that denudation in this region was not related to the Palaeogene underplating predicted by Al-Kindi *et al.* (2003).

Estimates of the thickness of the “underplated” material remaining at depth in the vicinity of the Central Complexes range from 4 - 8 km [Clift & Turner, 1995]. The flood-basalts of the HIP represent the residual liquids mantle melts that underwent ~ 70 % fractional crystallisation at the base of the lithosphere (~ 30 km depth) [Thompson, 1974], thereby corroborating the existence of underplating beneath the HIP, and suggesting volumes approximately three times that of the extrusive sequence.

Recent thermochronometry shows a distinct trend in the regional denudation, with 0.7 - 1.0 km section removed at Ballachulish in the Scottish Highlands, and ~ 1.8 - 3.0 km removed at Clisham in the Outer Hebrides [Persano *et al.*, submitted]. The AFT and AHe data suggest that a cooling event occurred between 61 - 47 Ma (Ballachulish) and 66 - 50 Ma (Clisham), and that this cooling event lasted between ~ 1 - 10 Myr [Persano *et al.*, submitted]. The crustal section removed at both Ballachulish and Clisham is equivalent to ~ between 30 - 40°C, and the increased crustal section removed at Clisham is a consequence of the lower palaeogeothermal gradients predicted in the Outer Hebrides (12 - 20°C/km) [Persano *et al.*, submitted]. The temporal resolution of this event is insufficient to distinguish the timing relative to the magmatic activity in the HIP. However the study provides a quantitative constraint on the timing of onshore denudation, and provides a framework for the interpretation of the thermochronological investigation presented here.

### 6.3.2 Questioning the existing hypothesis

Although there is evidence for rapid syn-magmatic denudation during the early emplacement of the Central Complexes, there are indications that the existing hypothesis may be overly simplistic.

#### 6.3.2.1 Existing low temperature thermochronology in the HIP

Within the plutonic units of the HIP there is a suggestion of prolonged heat flow which is difficult to interpret. Lewis *et al.*, (1992) present ZFT ages from the plutonic units of the Skye Central Complex, and AFT data from the surrounding country rocks (Figure 69) that suggest a complex thermal history. The AFT data shows the thermal overprint of the Palaeogene intrusion, with Jurassic and Torridonian samples yielding AFT ages ~ 50 Ma (Table 14) [Lewis *et al.*, 1992]. These are within error of ZFT ages obtained from the plutonic units (Table 15) [Lewis *et al.*, 1992], suggesting rapid cooling from ~ 250°C to ~ 80°C. The AFT data shows the spatial extent of the thermal overprint, and a trend of increasing age with increasing distance from the SCC. The track

lengths in the reset AFT samples are inconsistent with a rapid thermal re-heating event, and are significantly shorter than the  $\sim 14.5 \mu\text{m}$  that would be expected where rapid cooling occurred (Table 14).

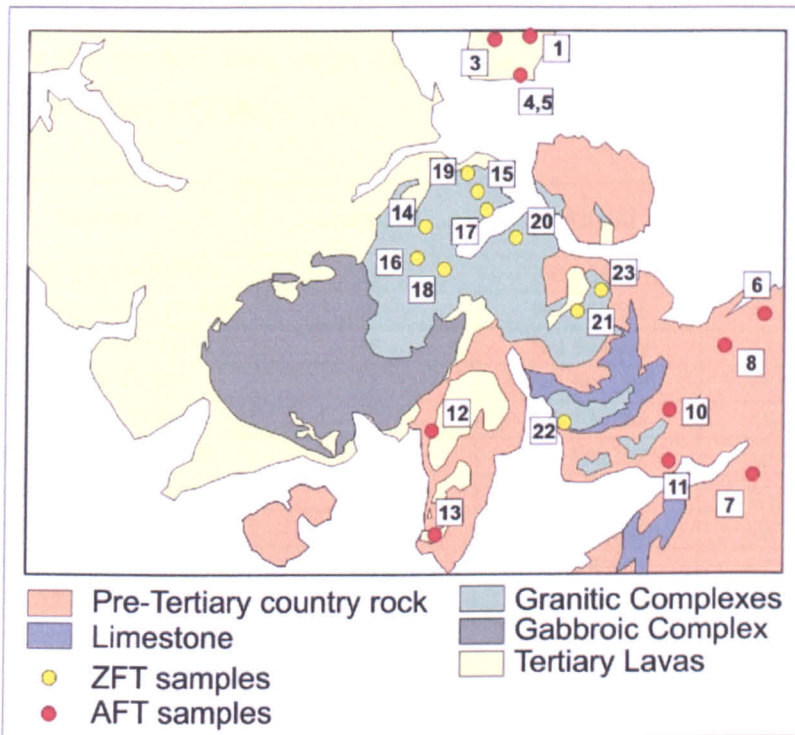


Figure 69 - The localities of published AFT and ZFT analyses from Skye

Grid references for all localities are given in Table 14 and Table 15 [from Lewis *et al.*, 1992]. Sample #2 is off the map north of sample #3, sample #9 is off the map to the east of sample #7.

Sample	Locality #	Grid Ref	Central Age (Ma)	Length ( $\mu\text{m}$ ) $\pm 1\sigma$	Number of tracks
Beinn na Leac	1	NG 593375	$52.60 \pm 6.00$	$14.12 \pm 0.23$	31
Rubha na Leac	2	NG 599382	$47.01 \pm 3.22$	$12.03 \pm 1.39$	5
Fearns Rd	3	NG 570361	$53.30 \pm 3.90$	$13.46 \pm 0.31$	13
Eyre	4	NG 575342	$68.80 \pm 6.20^*$	$12.94 \pm 0.32$	65
Eyre	5	NG 574341	$47.87 \pm 2.88$	$12.61 \pm 0.61$	25
Ob Lusa	6	NG 702248	$53.49 \pm 4.35$	$12.30 \pm 0.64$	13
Skulamus	7	NG 671122	$47.20 \pm 3.70$	$13.50 \pm 0.30$	29
Drumfearn	8	NG 672160	$49.70 \pm 3.80$	$13.18 \pm 0.23$	68
Loch na Dal	9	NG 700150	$72.80 \pm 6.60^*$	$13.05 \pm 0.63$	8
Loch Buidhe	10	NG 639196	$53.85 \pm 3.75$	$10.58 \pm 0.99$	13
Beinn nan Charn	11	NG 639178	$47.10 \pm 3.30$	$14.21 \pm 0.65$	9
Cammasunary	12	NG 516188	$52.37 \pm 3.91$	$13.15 \pm 0.35$	30
Strathaird	13	NG 528133	$56.93 \pm 5.31$	$13.49 \pm 0.66$	3

Table 14 - Published apatite fission track data from Skye

The majority of these AFT ages have been completely reset by the intrusion of the SCC. Only those marked \* contain a suggestion of a pre-Palaeogene cooling. Locality numbers refer to those shown in Figure 69 [from Lewis *et al.*, 1992].

The apparent inconsistency of reproducing AFT and ZFT ages (suggesting rapid cooling), and short AFT track lengths (suggesting prolonged cooling) is highlighted by the authors, but the origin of the anomalously short track lengths is not fully addressed. It is suggested that they represent temperatures that “remained elevated during cooling” [Lewis *et al.*, 1992, page 183]. Lewis *et al.* (1992) suggest that the AFT track length distributions are consistent with a monotonic cooling history from 110°C since ~ 52 Ma.

Sample	Locality #	Grid Ref.	Central Age (Ma) ± 1σ
Glaomaig granite (WRH)	14	NG 538300	51.90 ± 2.70
Maol na Gainmhich (WRH)	15	NG 561316	48.40 ± 2.50
Beinn Dearh Mhor (WRH)	16	NG 534298	51.00 ± 3.40
Loch Ainort (WRH)	17	NG 565298	45.80 ± 4.30
Loch Ainort (WRH)	18	NG 534288	45.90 ± 3.50
Northern Felsite (WRH)	19	NG 562307	49.60 ± 3.00
Glas Bheinn Mhor (ERH)	20	NG 585281	53.10 ± 3.70
Allt Feama (ERH)	21	NG 614234	49.70 ± 2.20
Beinn an Dubhaich (ERH)	22	NG 606198	47.50 ± 2.60
Beinn na Caillich (ERH)	23	NG 610232	53.60 ± 3.60

**Table 15 - Published zircon fission track ages from the Skye Central Complex**  
Locality numbers refer to those shown in Figure 69 [from Lewis *et al.*, 1992].

The ZFT ages reported by Lewis *et al.* (1992) suggest additional complexity in the cooling history, and range from 53.10 ± 3.70 Ma to 45.80 ± 4.30 Ma (Table 15). They show no trend with the crystallisation age of the plutons, and the ages are significantly younger than zircon U-Pb and Ar-Ar ages [Hamilton *et al.*, 1998; Chambers *et al.*, 2005] (Appendix D). The ZFT data are difficult to reconcile with a rapid convective cooling, accompanied by synchronous denudation, and Lewis *et al.* (1992) suggest that the heat required to maintain, or re-elevate the temperatures in these near surface plutonic units is supplied by hydrothermal transport from depth, as proposed by Taylor & Forrester (1971). Prolonged cooling associated with complex intrusions at depth is common, but in such a shallow magmatic system it is difficult to envisage how heat flow of sufficient magnitude can be achieved without almost continuous intrusion from 60 - 45 Ma, or a major magmatic event at ~ 45 Ma, for which there is no supporting field evidence.

### 6.3.2.2 Late stage magmatic activity in the North Atlantic

Recent high precision U-Pb and <sup>39</sup>Ar/<sup>40</sup>Ar age determinations [Hamilton *et al.*, 1998; Chambers *et al.*, 2005] have significantly reduced the duration of the early North Atlantic magmatism from that suggested by earlier studies [Mitchell & Reen, 1973; Dagley *et al.*, 1985; Dagley & Mussett, 1986; Dagley *et al.*, 1987; Ritchie & Hitchen, 1996]. The rapid magmatic evolution of the HIP occurred from 62 to 55 Ma [Hamilton *et al.*, 1998; Chambers *et al.*, 2005]. Younger crystallisation ages have been obtained from small volume dykes in Ireland (45 - 50 Ma) [Kirstein & Timmermann,

2000] and the Outer Hebrides ( $45.16 \pm 0.02$  Ma) [Timmermann, pers.com., unpublished data], and these are coeval with pulses of extrusive activity on seamounts in the Rockall Trough [O'Connor *et al.*, 2000] (Table 26; Appendix E). This late stage magmatic activity occurred ~ 8 - 10 Myr after the onset of rifting at ~ 55 Ma, and the cessation of voluminous shallow-level intrusion in the HIP.

### 6.3.3 Testing the hypothesis

The temperature a rock experiences at a given depth is dependant on the geothermal gradient. In the HIP, magmatic activity will have led to transient high geothermal gradients in the surrounding country rocks. This elevated geothermal gradient would decay rapidly as the plutonic complexes cooled. The application of the low temperature thermochronometers to a system undergoing conductive, convective and denudation driven cooling will produce cooling ages that may be controlled by one, or all of these processes. If the existing hypothesis is correct, and denudation was essentially instantaneous, the ages determined from all the low temperature thermochronometers should be indistinguishable from the high-temperature radiometric ages (U-Pb, Ar-Ar). Therefore the AFT ages reported by Lewis *et al.* (1992) do not support the existing model.

If denudation was more protracted, or occurred after the initial phase of magmatic cooling, the low temperature thermochronometry may be able to resolve separate events, and to distinguish between the thermal relaxation following emplacement, and the denudation driven cooling. Before accurate interpretation of the low temperature thermochronology can be achieved, the evolution of the geothermal gradient with time must be understood. With an understanding of the thermal evolution of the crust, the combined application of the fission track and (U-Th)/He thermochronometers to apatite and zircon has the ability to resolve the timing of the final stages of cooling in the HIP, and to differentiate between the geological processes driving that cooling.

Palaeogeothermal reconstructions deduced from AFT analysis and vitrinite reflectance from localities across the Hebridean region and the UK margin suggest that the overall geothermal gradient in the early Palaeogene was ~ 40°C/km [Green *et al.*, 1999], although there would have been substantial local variation. Immediately preceding intrusion the fissure-fed volcanism may have led to localised short lived geothermal gradients that were higher still. For the following consideration the pre- and post-intrusion geothermal gradient is assumed to be 40°C/km. Accurate modelling of the complex systems in the HIP cannot be achieved, as the former thickness of the denuded section is unknown. Furthermore, modelling of the convective hydrothermal system is impossible without constraints on the length of time it operated, the system geometry, the circulating water volume, the permeability and porosity of all country rocks; data that is absent across the HIP.

Despite the difficulty of accurately modelling the cooling systems in the HIP, some understanding of the cooling of the plutonic units can be achieved by the consideration of "end member" slow cooling systems. Modelling thermal re-equilibration after intrusion in the absence of hydrothermal activity, or denudation, will yield highly conservative Palaeogene cooling rates. This provides an indication of the slowest isothermal relaxation for a given intrusion scenario. The RCC has a simple and relatively well constrained intrusion, and denudation history, which allows the testing of the simulation against the geological evidence. The cooling of the RCC can be used to approximate the cooling of the ACC, as although the complexes have different structures and emplacement histories, both are similar in size, complexity and intrusion level. The evolution of the SCC was more complex, with protracted, pulsed intrusion. The SCC has the longest period of magmatic activity across all the complexes in the HIP, and therefore allows the slow cooling scenario to be investigated.

The 3-D thermal evolution of the cooling plutonic system can be modelled by solving the heat transport equation using numerical computation techniques. Modelling was performed using the HEAT-3D software, which uses a finite difference technique to solve the equations for energy and momentum conservation [Wohletz & Heiken, 1992]. The geological significance of the HEAT-3D simulations are controlled by the accuracy of the user-defined physical parameters for the country rocks (density, permeability, porosity, thermal conductivity) and the intruded melts (temperature, composition, chamber recharge, chamber geometry and convection etc.). In the HIP, many of these parameters are not known and appropriate input values must therefore be estimated. The physical parameters of the country rocks were collated from other localities along the UK, and from average values of similar lithologies (see Appendix E). The properties of the melts were supplied by the software (see Appendix E). The model of the RCC is shown in Figure 70, and that for the SCC is shown in Figure 71, in both examples the intrusion geometries were estimated from the dimensions of the field exposure, and the radius and volume at depth are as indicated from the free air gravity anomalies associated with each [Bott & Tuson, 1973; Bott & Tantrigoda, 1987] (see Appendix E for further detail)..

The hydrothermal system was not incorporated into the models, i.e. the simulation was run under "dry" conditions. The HEAT-3D model cannot include denudation-driven cooling. Modelling packages that allow the consideration of denudation have recently been developed (e.g. 4D-Therm [Ehlers *et al.*, 2005]), but the poor constraint on the thermal, physical, and temporal parameters required for such detailed modelling are not known for the HIP. The HEAT-3D simulations may be highly simplistic, but they can be used to determine conservative minimum cooling rates with the minimal assumptions.

The thermal evolution of the upper crust (< 5 km) shows that the decay of the thermal anomaly will be very rapid for all intrusions that are physically separated from their mantle sources at the time of emplacement (i.e. there is no continued melt supply from the mantle). For both models the 200°C isotherm (equivalent to a depth of ~ 5.0 km at 40°C/km) is colour coded as the transition from green to yellow. For the RCC (Figure 70), the 200°C isotherm has re-equilibrated within 2 Myr. For the SCC (Figure 71), the larger volume (See Appendix E) of the intrusion and a more protracted emplacement history means that cooling is slower, but the re-equilibration had occurred ~ 3 Myr after the final major intrusion event.

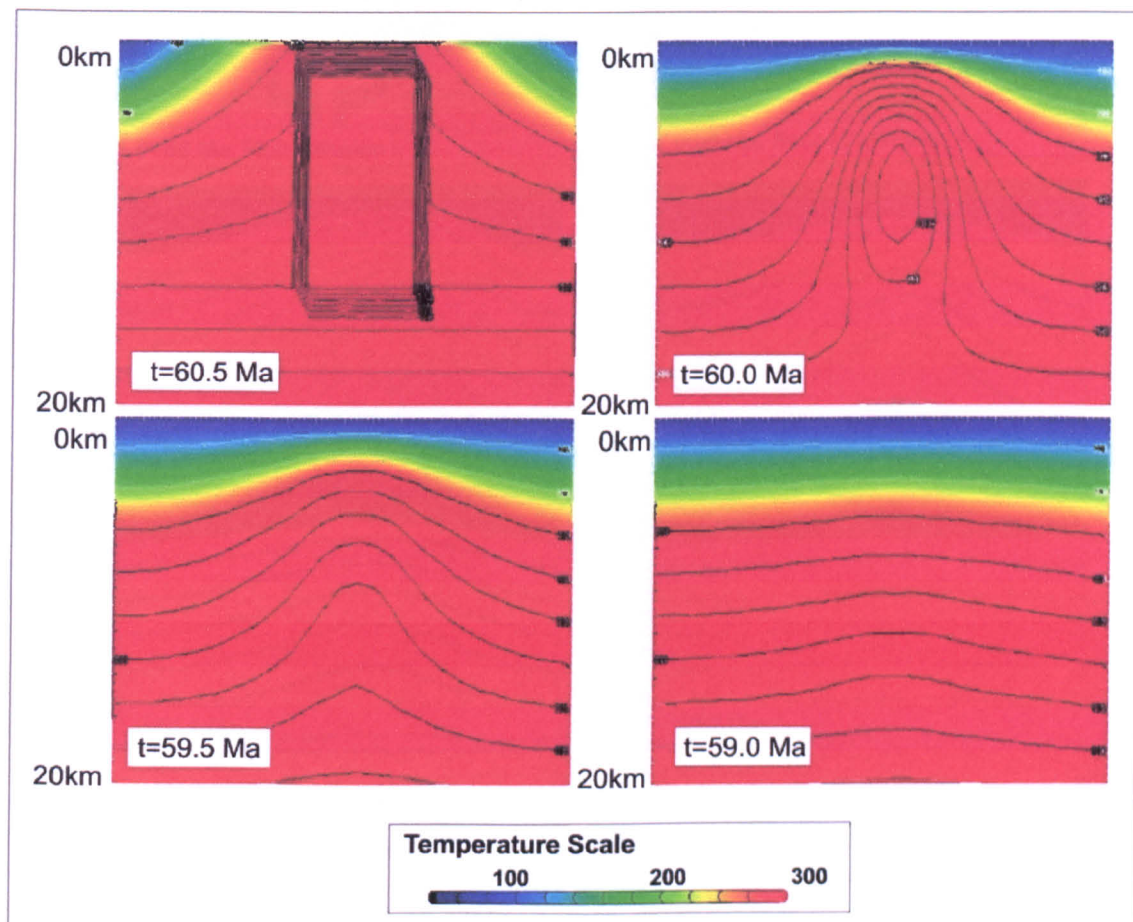


**Figure 70 - The modelled cooling of the Rum Central Complex.**

The cooling is shown as a series of time slices taken through the HEAT 3D simulation. Images are “screen dumps” of model time steps. The 200°C isotherm is represented by the change from green to yellow. Other isotherms are shown as the black lines and these delimit the intrusion in the first panel. Model input parameters are given in Appendix E. Initial intrusion is 12 km diameter. Expanding the mesh to move thermal boundaries further from pluton does not change the cooling rate and increases computation times. Model width is 50 km.

This highly simplistic modelling exercise suggests that pre-emplacement geothermal gradient would have been re-established very rapidly, even when the additional cooling effects of hydrothermal activity and denudation are ignored. This basic understanding of the timescale of the cooling of these shallow level plutonic systems suggests that the complexity in the AFT and ZFT data cannot easily be attributed to the initial phase of magmatic cooling, unless voluminous

magmatic activity continued until  $\sim 47$  Ma. The evidence for temperatures in excess of  $\sim 200^{\circ}\text{C}$ ,  $\sim 8$  Ma after the final emplacement [Lewis *et al.*, 1992] must be explained by another mechanism. The modelling also suggests that the application of low temperature thermochronology to constrain the thermal evolution will not be effected by significant changes in the geothermal gradient.

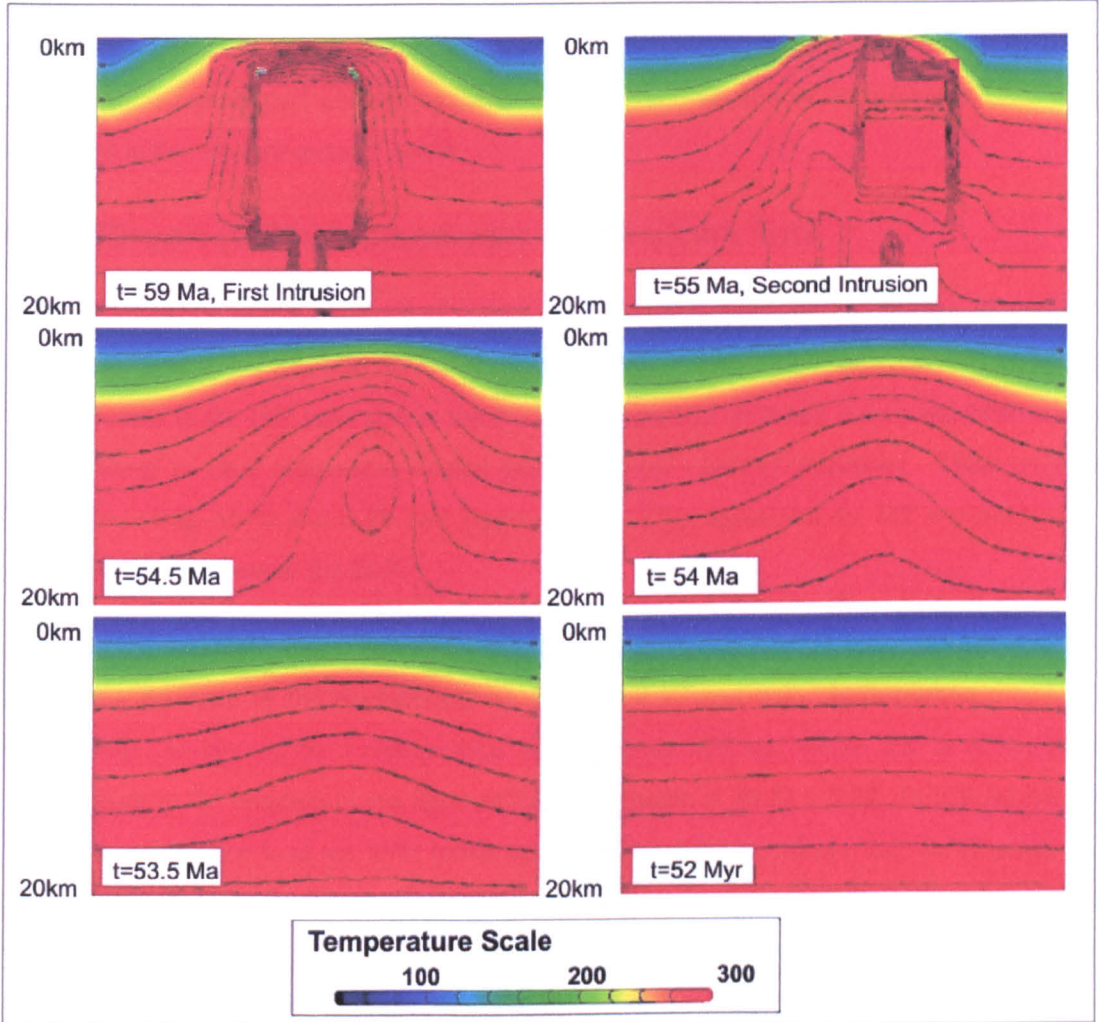


Figure 71 - The modelled cooling of the Skye Central Complex.

The cooling is shown as a series of time slices taken through the HEAT 3D simulation. Images are "screen dumps" of model time steps. The  $200^{\circ}\text{C}$  isotherm is represented by the change from green to yellow. Other isotherms are shown as the black lines and these delimit the intrusion in the first and second panels. Model input parameters are given in Appendix E. Each intrusion is 12 km diameter. Expanding the mesh to move thermal boundaries further from pluton does not change the cooling rate and increases computation times. Model width is 50 km.

## 6.4 A thermochronological investigation of the HIP

Low temperature thermochronology in the HIP has been limited to the Isle of Skye, where the evidence for complexity at the low temperatures cannot be explained by the existing evolutionary hypothesis. Further investigation into the origin of this low temperature complexity is required before accurate geological interpretation can be made. The source of this complexity may have

regional implications for the timing and amount of denudation across the HIP. Additional thermochronological investigation of the SCC and the RCC, ACC, and MCC was undertaken. This investigation used a multi-chronometer approach, and the cooling histories were determined through the application of the zircon (U-Th)/He, apatite fission track, and apatite (U-Th)/He techniques to individual plutons and individual hand specimens. Where possible, samples from plutons with high precision radiometric ages were chosen for investigation to enable complete thermal histories to be established. The sample localities and lithologies are listed in Appendix F. Any additional geological constraints on post-magmatic evolution of each Central Complex are discussed in the relevant sections below.

### 6.4.1 Zircon (U-Th)/He analysis of the Muck Tuff

The Muck Tuff (MT) is a sequence of reddened crystal-lithic tuffaceous sandstones that are found close to the base of the ELF, on the Island of Muck (Figure 67). These “tuffs” are one of the oldest volcanic units in the HIP (and also in the NAIP), and contain abundant zircon and fresh sanidine, making them an ideal radiometric marker horizon for the onset of volcanism. These units have been dated using Ar-Ar and U-Pb (see Appendix D). After deposition the MT was buried by the continued development of the ELF.

Although the maximum thickness of the ELF basaltic sequence is not known, the eruption of the ELF was superseded by the emplacement of the RCC at  $60.53 \pm 0.05$  Ma [Hamilton *et al.*, 1998]. Furthermore, on-lapping field relationships show that the MT was within 200 m of the palaeo-surface prior to the eruption of the Sgurr of Eigg Pitchstone at  $58.72 \pm 0.07$  Ma [Chambers *et al.*, 2005]. The sequence is at sea level today, and there is no field evidence that the eruption of the Sgurr of Eigg Pitchstone was long lived, or that the MT experienced significant or prolonged burial ( $> 500$  m). The MT is a good sample to use as an internal standard for the HIP, as it has an independently constrained thermal history characterised by rapid cooling. This sample was therefore chosen to test the methods for the treatment and interpretation of the zircon (U-Th)/He data discussed in previous chapters.

All zircons in the Muck tuff separate were of high quality, and were generally inclusion free. Analytical procedures followed those outlined in Chapter 3. Analytical uncertainty for all samples is less than  $\pm 3.2$  %, and is generally  $\pm 2.0$  %. The (U-Th)/He data are shown in Table 16, and all U and Th measurements are corrected for the procedural blank. Where analysed crystals have bulk U and Th of 0.3 ng the uncertainty associated with the procedural blank is 5 % of the total U and Th. This uncertainty means that all (U-Th)/He ages determinations with bulk U and Th below 0.3 mg should be treated with caution. Therefore MT1 is not used in the calculation of the average (U-Th)/He age. The values of  $F_T$  are calculated using the geometry specific equations (Section 4.6.4)

however using the tetragonal form of the  $F_T$  calculation yields values that are within 2 % of those shown in Table 16.

The MT highlights the importance of considering and assessing zonation in unknown samples before interpretation of the (U-Th)/He ages. The average recoil corrected (U-Th)/He age of the Muck Tuff is  $68.0 \pm 3.0$  Ma ( $1\sigma$ , 1.5 %), as shown in Table 16. Even at a 2 sigma level this is outwith error of the crystallisation age ( $60.45 \pm 0.03$  Ma [Chambers *et al.*, 2005] and  $62.4 \pm 0.6$  Ma [Pearson *et al.*, 1996; Chambers *et al.*, 2005]).

	$^{238}\text{U}$ (ng)	$^{232}\text{Th}$ (ng)	4He (cc)	% He reheat	Th/U	Anal. Uncert	Raw age (Ma)	$F_T$	Corrected Age (Ma)
MT1 <sup>a</sup>	0.24	0.28	1.82E-09	0.01%	1.19	2.11%	48.9	0.70	69.7
MT2	3.95	4.30	3.20E-08	0.00%	1.09	1.37%	52.8	0.78	67.3
MT3	0.47	0.55	3.96E-09	0.00%	1.16	3.16%	54.1	0.80	67.4
MT4	0.60	0.95	5.80E-09	0.00%	1.57	1.43%	57.3	0.82	69.6
MT5	2.49	4.08	2.17E-08	0.00%	1.64	1.57%	51.5	0.77	67.1
MT6	2.42	3.01	1.99E-08	0.00%	1.24	1.57%	52.0	0.76	68.5
Average							<b><math>53.5 \pm 4.6</math> Ma</b> ( $2\sigma$ , 8.6 %)		<b><math>68.0 \pm 3.0</math> Ma</b> ( $2\sigma$ , 3.2%)

**Table 16 - Zircon (U-Th)/He analyses of the Muck Tuff.**

All data are corrected for U and Th blank. Sample MT1 is not included in the calculated average.  $F_T$  calculated using the geometry specific fitting parameters.

#### 6.4.1.1 Zonation and $\alpha$ -recoil for the Muck Tuff

Figure 72 shows a selection of the pan-chromatic SEM CL images obtained from the Muck Tuff (white scale bars are 50  $\mu\text{m}$ ), showing high CL rims (5 - 20  $\mu\text{m}$  wide), mantling cores with much lower emission intensity. These images suggest significant depletion of U and Th in the rims of the MT zircons. Consequently the use of the homogeneous  $F_T$  to calculate the  $\alpha$ -recoil corrected ages will cause a variable, positive age bias (see Figure 27).

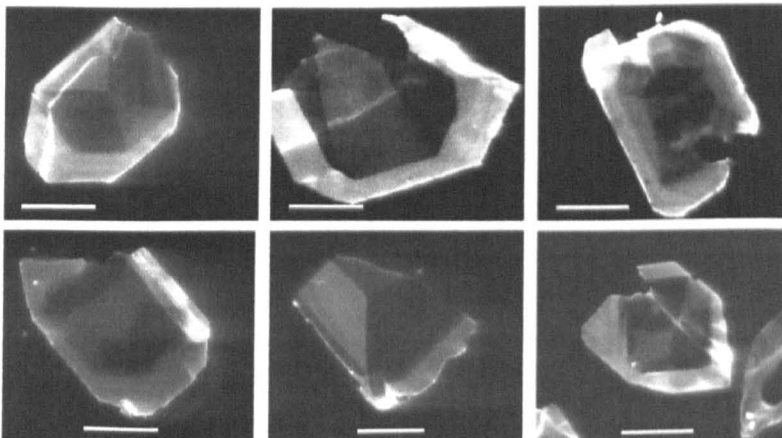


**Figure 72 - Panchromatic SEM CL images of zircons from the Muck Tuff. All white scale bars are 50  $\mu\text{m}$ .**

Selected crystals from the Muck Tuff were used for the inter-sample correlation of the CL-U-Th proxy (Section 5.7), and although SIMS analysis is unlikely to become routine, the analyses of this sample allows a quantitative assessment of the age bias introduced by assuming homogeneity. It also allows the assessment of the suitability of using CL as a proxy for U and Th distribution in other HIP zircons. The SIMS analyses (Table 13, page 128) of the low CL emission cores yield eU concentrations of ~ 650 ppm, while analyses of the high CL emission rims yields much lower concentrations (~ few 10's - few 100's ppm), corroborating and quantifying the U and Th zonation reflected by the zonation in the CL emission intensity. The rims in typical Muck Tuff samples are therefore depleted by a factor of ~ 5 - 10 compared to the cores, and so substantial age bias will be introduced by assuming homogeneity. The CL images also show that the cores of many MT zircons exhibit sector zonation. This effect of this zonation cannot be quantified using the current modelling techniques, but is unlikely to affect bulk fractional loss by more than a few %, substantially less than the effect of the strongly depleted rims.

	MT1	MT2	MT3	MT4	MT5	MT6	Average (2 $\sigma$ )
<b>Raw Age (Ma)</b>	48.9	52.8	54.1	57.3	51.5	52.0	<b>53.5 <math>\pm</math> 4.6 Ma (8.7 %)</b>
$F_T$	0.70	0.78	0.80	0.82	0.77	0.76	
<b><math>F_T</math> corrected age</b>	<b>69.7</b>	<b>67.3</b>	<b>67.4</b>	<b>69.6</b>	<b>67.1</b>	<b>68.5</b>	<b>68.0 <math>\pm</math> 2.1 Ma (3.1 %)</b>
$F_Z^1$	0.84	0.90	0.95	0.93	0.89	0.88	
<b><math>F_Z^1</math> corrected age</b>	<b>58.2</b>	<b>58.9</b>	<b>57.2</b>	<b>61.9</b>	<b>57.8</b>	<b>58.8</b>	<b>58.9 <math>\pm</math> 3.6 Ma (6.2 %)</b>
$F_Z^2$	0.88	0.92	0.96	0.95	0.92	0.92	
<b><math>F_Z^2</math> corrected age</b>	<b>55.6</b>	<b>57.1</b>	<b>56.3</b>	<b>60.5</b>	<b>55.8</b>	<b>56.7</b>	<b>57.3 <math>\pm</math> 3.7 Ma (6.5 %)</b>
$F_Z^3$ (10% age bias)	0.94	0.92	0.94	0.95	0.95	0.88	
<b><math>F_Z^3</math> corrected age</b>	<b>63.3</b>	<b>61.2</b>	<b>61.2</b>	<b>63.3</b>	<b>61.0</b>	<b>62.3</b>	<b>61.8 <math>\pm</math> 1.9 Ma (3.1 %)</b>
$F_Z^4$ (15 % age bias)	0.81	0.90	0.92	0.95	0.88	0.87	
<b><math>F_Z^4</math> corrected age</b>	<b>60.6</b>	<b>58.6</b>	<b>58.6</b>	<b>60.6</b>	<b>58.4</b>	<b>59.5</b>	<b>59.1 <math>\pm</math> 1.8 Ma (3.1%)</b>

Table 17 - The  $F_Z$  correction for the Muck Tuff (U-Th)/He ages.  $F_T$  = homogeneous  $\alpha$ -recoil correction.

$F_Z^1$  = The  $F_Z$  calculated from crystal specific modelling of a 10  $\mu$ m rim with  $\Delta C = 0.5$ .  $F_Z^2$  = The  $F_Z$  calculated from crystal specific modelling of a 10  $\mu$ m rim with  $\Delta C = 0.1$ .  $F_Z^3$  =  $F_Z$  calculated assuming that the  $F_T$  correction introduces a 10 % positive age bias.  $F_Z^4$  =  $F_Z$  calculated assuming that the  $F_T$  correction introduces a 15 % positive age bias. 10 % and 15 % age biases were estimated from Figure 27, through Figure 30.

The MT zircons are rarely tetragonal, and the analysed crystals have  $1.0 < W_1/W_2 < 1.5$ . Each crystal had terminations of differing lengths but in all cases the total termination length was less than 50% of the total crystal length. From the inspection of the CL images of crystals of similar size to those selected for analysis, the average rim width in any crystal is ~ 10  $\mu$ m. Crystal specific modelling of 10  $\mu$ m rims with  $\Delta C = 0.5$  and  $\Delta C = 0.1$  (minimum and maximum variation observed in the SIMS data), using the Hourigan *et al.* (2005) model, allowed zonation specific  $F_Z$  correction factors to be determined. These values are shown in Table 17.

For both concentration changes ( $F_z^1$ :  $\Delta C = 0.5$  and  $F_z^2$ :  $\Delta C = 0.1$ ) the crystal specific  $F_z$  values yield (U-Th)/He ages that are within error of the of the accepted crystallisation age at a 1 sigma error. The assessment of end member patterns allows a more accurate interpretation of the (U-Th)/He ages, even when the exact zonation within the analysed crystal cannot be known. The correct consideration of the zonation causes poorer age reproducibility (~ 6 - 7 %), but this it is still better than is obtained for the FCT.

Table 17 also includes the  $F_z$  values estimated from the modelling presented in Chapter 4. The estimations were based on the data presented in Figure 27 and Figure 28, and estimated the age biases introduced by a 10  $\mu\text{m}$  rim with  $\Delta C = 0.5$  ( $F_z^3$ ) and  $\Delta C = 0.1$  ( $F_z^4$ ), in a tetragonal crystal of ~ 100  $\mu\text{m}$ . This estimation makes the assumptions that the  $F_z$  is unaffected by crystal geometry and that the age bias introduced in a crystal ~ 100  $\mu\text{m}$  width adequately depicts that seen in the measured crystals. The good agreement in the ages calculated using the estimated age bias, and the modelled  $F_z$ , implies that the error introduced by assuming homogeneity is far larger that introduced by the estimation based on the observed variation in CL intensity.

#### 6.4.1.2 Using CL as a proxy for U and Th zonation in HIP zircons

The analysis of the Muck Tuff suggests that the use of CL zonation as a proxy for U and Th zonation in HIP zircons can allow the qualitative and semi-quantitative assessment of the effect of zonation on the (U-Th)/He ages. Without such interpretation the true geological significance of the data cannot accurately be determined. As outlined in Section 5.9.1.1 the ideal zircon (U-Th)/He analytical protocol would obtain CL images prior to crystal selection, allowing the identification, and avoidance, of samples exhibiting significant inter-crystalline variation in the style or intensity of zonation. In the HIP samples, the small numbers of zircons separated from many lithologies meant that the crystals were selected and prepared for analysis before CL imaging had been performed. CL images could then be obtained from the remaining crystal population. In some samples the low zircon yields prevented imaging using CL, and in others the need to use a small sub-population of a certain size or geometry, means that CL imaging of the remaining crystals may not be reflective of the zonation within those analysed.

#### 6.4.2 Zircon (U-Th)/He analysis in the HIP

Samples from all of the central complexes in the HIP were analysed using the zircon (U-Th)/He thermochronometer to constrain the rate and timing of magmatic cooling in each region. The localities of all (where known) are shown in Appendix F. All analyses were performed using the furnace extraction procedure (Chapter 3), and the (U-Th)/He data are presented in Table 18. A range of crystal geometries was observed, but all crystals used for analysis have  $W_1/W_2 < 1.2$  and terminations which make up < 50 % of the total length of the crystal.

Sample	Approx. crystal mass (g)	<sup>238</sup> U (ng)	U error (ng)	<sup>232</sup> Th (ng)	Th error (ng)	Total U-Th % error	4He (cc)	He uncert (%)	U blank (as % of sample)	Th blank (as % of sample)	<sup>238</sup> U % recovery	<sup>232</sup> Th % recovery	Th/U	Raw (Ma)	F <sub>T</sub>	Corrected (Ma)	Analytical Uncertainty	
<b>Skye</b>																		
SC/1	32.8	3.00	0.04	2.80	0.04	1.9%	2.51E-08	1.1%	3.6%	3.6%	100.0%	96.4%	0.94	56.2	0.88	64.0	2.2%	
SC/2	38.6	0.93	0.01	1.04	0.01	2.4%	6.48E-09	1.1%	11.6%	9.6%	100.0%	100.0%	1.12	45.2	0.75	60.0	2.6%	
SC/3	27.9	2.02	0.02	2.20	0.02	1.8%	1.55E-08	1.1%	5.3%	4.5%	100.0%	100.0%	1.09	50.1	0.86	58.1	2.1%	
SC/4	29.3	2.66	0.03	2.95	0.03	1.8%	2.14E-08	1.1%	4.1%	3.4%	100.0%	100.0%	1.11	52.2	0.85	61.6	2.1%	
SC/5	18.8	0.14	0.00	0.26	0.00	9.4%	1.43E-09	1.1%	77.1%	38.3%	90.4%	100.0%	1.78	57.2	0.65	87.5	9.4%	
GLA/1	8.5	0.09	0.00	0.10	0.00	17.6%	1.19E-09	1.1%	119.9%	99.7%	55.7%	40.6%	1.04	83.4	0.75	110.6	17.7%	
GLA/2	7.1	0.02	0.05	0.37	0.09	280.6%	9.96E-10	1.1%	239.5%	26.9%	64.6%	3.7%	20.90	77.0	0.65	118.6	280.6%	
GLA/3	12.7	6.17	0.15	11.85	0.15	2.7%	6.81E-09	1.1%	1.7%	0.8%	23.5%	4.9%	1.92	6.2	0.62	10.0	2.9%	
GLA/4	16.4	0.30	0.01	0.30	0.01	6.1%	3.13E-09	1.1%	36.0%	33.2%	100.0%	89.9%	0.98	66.2	0.74	91.9	6.2%	
LAV1	15.0	0.30	0.04	0.15	0.04	28.9%	2.34E-09	1.1%	36.0%	66.5%	61.5%	1.0%	0.49	56.5	0.85	66.4	28.9%	
LAV2	22.6	0.36	0.01	0.50	0.01	4.5%	5.05E-08	1.1%	30.0%	19.9%	53.8%	58.0%	1.40	809.8	0.91	891.5	4.7%	
LAV3	24.0	1.50	0.18	1.91	0.18	15.2%	1.19E-08	1.1%	7.2%	5.2%	62.9%	35.8%	1.27	50.0	0.89	56.4	15.2%	
LAV4	13.8	1.85	0.15	2.43	0.15	10.3%	2.40E-09	1.1%	5.8%	4.1%	62.8%	12.7%	1.32	8.1	0.74	10.9	10.4%	
SKIM-04/1	25.1	1.18	0.11	0.82	0.11	15.9%	3.43E-09	1.1%	9.1%	12.2%	40.6%	31.9%	0.70	20.6	0.78	26.2	15.9%	
SKIM-04/2	7.3	0.81	0.02	1.53	0.02	2.9%	8.99E-09	1.1%	13.3%	6.5%	77.1%	88.8%	1.89	62.7	0.71	88.5	3.1%	
SKIM-04/3	13.6	0.75	0.01	1.27	0.01	2.8%	6.20E-09	1.1%	14.4%	7.9%	64.0%	33.3%	1.70	48.5	0.77	63.4	3.0%	
SKIM-04/4	9.1	0.45	0.02	0.94	0.02	5.1%	4.36E-09	1.1%	24.0%	10.6%	76.8%	26.4%	2.11	53.5	0.75	71.3	5.2%	
S03-06/1	19.0	0.71	0.02	1.27	0.02	3.1%	5.40E-09	1.1%	15.2%	7.9%	19.6%	19.2%	1.78	43.9	0.76	57.6	3.3%	
S03-06/2 <sup>A</sup>	17.5	1.11	0.03	2.34	0.03	3.0%	1.15E-08	1.1%	9.7%	4.3%	45.3%	34.2%	2.11	56.7	0.77	73.8	3.2%	
S03-06/3 <sup>A</sup>	16.4	2.35	0.05	4.67	0.05	2.6%	1.76E-08	1.1%	4.6%	2.1%	99.2%	100.0%	1.99	41.9	0.70	59.2	2.8%	
GBM/1 <sup>A</sup>	10.7	0.60	0.01	0.55	0.01	3.4%	1.62E-09	1.1%	18.0%	18.1%	39.3%	87.3%	0.93	18.3	0.67	27.2	3.6%	
GBM/2 <sup>A</sup>	11.9	0.86	0.01	1.01	0.01	2.5%	4.34E-09	1.1%	12.5%	9.9%	100.0%	93.4%	1.18	32.5	0.68	47.8	2.8%	
GBM/3 <sup>A</sup>	15.2	0.72	0.01	0.75	0.01	2.9%	4.89E-09	1.1%	15.0%	13.3%	97.1%	89.0%	1.04	44.9	0.68	66.0	3.1%	
BnD/1	7.8	0.52	0.06	0.14	0.03	27.5%	3.05E-09	1.1%	20.8%	71.2%	81.4%	21.8%	0.27	45.0	0.74	60.9	27.5%	
BnD/2	5.1	0.49	0.01	0.25	0.01	6.9%	3.22E-09	1.1%	22.0%	39.9%	50.4%	16.4%	0.52	47.8	0.74	64.6	7.0%	
GP422/1 <sup>A</sup>	16.1	3.32	0.03	2.65	0.03	1.6%	2.15E-08	1.1%	3.3%	3.8%	97.0%	94.0%	0.80	44.8	0.73	61.0	2.0%	

Table 18 - Zircon (U-Th)/He data from the HIP (cont. over page)

Sample	Approx. crystal mass (g)	<sup>238</sup> U (ng)	U error (ng)	<sup>232</sup> Th (ng)	Th error (ng)	Total U-Th % error	4He (cc)	He uncert (%)	U blank (as % of sample)	Th blank (as % of sample)	<sup>238</sup> U % recovery	<sup>232</sup> Th % recovery	Th/U	Raw (Ma)	F <sub>T</sub>	Corrected (Ma)	Analytical Uncertainty	
<b>Ardnamurchan</b>																		
AR13/1 <sup>^</sup>	15.3	1.85	0.02	2.43	0.02	1.6%	1.12E-08	1.1%	5.8%	4.1%	92.0%	78.0%	1.32	38.0	0.68	56.2	1.9%	
<b>Rum</b>																		
SR131/1 <sup>^</sup>	11.1	1.49	0.02	1.95	0.02	2.2%	8.29E-09	1.1%	7.2%	5.1%	86.1%	70.1%	1.31	34.9	0.64	54.2	2.5%	
R03-11/1	15.8	0.51	0.07	1.44	0.07	14.4%	4.62E-09	1.1%	21.2%	6.9%	34.1%	14.2%	2.83	44.6	0.79	58.8	14.4%	
R03-11/2	14.3	0.21	0.02	0.48	0.01	11.4%	2.37E-09	1.1%	51.4%	20.8%	73.0%	20.5%	2.29	60.0	0.75	80.2	11.5%	
R03-11/3	14.8	2.85	0.07	2.84	0.07	3.7%	1.69E-08	1.1%	3.8%	3.5%	85.8%	16.8%	1.00	39.5	0.75	52.5	3.9%	
R03-11/4	18.6	1.27	0.03	2.72	0.03	3.1%	1.33E-08	1.1%	8.5%	3.7%	61.9%	5.0%	2.15	56.9	0.79	72.2	3.3%	
<b>Mull</b>																		
AM1/1 <sup>^</sup>	7.8	0.16	0.03	0.32	0.06	26.9%	1.74E-09	1.1%	67.4%	31.2%	73.6%	35.7%	2.05	61.7	0.68	91.2	26.9%	
AM1/2 <sup>^</sup>	6.7	0.11	0.03	0.23	0.03	28.1%	8.81E-10	1.1%	98.1%	43.3%	71.3%	25.6%	2.13	44.9	0.66	68.3	28.1%	
AM1/3 <sup>^</sup>	8.5	0.15	0.02	0.20	0.02	22.0%	9.48E-10	1.1%	71.9%	49.9%	82.8%	10.5%	1.35	40.2	0.67	59.8	22.0%	
ML3/1	12.6	0.42	0.01	0.22	0.01	9.4%	2.26E-09	1.1%	25.7%	45.3%	63.9%	12.5%	0.54	39.2	0.67	58.9	9.5%	
ML3/2	16.3	0.17	0.03	0.10	0.03	35.3%	8.61E-10	1.1%	63.5%	99.7%	78.2%	26.2%	0.56	36.4	0.64	56.9	35.3%	
ML3/3	8.7	0.36	0.00	0.18	0.00	8.0%	1.65E-09	1.1%	30.0%	55.4%	41.1%	28.3%	0.50	33.5	0.58	57.8	8.1%	
ML3/4	12.2	0.19	0.00	0.10	0.00	14.2%	4.28E-10	1.1%	56.8%	99.7%	88.4%	86.7%	0.52	16.2	0.63	26.0	14.3%	
ML5 <sup>^</sup>	16.4	0.60	0.01	0.71	0.01	3.2%	3.28E-09	1.1%	18.0%	14.0%	69.5%	72.2%	1.19	35.2	0.61	57.7	3.3%	

**Table 18 – (U-Th)/He data from the HIP**  
 Crystal masses are estimated using measured crystal volumes and a density of 4.66 g/cm<sup>3</sup>. All U and Th data are corrected for 0.1067 ng U and 0.0987 ng Th. Uncertainty in these corrections is approximately ± 0.01 ng (~10 % of blank measurement). This uncertainty is included in the analytical uncertainty. Approximately 0.93 ng <sup>238</sup>U and 2.28 ng <sup>232</sup>Th spikes were added to all samples. Yields were variable, and are shown as % spike recovered. Low yields do not prevent (U-Th)/He ages being determined, but there is greater uncertainty in the measured count rate, and therefore in the 230/232 and 236/238 ratios. Recoil correction, F<sub>T</sub>, calculated using Equation 17, with the geometry specific fitting parameters presented in Chapter 4. Uncertainty in F<sub>T</sub> is better than ± 3%. <sup>^</sup> - Multiple crystal aliquots, three crystals in each. More complete error calculations can be found in the data file on the included CD.

The values of  $F_T$  presented in Table 18 are calculated using the geometry specific form of the polynomial equations (Section 4.6.4), but as the values of  $W_1/W_2$  are  $< 1.2$ , the geometry specific  $F_T$  are within 2 % of those calculated using the Hourigan *et al.* (2005) tetragonal parameters. Replicate analysis of single crystal aliquots was performed for most samples, but where zircon yields were low, replication was not possible. Small crystal sizes and low bulk U and Th meant that some samples were analysed as multi-crystal aliquots (marked ^ in Table 18). Three crystals were selected for each aliquot, based on consistent crystal geometry, with minimum variation in widths ( $< \pm 5$  % in all length and width measurements),  $W_1/W_2$ , and  $\beta$ .

In the following discussion, both the uncorrected and  $F_T$  corrected (U-Th)/He ages are reported, modelled, and discussed. This allows the errors associated the application of the Farley (2002)  $\alpha$ -recoil correction to slowly cooled samples, and the age bias associated with the application of  $F_T$  to be assessed. The geological histories of all samples were investigated using the DECOMP program to forward model the predicted ages for a given thermal history.

#### 6.4.2.1 Ardnamurchan

The Ardnamurchan Central Complex (ACC) was emplaced beneath the northern margin of the MLF. Multiple cross cutting field relationships show that cone sheets emplaced during the earliest phase of ACC emplacement were synchronous with mass wasting of the MLF [Brown & Bell, 2006] implying that the earliest intrusion occurred at a very shallow level. No voluminous extrusive activity is associated with the ACC. The conductive and convective cooling of the ACC to near surface temperatures should therefore have occurred immediately after the cessation of magmatic activity. Little radiometric dating work has been undertaken on the ACC, but recent U-Pb analysis has corroborated the regional field relationships, and shows that intrusion occurred at  $\sim 58.63 \pm 0.31$  Ma [in Chambers *et al.*, 2005].

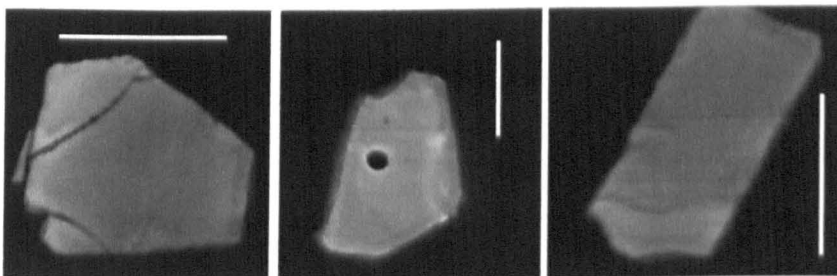


Figure 73 - Panchromatic SEM CL images of zircons from AR13, Ardnamurchan. White scale bars are 50  $\mu\text{m}$

(U-Th)/He analysis was performed on zircons from a quartz monzonite outcrop from the youngest plutonic units. Most zircons in this separate had extreme  $W_1/W_2$  ( $> 3.0$ ) and very narrow minimum dimensions ( $< 40$   $\mu\text{m}$ ), and were unsuitable for (U-Th)/He analysis. Replication was not possible, but a single aliquot containing three crystals ( $W_1/W_2 \sim 1.0$ ,  $W_1 \sim 50$   $\mu\text{m}$ ) yielded a recoil corrected

(U-Th)/He age of 56.2 Ma. CL images from the ACC zircons suggest that the U and Th distribution in these samples is relatively homogeneous (Figure 73), and that the application of  $F_T$  introduces minimal bias into the recoil corrected ages. The recoil corrected (U-Th)/He age is therefore consistent with the rapid cooling to near surface temperatures predicted for this sample. It should be noted that the CL were obtained on crystals with the extreme  $W_1/W_2$  and/or small minimum dimensions, and so may not reflect the zonation in the analysed zircons.

#### 6.4.2.2 Rum

The RCC is thought to have been emplaced at a very shallow (< 1 km) level and to have unroofed rapidly, immediately after emplacement at  $60.53 \pm 0.05$  Ma [Emeleus, 1997; Hamilton *et al.*, 1998; Holness, 1999]. The rapidity of this unroofing is evident from the unconformable relationship with the younger Canna Lava Formation (CLF). The CLF was erupted at  $59.98 \pm 0.24$  Ma [Chambers *et al.*, 2005] and fills valleys that had been incised into the RCC, pinning the duration of the cooling and denudation event to < 0.5 Myr. (U-Th)/He analysis was performed on two samples from the RCC (both collected from pegmatitic veins that cross cut the Layered Series). These samples were collected close to sea level, and are of similar depth to those thought to have crystallised at depths of < 1 km [Holness & Isherwood, 2003]. The short duration of the intrusive magmatism, and the rapid post-magmatic denudation, suggests that the U-Pb and ZHe ages should be concordant.

The zircon yield from sample SR131 (location shown in Figure 104, Appendix F) was very low, and the majority of crystals were very small (< 40  $\mu\text{m}$  width) and not suitable for (U-Th)/He analysis. To ensure that the measurement of U and Th from small (~ 50  $\mu\text{m}$  width) crystals was not significantly affected by the uncertainty in the procedural blank, three crystals were loaded as a single aliquot. The low zircon yields mean that replication of this analysis was not possible, and CL images could not be obtained.

The analysis of the other sample (R03-11, also shown in Figure 104, Appendix F) was performed prior to the addition of the trace HF was included in the final stage before measurement of U and Th (see Section 3.6.5.2). The U and Th yields during the initial measurement of all four single crystal aliquots were low (< 10 %  $^{230}\text{Th}$  spike recovered). A second reflux improved the % recovered for two of the aliquots, (R03-11/1 and R03-11/3) and because fractionation of the U and Th isotopes has not occurred, the ages can be calculated (see discussion in Section 3.6.5.4). The U and Th yield in the second reflux of aliquots R03-11/2 and R03-11/4 failed to recover additional  $^{230}\text{Th}$  spike, and the uncertainty in the  $^{230}\text{Th}/^{232}\text{Th}$  is in excess of  $\pm 6$  % because of the greater uncertainty associated with the lower count rate. These analyses cannot be confidently used in the interpretation of the cooling history. CL images of zircons from this sample could not be obtained because of low yields, and so the presence of U and Th zonation cannot be assessed.

The three age determinations (SR131, R03-11/1 and R03-11/3) have recoil corrected ages of 52 - 58 Ma, and an average age of  $55.1 \pm 6.8$  Ma (12 %,  $2\sigma$ ). This relatively poor reproducibility may be because of zonation, but the uncorrected ages range from 34.9 - 44.6 Ma, and exhibit a strong trend of increasing age with increasing crystal size. As there is tight geological constraint on the thermal history of these samples, forward modelling (using DECOMP [Meesters & Dunai, 2002a]) was used to assess the effects and range of possible zonation patterns. The forward modelling showed that the rapid cooling history predicted from the field relationships, predicts (U-Th)/He ages that are in good agreement with the measured values for all three aliquots when the zircons have effectively homogeneous U and Th distributions. As the cooling of these samples cannot have occurred before 60.5 Ma, significant rim depletion can be discounted. The modelling showed that the existence of enriched rims of variable width led to ages that were significantly younger (> 5 - 10 Myr) than the measured values, but it should be noted that DECOMP can only consider an infinite concentration gradient. It is probable that the observed scatter and 55 Ma average age may be caused by subtle rim enrichment, with a variable rim width. However, the zircon (U-Th)/He age is consistent with the geological history, and these data provide corroborative evidence that the plutonic units in the upper levels of the RCC had cooled to temperatures below  $\sim 180^\circ\text{C}$  at  $\sim 59$  Ma. The good agreement between the predicted and measured ages suggests that the effect of zonation in these samples is minimal; however CL images would be required before this can be confirmed, and these have not yet been obtained because of the low zircon yields.

#### 6.4.2.3 Mull

Few constraints can be placed on the post-magmatic evolution of the Mull Central Complex (MCC), but the MCC is thought to have been emplaced at a depth of  $\sim 2$  km based on the hydrothermal mineral assemblages [Walker, 1971], and denudation is generally assumed to have occurred rapidly [Walker, 1971; Bell & Williamson, 2002]. The emplacement of the MCC was more prolonged than that of the RCC and ACC, and the final phase of intrusion occurred at  $\sim 58$  Ma [Chambers & Pringle, 2001].

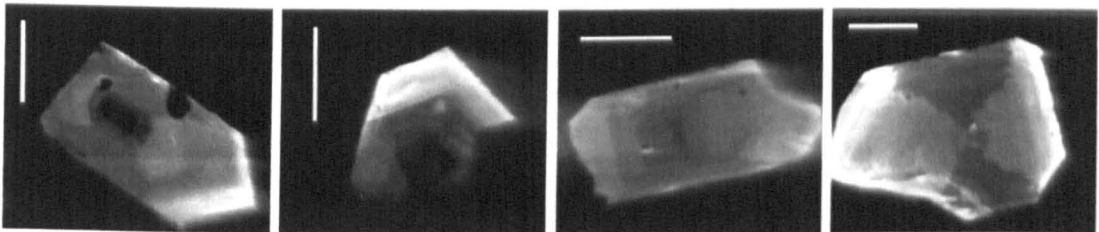
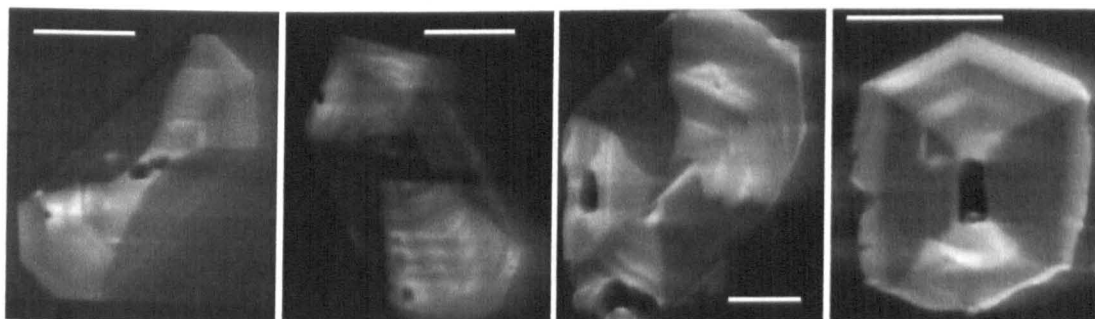


Figure 74 - Panchromatic SEM CL images of zircons from the AM1, Mull. White scale bars are 50  $\mu\text{m}$

(U-Th)/He analysis of the zircons from the Calgary Tuff (AM1), a volcanic tuff from the upper levels of the MLF (location shown in Figure 106, Appendix F), are impossible to interpret as low bulk U and Th contents mean that the uncertainty associated with the procedural blank is as much

as 10 % of the measured U and Th. CL imaging of this sample (Figure 74) reveals two styles of zonation within the crystal population, which implies that with sufficient single crystal analyses, two age populations should be expected. The (U-Th)/He analyses performed on samples from the MCC was more successful, however only one aliquot (three crystals) from the Centre 2 gabbro (ML5, exact location unknown, see Figure 106 and Table 28, Appendix F) could be prepared, as the majority of crystals from this sample had crystal widths < 40  $\mu\text{m}$ . The CL images of ML5 zircons show a self-similar oscillatory zonation with low-moderate intensity changes, over which a strong sector zonation is superimposed (Figure 75). Treating these crystals as homogeneous will therefore introduce a small age bias into the  $\alpha$ -recoil corrected ages. The limitations of current modelling techniques prevent the quantification of the age bias introduced, but it will probably be no more than a few %, as predicted by the modelling of subtle oscillatory zonation presented in Section 4.7.



**Figure 75** - Panchromatic SEM CL images of zircons from ML5, Mull. White scale bars are 20  $\mu\text{m}$

Two of the single crystal aliquots from the analyses of the Loch Ba felsite (ML3, exact location unknown, see Figure 106 and Table 28, Appendix F) have low U and Th, and therefore are not used in the interpretation. The other aliquots reproduce well, and are indistinguishable from the age determined on ML5. CL images from the Loch Ba felsite show a range of zonation patterns (Figure 76), but the majority of these can be broadly described as sector zonation. Only the larger crystals (shown far right, Figure 76), with poor crystal form and more abundant fluid inclusions, have a distinct rim depleted U and Th distribution. From the CL images, the assumption of homogeneity for the analysed crystals (~ 60  $\mu\text{m}$  width) will generally introduce minimal age bias.

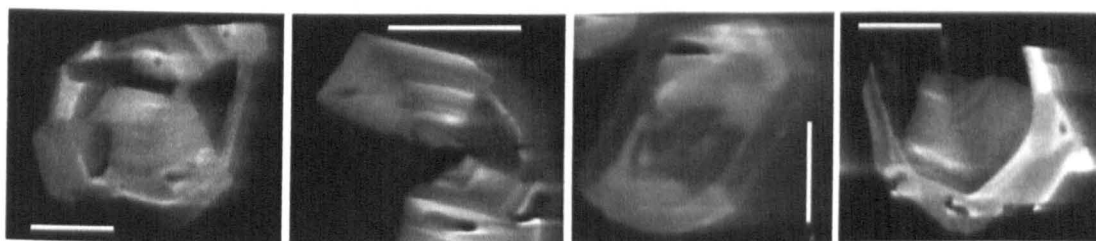


**Figure 76** - Panchromatic SEM CL images of zircons from ML3, Mull. White scale bars are 100  $\mu\text{m}$

The  $F_T$  corrected ages from the three analyses are in close agreement, with an average corrected age of  $58.1 \pm 2.5$  % ( $2\sigma$ ,  $n = 3$ ). This implies that the MCC cooled rapidly to  $< \sim 200^\circ\text{C}$ . Forward modelling of the He accumulation (assuming homogeneous U and Th distribution) during a single phase rapid cooling history predicts ages within  $\pm 2$  Ma of the measured values.

#### 6.4.2.4 Skye

The Skye Central Complex (SCC) has the most protracted intrusion history observed within the HIP, with the final phase of granite emplacement at  $\sim 55$  Ma [Hamilton, unpublished data]. The amount and timing of post-magmatic denudation is not constrained, but the SCC is thought to have been emplaced at a depth of 1 - 2 km, based on pressure sensitive quartz polymorphs [Holness, 1997], and the thickness of the preserved lava field [Bell & Williamson, 2002] combined with palynological evidence [Jolley, 1997]. The modern relief is  $\sim 1$  km, and so if these estimates are correct, all HIP samples will have crystallised within  $\sim 3$  km of the palaeosurface [Bell & Williamson, 2002]. The application of the ZHe system to the SCC allows the investigation of the apparent spread in the ZFT ages reported by Lewis *et al.* (1992). The locations of all samples are shown in Figure 105 and Table 28, Appendix F.

CL imaging of zircons from the oldest of the plutonic units (the Outer Gabbro of the Cuillins Complex), shows sector zonation in  $\sim 95$  % of the crystal population. Treating sector zoned samples as having a homogeneous distribution of U and Th will typically introduce age bias of no more than a few % even when the zonation is extreme.

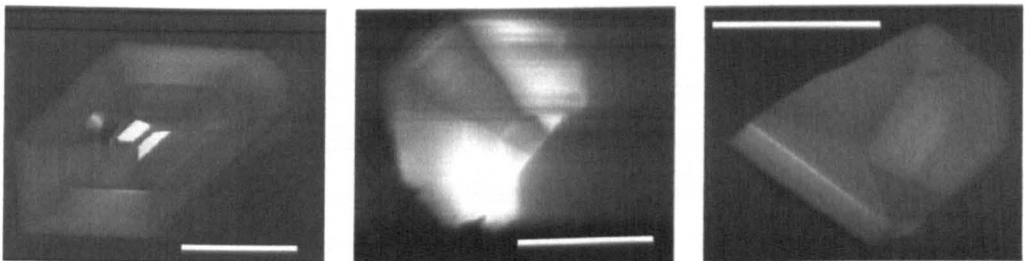


Figure 77 - Panchromatic SEM CL images of zircons from SC, Skye White scale bars are 100  $\mu\text{m}$ .

As expected, the (U-Th)/He ages determined on this sample reproduce fairly well, with an average recoil corrected age of  $60.9 \pm 8.0$  % ( $2\sigma$ ,  $n = 4$ ). SC/5 is not included in this average age because of the large age uncertainty associated with the U and Th blank for this low U and Th crystal. The good age reproducibility across a range of crystal sizes suggests that cooling was rapid, and followed immediately after the cessation of intrusive activity. The reproducibility of the measured ages, and the agreement between the measured ages and forward modelling of a rapid cooling history implies that the distribution of U and Th is consistent with the CL zonation.

Two granitic samples from the Western Red Hills granitic complex were analysed, but the ages cannot be interpreted. Zircons from the oldest granitic pluton, the Glamaig Granite (GLA/1 - 4) yield low U and Th contents in three of the four single crystal aliquots, and therefore little confidence can be placed in the (U-Th)/He ages. Furthermore, even allowing for substantial inter-crystalline variation in U and Th contents, the high bulk U and Th in the remaining aliquot (GLA/3), coupled to a low He content, suggests the addition of contaminant U and Th during analysis. Only four zircons from the Loch Ainort Granite were suitable for (U-Th)/He analysis, and these show extreme variation in the measured zircon (U-Th)/He ages, beyond that which can be typically attributed to zonation (see the discussion in Section 4.7). The anomalously old age determined on aliquot LA/2 suggests that there is substantial excess He within this crystal. When this sample is discounted the  $F_T$  corrected ages range from ~ 11 Ma to ~ 66 Ma. The origin of the ~ 11 Ma zircon (U-Th)/He age is unclear. This age cannot be obtained by even the most extreme zonation, and it is known that there was some contamination of the Teflon beakers when this sample was processed for U and Th. Contamination of the sample solution by the introduction of U and Th from an external source during analysis is therefore considered probable. Analysis of this sample was performed in the same batch as of GLA/3. Two of the aliquots (LA/1 and LA/3) yield raw (U-Th)/He ages that are within error of the age determined from the Cuillins Complex; however the 10 Myr difference in the ages, the absence of CL images, and high analytical uncertainties prevent further interpretation.

CL images of two samples collected from the youngest intrusion in the Western Red Hills, the Marscoite Suite show highly variable zonation (Figure 78). Most crystals exhibit narrow oscillatory zonation, but rim-enrichment, rim-depletion and more complex zonation patterns are observed. The variability in the zonation makes accurate interpretation of the (U-Th)/He ages difficult, and poor age reproducibility is expected. Single crystal analyses of these samples (SKM & S03-06) show poor age reproducibility. Aliquot SKM04/1 has an  $F_T$  corrected (U-Th)/He age of 26.2 Ma, and the other aliquots range from 59.2 - 88.5 Ma.

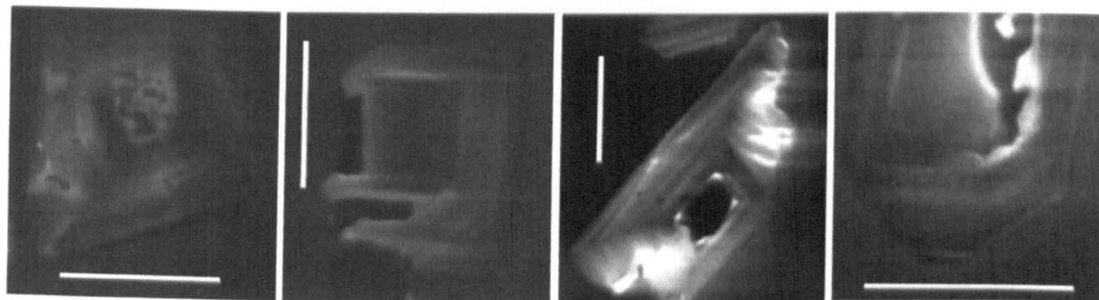


Figure 78 - Panchromatic SEM CL images of zircons from the SKM & S03-06. White scale bars are 100  $\mu$ m

The broad range in ages could be attributed to highly variable U and Th zonation (see discussion in Section 4.10.2). However, the range seems extreme given that the CL images did not show strongly depleted rims to be common. In many cases more detailed analysis of the CL images shows that the narrow oscillatory zonation mantles a more homogeneous, low CL core (centre left image, Figure 78). From comparison with the FCT and MT data discussed in Section 5.7, the apparently broadly exponential relationship between CL intensity and eU means that for minor changes, at low CL intensities, there can be substantial differences in U and Th concentration. Accurate differentiation between the intensity of the CL signal from CL zones is difficult, and it is possible that the broad zone of oscillatory zonation in this sample, actually represents significant rim depletion. More detailed CL work, coupled to quantitative analysis would be needed to confirm this. The zonation would have to be extreme (up to 25 - 30 x relative depletion) to account for the full range of values observed. Fractures and voids within the crystals observed under CL may also affect the helium retention characteristics of the crystals.

The small size of the zircons from the Glas Bein Mhor Granite (GBM) (Eastern Red Hills Complex) meant that multiple crystal aliquots were required to ensure sufficient precision in the measurement of U and Th. This sample does not reproduce, and CL images obtained after (U-Th)/He analysis suggest the GBM zircons exhibit strongly depleted rims of very variable width. In most crystals the zonation appears to have a fairly consistent concentration change across a step function zone boundary. The rim widths are often wide, and are variable both within and between crystals. Poor age reproducibility is therefore to be expected (Section 4.10), as depleted rims will lead to a variable positive age bias upon the application of the  $F_T$  correction. All aliquots have the same average crystal size, and contain the same number of crystals. The random separation of suitable crystals into these aliquots would therefore be expected to yield “zonation averaged” (U-Th)/He ages, thereby reducing the effect of the crystals with extreme zonation.

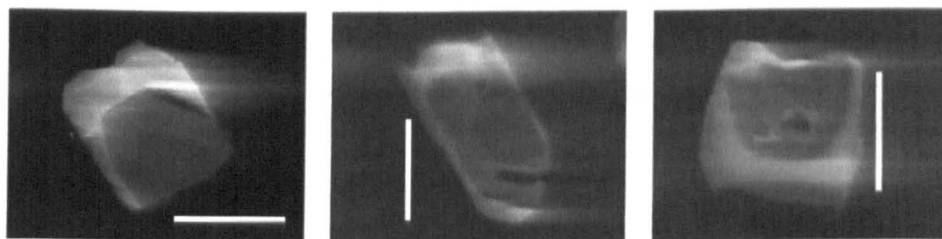


Figure 79 - Panchromatic SEM CL images of zircons from GBM, Skye. White scale bars are 100  $\mu\text{m}$

The  $F_T$  corrected (U-Th)/He ages of the three aliquots are 27.2 Ma, 47.8 Ma and 66.0 Ma. The zonation observed in this sample would suggest that all  $F_T$  corrected (U-Th)/He ages should overestimate the age of the sample, as assuming homogeneity over estimates the fraction of He generated in the crystal rims. The 27.2 Ma  $F_T$  corrected (U-Th)/He age (GBM/1), is therefore

difficult to explain, as this sample has U and Th comparable to the other aliquots, and no reheat He was observed. Furthermore, while the ~ 18 Myr difference in the  $F_T$  corrected (U-Th)/He ages of GBM/2 and GBM/3 may be a result of variable zonation, it seems extreme. Replicate analyses performed on single crystals would be required to fully determine the origin of this poor reproducibility of this sample, and the bulk U and Th measurements suggest that this may not be possible (crystal U and Th would be < 0.3 ng). Following He extraction from single crystals it may be possible to separate different zonation populations, and therefore a "pooled" U and Th analysis may be applicable (see discussion in Section 4.10).

The Beinn an Dubhaich Granite (BnD/1-3 and GP422) is one of the younger intrusions of the SCC (see Appendices D and F). Two single crystal aliquots BnD/1 and BnD/2 have low bulk Th, and the uncertainty associated with these measurements dominates the total analytical uncertainty. The greater precision of the U measurement and the low Th/U of these samples means that the uncertainty in the Th measurement has minimal effect on the calculated age ( $\pm < 2$  Ma), and the data are therefore included in the interpretation. These are the only two analyses where low Th is not accompanied by low U, and so are the only examples where this applies. The third aliquot from this granite contained three crystals, and the average  $F_T$  corrected (U-Th)/He age for all three aliquots is  $62.1 \pm 6.8 \%$  ( $2\sigma$ ,  $n = 3$ ).

CL images could not be obtained as the mineral separates supplied for this sample contained very few crystals. The majority of the crystals had large irregular fluid inclusions, and many were broken. The 20 - 25 crystals that remained, after picking for (U-Th)/He analyses, were mounted in epoxy resin, but were lost during the polishing process. The good reproducibility of the (U-Th)/He ages for both single crystal aliquots, and the multiple crystal aliquot suggests that any U and Th zonation is very consistent. A net age bias cannot be discounted. The (U-Th)/He age is older than the crystallisation age of this sample ( $55.89 \pm 0.18$  Ma, [Hamilton *et al.*, 1998]), suggesting that these crystals may have subtle rim depletion. The analytical uncertainties associated with two single crystal analyses prevent further constraint, and the data is consistent with the rapid cooling of the younger units of the SCC immediately after emplacement.

#### 6.4.2.5 Summary

With the correct consideration of the zonation in the HIP samples it is possible to perform confident interpretation of the data. The effects of variable zonation meant that the accurate determination of the (U-Th)/He ages from several poorly reproducing samples could not be determined. However, the data from samples with good age reproducibility suggests that all four central complexes (ACC, RCC, MCC and SCC) experienced rapid cooling to temperatures below ~ 180°C immediately after the cessation of shallow intrusive activity. In the samples where variable

zonation prevents accurate interpretation zircon (U-Th)/He data, there are analyses which are consistent with the rapid cooling of the plutonic units. The rapid cooling history suggested by the analyses from the SCC, is inconsistent with the published ZFT data [Lewis *et al.*, 1992].

### 6.4.3 Apatite fission track analysis

Apatite fission track analysis was performed on samples from all four central complexes (ACC, RCC, MCC and SCC). AFT ages and track lengths were measured by Dr. Cristina Persano ( $\xi = 368 \pm 8$ ), following the procedure outlined in Chapter 3. The data is presented in Table 19, and the radial plots are shown in Appendix G. The majority of the samples are within error of the crystallisation age, and are indistinguishable from the ZHe ages determined for these plutons. This implies that the rapid cooling of the central complexes immediately after emplacement continued to temperatures of  $\sim 80^\circ\text{C}$ . However, a rapid cooling cannot explain two aspects of the data set: the  $\sim 48$  Ma age determined on sample SKM04, and the  $13.6 \pm 1.65 \mu\text{m}$  mean track length measured in sample R03-11.

#### 6.4.3.1 Mull & Ardnamurchan

Two samples were analysed from each of the Mull and Ardnamurchan Central Complexes. For each complex the AFT ages are within error ( $1\sigma$ ) of each other, and are indistinguishable from the crystallization ages (Appendix E), and the ZHe ages of these plutons. The data from both samples are consistent with rapid cooling to temperatures of  $\sim 80^\circ\text{C}$  immediately after the cessation of magmatic activity. The absence of confined tracks (see discussion in Section 6.4.3.4) in these samples means that the rate at which these samples cooled through the PRZ cannot be constrained.

#### 6.4.3.2 Rum

R03-11 was the only sample in which confined tracks were observed (see discussion in Section 6.4.3.4). The AFT age of  $58.6 \pm 6.6$  Ma is consistent with the tightly constrained geological history of the RCC, and rapid cooling to  $\sim 80^\circ\text{C}$ . However, the track length distribution suggests that the low temperature evolution is more complex, and is not consistent with the rapid conductive and convective cooling synchronous with denudation, that caused the unroofing of the plutonic complex prior to the CLF basaltic volcanism at  $\sim 60$  Ma.

Inverse modelling of track length distributions is generally performed on samples where  $\sim 100$  confined track lengths have been measured. In this sample only 26 track lengths could be determined. Despite the low numbers of track length measurements, the short mean track length and high proportion of short ( $< 10 \mu\text{m}$ ) tracks made further investigation necessary, as this distribution cannot easily be generated by rapid cooling history to shallow temperatures as predicted from the existing hypothesis. The inverse modelling (using AFTSolve [Ketcham *et al.*

Sample	N. grains	$\rho_s^{D_0}$ $10^5 \text{ cm}^{-2}$	$\rho_s$ $10^5 \text{ cm}^{-2}$	$N_s$	$\rho_i$ $10^5 \text{ cm}^{-2}$	$N_i$	P (%)	AFT Age ( $\pm 1\sigma$ )*	Dpar $\pm 1\sigma$	Tr. Length ( $\pm 1\sigma$ ) (n)	Std Dev $\pm 1\sigma$
<b>Rum</b>											
R03-11**	25	12.16	0.861	106	3.272	403	97.6	58.6 $\pm$ 6.6	2.26 $\pm$ 0.28	13.6 $\pm$ 0.02 (26)	1.65 $\pm$ 0.02
<b>Ardnamurchan</b>											
AR2	22	11.63	1.108	129	3.969	462	100	57.2 $\pm$ 6.4	1.93 $\pm$ 0.23		
AR13	22	11.64	1.158	107	4.317	399	99.9	59.1 $\pm$ 7.0	2.01 $\pm$ 0.25		
<b>Mull</b>											
ML3	30	11.52	1.400	200	4.908	701	25.6	60.2 $\pm$ 5.1	2.20 $\pm$ 0.20		
ML5**	22	11.63	1.108	129	3.969	462	100	59.5 $\pm$ 6.1	1.82 $\pm$ 0.21		
<b>Skye</b>											
S03-03	21	11.95	0.943	96	3.369	343	100	61.2 $\pm$ 7.2	1.73 $\pm$ 0.34		
SKM-04	14	10.24	4.391	389	17.259	1529	12.58	47.8 $\pm$ 3.0	Not measured		

Table 19 - New AFT data from the HIP.

\*The ages are all pooled.  $N_0$  is 4973 for all samples except SKM04 where it is 6368. \*\* 75 % of the crystals have U rich rims. Ages measured by Dr. C. Persano with a zeta of  $368 \pm 8$ . All samples are etched with for 15 seconds in 5 M  $\text{HNO}_3$

1999]) of the measured track length data yields a wide range of possible thermal histories, because of the low number of horizontal confined tracks that were observed. At low track densities the probability of the etchant intersecting a short confined track is greatly reduced, and the measured track length distribution may be biased towards the longer track lengths. However it is also possible that when track numbers are low, observer bias may lead to increased numbers of short track lengths being recorded [Carter, pers. com.]. The inverse modelling presented here (Figure 80) should be considered with caution, but can be used with the known geological constraints to provide a visual representation of the possible thermal evolution of the RCC.

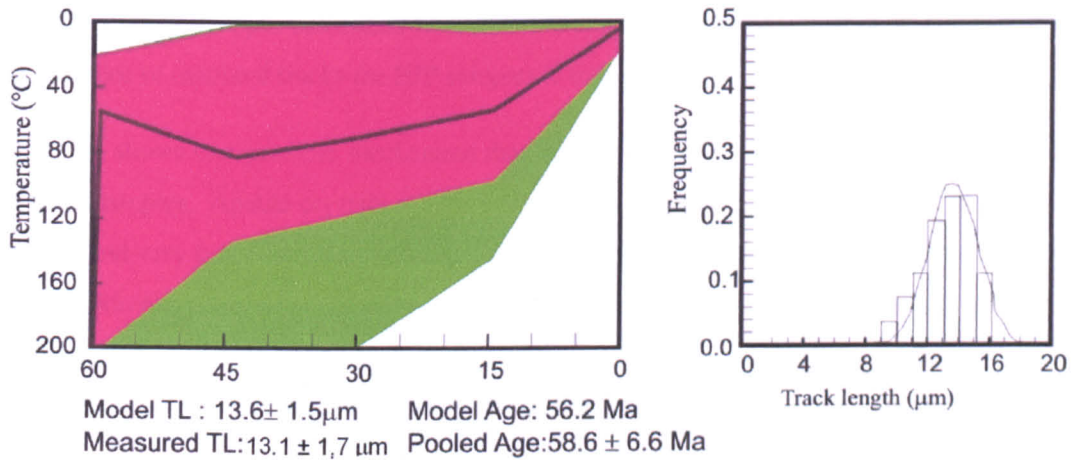


**Figure 80 - Inverse modelling of the apatite fission track data from R03-11 using AFTSolve.**

The pink envelope shown represents the good thermal histories ( $\chi^2 > 0.5$ ), the green envelope represents the acceptable thermal histories ( $\chi^2 > 0.05$ ); and the solid black line represents the modelled best fit thermal history for which the track length distribution is given.

Although the rapid cooling predicted from the field evidence falls within the envelope of thermal histories produced by the inverse modelling, this time-temperature path predicts a mean track length of  $14.5 \pm 1.1 \mu\text{m}$ , over  $1 \mu\text{m}$  longer than is observed. The AFT data suggests that while an initial phase of rapid cooling is required to obtain the measured AFT age, a more protracted low temperature evolution with prolonged residence at  $\sim 90 - 80^\circ\text{C}$ , is needed to achieve the observed track shortening. The “best fit” thermal history implies that these samples spent a prolonged period above  $\sim 80^\circ\text{C}$ , which is inconsistent with the well constrained rapid exhumation to near surface conditions [Emeleus, 1997]. Further modelling and interpretation using the additional geological constraints, and other thermochronometry is presented in Section 6.5.

### 6.4.3.3 Skye

The Glamaig Granite (Sample S03-03) is the oldest of the granitic plutons in the SCC [Bell & Harris, 1986], and has an AFT age of  $61.2 \pm 7.2 \text{ Ma}$ , within error of the crystallisation age, and the ZHe age. This implies that this pluton experienced rapid cooling to  $\sim 80^\circ\text{C}$  immediately after the cessation of magmatism. The only other sample from the SCC that yielded sufficient apatite for

AFT analysis was the ferrodiorite sample SKM-04. This sample has a much younger AFT age of  $47.8 \pm 3.0$  Ma. No confined tracks were observed in either S03-03 (two mounts) or SKM-04 (3 mounts). The origin of the differences in these ages is discussed in Section 6.6.

#### 6.4.3.4 Fission track length distributions

The low U contents of the apatites meant that confined tracks were only observed in one sample (R03-11). In attempt to obtain track length distributions from the other samples, grain mounts were irradiated under a Cf source [Donelick & Miller, 1991], but no confined tracks were observed. All samples except SKM-04 have a similar spontaneous track densities ( $0.86 - 1.40 \cdot 10^5 \text{cm}^{-2}$ ), and U content (3.56 - 6.18 ppm calculated from the induced track densities) to that observed in R03-11. The absence of confined tracks the HIP samples is therefore difficult to explain.

Figure 81 shows one possible mechanism that would lead to low numbers of horizontal confined tracks in samples. Apatite crystals in a grain mount are generally orientated parallel to the polished surface, and very few c-axis perpendicular, hexagonal faces are observed. Where the crystals have an approximately consistent zonation and grain size, it is possible that the polished surface intersects only one zone within the crystal population. If the crystal is homogeneous, or the zone boundary is more than one track length from the polished surface, the number of horizontal confined tracks will be proportional to the spontaneous track density on the polished surface (i.e. Figure 81 A). If the zone boundary is less than one track length below the polished surface, the etchant will penetrate into the low U zone, and number of horizontal confined tracks that will be intersected and etched will be reduced (i.e. Figure 81 B).

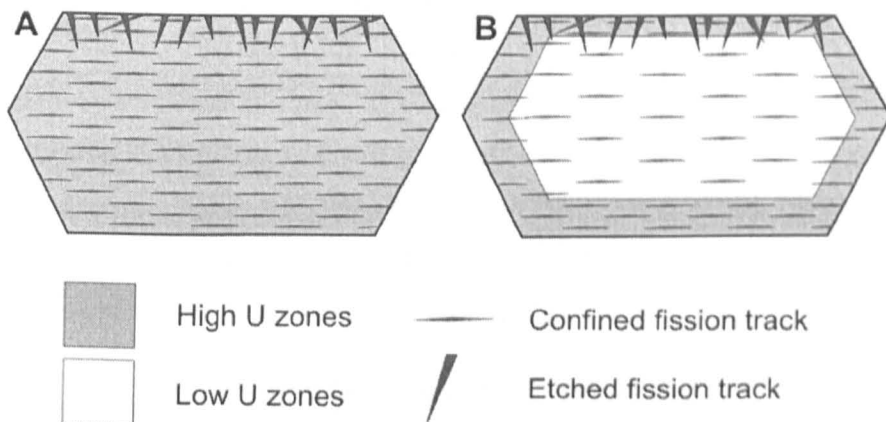


Figure 81 - Schematic representation of the effect zonation may have on the number of confined tracks revealed during etching.

Both crystal A and crystal B have the same spontaneous track density on the polished surface. Confined tracks will be randomly orientated, but to simplify the schematic, only the horizontal confined tracks (HCTs) are shown.

A) A homogeneous distribution of U (the homogeneous region only needs to extend for one track length below the polished surface).

B) A heterogeneous U distribution with the zone boundary less than one track length below the polished surface. The density of HCTs in the high U zone is the same as in crystal A, but the etchant intersects fewer HCTs at depth.

In many of the analysed samples the majority of crystals have similar widths ( $\sim \pm 10 \mu\text{m}$ ), and consequently many crystals will be intersected at approximately the same level. U zonation may therefore be more common than is suggested by the track densities on the polished surface, and the absence of confined tracks may be a consequence of the low U zone that lies beneath the plane of the polished surface. The low U content of the HIP apatites implies that if the zonation exists, very few horizontal confined tracks would form in the low U zone, and when the volume of the high-U zone that remains after polishing is small, very few confined tracks in any orientation would be seen. Zonation was observed in two of the HIP samples; R03-11 and ML5. Approximately 75 % of crystals in both samples showing U-rich rims. As the majority of crystals in each sample have the same widths, zonation may also exist in the apparently homogeneous crystals (as in Figure 81B). If the issue of zonation is effecting *all* the HIP samples it is still difficult to reconcile the complete absence of confined tracks in the HIP apatites, and the failure of Cf irradiation to increase the number of confined track that are observed.

This mechanism also has implications for the measured AFT ages, as the assumption that the crystal is homogeneous across the plane of the polished surface fails (see Section 2.2.3), and AFT ages may be increased as the number of fission events that are induced will be fewer than generated the spontaneous tracks. Additional investigation of these samples using repeated polishing-etching steps to investigate the U distribution in 3-dimensions is currently prevented by the low volumes of apatite.

#### 6.4.4 Apatite (U-Th)/He analysis

Apatite is not a common accessory mineral in the HIP. When present, it is generally of poor quality and is unsuitable for (U-Th)/He analysis. Many of the samples collected from the HIP show pervasive hydrothermal alteration, which may suggest that magmatic apatite may once have been more common, but has subsequently been dissolved out during the movement of acidic fluids through the Complex. The P-rich (few wt % [Thompson, 1969]), hybrid Marscoite suite from Harker's Gully on Skye, was the only lithology from which large volumes of apatite were recovered.

All apatites separated from the plutonic HIP samples had un-abraded hexagonal morphologies (e.g. Figure 82). In thin section, crystals were generally acicular, with high aspect ratios (5 - 10) (see Figure 82). Few crystals in the mineral separates were complete, and crystal terminations were rarely observed. Crystals were generally transparent, allowing easy observation of the large numbers of inclusions present in many samples.

In some samples the yield of apatite was lower than would be expected from the thin-sections, suggesting that many crystals were broken during crushing. Crystals were generally small, and

those suitable for (U-Th)/He analysis did not exceed 100  $\mu\text{m}$  diameter. Large numbers of inclusions were observed in all samples, and while fluid inclusions dominate (e.g. Figure 82 C), small acicular inclusions of monazite were also observed (e.g. Figure 82 D). The large numbers of fluid inclusions observed in these samples may explain the low yield and common breakage.

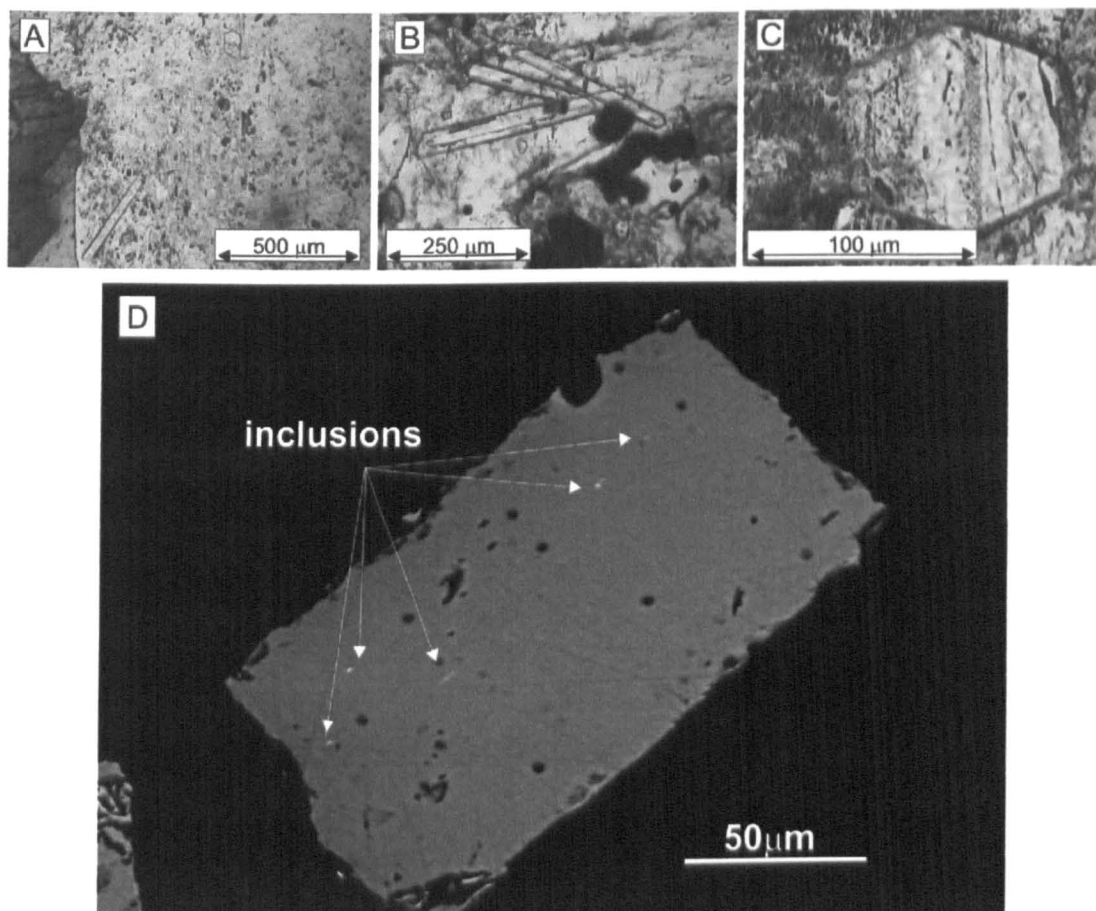


**Figure 82 - Representative apatites collected from the HIP.**

**A) Skye :** Photomicrograph of apatite in the Glamaig Granite. **B) Skye:** Photomicrograph of the apatite in the ferrodiorite showing mineral and fluid inclusions. **C) Rum:** Photomicrograph of apatite from the pegmatitic veins, showing abundant mineral and fluid inclusions **D) SEM BSE image** showing the location of small acicular monazite (high contrast) inclusions within the apatite from SKM04, ferrodiorite, Skye.

Every effort was made to ensure crystals selected for (U-Th)/He analysis were inclusion-free. Samples were analysed using the furnace extraction technique (Chapter 3) with 4 - 5 crystals loaded into each aliquot. Crystals within each aliquot were selected for consistent radii, and in most samples the difference between crystal radii within an aliquot is  $< 5\%$  ( $1\sigma$ ). Because of low apatite yields, poor quality samples, and low U and Th contents, some sample aliquots had greater variation (S03-07, JF 2003 and S03-03/2 have 8 - 10% ( $1\sigma$ )). The data from the AHe analyses from all samples are shown in Table 20.

### 6.4.4.1 Rum

Sample R03-11 has been discussed above and has been analysed by all three thermochronometers used during this study. JF2003 is another of the rare apatite-bearing pegmatitic veins that invade the RCC. The apatites from both localities contained abundant fluid and mineral inclusions, and each aliquot represents all crystals suitable for (U-Th)/He analyses. The anomalously old age obtained from JF2003/1 suggests that despite the effort made to ensure all inclusion hosting grains were discarded, some small inclusions remained. The AHe age obtained from sample R03-11, is younger than would be expected from the existing evolutionary model, but corroborates the short mean fission track length of this sample. The lack of replication of this sample limits the interpretation that can be made.

Sample	L	Th (ng)	U (ng)	4He (cc)	Th/U	Raw Age (Ma)	FT	Corrected Age (Ma)	Analytical error (%)
<b>Rum</b>									
R03-11/1	P	0.062	0.031	1.51E-10	2.01	27.2	0.65	41.5	2.7%
JF2003/1	P	0.048	0.011	2.26E-10	4.33	82.6	0.60	> formation	3.0%
<b>Skye</b>									
S03-03/1	G	0.035	0.015	1.49E-10	2.37	53.2	0.63	84.4	3.33%
S03-03 2	G	0.098	0.027	2.18E-10	3.67	35.8	0.63	56.9	3.42%
S03-03 3	G	0.058	0.024	2.95E-09	2.40	609.9	0.57	> formation	4.08%
SKM-04/1	F	0.053	0.013	7.62E-11	4.20	24.9	0.55	45.3	4.89%
SKM-04/2	F	0.021	0.012	6.60E-11	1.76	32.6	0.57	57.1	5.40%
SKM-04/3	F	0.032	0.035	5.99E-11	0.92	11.6	0.61	19.0	3.72%
SKM-04/4	F	0.020	0.013	7.13E-11	1.55	34.0	0.61	55.7	5.21%
SKM-04/5	F	0.068	0.020	1.70E-10	3.31	38.2	0.65	58.8	2.96%
SKM-04/6*	F	0.568	0.569	7.89E-10	1.00	9.2	0.60	15.3	2.62%
SKM-04/7*	F	0.050	0.012	9.81E-11	4.26	34.1	0.63	54.2	5.88%
SKM-04/8*	F	0.026	0.021	3.71E-10 <sup>#</sup>	1.29	113.0	0.62	> formation	3.67%

Table 20 - Apatite (U-Th)/He analyses from the HIP.

L = Lithology: F = ferrodiorite (Harker's Gully), G = Glamaig Granite, P = Pegmatite veins. \* analysed crystals contain a few small monazite inclusions, see text for details. # Sample had 2 % total He in first reheat cycle. In all other samples the 3He/4He reheat was indistinguishable from the preceding blank. § very high U, probable contamination All aliquots contained 4 - 5 crystals

### 6.4.4.2 Skye

Three aliquots of were prepared from the Glamaig Granite sample S03-03. The ages of the three aliquots do not reproduce, and although every effort was made to avoid selection of inclusion hosting crystals, it is possible that some were over looked. The anomalously old age of S03-03/3, is assumed to arise from a large volume of "parentless" fluid ± mineral inclusion hosted He. Given the small size of the fluid inclusions that were observed, and avoided, the aliquots with younger (U-Th)/He ages may still have a component of parentless He. The 56.9 Ma age determined on aliquot S03-03/2 may suggest that cooling was rapid, as this is within error of the AFT age for this sample,

however, as there is poor age reproducibility, and parentless He may effect all samples, further interpretation is invalid.

The analysis of SKM04 was performed in two batches (Table 20). The first batch consisted of five aliquots (SKM-04/1 - 5), and the calculated (U-Th)/He ages have an unusual distribution. Three aliquots have (U-Th)/He ages that appear to reproduce well (55.7 - 58.8 Ma,  $F_T$  corrected). The other two aliquots have younger (U-Th)/He ages (45.3 Ma and 19.0 Ma). There is no simple mechanism that can account for this age distribution. No reheat He was measured in any of these samples, and so the young ages are not due to incomplete helium extraction. Inclusions may have been overlooked during the crystal selection, but this would generate (U-Th)/He ages that are anomalously old, and that do not reproduce. If the youngest age is to be accepted as "correct" (the older ages reflect an increasing component of excess He), it is difficult to explain the reproducibility of the older three analyses. The U and Th content of the older aliquots is variable, and a large and variable quantity of excess He would be required to generate reproducing ages.

Small (< 1  $\mu\text{m}$  diameter) acicular monazite inclusions were common in SKM04 (Figure 82 D), and were difficult to detect because of their small crystal size, and orientation parallel to the crystallographic *c*-axis of the apatite. The number of acicular monazite inclusions within the SKM-04 apatites is highly variable. If monazites were overlooked during crystal selection the quality of the analyses may be compromised. The small inclusion size means that all He will be recoiled into the host apatite and recovered by standard He extraction procedures. While the He will be fully recovered, the apatite dissolution procedure is unlikely to achieve complete dissolution of even these small monazites. Ages determined on inclusion bearing crystals should therefore be older than the "true" (U-Th)/He age. The number and size of these inclusions is highly variable, and although small inclusions may have been overlooked, it is difficult to envisage how the partial dissolution of a variable inclusion volume would yield reproducing data. Furthermore the U, Th and Th/U contents of these crystals are variable but show no trend with the (U-Th)/He ages.

To investigate whether overlooked monazite inclusions could explain the initial data set, three further aliquots were prepared (SKM04/6 to SKM04/8). All crystals loaded into these aliquots contained a few, very small inclusions that could just be seen at 500 x magnification. None of these crystals would have been selected for (U-Th)/He analysis using standard selection protocols, and all crystals were checked by Dr. Cristina Persano. Only those crystals for which the number and location of all inclusions were agreed upon by both analysts were included. Selection of inclusion-bearing apatites required that all mineral inclusions were less than 10  $\mu\text{m}$  in length, and were orientated parallel to the crystallographic axis of the host apatite. All crystals with inclusions close (< 20  $\mu\text{m}$ ) to the crystal surfaces were also discarded. The three aliquots had approximately the same volume of apatite (three crystals, same radii and same length for all crystals) and each

apatite contained approximately the same number of inclusions. It should be noted that although these criteria were introduced to ensure that the same volume of inclusion was introduced, the very small inclusions overlooked during standard crystal selection procedures may also have been overlooked here. However, given the much larger size of the observed inclusions the impact of the unobserved monazites on the (U-Th)/He age should be minimal.

The high % reheat He and anomalously old age of SKM04/8 (113 Ma raw age) probably reflects the presence of a small fluid inclusion, or small zircon crystal, and is not considered further. The other two aliquots yield (U-Th)/He ages that fall within the range of ages determined for the initial analyses (Table 20). As the volume of mineral inclusions in these analyses was much higher than would have been overlooked during standard crystal selection, any effect that the inclusion have on the (U-Th)/He analysis should be increased. The larger inclusion volumes should generate more He, and should also release more U and Th during the apatite dissolution procedure. The small size of the inclusions, and the absence of any reheat He suggests that any inclusion generated He has been recoiled into the apatite lattice, and was fully extracted.

A trend of increasing age with increasing He content would suggest that the He is fully recovered, but that the U and Th is not. If so, the older group of ages is effected by excess He. Alternatively a trend of decreasing age with increasing U ± Th would suggest that while the He is fully extracted, dissolution is incomplete, with the younger ages reflecting more complete U and Th recovery from the monazite. Neither trend is observed. The low bulk U, Th of several of these samples suggests that there is a negligible U and Th release from the < 40 μm<sup>3</sup> monazite during the apatite dissolution. The inclusions within these aliquots cannot explain the range of ages observed.

The nucleation and growth of monazite within apatite, to form suites of aligned inclusions has been documented elsewhere [Harlov *et al.*, 2002; Harlov & Forster, 2003], and occurs in-situ in response to the interaction of H<sub>2</sub>O rich fluids with the host apatite. Experimental evidence suggests that these reactions can occur over a wide range of pressure-temperature conditions, and that it is the presence of the fluid that is the driving mechanism [Harlov *et al.*, 2002; Harlov & Forster, 2003]. It is therefore probable that the mineral inclusions observed in the SKM04 apatites formed during a spatially variable fluid-rock reaction significantly later than crystallisation. The interaction between the apatite and H<sub>2</sub>O- Y-, and REE-rich fluids provides another mechanism whereby the younger (U-Th)/He ages could be explained.

The interaction between fluids and the apatites may result in the precipitation of U and Th rich minerals onto the crystal surfaces, and into cracks and other defects. Partially annealed cracks are observed in some SKM04 crystals, and the high contrast BSE regions suggest that they may be enriched in REE relative to the host apatites (e.g. Figure 83). All the crystals that exhibit these

features under BSE would not have been selected for (U-Th)/He analysis, but it is possible that the crystals containing fully annealed cracks were not identified during crystal selection, as they would not be observable using standard optical microscopy.

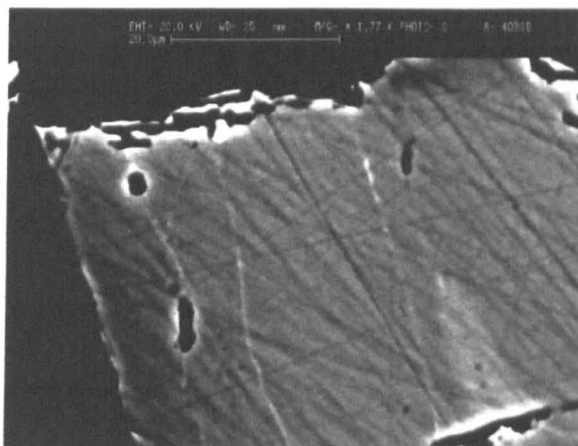


**Figure 83 - SEM BSE image of an apatite crystal separated from SKM-04.**

**Note the high REE (bright regions) along annealed micro cracks and at the crystal margins. Field of view ~ 70  $\mu\text{m}$ .**

The crystals with young (U-Th)/He ages have lower Th/U than the older crystals (Table 20), suggesting that these ages could also be caused by the precipitation of U-rich phases during a fluid-rock interaction. To produce the measured ages, the two aliquots would each need to contain an apatite with a U rich rim containing ~ 4 - 5 x the bulk U of the apatite aliquot (16 - 20 x the U and Th in an individual crystal). Such high concentrations of U would be expected to produce some fission tracks that would penetrate into the crystal, these are not observed in the AFT mounts or after etching of complete, unpolished crystals. The existence of these rims cannot be corroborated. If the precipitating phase is apatite or another He-retentive mineral, then precipitation must have occurred very recently to allow increased U and Th without the accumulation of He in the host apatite.

As the young ages were obtained from both inclusion-free and inclusion-bearing apatite this phenomenon requires additional investigation. It is difficult to provide a mechanism whereby the good reproducibility observed in the four aliquots that yield uncorrected (U-Th)/He ages of  $35 \pm 2.9$  Ma ( $2\sigma$ ) can be explained, *unless* this reflects the true (U-Th)/He age of the sample.

## 6.5 Interpretation of multi-chronometer data: Rum

The Rum Central Complex was the only plutonic sequence on which data from all three thermochronometers was obtained. In addition it was the only sample for which track lengths were determined. This sample can therefore be used to investigate the final cooling history of this

sample (200°C - 40°C), by using inverse and forward modelling techniques to determine possible thermal histories that would generate the measured ages for all thermochronometers.

### 6.5.1 Geological constraints

The RCC is known to have been unroofed very rapidly during and immediately after the cessation of magmatic activity [Emeleus, 1997]. The samples on which these analyses were performed were taken from the south-western part of the RCC, several km from the ~ 500 m thick sequence of the CLF preserved in the northwest. However, despite this spatial separation, the rapid denudation of the topographic high of the RCC is unlikely to have been limited to the northern boundary of the complex, and therefore this sample would have been within ~ 800 m of the palaeosurface at ~ 60 Ma (maximum current topography).

The former thickness of the CLF lavas is unconstrained, and it is possible that it was substantially thicker than the ~ < 500 m preserved today. There is no constraint on the former thickness of the CLF, and the only evidence for the timing of post-eruptive denudation, is in the southern part of the SLF. On the skerries of Oigh-sgeir to the SW of Canna (Figure 67), an exposure of pitchstone unconformably overlies the deeply denuded CLF in sea level exposures. This unit has been associated with the Sgurr of Eigg Pitchstone Formation [Emeleus, 1997], and therefore unless the denudation at Oigh-sgeir was highly localised, the CLF would have been denuded to its present level by ~ 58.7 Ma. The magma chamber that sourced the Sgurr of Eigg Pitchstone Formation has not been identified, but late stage magmatic activity in the RCC has not been discounted.

#### 6.5.1.1 Geological and thermochronological inconsistency

The zircon (U-Th)/He and apatite fission track ages from the RCC are within error of the emplacement age, implying a rapid cooling event early in the history of this sample. This is consistent with the field evidence, and with the rapid cooling predicted from the thermal modelling presented in Section 6.3.3. The track length distribution, short mean track length, and younger apatite (U-Th)/He age are inconsistent with the existing evolutionary model, in which there has been little cooling since 60 Ma. Instead the inverse modelling of the AFT age and limited track length data (Section 6.4.3.2) suggest these samples experienced monotonic cooling from ~ 80°C since ~ 60 Ma. Combined consideration of the geological evidence, and the data from all three thermochronometers is required if the apparent conflict is to be resolved.

### 6.5.2 Modelling of the multi-chronometer data

Inverse modelling (HeFTy [Ketcham, 2005]) was used to incorporate the geological time-temperature constraints with the thermochronological data, to constrain the possible thermal history of the RCC. HeFTy allows the simultaneous incorporation of the data from all three

thermochronometers, geological constraints, and can also include the effect of zonation on the (U-Th)/He ages (apatite and zircon). However, there are differences in the way that HeFTy (recoil then diffusion) [Ketcham, 2005] and DECOMP (simultaneous recoil and diffusion) [Meesters & Dunai, 2002a] treat the helium recoil and diffusion process and this can lead the models to predict different (U-Th)/He ages for the same thermal history (see Section 2.4.4). These differences are most apparent when samples have cooled slowly, or have spent long periods at low temperatures. To ensure that the differences between the models did not effect the geological interpretation, the thermal histories predicted from one model were tested in the other. In all cases there was less than ~ 4 - 6 % variation in the predicted AHe and ZHe ages. For this sample the computation technique has little effect on the predicted thermal history, mainly because these samples are relatively young.

Approximately 75 % of the apatite crystals in this samples exhibited U rich rims, and these were generally of better quality, and had fewer inclusions than the non-zoned examples. It is therefore probable that the apatites selected for (U-Th)/He analysis were zoned. Modelling of the AHe age for this sample includes an appropriate zonation: a 2 x enriched rim that is 50 % of the crystal radius. The low U and Th concentration in this sample made more accurate determination of the relative concentration changes impossible. It should also be noted that a recent study by Shuster *et al.* (2006) suggests that the closure temperature of the apatite (U-Th)/He system is dependant on the eU content of the crystals. For the samples analysed during this research, this suggest a closure temperature of ~ 60°C for a cooling rate of 10°C/Myr, and of ~ 50°C for cooling rates of ~ 1°C/Myr [Shuster *et al.*, 2006]. If correct, this revision makes no change to the modelled thermal histories.

Etching conditions strongly control the value of Dpar, and the temperature of the acid etchant is only known to  $\pm$  ~ 2 - 3°C (a water bath was not used, and laboratory room temperatures generally range from 20 - 23°C). Consequently there is a considerable uncertainty around the value of Dpar, and hence in the annealing behaviour. To investigate what effects this uncertainty has on the predicted thermal history, inverse modelling of the combined data set was performed using a range of average Dpar values (1.7 - 2.3). For each of the model parameters the form, and width, of the acceptable thermal history envelope did not change significantly. The plots shown below (Figure 84 and Figure 85), show the model run with the measured Dpar values.

The modelling of the data from the three thermochronometers (Figure 84) predicts a suite of thermal histories that are very similar to the "best" fit curve determined by the AFTSolve modelling presented in Figure 80 (Section 6.4.3.2). The incorporation of the ZHe and AHe data into inverse modelling eliminates a large number of possible cooling paths, including those characterised by two stage cooling (rapid then slow, or slow then rapid). The cooling path predicted by the field relationships is among the eliminated histories.

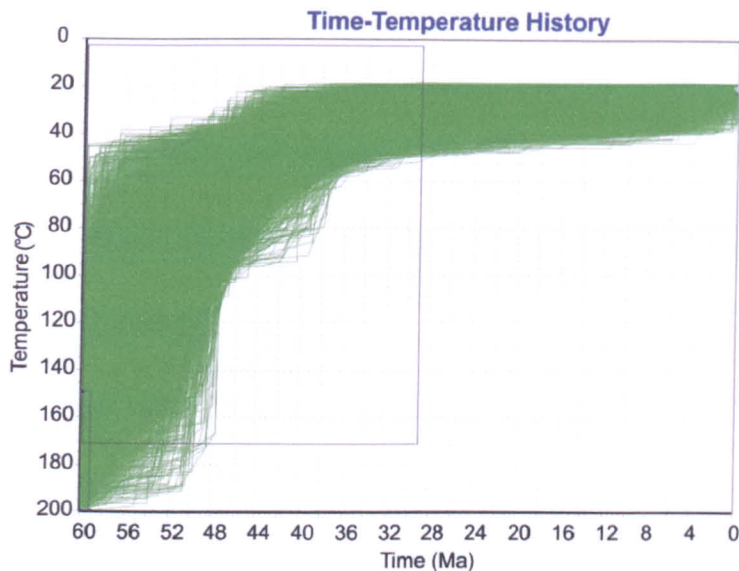


**Figure 84 - Inverse modelling of multi-chronometer data from the RCC (I).**  
**The thermochronological data was modelled with no geological constraints.**  
**Statistical definition of these populations as for Figure 80.**

The former thickness of the CLF is unconstrained, and a thicker sequence of basalts could have overlapped, and over-topped, the palaeo-topography of Rum. Samples that were unroofed very rapidly would have immediately been reburied ( $< 0.5$  Myr age difference between the plutons and the onlapping lavas) and reheated. The thermal history predicted by the modelling would be consistent with re-burial to depths of  $\sim 2$  km ( $\sim 80^{\circ}\text{C}$ ), followed by the slow removal of the basaltic lava pile from  $\sim 60$  Ma to the present. The eruption of a 2 km thick volcanic sequence is possible given the rapid, voluminous magmatism associated with the SLF, and there is no direct field evidence to support or contradict this interpretation. However, this history would require the preservation, and slow denudation of a 2 km thick lava pile, immediately after a rapid denudation event had removed the  $\sim 1 - 2$  km topographic high of the RCC. Continued rapid isostatic re-equilibration of the crustal section is identified in the rapid denudation prior to the eruption of the CLF, and in the continued preservation of the transition from sub-marine to sub-aerial eruption close to the modern sea-level in this region. A cooling history such as that shown in Figure 84 is therefore not considered a probable time-Temperature path for the RCC, as the period of initial cooling must have brought these samples to near surface temperatures, and subsequent burial would have been limited, and short lived. It is more probable that the RCC samples have remained close to their present elevation since  $\sim 60$  Ma.

Further modelling included the additional geological constraint indicated by the onlapping of the CLF onto the denuded RCC. This model sequence produced a very different envelope of acceptable time-Temperature paths (Figure 85). The majority of paths now require a two-stage cooling history, with a thermal pulse several Myr after the initial exhumation, to generate the observed track shortening without causing significant AFT age reduction. Within the limits of the

errors ( $\pm 6$  Ma) the thermal maximum of this pulse is  $\sim 90^\circ\text{C}$ , and if the mean AFT age is to be preserved the thermal maximum is closer to  $80^\circ\text{C}$ .

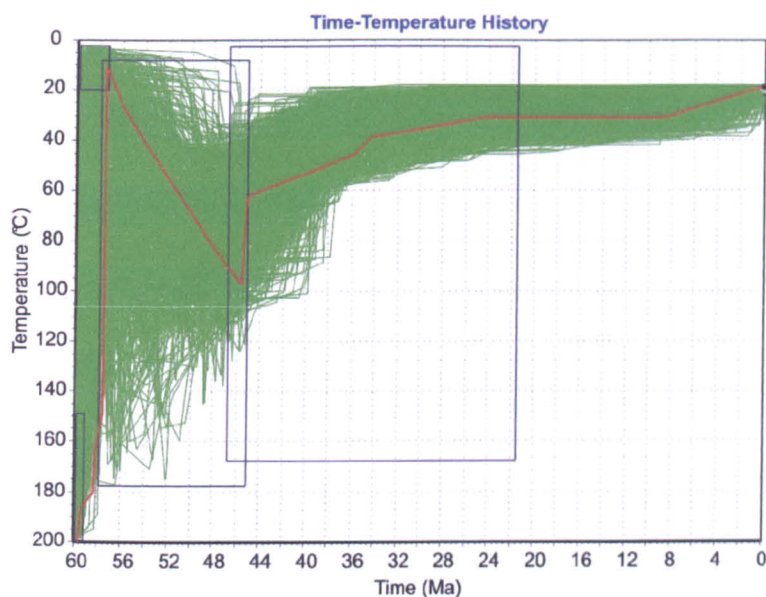


**Figure 85 - Inverse modelling of multi-chronometer data from the RCC (II).**  
The thermochronological data was modelled with the additional geological constraint provided by the field evidence. Statistical definition of these populations as for Figure 80.

The inverse modelling allows the onset of this thermal event at any point before approximately 48 Ma, and the duration is not tightly constrained. The absence of any evidence for significant reburial, and forward modelling of a range of the acceptable thermal histories (DECOMP and HeFTy), suggests that the data is best fit by a thermal history in which there are two distinct phases of cooling: one that occurs at  $\sim 60$  Ma (forced by the model) and a second that begins between 48 - 40 Ma. It should be noted that approximately 25 % of the acceptable time-Temperature paths still have a very similar form to those shown in Figure 84, and these have the initial cooling followed by an immediate, and rapid re-heating event.

The prolonged preservation of a thick lava sequence is improbable in a system showing rapid dynamic response to the volcanic activity, and the field relationships therefore suggest that the RCC samples were close to, and have remained at near surface conditions since  $\sim 60$  Ma. The re-heating of these samples from surface temperatures to  $\sim 80^\circ\text{C}$ , in the absence of significant burial implies a dramatic increase in the heat flow in the region. There is no evidence that this region of the HIP has experienced burial beneath 0.75 - 2.50 km of volcanic or sedimentary units after the end of the Palaeogene activity.

The thermal maximum experienced by these samples is relatively well constrained because of the preservation of old AFT ages, but duration of this thermal perturbation and therefore the mechanism driving the event is poorly constrained. These samples experienced a  $\sim 50^\circ\text{C} - 70^\circ\text{C}$

increase in temperature prior to the onset of cooling at ~ 48 Ma, and the shallow level of these samples therefore implies geothermal gradients in excess of 60 - 70°C/km, several Myr after the intrusion of the RCC. The thermal modelling presented in Section 6.3.3, shows that this perturbation cannot be as a result of the initial magmatic cooling of the RCC, suggesting that an elevated geothermal gradient must have been re-established during a later thermal event. The most probable source of this heat is magmatic activity.

Renewed intrusion would increase heat flow, and potentially drive a hydrothermal system, thus allowing the rapid transport of heat to the near surface. The youngest magmatic activity preserved in the HIP is the Sgurr of Eigg Pitchstone Formation which was erupted at  $58.72 \pm 0.07$  Ma [Chambers *et al.*, 2005]. This is ~ 10 Myr before the onset cooling that occurs after ~ 48 Ma, and so this event cannot account for the predicted thermal history unless it was associated with a large, and very long lived magma chamber. Intrusive activity on Skye occurred over ~ 4 Myr, but more prolonged magmatism is not recorded among the Palaeogene Igneous Provinces on the European margin. The operation of a large, long lived magmatic system is therefore not thought to be a viable mechanism for providing a heat source. Short lived intrusive activity can provide a mechanism to lead to locally elevated temperatures. The emplacement of small volume melts at depth over ~ 10 Myr, or as a distinct second phase of intrusion at ~ 52 - 48 Ma could provide the heat source, and drive a hydrothermal system. The upward transport of a heat from a small-moderate intrusion at depth would allow the partial annealing of the AFT lengths, without generating voluminous volcanic products.

### 6.5.3 Synthesis

The uncertainties associated with the thermochronology (low numbers of track lengths, non-replication of AHe analysis, the effect of zonation in apatite and zircon), currently prevents tighter constraint, or more detailed analysis, of the predicted thermal histories. However, the thermochronology shows that the existing model for the thermal evolution of the RCC is incorrect. If current understanding of the geological constraints on the system is correct and the CLF did not achieve and maintain a substantial thickness, the data suggests that a later phase of reheating must have occurred. A limited magmatic emplacement at depth is the favoured mechanism for explaining the thermochronology; implying that while the main magmatic episode occurred between 60.5 - 57.8 Ma, pulses of small volume magmatic activity occurred up to ~ 48 Ma.

## 6.6 Interpretation of multi-chronometer data: Skye

The thermochronology from the SCC is also difficult to reconcile with the existing model for the geological evolution of the SCC. The final phase of voluminous shallow level intrusion in the SCC

occurred at  $55.7 \pm 0.1$  Ma [Hamilton, unpublished data], and although the ZHe ages, and the AFT age of  $61.2 \pm 7.2$  Ma obtained from the Glamaig granite implies rapid cooling to  $\sim 80^\circ\text{C}$ , there is a spatial variation in the AFT ages that must be explained. A rapid cooling event to near surface temperatures is consistent with the existing hypothesis for the geological evolution of the HIP, the evidence for an extensive hydrothermal system, and the thermal modelling presented in Section 6.3.3, but is *not* in agreement with the younger ZFT data from the SCC [Lewis *et al.*, 1992]. This discrepancy is discussed below (Section 6.6.1.1).

A distance of less than 4 km separates the samples on which the two AFT ages were determined. These samples are at approximately the same elevation, and there is no field evidence for faulting since the time of emplacement. The very short distance between these samples suggests highly localised heat flow was responsible for the resetting of the ferrodiorite sample (SKM-04). The ferrodiorite is one of a suite of intrusions that was emplaced as a cone-sheet type structure along pre-existing caldera bounding faults [Bell & Harris, 1986] (see Figure 105, Appendix F). The structure of the ferrodiorite intrusion, and the localised nature of the resetting, therefore suggests that convective transport of heat by hydrothermal activity may have exploited the existing conduit provided by the intrusion. High temperature fluids following the planar conduit of the narrow intrusion would effect the AFT ages in the ferrodiorite, but leave the surrounding plutons unaffected. Resetting the AFT ages to  $\sim 47$  Ma would require temperatures of between  $\sim 130^\circ\text{C}$  ( $> 1$  Myr duration) and  $\sim > 180^\circ\text{C}$  ( $< 0.25$  Myr), and as the hydrothermal system in the country rocks records temperatures in excess of  $\sim 500^\circ\text{C}$ , the resetting of the ferrodiorite by a hydrothermal event is feasible. This hypothesis could be tested by determining AFT ages from a suite of samples taken at increasing distances from the margin of the ferrodiorite. It should also be noted that forward modelling of a re-setting thermal pulse event at  $\sim 47$  Ma, requires the decay of the event to be very rapid ( $\sim < 1$  Myr) in order to predict the observed AHe of this sample. This is consistent with a very short-duration event such as a pulse of hydrothermal activity. Although this work would benefit enormously by the measurement of track length distributions, the analyses still provide new insight into the duration of thermal activity in the SCC.

## 6.6.1 Expansion to include the existing thermochronology

### 6.6.1.1 Zircon fission track data

The published ZFT ages from the SCC range from  $53.1 \pm 3.7$  Ma to  $45.8 \pm 4.3$  Ma (see Table 15, Section 6.3.2.1) [Lewis *et al.*, 1992], and are consistently younger than the ZHe ages. This is inconsistent with the relative position of the closure temperatures of these two dating systems. The ZHe data obtained from the oldest and youngest plutons are within error of each other at a  $1\sigma$  level, suggesting that samples from all units in the SCC had a very similar thermal history with cooling to

< 200°C immediately after the cessation of magmatic activity. The spread observed in the ZFT data set is harder to explain, and shows no trend of ZFT age with the crystallisation sequence. The observed age range is significantly wider than would be expected from the predicted cooling of the central complex, and implies that cooling to ~ 250°C was a much slower process.

Both the ZHe and ZFT datasets have a degree of uncertainty associated with them. As discussed extensively in Chapters 4 & 5, the ZHe ages can be affected by U and Th zonation. The ZFT data will be affected by the procedural uncertainty associated with crystal specific etching and annealing behaviour. The differences between these data sets must be addressed if the geological and thermal history of the SCC is to be fully understood. To investigate the source of this discrepancy, the data from three samples: the Cuillins (SC), Glamaig (GLA), and Beinn an Dubhaich (BnD/GP422) are compared. These plutons have been dated by multiple techniques and allow the direct comparison of the ages (see Table 21).

The oldest intrusion of the SCC (Cuillins, SC) exhibits subtle sector zonation, which means that negligible age bias is introduced into the (U-Th)/He by the recoil correction. From the inspection of all the CL images from this sample, the proportion of each crystal that is relatively enriched, and the proportion that is depleted are approximately equal, both across the entire section and within the rim (the region that experiences He loss by  $\alpha$ -recoil). This means that the magnitude of any net age bias will be in the order of a few %, and within the uncertainty on the (U-Th)/He age ( $\pm 8.0$  %,  $2\sigma$  age reproducibility). This (U-Th)/He age is within error of the crystallisation age (Table 21) and this age is considered reliable.

Study and method		Cuillins (SC)	Glamaig (GLA)	Beinn an Dubhaich (BnD)
Hamilton, <i>et al.</i> (1998)	U-Pb	58.91 $\pm$ 0.07 Ma	N/A	55.89 $\pm$ 0.18 Ma
Lewis <i>et al.</i> (1992)	ZFT	N/A	51.9 $\pm$ 2.7 Ma	47.5 $\pm$ 2.6 Ma
This study	ZHe	60.9 $\pm$ 3.6 Ma	N/A	62.1 $\pm$ 4.2 Ma
This study	AFT	N/A	61.2 $\pm$ 7.2 Ma	N/A

Table 21 - A comparison of the U-Pb, ZFT and AFT ages from plutons dated by multiple chronometers, sources as shown.

The Glamaig Granite has been dated using both the ZFT [Lewis *et al.*, 1992] and AFT (this study), and has a stratigraphic position that suggests crystallisation occurred at ~ 59 Ma (slightly earlier than the Loch Ainort Granite which crystallised at 58.58  $\pm$  0.13 Ma [Chambers *et al.*, 2005]). The ZFT age is significantly younger than the suggested crystallisation age, and is also younger than the AFT age (Table 21). The need for sample specific etch times to ensure optimal track revelation for ZFT analysis introduces a potential source of uncertainty in the ZFT age. The determination of

AFT ages is routine, and subject to lesser methodological uncertainty, and inter-laboratory standardisation of etch times for all samples, has enabled differences in etching to be used as a kinetic constraint on annealing behaviour (Dpar) (see Section 2.2). The large uncertainties on the AFT age is because of the low U content of these apatites, and although this sample has a low track density the AFT age is considered the more reliable. This discrepancy between the AFT and ZFT ages questions the validity of the other ZFT data.

The Beinn an Dubhaich Granite has been dated using all three techniques (Table 21). Once again the ZFT age is younger than the ZHe age, and here the ZHe age is also ~ 6.3 Myr older than the U-Pb age. The issues surrounding the ZFT data have been highlighted above, and this age is to be considered with caution. It should be noted that the ZHe and U-Pb ages would have been within error if the FCT age uncertainty had been applied. However, the apparent discrepancy between the ZHe and U-Pb ages must also be addressed. Zonation of U and Th in these zircons would be the most probable cause of this age discrepancy. No CL images could be obtained from this sample (see Section 6.4.2.4, page 170), and so there can be no assessment of the age bias introduced by the  $F_T$  correction of these ZHe ages. The crystals analysed for (U-Th)/He were of the same size, and so the good age reproducibility from single and multiple crystal aliquots suggests that the effect of the zonation on the (U-Th)/He age is consistent between crystals.

The ~ 6 Myr difference is the equivalent to + 6 - 11 % age bias in these crystals, and would relate to rim depletion. For the analysed crystals it is equivalent to between a ~ 2  $\mu\text{m}$  ( $\Delta C = 0.05 - 0.2$ , see Equation 33) and ~ 11  $\mu\text{m}$  ( $\Delta C = 0.5$ ) rim. Narrow rims with extreme zonation have not been imaged in the HIP samples, but broad depleted rims are relatively common (e.g. GBM, Figure 78). Broad rims with moderate depletion do not preclude good age reproducibility, as is seen in this sample. This consideration suggests that the ZHe data are not inconsistent with the rapid cooling of this sample; however CL imaging would be required to confirm this.

Conversely, a similar investigation showed that the zonation required to reconcile the ZHe age with the ZFT age, would need to introduce an age bias of ~ + 30 %. Such an age bias can only be introduced by very extreme rim depletion. To bring the  $F_Z$  corrected ZHe age within error of the ZFT age (at  $\pm 7$  %), the concentration change across the zone boundary  $\Delta C$  need to be greater than 0.05 to 0.01 (a 20 x to 100 x depletion). This is not considered probable in these samples, because as extreme concentration changes even minor variation in rim width between crystals will result in poor age reproducibility ( $> \pm 10$  %).

The ZHe age of the Beinn an Dubhaich Granite cannot be accurately determined until CL analysis has been performed, however unless the zonation is extreme the  $F_T$  corrected (U-Th)/He age is consistent with the rapid cooling of the SCC to below 200°C immediately after emplacement.

Following the comparison of these analyses, it is proposed that the remaining ZFT ages also underestimate the age of the cooling of the SCC, this consistent under estimation may be as a result of slight under etching.

### 6.6.1.2 Apatite fission track

The new AFT thermochronology from the SCC is generally consistent with the existing AFT data set from surrounding country rocks [Lewis *et al.*, 1992]. If hydrothermal fluids were transported rapidly from depth along the structural conduit of the ferrodiorite at ~ 47 Ma, the same thermal pulse is likely to have driven further hydrothermal activity in the surrounding country rocks. Lewis *et al.* (1992) present the AFT track length distributions from samples: Eyre: AFT age =  $68.8 \pm 6.2$  Ma, mean track length =  $12.94 \pm 0.32$   $\mu\text{m}$ , and Drumfearn: AFT age =  $49.7 \pm 3.8$ , mean track length =  $13.18 \pm 0.23$   $\mu\text{m}$ . Lewis *et al.* (1992) suggest that the track length data is consistent with a monotonic cooling from ~ 110°C since 52 Ma. Forward modelling of the predicted history for the ferrodiorite sample was investigated using the range of Dpar values seen in the HIP samples. The mean track length of this predicted history was between 13.6  $\mu\text{m}$  and 14.2  $\mu\text{m}$ , and was below 14  $\mu\text{m}$  when the single pulse has a thermal maximum between 120°C and 170°C. The kinetic parameters of the sedimentary samples are not known, but the forward modelling shows that a thermal pulse of between 120 - 150°C at ~ 47 Ma is consistent with the track length distribution in the sedimentary units.

## 6.6.2 Synthesis

On Skye the combination of the new and existing thermochronology has revealed a spatially variable thermal perturbation that is consistent with the transport of high temperature fluids (120 - 150°C) along pre-existing structural weaknesses. This event occurred at ~ 47 Ma, ~ 8 Myr after the final stages of voluminous shallow level intrusion. A hydrothermal system requires a driving heat source, and this event therefore implies that there was a pulse of magmatic activity at depth, at this time. Without the application of the multiple thermochronometers, the timing and duration of this event could not have been constrained.

## 6.7 The St Kilda Central Complex

In addition to the samples from the HIP, a preliminary investigation into the low temperature evolution of the St Kilda Central Complex was also undertaken. The St Kilda Central Complex lies ~ 100 km west of the Outer Hebrides (Figure 86, inset), and is one of the larger, and better understood of intrusive complexes along the offshore UK continental margin. The study will help determine the accuracy of the underplating models, which predict 4 km ( $\pm$  1 km) denudation (see

Section 6.7.1 below). It also allows the post-magmatic evolution of an intrusive centre close to the rifted margin to be investigated.

### 6.7.1 Geological setting

The intrusion of the St Kilda Complex followed that of the onshore HIP, with early emplacement of mafic magmas, superseded by intermediate and silicic melts. The current level of unroofing exposes both silicic and mafic plutons, and preserves evidence for melt mixing between the silicic and mafic end members (Figure 86). There is no preservation of an overlying volcanic superstructure, and outcrops of Lewisian gneiss found on the seabed, suggest substantial denudation.

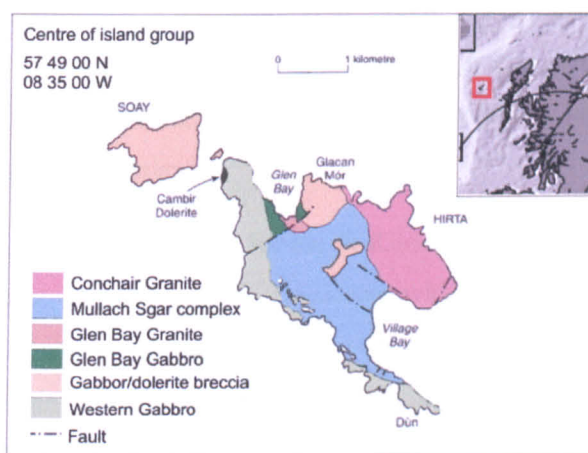


**Figure 86 - A geological map of the St Kilda Central Complex. The inset shows the location of the Complex relative to Scotland.**

Underplating models suggest that St Kilda is underlain by a  $\sim 12$  km thick sequence of lower crustal mafic material [Al-Kindi *et al.*, 2003], and denudation should therefore be in the order of  $\sim 4$  km ( $\pm \sim 1$  km) [Tiley *et al.*, 2004]. A recent seismic survey line, suggest that the thickness of underplated material beneath the Hebridean shelf is 4 - 6 km [Klingelhöfer *et al.*, 2005], broadly consistent with that predicted from the Al-Kindi *et al.* (2003) model away from the intrusive centre. In contrast to earlier studies [Bott & Tuson, 1973; Bott & Tantrigoda, 1987], the Al-Kindi *et al.* (2003) model does not show a “bulls eye” gravity anomaly centred on each of the SCC and MCC. The reason for this is not addressed. In Bott & Tuson (1973), and Bott & Tantrigoda (1987), the extension of the SCC and MCC to depths of  $\sim 14$  km, generated large positive gravity anomalies, similar to that centred on St Kilda in the Al-Kindi *et al.* (2003) model. It is possible that the local gravity anomalies for SCC and MCC were beyond the spatial resolution of the Al-Kindi *et al.* (2003) model, or that the local signatures were removed to resolve the regional signal. If the latter is correct, it is unclear if the same procedure has been applied to St Kilda.

In the SCC and MCC, the gravity anomalies suggest that the granites form only a thin cap to a dominantly gabbroic complex, and only extend a few km below the modern surface [Bott & Tuson, 1973; Bott & Tantrigoda, 1987]. If the same sequence is observed on St Kilda, the preservation of granitic plutons implies a limited level of erosion. If the Al-Kindi *et al.* (2003) prediction is accurate, the current exposure will represent the deepest granitic units.

There are no high precision radiometric ages for units of the St Kilda Complex, however the complex is thought to have intruded at ~ 55 Ma [Mussett *et al.*, 1988]. This age is younger than the majority of the onshore HIP magmatism, and many of the ages presented by Mussett *et al.* (1988) have been revised by several Myr following more recent U-Pb and Ar-Ar analyses. However, a younger age for the St Kilda Complex is not inconsistent with its proximity to extrusive activity at the seamounts in the Rockall trough [O'Connor *et al.*, 2000], where pulsed magmatism occurred at 62, 51, 47 and 42 Ma (see Appendix D). The low temperature thermochronological investigation of the Complex will allow insight into post-magmatic cooling history, and may also provide new constraint on the timing of magmatism.

The absence of high precision radiometric for the St Kilda Complex means that the ~ 55 Ma age reported by Mussett *et al.* (1988) should be considered with caution, as many other earlier K-Ar dates for HIP rocks have undergone significant revision with improved techniques [Mussett *et al.*, 1988; Chambers & Pringle, 2001; Chambers *et al.*, 2005]. However, the Complex is Palaeogene in origin, and therefore the earliest probable age of cooling is ~ 60 Ma. If the denudation predicted by the underplating models is correct, surface samples would have crystallised at a depths of ~ 3 - 6 km. With geothermal gradients of ~ 30 - 40°C/km, these samples would have resided at a temperature of ~ 120 - 250 °C, and were probably close to, or in the ZHe PRZ at crystallisation. If denudation was syn- or immediately post-intrusion, the ZHe will be indistinguishable from the crystallisation ages. It is also possible that the AHe ages will record the same, single cooling event. If denudation was protracted, pulsed, or occurred several Myr post-intrusion, then the AHe ages, and probably the ZHe ages will reflect the later cooling event.

### 6.7.2 Thermochronological Investigation of the St Kilda Complex

A sample from the Conachair Granite (Figure 86) was used for this preliminary investigation. Further investigation is ongoing, and AFT analysis has not yet been performed. The apatite and zircon (U-Th)/He ages were obtained following the techniques outlined in Chapter 3, and helium extraction from both apatite and zircon was performed using the diode laser system. The (U-Th)/He data are presented in Table 22.

Zircons are not common, but are generally large (> 100 µm in width), orthorhombic, and of good quality. The selected crystals have  $W_1/W_2$  of between 1.0 - 1.4 and all the crystals in each aliquot

have the same  $W_1/W_2$ . The weighted mean  $F_T$  values shown in Table 22 are calculated from the geometry specific fitting parameters. The  $F_T$  values calculated using the Hourigan *et al.* (2005) fitting parameters are  $\leq 1.5\%$  larger than those in Table 22. The St Kilda zircons have high bulk U and Th contents, and additional analyses of single crystals would be possible. The average  $F_T$  corrected zircon (U-Th)/He age for the St Kilda Complex is  $44.8 \pm 2.9$  Ma ( $2\sigma$ , 6.5 %).

	# xls	$^{238}\text{U}$ (ng)	$^{232}\text{Th}$ (ng)	4He (cc)	% reheat	Th/U	Uncert	Raw age (Ma)	$F_T$	Corrected Age (Ma)
<b>Zircon</b>										
StK Z1	3	3.70	4.26	1.94E-08	0.78 %	1.15	4.2 %	33.9	0.77	43.9
StK Z2	2	4.63	6.68	2.76E-08	1.84 %	1.44	3.3 %	36.5	0.83	44.1
StK Z3	3	4.18	5.38	2.21E-08	1.75 %	1.29	3.7 %	33.3	0.72	46.5
<b>Apatite</b>										
StK A1	3	0.104	0.027	1.79E-10	0.1 %	3.9	2.80 %	28.7	0.80	35.8

**Table 22 - Zircon and apatite (U-Th)/He ages from the St Kilda Complex.**

All zircon ages are corrected for blank U and Th (0.1076 ng U, 0.0997 ng Th), no correction required for apatite (U-Th)/He analyses. # xls = number of crystals in each aliquot.  $F_T$  for the zircons is calculated using geometry specific form of the polynomial equation  $F_T = 1 + a\beta + b\beta^2$  (Section 4.9.1). The apatite  $F_T$  calculated after Farley (2002).

Apatites from this sample were generally acicular, with euhedral hexagonal geometries (crystal half width  $> 50\mu\text{m}$ ). Although only one apatite aliquot was analysed during this preliminary investigation, the young (U-Th)/He age and low analytical uncertainties suggest the age should be accepted. The  $F_T$  apatite (U-Th)/He age is  $\sim 10$  Ma younger than the ages obtained from the zircon (U-Th)/He analyses.

### 6.7.2.1 Interpretation of the zircon and apatite (U-Th)/He data

The reproducibility of the ZHe ages across different crystal sizes implies rapid cooling (see Chapter 2). The age reproducibility of the zircon (U-Th)/He analyses also suggests that if the analysed crystals are zoned, the zonation has a consistent effect on the (U-Th)/He ages of all crystals. As the  $F_T$  corrected ages from multiple crystal aliquots of different crystal sizes are in close agreement, it is therefore probable that U and Th zonation can be approximated as a homogeneous distribution (i.e. these zircons are sector zoned or have very fine and regular oscillatory zonation). No CL images could be obtained because of the low zircon yield in the trial separate, and all crystals were used for (U-Th)/He analysis. Without CL images the existence of depleted- or enriched- rims cannot be discounted (see discussion in Section 4.10.2), however it is considered unlikely.

Forward modelling of the predicted rapid Palaeogene cooling event, some time between 60 and 55 Ma, is inconsistent with the measured ZHe ages, unless the analysed crystals exhibit extreme zonation. This zonation requires strongly enriched rims of between 20 - 43 % of the effective crystal radius, (dependant on crystal size). Small changes in the width of the strongly enriched rims will cause significant changes in the measured (U-Th)/He age for each individual crystal, and

so good age reproducibility is not to be expected (see discussion in Section 4.10). Multiple crystal aliquots were used for this sample, and so the effect of any variable U and Th zonation on the measured (U-Th)/He age will be reduced, however it seems improbable that the size selection criteria would cause such accurate separation of crystals with very different zonation.

Depleted rims may also generate reproducing (U-Th)/He ages. If these zircons exhibit depleted rims, the age of the cooling event may be significantly younger. From the forward modelling, the reproducible ZHe ages are also generally inconsistent with slower cooling histories, unless zonation is extreme and of variable width.

If the good age reproducibility of this sample is because the U and Th distribution can be approximated as homogeneous, the forward modelling suggests that the observed ZHe ages are consistent with a rapid cooling event at ~ 47 Ma. The interpretation of a ~ 150 - 200°C cooling event at 47 Ma implies one of three scenarios:

- Plutonic intrusion occurred at ~ 55 Ma (or earlier), and the initial phase of cooling was accompanied by rapid denudation. A later thermal event then re-set the ZHe data ~ 47 Ma. This event must have been high-temperature to re-set the ZHe ages, and may be associated with intrusion at shallow levels.
- Plutonic intrusion occurred at ~ 55 Ma (or earlier), and denudation was not synchronous with the plutonic cooling of the complex. Significant and rapid denudation then occurred at 47 Ma (equivalent to 150 - 200°C cooling event).
- Plutonic intrusion occurred at, or continued to ~ 47 Ma. The ZHe data then represents the magmatic cooling of the Complex, synchronous with the major phase of denudation.

When combined with the ZHe data, the AHe data is ambiguous, and can be described by a monotonic cooling over 45 - 55 Myr from initial temperatures of ~ 90 - 100°C, or by more rapid cooling at ~ 37 Ma. Apatite (U-Th)/He analyses of aliquots of different size fractions, and AFT analysis will enable these scenarios to be distinguished.

## 6.8 The post-magmatic evolution of the HIP: Insight and implications

The thermal evolution that has been constrained by this study shows that the existing hypothesis, of rapid cooling and denudation, is a considerable oversimplification. The key events in the thermal evolution of the HIP can now be summarised as follows:

- Initial post-intrusive cooling was rapid across all the Central Complexes (ACC, MCC, RCC and SCC). This event cooled rocks currently at surface to approximately 80°C

immediately after intrusion (approximately 60 Ma, RCC, ACC and MCC and approximately 55 Ma, SCC).

- The subsequent thermal history of the Mull and Ardnamurchan complexes cannot be constrained without further low temperature thermochronometry.
- The initial rapid cooling and denudation that unroofed the Rum Central Complex was followed by a subtle reheating event. This heated rocks within 800 m of the palaeosurface to between 80 - 90°C. Cooling after this thermal maximum began at approximately 48 Ma. Once the thermal perturbation had decayed the RCC has experienced slow cooling from less than 40°C (limited evidence)
- The initial rapid cooling and denudation of the Skye Central Complex was followed by a short lived reheating event at approximately 47 Ma. This event peaked at 120 - 160 °C, and the decay of the thermal pulse was very rapid. The highly localised resetting of AFT ages along existing structural weaknesses strongly suggests a hydrothermal origin. Once the thermal perturbation had decayed, the SCC samples experienced slow cooling from less than 40°C.

The thermal perturbation identified during the post-rifting history of the HIP can be accounted for by a phase of localised, small volume intrusive activity beneath both Rum and Skye at ~ 47 Ma. Voluminous shallow level intrusion ceased at ~ 55 Ma, and no younger rocks have been identified in the HIP. However, multiple phases of dyke emplacement across the HIP [Bell & Williamson, 2002] mean that small volume intrusions may have been overlooked. Dyke emplacement may provide a mechanism for rapid heat transfer to shallow levels. The geological constraint implies that the RCC samples were at very shallow crustal levels prior to the reheating event [Emeleus, 1973, 1985; Holness & Isherwood, 2003]. Such tight constraints cannot be applied to the SCC samples. However, the new AFT and AHe ages, and the existing AFT length distributions [Lewis *et al.*, 1992] suggest that only limited erosion has occurred after an initial rapid denudation event. The effects of these thermal anomalies are spatially limited within the individual complexes, and this suggests that the thermal input was insufficient to trigger localised denudation. The heat from the intrusion was dissipated by hydrothermal circulation.

Although this event is only resolved on Rum and Skye, the low yields of apatite in the plutonic rocks from the Mull and Ardnamurchan Central Complexes prevents the more detailed investigation of the thermal evolution in these regions. The ~ 60 Ma AFT ages from the ACC and MCC suggests that significant re-heating did not occur. The lithologies from the RCC and SCC that reveal the effects of the re-heating event, are those associated with structural weaknesses in the Central Complexes (pegmatitic veins and fault bounded intrusions). These may have acted as

preferential fluid pathways. The sampled lithologies from the ACC and MCC are generally more massive plutonic units, and so the thermal event is less likely to be recorded. Further constraint of the low temperature thermal histories of the ACC and MCC will determine if these complexes also experienced a similar late-stage thermal event. The existence of such anomalies in the ACC and MCC would indicate widespread late-stage magmatic activity in the HIP, and therefore infer that these effects were triggered by a regional event.

The timing of emplacement of the St Kilda Central Complex has not been tightly constrained, nor has the depth of intrusion. The preliminary thermochronology resolves a significant cooling event, but cannot determine if this is because of isothermal relaxation following the initial intrusion, a later pulse of emplacement (which may, or may not be accompanied by denudation), or because of rapid denudation significantly after intrusion. These scenarios imply very different geological events. However they all require a substantial change in the crustal regime at ~ 47 Ma. Determination of the geological significance of the young, post-rifting cooling ages from the St Kilda Central Complex is paramount to understanding the lithospheric response to the early Palaeogene magmatism and rifting, and for constraining the mechanism driving the post-rifting cooling event.

### 6.8.1 Possible sources for a mid-Eocene thermal anomaly

The thermochronology shows that the magnitude of the thermal anomaly increases towards the NW (Rum ~ 80 - 90°C  $T_{max}$ , Skye ~ 120 - 180°C  $T_{max}$ ), culminating with a significant cooling event at St Kilda that is in excess of 200°C, which may represent a phase of voluminous intrusion. The temporal correlation between these events suggests that the driving mechanism in all three regions is related. Several isolated dykes, emplaced between ~ 45 - 50 Ma (the Loch Roag Dyke, Outer Hebrides, 45.16 ± 0.02 Ma [Timmermann, *pers. com.* unpublished data], and the Inver Dykes, Northern Ireland, 44 - 41 Ma, [Kirstein & Timmermann, 2000]) and more voluminous basaltic magmatism in the Rockall Trough (see Table 26) [O'Connor *et al.*, 2000], provide corroborative evidence for a magmatic episode along the UK margin at ~ 47 Ma. The dykes from Northern Ireland [Kirstein & Timmermann, 2000] suggest that limited magmatic intrusion may have occurred over a wide region, and the thermochronology from St Kilda also suggests that this complex may have experienced shallow level intrusion at this time.

The new thermochronology suggests that an intrusive episode affected a much wider region of continental shelf, and extends the spatial extent of the post-rift magmatic activity to the HIP. A thermal anomaly has now been recorded in Rum, Skye, and St Kilda. In these areas shallow level intrusive magmatic activity had previously thought to have ceased ~ 8 Myr prior to the thermal event. The thermochronology and geological constraints are generally inconsistent with *continued*

magmatic activity at depth, and the magmatic system must therefore have been re-established at ~ 47 Ma. The reestablishment of intrusive activity could be caused by a re-organisation of the stress regime (structural control), allowing localised melt generation, or by the rejuvenation of a thermal anomaly in the mantle (thermal control).

Magmatic activity along both flanks of the North Atlantic margin is pulsatory, and is typified by short-lived high-volume events [Saunders *et al.*, 1997 and references therein]. In Greenland, the continental volcanism is separated into three discrete phases associated with plume impact (62 - 59 Ma) [Saunders *et al.*, 1997], continental break up (57 - 54 Ma) [Larsen & Saunders, 1988], and the passage of the plume beneath the rifted margin (50 - 47 Ma) [Clift & Turner, 1995; Tegner *et al.*, 1998; Storey *et al.*, 2004]. The main phase of emplacement in the HIP is considered part of the plume impact event, associated with the sub-lithospheric diversion of a large plume head containing anomalously hot mantle material [Thompson & Gibson, 1991]. It has also been suggested that the youngest units (the later Skye Granites and perhaps the Sgurr of Eigg pitchstone) are associated with the pulse of syn-rift magmatism. The correlation between the newly resolved thermal event at ~ 47 Ma, the younger phase of magmatism seen in Greenland, and the basaltic eruptions in the Rockall Trough is striking. Palaeoreconstructions of the NAIP showing the positions of Greenland and the UK, relative to the location of the Iceland plume are shown in Figure 87, Figure 88 and Figure 89 [Torsvik *et al.*, 2001]. These figures show the width of the pre-rifted basin, the extent of oceanic crust at 47 Ma, and the modern North Atlantic for reference, and illustrate the large distances over which the plume material was transported before melting occurred beneath the HIP.

Correlation of post-rifting magmatic events at ~ 47 Ma across the large regions of the NAIP, and across both rift flanks may suggest that the emergence of the Iceland plume into the oceanic basin was a triggering mechanism for late-stage magmatic events across the entire North Atlantic. This implies that the effect of this event must have crossed the spreading centre. Evidence for a largemantle event in the mid-Eocene is perhaps reflected in the short-lived, increase in the spreading rate recorded at this time (Figure 90) [Torsvik *et al.*, 2001], and the high-volume volcanic events in the Rockall Trough. If material is to be transported across the spreading centre, the volume, depth at speed at which this motion occurred would have to be sufficient to prevent complete dissipation along the rift axis. The voluminous basaltic extrusive events in the Rockall Trough imply that substantial volumes of hot mantle material existed beneath the European margin at this time, and the trace element and isotopic signatures of the Rosemary Bank basaltic sequence (see Appendix F for location) are similar to the present day Iceland plume [Hitchen *et al.*, 1997]. The thermal events affecting the HIP could therefore represent the lateral extension of this hot

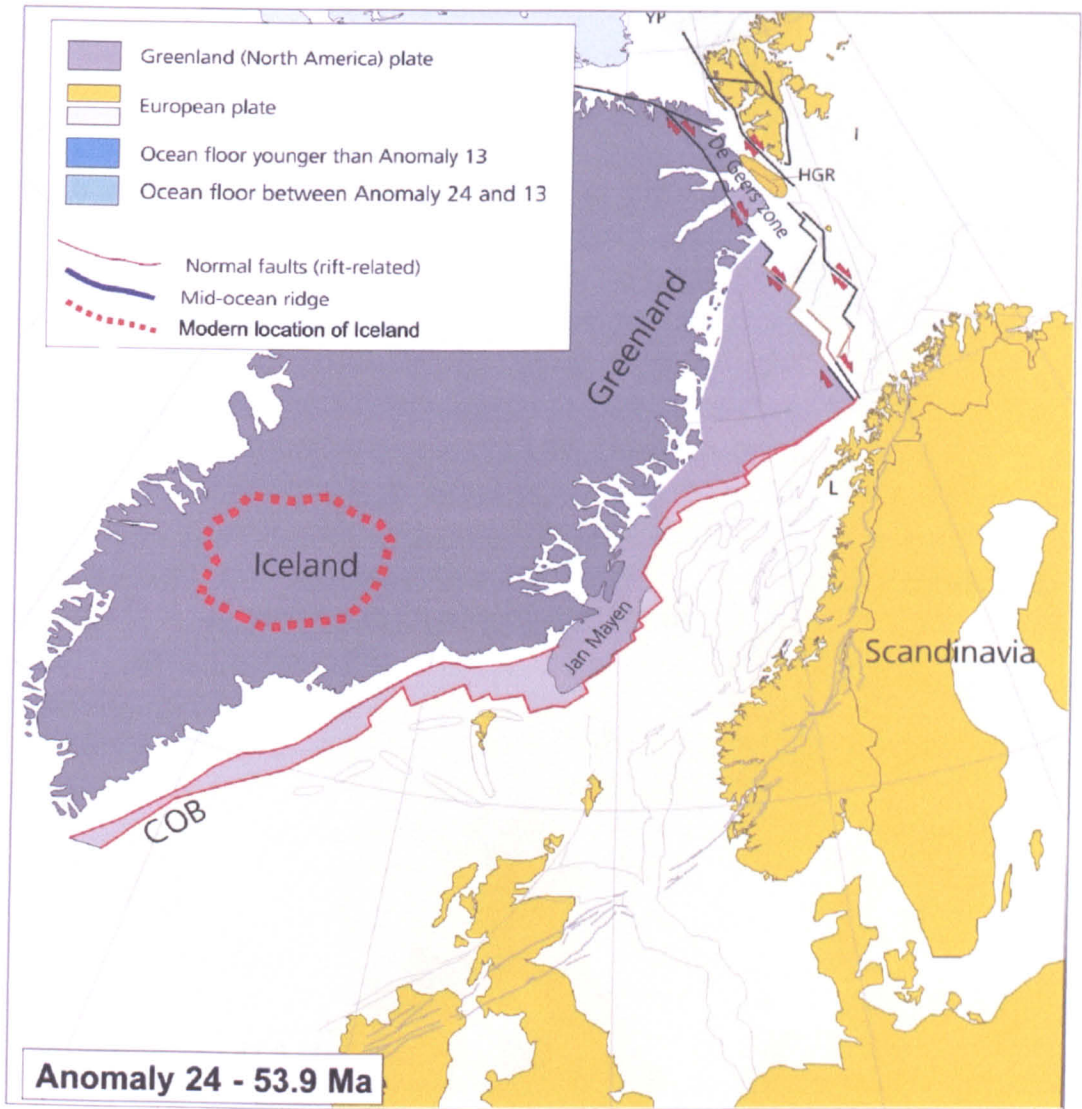


**Figure 87 - Palaeo-reconstruction of the North Atlantic at ~ 55 Ma**  
 [modified from Mosar *et al.*, 2002; Moser & Torsvik, 2002], showing the pre-rifting geometry of the incipient margin and the location of the land masses relative the modern day Iceland plume.

mantle material beneath the continental shelf. The mid-Miocene ages from dykes in Ireland implies that this material magmatic activity could have extended over a large region, and that the transport of this material may have exploited the same sub-lithospheric topography as the early-Palaeogene event. It is possible that both thermal and structural mechanisms controlled the melt generation at this time. Pre-existing lithospheric structures are thought to have controlled the transport and sub-lithospheric ponding of high temperature mantle material during the initial impingement of the plume head [Thompson & Gibson, 1991]. These crustal features may also control later magmatic events. The intersection of the Caledonian faults, with Palaeogene NW-trending zones of high crustal dilation, is thought to have controlled the location of initial phase of intrusion in the HIP (see Figure 67) [Richey, 1961; Preston, 1982; Butler & Hutton, 1994].

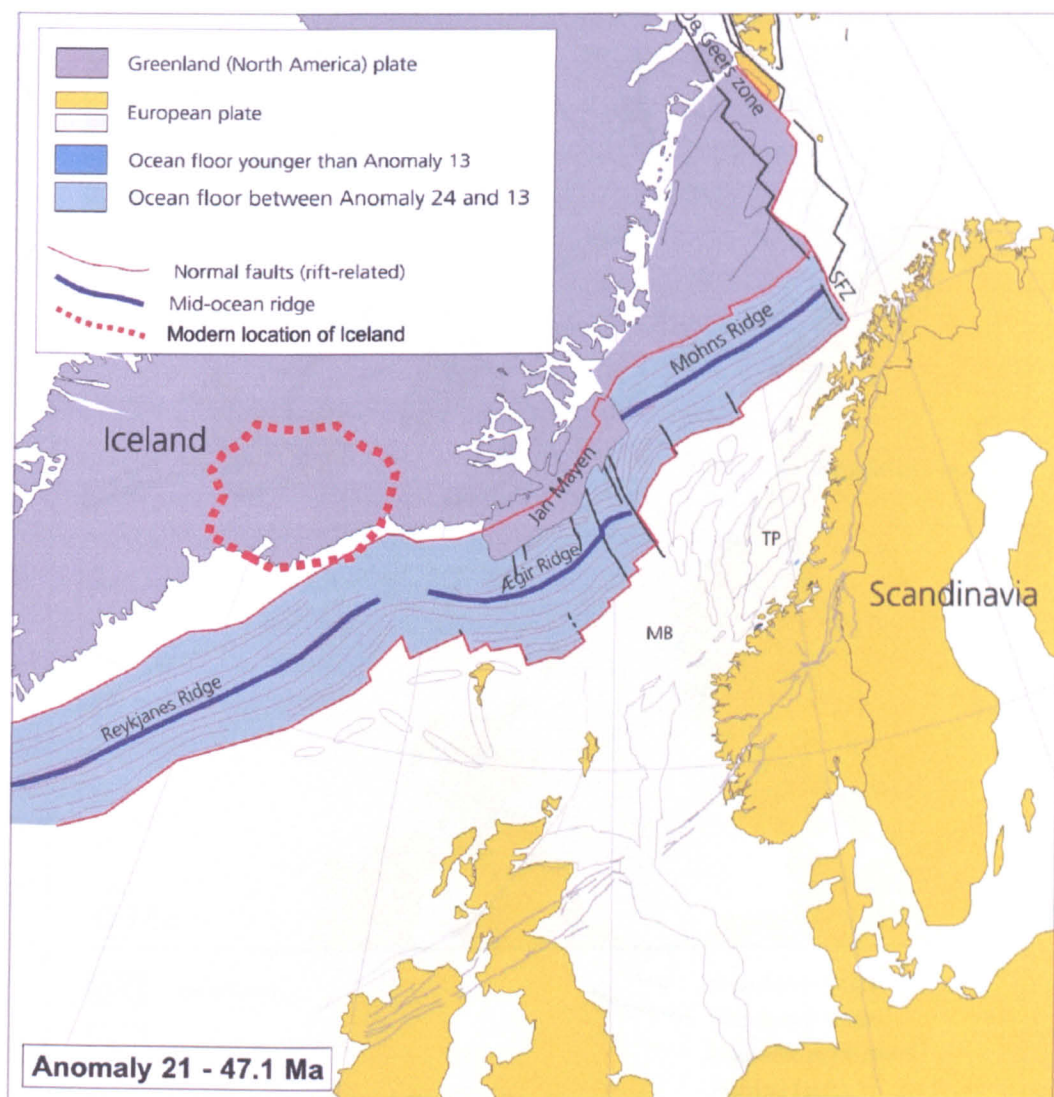


**Figure 88 - Palaeo-reconstruction of the North Atlantic at ~ 47 Ma**  
 [modified from Mosar *et al.*, 2002; Moser & Torsvik, 2002], showing the pre-rifting geometry of the incipient margin and the location of the land masses relative the modern Iceland plume.

Changes in the volume of melt within the upwelling plume would affect the thermal structure of the mantle, and would also alter the stress regimes in the overlying crust. Changes in the mantle flow regime may therefore have caused the further re-activation of the Caledonian structures, permitting intrusion at ~ 47 Ma.

Application of low temperature thermochronology to the other intrusive complexes across the European margin, that were inactive at ~ 47 Ma, would allow the spatial extent of the anomaly to be determined. This is a critical study if the spatial extent and volume of the thermal anomaly are to be constrained, and the regional impact of such a large scale mantle event is to be understood. The absence of accurate radiometric ages from the offshore seamounts currently prevents such an investigation. Furthermore, many of the offshore sequences contain few lithologies suitable for

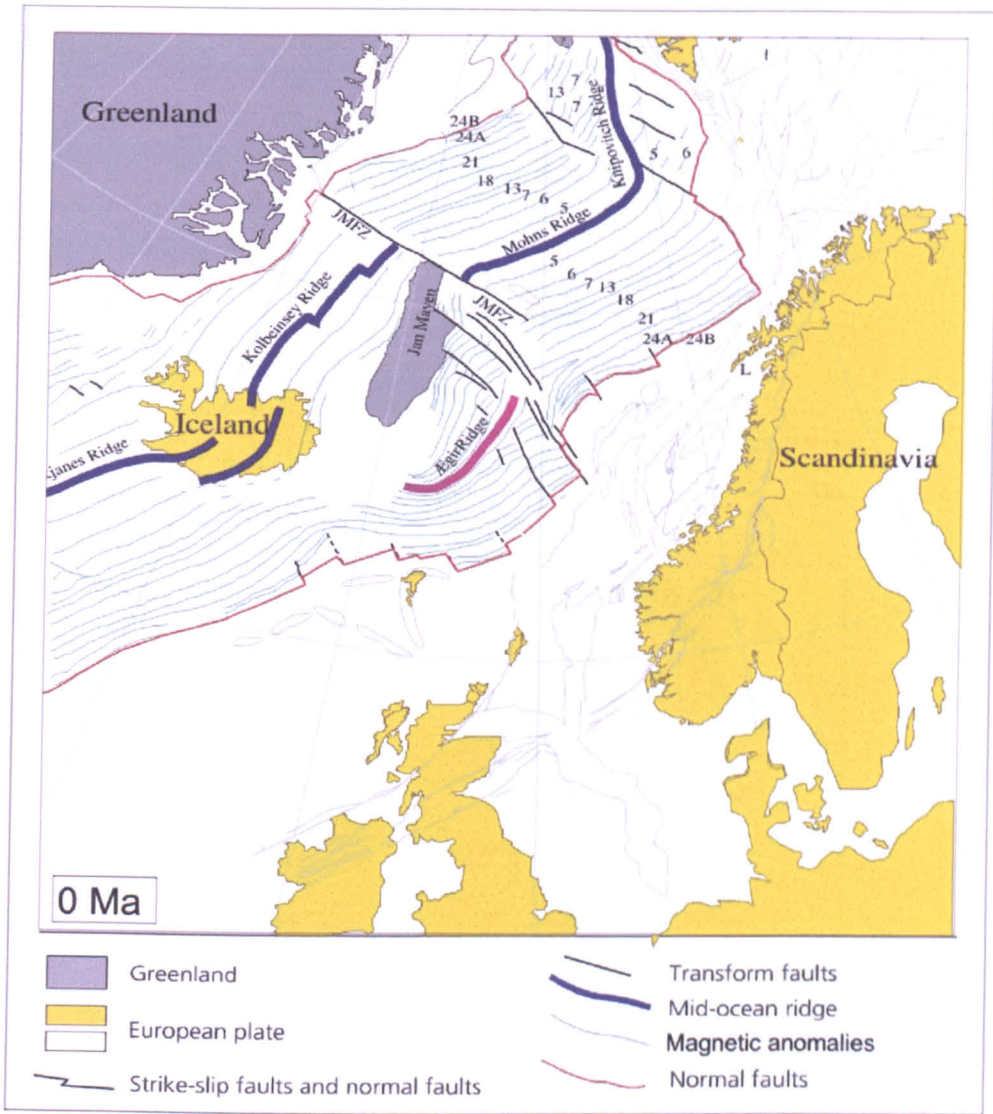


**Figure 89 - The North Atlantic at present day** [modified from Mosar *et al.*, 2002; Moser & Torsvik, 2002], showing the magnetic polarity Chrons (green) as numbered.

low temperature thermochronometry, and the volumes of samples obtained from boreholes and dredging is usually limited.

No intrusive or extrusive unit in the HIP has been correlated to a mid-Eocene event, but the thermochronology has resolved a previously unidentified component to magmatism in this region. The low temperature event recorded in the HIP may represent the later stages of magmatic underplating; however no pulse of denudation is recorded at this time. Furthermore, shallow level of emplacement is generally expected, if late-stage magmatism exploits existing structural weaknesses that previously permitted volcanism. It is therefore surprising that extrusive and intrusive units are not seen. In the HIP it is possible that the silicic emplacement, during syn-rift magmatism, may act as a barrier to the ascent of denser mafic material [e.g. Bell & Williamson,

2002]. The hydrothermal activity in the SCC is suggestive of small volume emplacement at a relatively shallow depth.

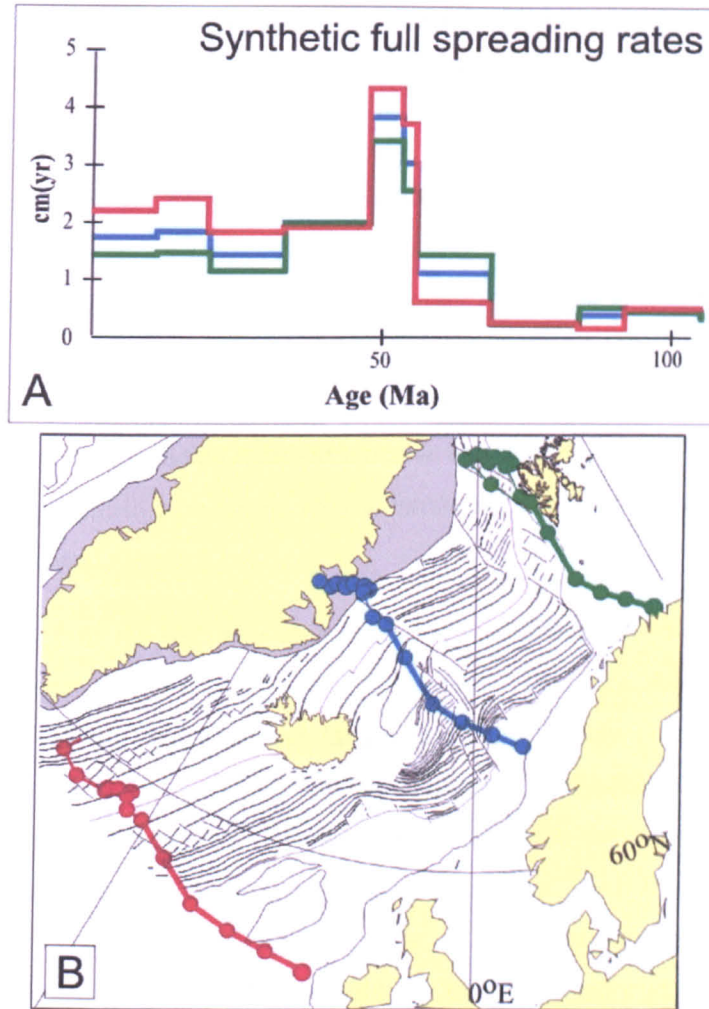


**Figure 90 - Full palaeo-spreading rates for the Mid Atlantic Ridge**  
**A)** Spreading rates calculated for Europe vs. Greenland) for the North Atlantic along three traverses. Rockall (red), Mid Norway (blue) and Northern Norway (green). **B)** The location of the traverses. Colours as for A [modified from Torsvik *et al.*, 2001].

## 6.9 The HIP in the global context

The HIP and the North Atlantic contain some of the most extensively studied igneous rocks in the world, yet debate continues to surround many aspects of the formation of the NAIP. Dominant among the issues is the nature of the Iceland plume [Coffin & Eldholm, 1994; Foulger *et al.*, 2005], and its role in the initiation of rifting [Coffin & Eldholm, 1994; Barton & White, 1995; Lundin & Dore, 2002; Foulger *et al.*, 2005], the dynamic support of the North Atlantic sedimentary basins [White & Morton, 1995; Clift, 1997; Clift *et al.*, 1998], and the generation of magmatism [Coffin & Eldholm, 1994; Barton & White, 1995; Tegner *et al.*, 1998; Storey *et al.*, 2004; Foulger *et al.*, 2005]. In the NAIP, pulses of magmatic activity pre-, syn-, and post-date the onset of sea-floor

spreading, however the timing of peak LIP formation on other volcanic rifted margins is highly variable. In the Parana-Etendeka peak LIP formation is syn-rifting, and in the Central Atlantic province it is syn-rift in North Africa, but post-dates rifting in SE USA [see reviews in Mahoney & Coffin, 1997; Menzies *et al.*, 2002 and references therein]. However, where radiometric dating has provided accurate constraints, discrete pulses of magmatic activity are observed along many volcanic rifted margins.

In LIPs the rapid formation, and equally rapid denudation of central volcanic edifices, means that pulsed magmatism may cause repeated heating and cooling events during the development of an individual magmatic province. In a rapidly evolving landscape, younger volcanic sequences may be constructed on, or at the margins of older plutonic complexes. The process of repeated structural re-activation may not be limited to the accommodation of late-stage magmatism. When fertile mantle anomalies are generating localised intrusive or extrusive activity, changes in the local stress regime may trigger small- to moderate volume intrusion along existing structural weaknesses elsewhere above the anomaly.

The thermochronology from the HIP, also suggests that re-activation of structural elements within the crust can permit later intrusive activity over large areas. This may also imply that mantle material continues to exploit long-lived sub-lithospheric heterogeneity [Thompson & Gibson, 1991] for several Myr after the initial plume head has dissipated. In the HIP late-stage magmatism appears to exploit existing weaknesses, generating intrusion within the boundaries of the older complexes, but elsewhere, dyke intrusion in basement lithologies (Loch Roag, Outer Hebrides) suggests crustal dilation can be initiated along new, or previously unexploited weaknesses. Structural re-activation and variable local stress fields are to be expected when the volume of melt generated in the sub-lithospheric changes, or fresh fertile mantle is injected into the system. The HIP data suggest that re-activation can occur more than 10 Myr after the initial intrusive exploitation.

Given the common occurrence of pulsed intrusive activity on volcanic rifted margins, it is surprising that low temperature events are not more common. However, the thermal anomalies associated with increased, generally short-lived heat flow above intrusion, are generally below the thermal resolution of the most commonly applied dating techniques (U-Pb and Ar-Ar). Therefore it is unlikely that low temperature events would be easily recognised without the application of low temperature thermochronometry.

### 6.9.1 Low temperature thermochronology in LIPs

There is a considerable body of literature on the low temperature evolution of rifted margins; however volcanic margins are generally under represented. The majority of studies that have

investigated the denudation along passive margins have applied AFT and AHe to the pre-rift sedimentary and basement assemblages. These studies have generally ignored the pre-, syn- and post-rift volcanic units.

Low temperature thermochronology is uniquely suited to investigating if re-heating events associated with late-stage magmatism are a commonly occurring component of LIPs. However, the generally poor preservation, and dominantly mafic lithologies in many LIPs may limit the application of these techniques. Regional exhumation generally follows LIP emplacement and this typically generates between 1 and 3 km of denudation [see review in Bryan *et al.*, 2002]. This leads to the removal of the lithologies suitable for low temperature thermochronology, as the volcanic sequences generally become more evolved up-section. In addition, the relative timing and rate of the denudation is often poorly constrained, and magmatic activity can occur before, during or after the denudation event. Unless the timing of denudation is constrained, the low temperature thermochronology may not be able to resolve distinct cooling events. When the denudation is post-magmatic, i.e. significantly after the major intrusive event, the thermochronology may be unable to distinguish between the rapid removal of a 1 - 3 km crustal section, and the cooling associated with late-stage intrusion. This ability to resolve separate event will often depend on constraints provided by field evidence. Preferential selection of samples from the root zones of the Central Complexes should improve the ability to resolve these events, as protracted preservation of the topographic high of the volcanic edifice is improbable. However, the local tectonic and structural controls should be considered.

The age of many LIPs will also limit the resolution of late-stage thermal events. The HIP samples are relatively young, and have had an apparently simple thermal history since ~ 45 Ma. It is therefore possible to resolve the different signatures of the two cooling events (initial rapid cooling accompanied by denudation, and later cooling from the maximum temperature of the thermal event). In older LIPs, the limited temporal resolution that can be achieved using thermochronology becomes a factor. For example: for a 60 - 70 Ma emplacement age (e.g. NAIP, Deccan) the use of multiple thermochronometers can separate the signatures of a 60 Ma and a 47 Ma cooling event, a temporal scale that is comparable with the age uncertainty on (U-Th)/He determinations. For samples emplaced at 120 - 130 Ma (e.g. Parana-Etendeka, Australia), resolution of 10 Myr is much more difficult, and at 180 - 200 Ma (e.g. Karoo, Central Atlantic), it will generally be impossible, as age uncertainties will typically be  $\pm 16$  Myr. If these late-stage magmatic events more than 10 Myr after the major intrusive phase, then resolution in older LIPs may be possible. However, extraction of information from AFT length distributions will be complicated for older samples, as both the country rock and the LIP units have experienced long, and potentially complex low temperature thermal histories. This will increase the complexity in the observed fission track

length distributions, and the number of short tracks, and will also increase the impact of diffusion on AHe ages. Both factors will make accurate interpretation of the data very difficult, except where there is a significant difference in the age of the LIP and the country rocks.

## 6.10 Testing the hypothesis

Although pulsed magmatic activity is known to be a feature of LIP and rifted margin formation, the corroboration of low temperature thermal events in other LIPs will be difficult. Constraining the spatial distribution and frequency of these late-stage thermal events is important, if the true volume, duration, and impact of LIP magmatism is to be assessed. A better understanding of the NAIP event is required before comparison with other LIPs can be attempted, and tighter constraint of the low temperature evolution of other European margin central complexes is needed. Testing the hypothesis; that late-stage intrusive activity is a widespread feature of LIP magmatism, and determining the causal mechanisms will be challenging. However, the intrusive silicic complexes associated with the Deccan-Seychelles, Columbia River, and Ethiopia-Yemen LIPs seem the most suitable regions in which to begin.

The generally poor preservation of LIPs, and the potentially subtle nature of later magmatic episodes, means that the low temperature thermochronometers are the only techniques that have the ability to resolve the geometry and behaviour of the mantle plume, and determine the true nature and extent of the plume-lithosphere interaction.

# A

## Column Calibration

### A.1 Calibration procedures

Calibration of the columns was achieved by sequential collection of elutes to determine the exact location and duration of U and Th release. Initial calibration used 1 ml of an  $^{230}\text{Th}$  and  $^{235}\text{U}$  spiked Durango apatite solution and clearly showed the peak U and Th discharge from the columns (Figure 91). Yields and isotope ratios were indistinguishable from a control sample solution, and elution of the U and Th occurred before 5 ml of the stripping solution had been passed through the columns.

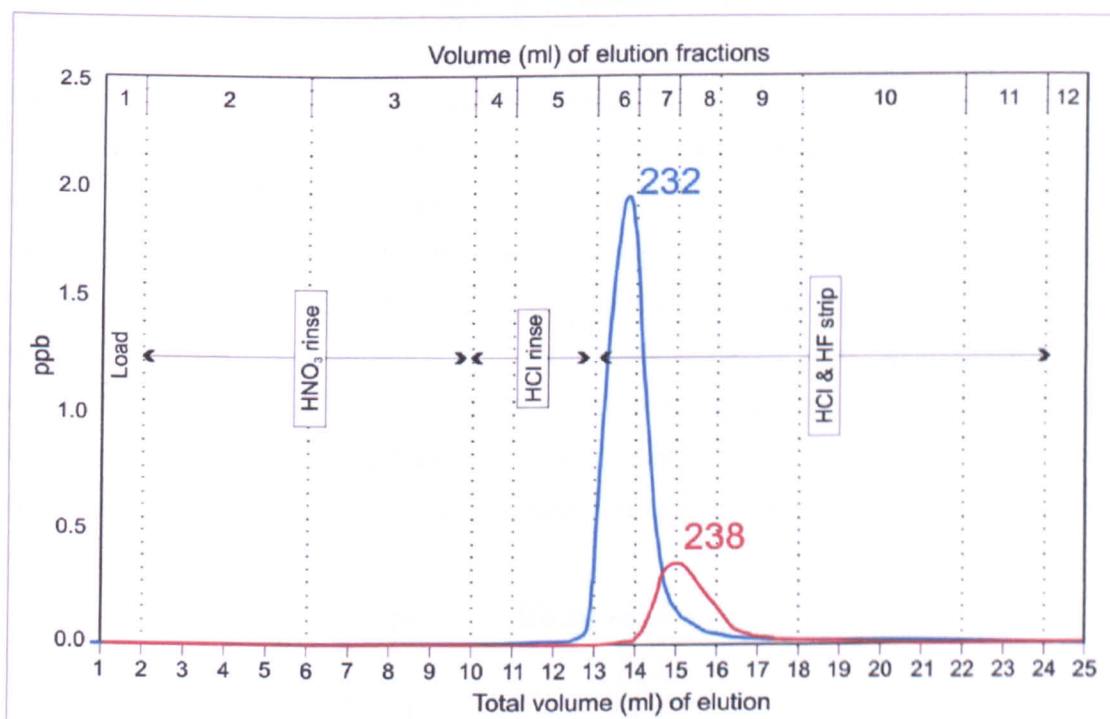


**Figure 91 - The natural U and Th measured in each sequential elution fraction. The volume of each of the 12 elution fractions is indicated on the upper x-axis.**

Figure 92 shows the results of further calibration to corroborate that zircon behaved in a similar manner on the resin. The figure shows the measured counts per second for each of the four masses routinely measured. For a synthetic zircon solution containing no dissolved Pt (shown in blue) the

elution of the U and Th occurs during the first 2 ml stripping step, 1 - 15% of the  $^{230}\text{Th}$  spike was released between 2 - 8 ml, and the volume of this final elution step was therefore increased to 12 ml to ensure complete elution of U and Th.

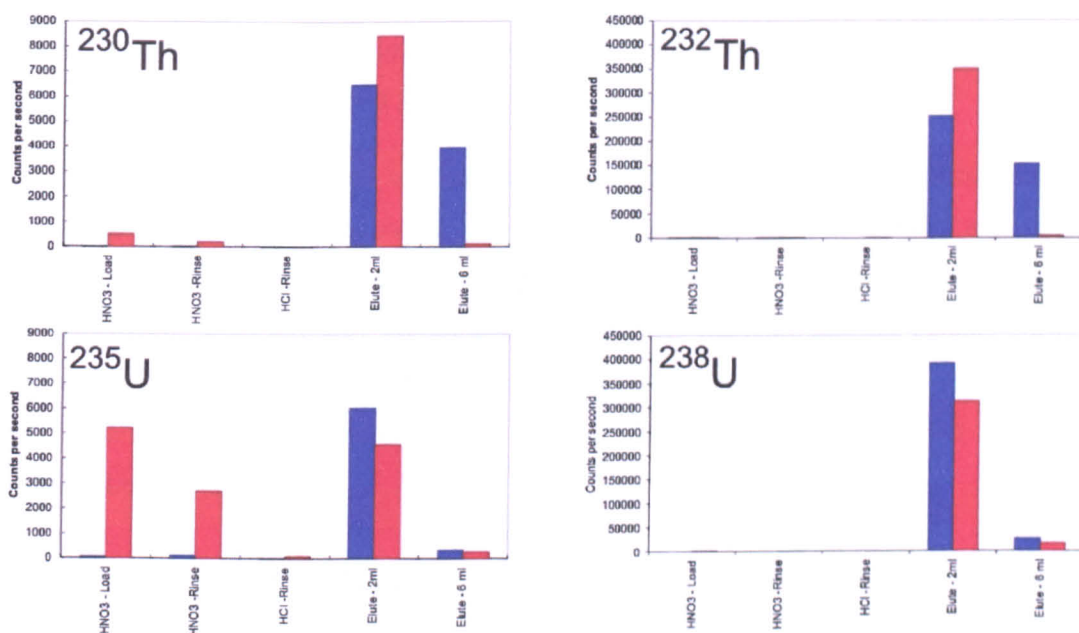


**Figure 92 - Column calibration using a synthetic zircon solution (blue) and a synthetic zircon solution with ~ 200 ppm Pt.**

The second set of calibration curves shown on Figure 92 were obtained from a synthetic zircon solution with ~ 200 ppm Pt, equivalent to a dissolved Pt foil tube (shown in red). The counts recorded on all masses were above background during the load and rinse stages, with masses 230 and 235 having the highest number of counts. The relative abundances of these peaks does not correspond to the mass of the  $^{230}\text{Th}$  and  $^{235}\text{U}$  spikes added to the solutions. The measured cps at masses 230 and 235 in the stripping elutions corresponds well to the known spike volumes added, with ~ 98 % yield. The source of the above background measurements on during the load and rinse stages therefore represents  $\text{PtAr}^+$  formation in the mass spectrometer. The relative natural abundance of Pt isotopes (Table 23) corroborates this observation, with the relative cps at each mass reflecting the relative abundance.

Isotope	Natural Abundance (%)
190 Pt	0.014
192 Pt	0.782
194 Pt	32.967
195 Pt	33.832
196 Pt	25.242
198 Pt	7.163

**Table 23 - The relative natural abundance of Pt isotopes.**

The yields of both the Pt-free and Pt-bearing solutions during the stripping stage are within error, suggesting that complete elution of Pt occurs during the rinse stage. To ensure this is the case the volume of  $\text{HNO}_3$  used as a rinse was increased from 9 ml to 12 ml.

To corroborate that all Pt was removed prior to the U and Th elution, and therefore that there are no interference issues when measuring U and Th on unknown samples, a more detailed analysis of the HNO<sub>3</sub> and HF elute was undertaken. This analysis focussed on the most abundant of the platinum isotopes <sup>195</sup>Pt, and used Micromass Isoprobe MC-ICPMS analysis (at S.U.E.R.C.) to compare the volumes of Pt in the elution against known stock solutions. 100 ppb Pt solution produced a 0.73 V signal at mass 195. Triple distilled 5% HNO<sub>3</sub> recording a -0.002 V signal.

An unspiked Pt bearing solution was passed through the column chemistry outlined below (and Section 3.6.5.2). The final elute collected from the Pt-bearing solution was analysed and generated a signal of 0 V on mass 195, implying ~ 250 ppt Pt in the final elution. The peak at mass 235 was indistinguishable from the daily background measurement, implying that the column chemistry procedure successfully prevented the formation of PtAr<sup>+</sup>. The Pt measured in the elution was below the background measurement on the VG PlasmaQuad PQ2 + used for routine determinations.

## A.2 Resin preparation

To remove the potential for cross contamination, fresh resin was used for each sample, with the Teflon columns cleaned thoroughly between analyses. However, the degradation of the resin over time can also influence the timing and yield of Pt, U and Th from the columns. Resin was therefore activated in small batches to prevent overlong storage. Eichrom TRU Resin (Blue) resin was activated using a solution of concentrated Aristar<sup>®</sup> HNO<sub>3</sub>, concentrated ultrapure HCl and MilliQ H<sub>2</sub>O in a 1:1:1 ratio. 10 - 20 ml of fresh resin was agitated in ~150 ml of the acid solution, then allowed to settle for one hour. The acid and any suspended resin was then decanted and replaced by fresh acid. The solution was agitated and left overnight. The acid was then decanted and the resin rinsed with copious volumes of MilliQ H<sub>2</sub>O. Activated acid was stored in MilliQ H<sub>2</sub>O in pre-cleaned 50 ml Teflon™ beakers until required. Regular column blanks and yield tests were performed using spiked (<sup>230</sup>Th and <sup>235</sup>U) solutions containing 5, 10 and 20 ppb natural U-Th.

## A.3 Column chemistry procedure

The following column chemistry procedure was performed on all zircon samples analysed.

### A.3.1 Column preparation

- 1) Rinse teflon column and frit with MilliQ H<sub>2</sub>O
- 2) Rinse column and frit with distilled ethanol
- 3) Add 1ml Eichrom TRU (blue) resin.
- 4) Rinse teflon column and frit with ~ 10 ml MilliQ H<sub>2</sub>O

### A.3.2 Column chemistry procedure

- 1) Clean resin with 1 ml then 8 ml of 0.2 M HCl
- 2) Clean resin with 1 ml then 8 ml of 0.1 M HCl + 0.3 M HF
- 3) Pre-condition column with 1 ml then 8 ml of 1.5 M HNO<sub>3</sub>
- 4) Load sample in 1 ml 1.5 M HNO<sub>3</sub>
- 5) Rinse with 12 ml of 1.5 M HNO<sub>3</sub>
- 6) Rinse with 2.5 ml 3 M HCl
- 7) Discard all previous elutions with copious volumes of water
- 8) Place 15 ml beaker for Th and U
- 9) Elute U and Th using 2 ml then 10 ml 0.1 M HCl + 0.3 M HF
- 10) Place 15 ml beakers on a hot plate (80°C) and evaporate to dryness
- 11) Rehydrate samples in 2 ml 5 % HNO<sub>3</sub> and trace HF (0.01%).
- 12) Equilibrate sample solutions on a hotplate at 100°C for 48 hours

### A.3.3 Column cleaning

After use the resin is discarded and the column and frit rinsed with MilliQ H<sub>2</sub>O. The columns are then rinsed 5 times with 0.1 M HCl + 0.3 M HF, then rinsed with MilliQ H<sub>2</sub>O before storage in 1.5M HNO<sub>3</sub>. If storage time is substantial, the 1.5M HNO<sub>3</sub> is discarded and the columns rinsed with fresh 0.1 M HCl + 0.3 M HF on a regular basis. If left unused for any long periods the columns were cleaned by refluxing them with 0.1 M HCl + 0.3 M HF in a warm water bath (~ 80°C) for 2 - 6 hours.

# B

## The calculation of geometry specific $\beta$

### B.1 Complex crystal geometries

For the complex crystal and termination geometries discussed in Section 4.4 and shown in Figure 13, it is easier to calculate the surface area-to-volume ratio by considering the body and the terminations separately. Figure 3 is repeated here.

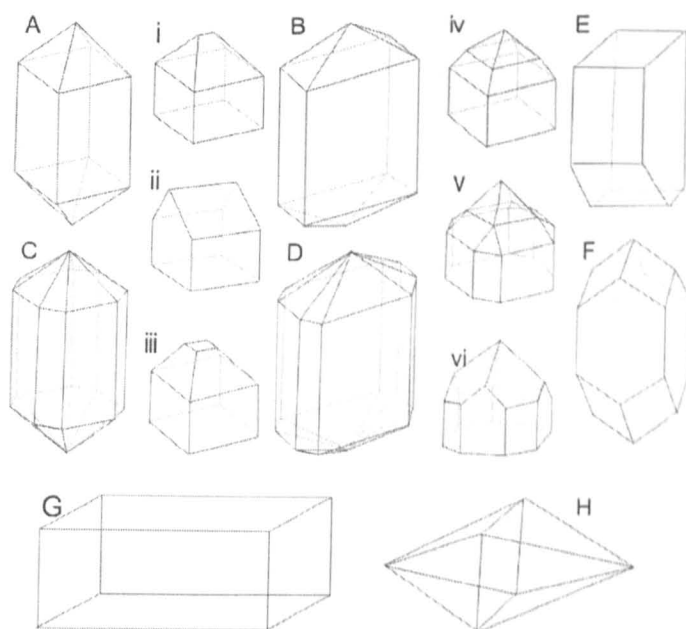


Figure 93 - Typical crystal and termination geometries seen in magmatic zircon.

### B.2 The body of the crystal

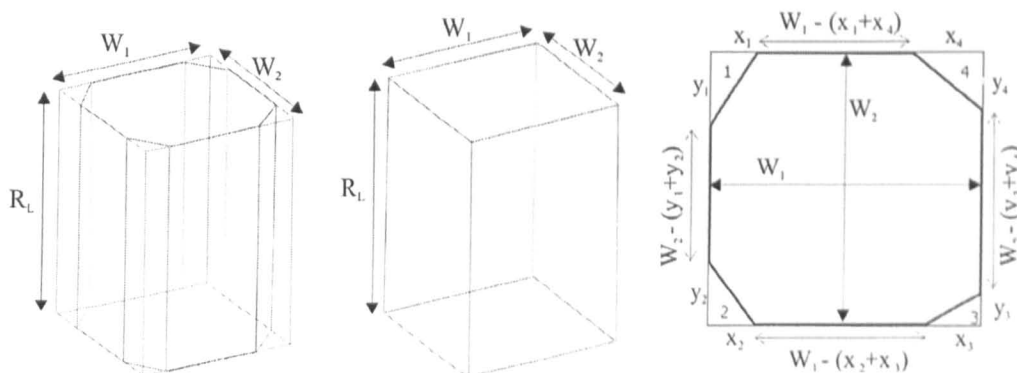
The body of the crystal is defined as the volume of the crystal that has a constant cross section (area and shape). Zircons generally have tetragonal or octagonal cross sections, with two sets of parallel faces which are orthogonal to each other. Therefore all basal sections are bounded by a quadrilateral defined by  $W_1$  and  $W_2$ , as shown in Figure 94.

This definition enables all measurements to be taken in two planes, parallel to the orthogonal maximum crystal widths,  $W_1$  and  $W_2$  (Figure 94). As the calculation of the surface area and

volume of the body of the crystal is independent of the form of the termination, it is considered separately, to simplify the procedure. The surface area includes only the faces parallel to the  $c$ -axis, and is calculated from:

$$\text{Surface Area} = \text{Perimeter} \times \text{body length } (R_L)$$

Equation 35

Figure 94 - The measurements needed for  $\beta$ , volume of the crystal

Which using the measurements defined in Figure 94:

$$\text{Surface Area} = R_L \left[ (2W_1 - (x_1 + x_2 + x_3 + x_4)) + (2W_2 - (y_1 + y_2 + y_3 + y_4)) + \sqrt{x_1^2 + y_1^2} + \sqrt{x_2^2 + y_2^2} + \sqrt{x_3^2 + y_3^2} + \sqrt{x_4^2 + y_4^2} \right]$$

Equation 36

When the prism has a quadrilateral cross section  $\sum_{n=1}^{n=4} x_n + y_n = 0$ , and Equation 36 simplifies to :

$$\text{Surface Area} = 2R_L W_1 + 2R_L W_2$$

Equation 37

The volume of the prism is calculated by:

$$\text{Volume} = R_L \left[ W_1 W_2 - \left( \frac{x_1 y_1 + x_2 y_2 + x_3 y_3 + x_4 y_4}{2} \right) \right]$$

Equation 38

Equation 36 and Equation 38 describe the surface area and volume of the body of all crystals that can be bounded by a quadrilateral with orthogonal dimensions of  $W_1$  and  $W_2$  and simplifies to  $R_L W_1 W_2$  when  $\sum_{n=1}^{n=4} x_n + y_n = 0$

### B.3 The terminations

Calculation of the surface area and volume of the different termination styles is more complex, and a number of additional measurements are required in order to perform the calculations for the different termination forms (i - vi, Figure 93), and different base section geometries (quadrilateral and octahedral). The following calculations deal with one termination only, thereby simplifying

the calculations as much as possible, and allowing the incorporation of the variable termination geometry and length that is commonly seen. The basal surface area of all terminations is described by:

$$\text{Base Area} = W_1 W_2 - \left( \frac{x_1 y_1 + x_2 y_2 + x_3 y_3 + x_4 y_4}{2} \right)$$

Equation 39

The calculations for surface area and volume for complex terminations can often be simplified, and the number of required measurements is reduced by the use of the geometric scaling factors:

$$\frac{\text{Area}^A}{\text{Area}^B} = \left[ \frac{\text{Length}^A}{\text{Length}^B} \right]^2$$

Equation 40

$$\frac{\text{Volume}^A}{\text{Volume}^B} = \left[ \frac{\text{Length}^A}{\text{Length}^B} \right]^3$$

Equation 41

The calculation of the volume and surface area of the terminations requires the height of the apex of the termination to be known. When terminations have the simple form, the projected height of the apex is measured directly ( $T$ ), however for truncated (types i - iii, Figure 93), or compound (types iv - vi, Figure 93) terminations the projected height ( $H$ ); i.e. the height of the termination if it were not truncated, is required (see Figure 95).

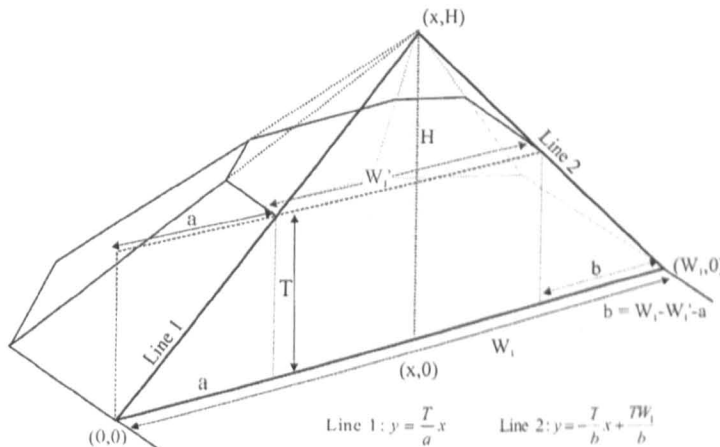


Figure 95 - The measurements required for  $\beta$ , projected termination height

To calculate the projected height, the  $c$ -axis parallel downward projection from the apex is taken. This may not be at the centre of the basal plane ( $W_1, W_2$ ), but both the projected height and the location of apex in the  $W_1 W_2$  plane can be calculated. A cross section through the projected apex is taken so that the intersection with the basal plane is parallel to  $W_1$  and that the cross section intersects both  $W_2$  parallel faces. When the origin of the co-ordinate system is defined as in Figure 95, the equations of the two lines can be written as:

$$\text{Line 1} = \frac{T}{a}x$$

Equation 42

$$\text{Line 2} = \frac{W_1T}{b} - \frac{T}{b}x$$

Equation 43

which can be combined and solved for x:

$$x_{w_1} = \frac{W_1T}{b\left(\frac{T}{a} + \frac{T}{b}\right)}$$

Equation 44

x can then be substituted into either Equation 42 or Equation 43 to calculate the H.

$$\text{Line 1} = \frac{T}{a} \left[ \frac{W_1T}{b\left(\frac{T}{a} + \frac{T}{b}\right)} \right]$$

Equation 45

$$H = \frac{W_1T^2}{ab\left(\frac{T}{a} + \frac{T}{b}\right)}$$

Equation 46

Of the two additional dimensions ( $a$  and  $b$ ) only one has to be measured, as  $a + W_1' + b = W_1$  (see Figure 95). The process is then repeated for a  $W_2$  parallel cross section.

$$x_{w_2} = \frac{W_1T}{b\left(\frac{T}{a} + \frac{T}{b}\right)}$$

Equation 47

### B.3.1 Type iii terminations

This style of termination is considered first as these calculations can be utilised in surface area and volume calculations for other termination styles. For pyramidal terminations, which have similar base section parallel cross sections (i.e. the shape of all base parallel cross sections is the same and the size scales with the height of the section), only two additional measurements are required. The first measurement,  $a$ , is that used above (see Figure 95) to calculate the position of the apex in the  $W_1 W_2$  plane. The second,  $W_1'$  is used with  $W_1$  to calculate the scaling factor:

$$\frac{W_1'}{W_1}$$

Equation 48

The length scaling factor can be calculated from any pair of like dimensions, but  $W_1'$  or  $W_2'$  are the longest dimensions of the terminal face, and so minimises the uncertainties. Using the scaling factors (Equation 40 & Equation 41) the termination volume is calculated by:

$$\text{Volume} = \left[ \frac{\text{Base area} \times H}{3} \right] \left[ 1 - \left( \frac{W_1'}{W_1} \right)^3 \right]$$

Equation 49

Substituting the equations for base area and H, Equation 49 becomes:

$$\text{Volume} = \left[ 1 - \left( \frac{W_1'}{W_1} \right)^3 \right] \left[ \frac{W_1 T^2 \left( W_1 W_2 - \left( \frac{x_1 y_1 + x_2 y_2 + x_3 y_3 + x_4 y_4}{2} \right) \right)}{3ab \left( \frac{T}{a} + \frac{T}{b} \right)} \right]$$

Equation 50

Surface area calculations are more complex, as  $W_1/W_2 > 1.0$  prevent the simple calculation for the surface area (Equation 51), as the slope height will vary for each face. All terminations where the projected apex is off-centre will also have variable slope heights

$$\text{Surface Area} = \frac{1}{2} \text{perimeter} \times \text{slope height}$$

Equation 51

For all pyramidal terminations the surface area can be calculated using:

$$\text{Surface Area} = \left[ \frac{1}{2} [AA' + BB' + CC' + DD' + EE' + FF' + GG' + HH'] \right] \left[ 1 - \left( \frac{W_1'}{W_1} \right)^2 \right] + \left[ \text{Base area} \left( \frac{W_1'}{W_1} \right)^2 \right]$$

Equation 52

where the base area is calculated using Equation 39, and incorporates the surface area of the terminal face when terminations are truncated. A-H are the perimeter measurements that form the base edges of each face (shown in Figure 94, and Figure 96), A'-H' are the slope heights of each face calculated from the perimeter normal distance of each face from the downward projection of

the apex, as shown in Figure 96. The calculations for A-H, the perimeter normal distance, and A'-H' are shown in Table 24.

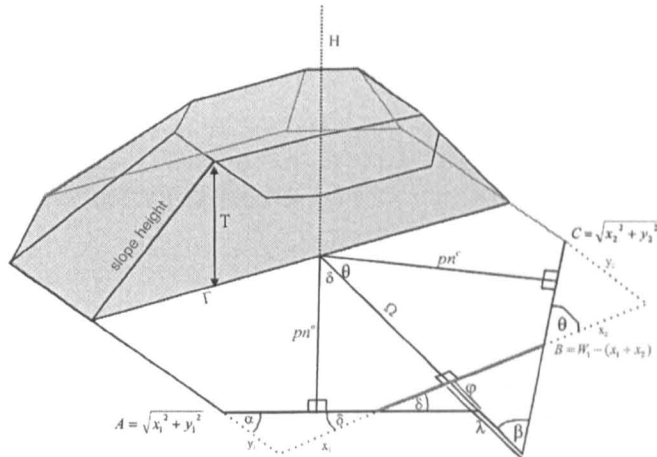


Figure 96 - The measurements required for  $\beta$ , Type iii terminations.

Perimeter measurements	Perimeter normal measurements	Slope heights
$A = \sqrt{x_1^2 + y_1^2}$	$pn^A = \frac{x_1}{\sqrt{x_1^2 + y_1^2}} \left[ \frac{y_1}{x_1} (\Gamma - x_1) + (W_2 - \Omega) \right]$	$A' = \sqrt{H^2 + (pn^A)^2}$
$B = W_1 - (x_1 + x_2)$	$pn^B = \Gamma$	$B' = \sqrt{H^2 + (pn^B)^2}$
$C = \sqrt{x_2^2 + y_2^2}$	$pn^C = \frac{x_2}{\sqrt{x_2^2 + y_2^2}} \left[ \frac{y_2}{x_2} (\Gamma - x_2) + \Omega \right]$	$C' = \sqrt{H^2 + (pn^C)^2}$
$D = W_2 - (y_2 + y_3)$	$pn^D = W_1 - \Omega$	$D' = \sqrt{H^2 + (pn^D)^2}$
$E = \sqrt{x_3^2 + y_3^2}$	$pn^E = \frac{x_3}{\sqrt{x_3^2 + y_3^2}} \left[ \frac{y_3}{x_3} (W_1 - \Gamma - x_3) + \Omega \right]$	$E' = \sqrt{H^2 + (pn^E)^2}$
$F = W_1 - (x_3 + x_4)$	$pn^F = W_2 - \Gamma$	$F' = \sqrt{H^2 + (pn^F)^2}$
$G = \sqrt{x_4^2 + y_4^2}$	$pn^G = \frac{x_4}{\sqrt{x_4^2 + y_4^2}} \left[ \frac{y_4}{x_4} (W_1 - \Gamma - x_4) + (W_2 - \Omega) \right]$	$G' = \sqrt{H^2 + (pn^G)^2}$
$H = W_2 - (y_1 + y_4)$	$pn^H = \Omega$	$H' = \sqrt{H^2 + (pn^H)^2}$

Table 24 - The calculation of the lengths of the segmented perimeter, perimeter normal lengths and slope heights for each face.

In Table 24,  $\Gamma$  and  $\Omega$  define the position of the downward projection from the apex onto the  $W_1$   $W_2$  plane:

$$\Gamma = \frac{W_1 T}{b \left( \frac{T}{a} + \frac{T}{b} \right)}$$

Equation 53

$$\Omega = \frac{W_2 T}{d \left( \frac{T}{c} + \frac{T}{d} \right)}$$

Equation 54

The projected termination height  $H$  is as defined in Equation 46.

### B.3.2 Type i and ii terminations

The type i and ii terminations are best considered as simple compound geometries, with a triangular prism bounded by two halves of a pyramid (as shown in Figure 97).

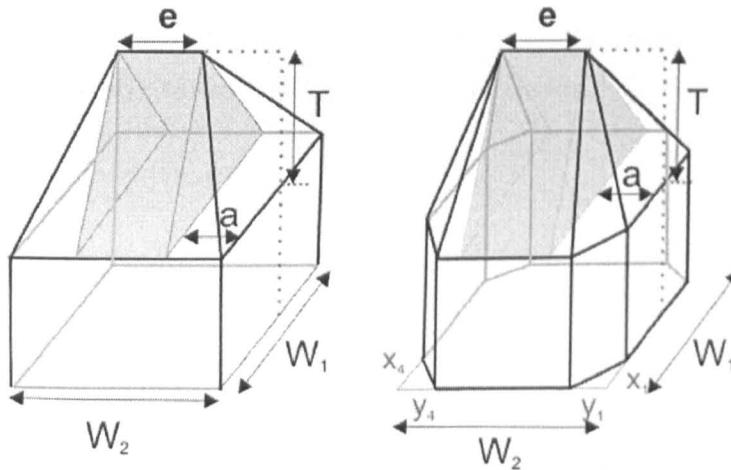


Figure 97 - The measurements required for  $\beta$ , Type i and ii terminations

The volume and surface area of this prism can be calculated using Equation 55 and Equation 56.

$$\text{Volume} = \frac{1}{2} [e W_1 T] + \frac{T}{3} \left[ \left( W_1 W_2 - \left( \frac{x_1 y_1 + x_2 y_2 + x_3 y_3 + x_4 y_4}{2} \right) \right) - (e W_1) \right]$$

Equation 55

$$\text{Surface Area} = \frac{(e + W_2) \sqrt{a^2 + T^2}}{2} + \frac{(e + W_2) \sqrt{(W_1 - a)^2 + T^2}}{2} + \text{surface area of pyramid}$$

Equation 56

Where  $a$ ,  $c$  and  $e$  are the measurements shown in Figure 97, and  $a$  and  $c$  are the equivalent measurements required in the calculation of type iii geometries above. The surface area of the pyramid is calculated using a modified, simplified version of Equation 52.

$$\text{surface area of pyramid} = \frac{1}{2} [AA' + BB' + CC' + DD' + EE' + FF' + GG' + HH']$$

Equation 57

with the A-H and A'-H' are as shown in Figure 97. The orientation of edge  $e$  can be parallel to either  $W_1$  or  $W_2$ , and in the above equations  $W_1$  and  $W_2$  can be exchanged if required, so that  $W_1/W_2 \geq 1.0$ .

### B.3.3 Type iv terminations

Each of the constituent parts of more complex compound terminations should be considered separately in the calculation of surface area and volume. For type iv terminations (Figure 93), the lower section is a truncated pyramid (with height  $T_1$ ), and upper section is generally a pyramid and has a projected height  $T_2$ , that can be measured directly. In the majority of the crystals inspected, the downward projection of both projected apexes identical, and can be measured directly. The projected height of the lower, truncated pyramid can then be calculated from Equation 42, and the surface area and volume following Section B.3.1. As the base area of the upper pyramid is the upper surface of the lower section, the scaling factor  $W_1'/W_1$  can be used to calculate all base lengths of all faces and the base area., and then the volume and surface area can be calculated as in Section B.3.1, substituting the values of  $W_1'$  and  $W_2'$  for  $W_1$  and  $W_2$ .

### B.3.4 Type v terminations

Compound geometries where the shape of the  $W_1$   $W_2$  parallel cross section changes are only found in crystal which have octahedral body sections. Type v terminations (Figure 93) have octahedral basal faces, and quadrilateral upper faces (Figure 98).

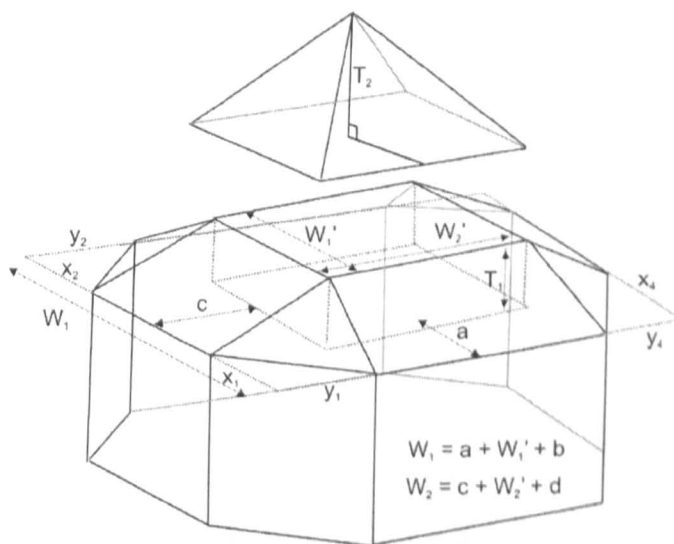


Figure 98 - The measurements required for  $\beta$ , Type v terminations

The terminations can be simple (have a quadrilateral terminal face) or compound (with the quadrilateral face forming the base of a pyramid). The surface area and volume calculations for this type of termination geometry are relatively simple. The volume and surface area of the upper quadrilateral based pyramid can be calculated using the measurements of  $W_1'$ ,  $W_2'$  and  $T_2$  (Figure 98)

The volume and surface area of the lower prism can be calculated using Equation 58 and Equation 59. In these equations the dimensions  $a - d$  and  $pn^n$  are as shown in Figure 98.  $pn^n$  values can be calculated from the technique described in Table 24 and Figure 96.

$$\text{Volume} = W_1 W_2 T_1 - \left[ \frac{aW_2 T_1 + bW_2 T_1 + cW_1 T_1 + dW_1 T_1}{2} \right] + \left[ \frac{acT_1 + bcT_1 + adT_1 + bdT_1}{3} \right] - \left[ \frac{T_1}{3} \left( \frac{x_1 y_1 + x_2 y_2 + x_3 y_3 + x_4 y_4}{2} \right) \right]$$

Equation 58

$$\text{surface area} = \left[ \frac{(W_1 + W_1')}{2} \left( \sqrt{c^2 + T_1^2} + \sqrt{d^2 + T_1^2} \right) \right] + \left[ \frac{(W_2 + W_2')}{2} \left( \sqrt{a^2 + T_1^2} + \sqrt{b^2 + T_1^2} \right) \right] + \frac{1}{2} \left[ pn^1 \sqrt{x_1^2 + y_1^2} + pn^2 \sqrt{x_2^2 + y_2^2} + pn^3 \sqrt{x_3^2 + y_3^2} + pn^4 \sqrt{x_4^2 + y_4^2} \right] + W_1' W_2' \text{ (if terminal face exists)}$$

Equation 59

In the majority of type v terminations seen in this study,  $W_1' = W_1 - (x_1 + x_2) = W_1 - (x_3 + x_4)$ , and  $W_2' = W_2 - (y_2 + y_3) = W_2 - (y_1 + y_4)$ . Which allows some simplification of the both calculations as  $x_1 = x_2 = a$ , and  $y_1 = y_4 = c$ . Equation 58 and Equation 59 therefore be rewritten as:

$$\text{Volume} = W_1' W_2' T_1 + \left[ \frac{x_1 W_2' T_1 + x_2 W_2' T_1 + y_1 W_1' T_1 + y_2 W_1' T_1}{2} \right] + \frac{1}{3} \left[ \frac{(x_1 y_1 + x_2 y_2 + x_3 y_3 + x_4 y_4)}{2} \right]$$

Equation 60

$$\text{Surface area} = \left[ W_1' \left( \sqrt{y_1^2 + T_1^2} + \sqrt{y_2^2 + T_1^2} \right) \right] + \left[ W_2' \left( \sqrt{x_1^2 + T_1^2} + \sqrt{x_2^2 + T_1^2} \right) \right] + W_1' W_2' + \frac{1}{2} \left[ \sqrt{T^2 + \frac{x_1^2 + y_1^2}{4}} \left( \sqrt{x_1^2 + y_1^2} \right) + \sqrt{T^2 + \frac{x_2^2 + y_2^2}{4}} \left( \sqrt{x_2^2 + y_2^2} \right) + \sqrt{T^2 + \frac{x_3^2 + y_3^2}{4}} \left( \sqrt{x_3^2 + y_3^2} \right) + \sqrt{T^2 + \frac{x_4^2 + y_4^2}{4}} \left( \sqrt{x_4^2 + y_4^2} \right) \right]$$

Equation 61

### B.3.5 Type vi terminations

Type vi compound terminations also have a change in the shape of the  $W_1 W_2$  parallel cross section, and are found in both quadrilateral and octagonal crystals. These geometries were not seen in any sample analysed during this study and so the precise equations have not been calculated.

The upper section of these terminations can be considered as a quadrilateral based prism, where basal plane dimensions, the position of the downward projection from the apex and H can be measured directly (see Figure 99).

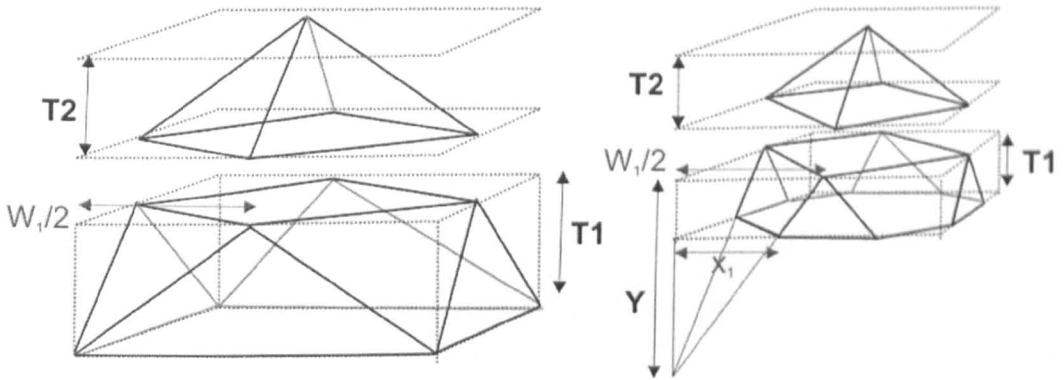


Figure 99 - The measurements required for  $\beta$ , Type vi terminations.

In the case where the apex is above the centre of the basal face, the calculation of the surface area and volume can be achieved using the length and volume scaling factors. When the apex is not located centrally, the measurements marked  $W_1/2$  in Figure 99 should be measured directly.

## B.4 Type E crystal geometries

When crystals are true trapezoids, (Type E, Figure 93) no termination measurements are required. Instead measurements of  $L_1$  and  $L_2$  (Figure 100)  $W_1$  and  $W_2$  are required, and the volume and surface area can be calculated using Equation 62 and Equation 63.

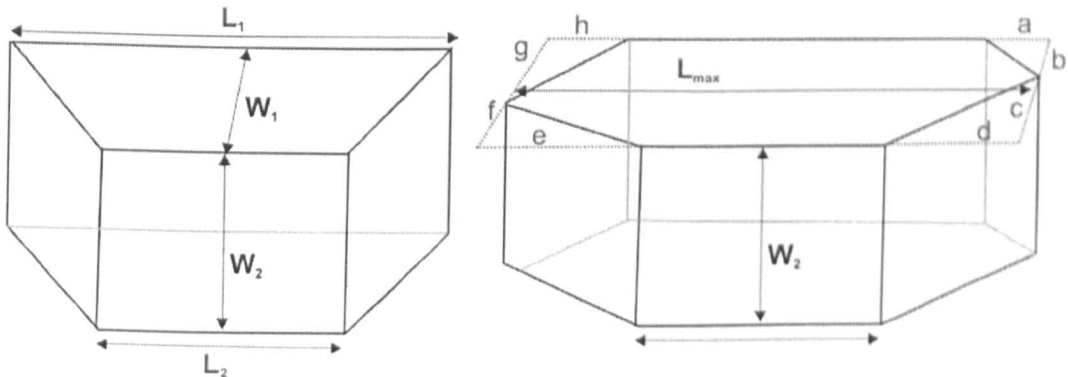


Figure 100 - The measurements required for  $\beta$ , Type E crystals

$$\text{Volume} = \left[ W_1 W_2 \left( \frac{L_1 + L_2}{2} \right) \right]$$

Equation 62

$$\text{Surface area} = [W_2 L_1 + W_2 L_2 + W_1 (L_1 + L_2)]$$

Equation 63

The orientation of the trapezoidal face can be parallel to either  $W_1$  or  $W_2$ , and in Equation 63 the values of  $W_1$  and  $W_2$  can be exchanged if required, so that  $W_1/W_2 \geq 1.0$ . In some trapezoidal

crystals, type ii terminations are seen (Figure 100 B), and in these cases the area of the hexagonal face is calculated using nine additional measurements ( $a - h$ , and  $L_{max}$ ) as shown. These are analogous to the measurements of  $x_{1-4}$  and  $y_{1-4}$  for the octagonal system, but are taken in the  $W_1L$  plane..

$$\text{Face Area} = \left[ L_{max} W_2 - \frac{1}{2} (ab + cd + ef + gh) \right]$$

Equation 64

Equation 62 and Equation 63 then become:

$$\text{Volume} = W_1 \left[ L_{max} W_2 - \frac{1}{2} (ab + cd + ef + gh) \right]$$

Equation 65

$$\text{Surface Area} = 2 \left[ L_1 W_2 - \frac{1}{2} (ab + cd + ef + gh) \right] + W_1 \left[ \sqrt{a^2 + b^2} + \sqrt{c^2 + d^2} + \sqrt{e^2 + f^2} + \sqrt{g^2 + h^2} + L_1 + L_2 \right]$$

Equation 66

Again,  $W_1$  and  $W_2$  are interchangeable depending on the orientation of the hexagonal face.

## C

## Model concentration profiles for the FCT

The values in Table 25 were determined from the CL greyscale intensities and the U and Th concentrations observed in the SIMS analysis of the FCT zircons. The ranges were defined using the different ranges of CL values from all the FCT zircons shown in Figure 46.

CL Intensity (greyscale)	U, Th (ppm)	eU (ppm)
< 30	3000, 3000	3720
30 - 50	1500, 2000	1980
51 - 60	1000, 1000	1240
61 -70	400, 800	592
71 -100	250, 550	388
101 -150	300, 300	348
151 - 200	200, 200	248
200 - 220	100, 100	124
> 230	15, 50	27

**Table 25 - The conversion from CL intensity to U and Th content. Values determined from data from the SIMS traverse of FCT4 (Crystal I, Figure 46).**

The CL intensity ranges reflect a particular population observed with the measured greyscale values. The U and Th concentrations were estimated using these ranges, and the average U and Th determined from the SIMS traverse of FCT 4. The CL images were used to determine CL profiles. These were then converted to absolute U and Th concentration profiles. As the  $\alpha$ -recoil correction calculated is dependant on the relative concentration changes within a zonation pattern, the profiles were then converted relative to the maximum U and Th content within each profile, before being input into the Hourigan *et al.* (2005) model. The model relative concentration profiles are shown in Figure 101, the measured U and Th profiles from FCT 4 are shown in Figure 102.

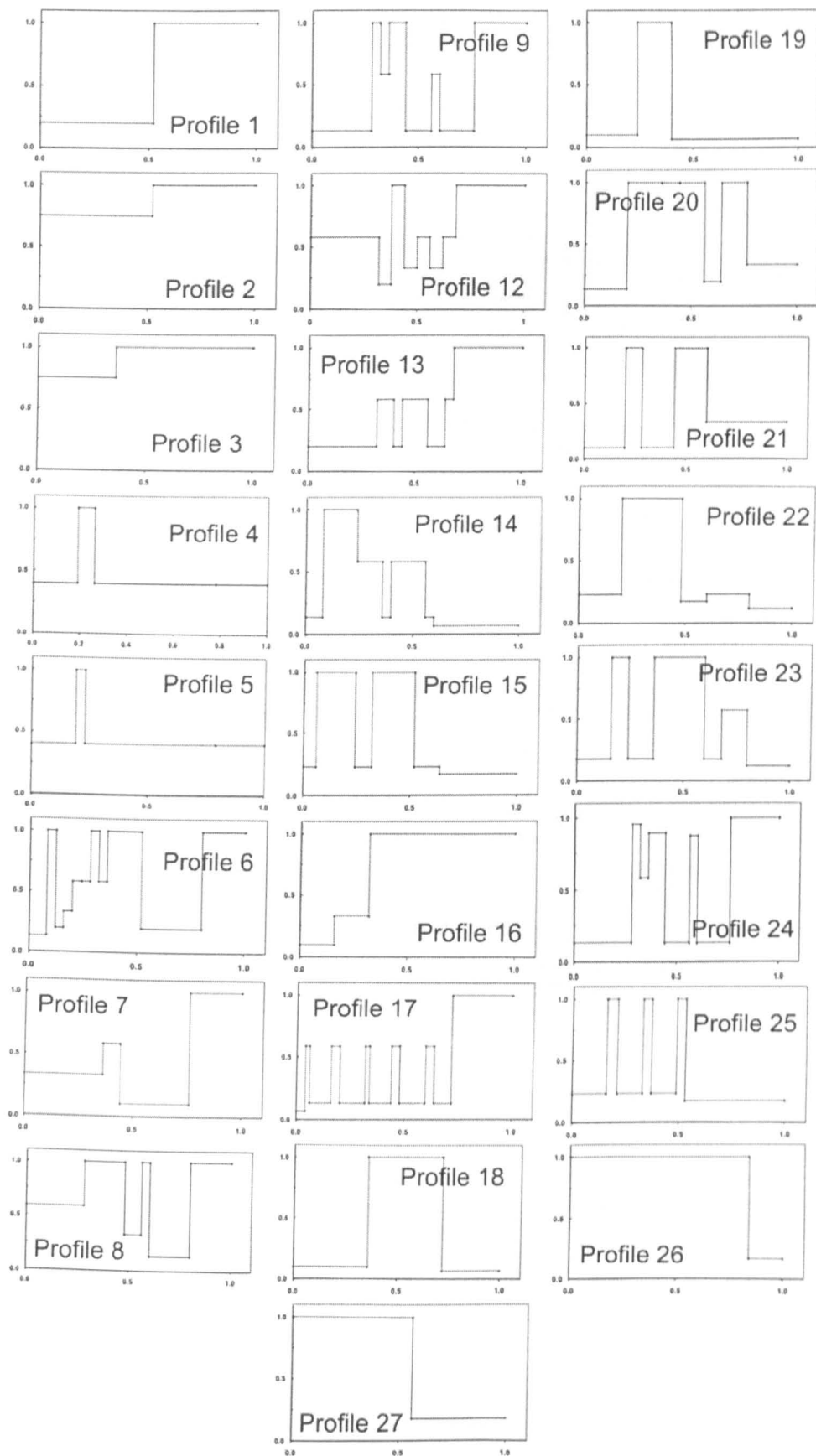
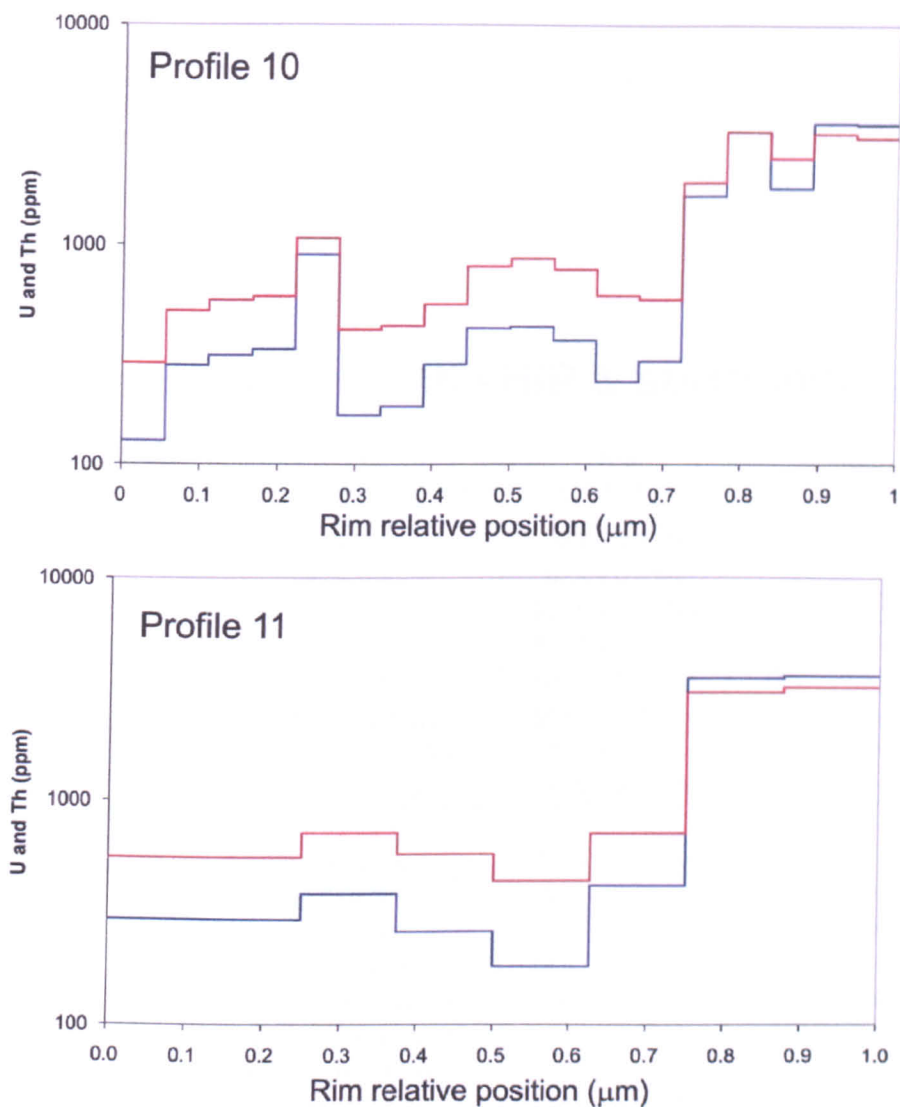


Figure 101 - The model FCT concentration profiles generated from the CL images in Figure 46. The zonation patterns shown are normalised to crystal width. The profile number refer to the those shown in Figure 60



**Figure 102 - The model FCT concentration profiles generated from crystal FCT 4. The zonation patterns shown are normalised to crystal width. The profile number refer to the those shown in Figure 60**

## D

## Radiometric ages from the HIP &amp; surrounding area

Radiometric system	Unit	Age	Reference
<b>Rum, Eigg &amp; Muck</b>			
Ar-Ar	Muck Tuff	62.8 ± 0.6 Ma	Pearson <i>et al.</i> (1996)
Ar-Ar	Muck Tuff	62.4 ± 0.6 Ma	Pearson <i>et al.</i> (1996)
U-Pb	Muck Tuff	61.15 ± 0.25 Ma	Chambers <i>et al.</i> (2005)
Ar-Ar	Muck Tuff	60.65 ± 0.07 Ma	Chambers <i>et al.</i> (2005)
Ar-Ar	Muck Tuff	60.45 ± 0.03 Ma	Chambers <i>et al.</i> (2005)
U-Pb	Rum Central Complex	60.53 ± 0.05 Ma	Hamilton <i>et al.</i> (1998)
Ar-Ar	Rum Central Complex	60.2 ± 1.2 Ma	Hamilton <i>et al.</i> (1998)
Ar-Ar	Eigg Pitchstone	58.72 ± 0.07 Ma	Chambers <i>et al.</i> (2005)
<b>Skye</b>			
Ar-Ar	Canna Lavas	60.00 ± 0.23 Ma	Chambers <i>et al.</i> (2005)
Ar-Ar	Sleadale Tuff	58.91 ± 0.18 Ma	Bell & Williamson (2002)
Ar-Ar	Trachyte dyke	57.6 ± 1.2 Ma	Hamilton <i>et al.</i> (1998)
Ar-Ar	Main lava series	59.83 ± 0.12 Ma	Chambers & Pringle (2001)
Rb/Sr	Coire Uagneich granite	59.3 ± 1.4 Ma	Dickin 1981)
U-Pb	Cuillins pegmatite vein	58.91 ± 0.07 Ma	Hamilton <i>et al.</i> (1998)
Ar-Ar	Ruadh Stac Granite	57.5 Ma	Chambers (2000)
Ar-Ar	Loch Ainort Granite	58.58 ± 0.13 Ma	Chambers & Pringle (2001)
U-Pb	Southern Porphyritic Granite	57 ± 2.1 Ma	Hamilton (unpubl. data)
U-Pb	Marsco Granite	58.4 ± 2.1 Ma	Hamilton (unpubl. data)
Rb/Sr	Beinn an Dubhaich	53.4 ± 0.8 Ma	Dickin 1981)
U-Pb	Beinn an Dubhaich	55.89 ± 0.18 Ma	Hamilton (unpubl. data)
Ar-Ar	Beinn an Dubhaich	55 Ma	Chambers <i>et al.</i> (2005)
U-Pb	Pitchstone Dyke	55.7 ± 0.1 Ma	Hamilton (unpubl. data)
<b>Mull</b>			
Ar-Ar	Base of Mull lavas	60.0 ± 1.0 Ma	Mussett (1986)
Ar-Ar	Staffa Lavas	60.56 ± 0.3 Ma	Chambers & Pringle (2001)
U-Pb	Calgary Tuff	60.5 ± 0.3 Ma	Hamilton (unpubl. data)
Ar-Ar	Calgary Tuff	60.57 ± 0.24 Ma	Kelley (unpubl. data)
Ar-Ar	Plateau Lavas	58.35 ± 0.19 Ma	Chambers & Pringle (2001)
Ar-Ar	Plateau group lava	58.66 ± 0.25 Ma	Chambers & Fitton (2000)
U-Pb	Corra Bheinn Gabbro, C2	58.3 Ma	Hamilton (unpubl. data)
Rb-Sr	C3 Granite	58.2 ± 1.3 Ma	Walsh (1979)
Ar-Ar	Loch Ba felsite	56.5 ± 2.0 Ma	Mussett (1986)
U-Pb	Loch Ba felsite	58.47 ± 0.13 Ma	Hamilton (unpubl. data)
Ar-Ar	Loch Ba felsite	58.48 ± 0.18 Ma	Chambers & Pringle (2001)
U-Pb	Loch Ba felsite	58.7 ± 0.1 Ma	Jolley & Bell (2002)
Ar-Ar	Young suite dykes	58.12 ± 0.13 Ma	Chambers <i>et al.</i> (2005)

cont.

Radiometric system	Unit	Age	Reference
Ardnamurchan U-Pb Ar-Ar	Quartz monzonite, C3 Great Eucrite	58.63 ± 0.31 Ma 59.05 Ma	Hamilton (unpubl. data) Chambers (2000)
Lewis Ar-Ar	Loch Roag Dyke	45.16 ± 0.02 Ma	Timmermann (unpublished data)
Ireland U-Pb (z) K/Ar K/Ar K/Ar K/Ar K/Ar K/Ar K/Ar K-Ar Ar-Ar	Tardree Rhyolite Irish Sea Dyke Swarm Irish Sea Dyke Swarm Blind Rock Dyke Carlingford Granophyre Antrim Lavas Antrim Lavas Mourne Mountains Inver Dykes Inver Dykes	58.4 ± 0.4 Ma 65.5 ± 1.0 Ma 61.5 ± 0.8 Ma 61.7 ± 0.5 Ma 60.9 ± 0.5 Ma 58.3 ± 1.1 Ma 61.0 ± 0.6 Ma 53.3 ± 0.6 Ma 44.1 ± 2.5 Ma 41.9 ± 0.5 Ma	Gamble <i>et al.</i> (1999) Arter & Fagin (1993) Arter & Fagin (1993) Thompson (1986) Thompson (1986) Wallace <i>et al.</i> (1994) Wallace <i>et al.</i> (1994) Thompson <i>et al.</i> (1987) Kirstein & Timmerman (2000) Kirstein & Timmerman (2000)
St Kilda K-Ar	St Kilda Central Complex	55 ± 1 Ma	Mussett <i>et al.</i> (1988)
Arran Rb/Sr Ar-Ar	Northern Granite Northern Granitic Centre Ailsa Craig Granite	60.3 ± 0.8 Ma 58.5 ± 0.8 Ma 61.5 ± 0.5 Ma	Evans <i>et al.</i> (1973) Dickin <i>et al.</i> (1981) Harrison <i>et al.</i> (1987)
Lundy Rb/Sr Ar-Ar	Lundy Granite Dykes intruding granite	54 ± 4 Ma 56.4 ± 0.3	Hampton & Taylor (1983) Mussett <i>et al.</i> (1976)
Offshore UK Ar-Ar Ar-Ar Ar-Ar Ar-Ar Ar-Ar Ar-Ar Ar-Ar Ar-Ar Ar-Ar Ar-Ar Ar-Ar Ar-Ar K/Ar K/Ar Ar-Ar	Rosemary Bank Rosemary Bank Anton Dohm Anton Dohm Anton Dohm Anton Dohm Hebrides Terrace Hebrides Terrace Hebrides Terrace Borehole 85/5B lava OPD leg 81 Site 555 OPD leg 81 Site 555 Lava from site 555	52 ± 1 Ma 42 ± 1 Ma 70 ± 1 Ma 62 ± 1 Ma 47 ± 1 Ma 41 ± 1 Ma 62 ± 1 Ma 51 ± 1 Ma 48 ± 1 Ma 56.4 ± 0.7 Ma 52.3 ± 1.7 54.5 ± 2.0 57.6 ± 1.3	O'Connor <i>et al.</i> (2000) O'Connor <i>et al.</i> (2000) Sinton <i>et al.</i> (1998) Macintyre & Hamilton (1984) Macintyre & Hamilton (1984) Sinton & Duncan (1996)

Table 26 - Selected radiometric ages from the HIP, Ireland and the offshore UK margin. Radiometric systems shown where reported and sources as shown. Dashed lines separate different sub-complexes or the ages from the lava fields

# E

## Modelling the cooling of the plutonic complexes

The modelling of the plutonic complexes was performed using the HEAT-3D software program [Wohletz & Heiken, 1992; Wohletz *et al.*, 1999]. The thermal parameters shown in Table 27 were used to perform the thermal modelling of the plutonic cooling in the HIP. Values for all lithologies in the HIP are not reported, and so lithology average values have been collated from various sources [Clauser & Huenges, 1995; Green *et al.*, 1995; Clift, 1997; Clift & Turner, 1998; Green *et al.*, 1999]. The values for the melts are those provided by the software. A range of thermal conductivity values were investigated (bracketed values), those used in the models presented in Chapter 6 are shown.

### Country rocks

Lithology	Density (kg/m <sup>3</sup> )	Thermal conductivity (W/mK)	Heat capacity (J/kgK)
Basalt (Palaeogene)	2700	3.0, (2.5 – 3.5)	980
Gneiss (Lewisian)	2700	2.5, (1.5 – 3.5)	980
Sandstone (Torridonian)	2400	4.2, (4.0 – 5.0)	730
Limestone (Jurassic)	2600	3.4, (3.0 – 4.0)	700

### Magma

Melt composition	Intrusion Temp	Thermal conductivity (W/mK)	Heat capacity (J/kgK)
Mafic	1250°C	1.8	1200
Intermediate	1100°C	1.3	1150
Silicic	1000°C	1.5	1100

Table 27 - The input parameters used to perform the Heat 3D simulations.

## E.1 Initial model conditions

For both the Rum and Skye models the intrusion was emplaced into a stratified sequence of country rocks with a geothermal gradient of 40°C/km. The model forces this geothermal gradient to be maintained at the edges of the model space [Wohletz & Heiken, 1992; Wohletz *et al.*, 1999], so initial models were run using a horizontal scale of 100 km, to ensure that this boundary condition did not force the cooling. At shallow levels, the horizontal limit of the thermal perturbation

surrounding the intrusions did not exceed 25 km from the centre of the pluton; therefore the horizontal scale was reduced to 50 km. This significantly reduced computing time.

In both models a basement unit approximating Lewisian Gneiss is overlain by 3 km of a lithology representing the Torridonain sandstones. Above this lies a sequence representing the 0.5 km of Mesozoic sediments, and a 2 km Palaeogene basaltic lava pile. All boundaries are horizontal. Additional models were run using a variety of different thickness for the Torridonian, Mesozoic and Palaeogene units, but there was little change ( $< 0.2$  Myr change) in the rate of cooling.

## **E.2 Intrusion characteristics**

### **E.2.1 Rum**

A single intrusion event emplaced a cylindrical pluton with a flat roof at 2 km beneath the surface at the centre of the model. The entirely mafic pluton had a diameter of 12 km and extended to a depth of 14 km. Models that included an early phase of granitic emplacement showed no change in the rapid cooling rate observed after the emplacement of the gabbroic complex. The pluton was isolated from the mantle source immediately after emplacement, i.e. and the cooling of the conduit was not modelled. Models run that included the cooling of the conduit showed no difference in the cooling rate. Once emplaced the pluton was allowed to cool, with "screen dump" time slices taken at regular intervals.

### **E.2.2 Skye**

The model for Skye emplaced two large plutons. The first corresponded to the emplacement of the Cuillins gabbroic suite, and was emplaced as a cylindrical flat-topped mafic pluton with a diameter of 14 km. The pluton was emplaced at 2 km depth, and extended to 14 km below the surface. The second intrusion event represented the emplacement of the Red Hills Complex. This was modelled as a single event that occurred synchronous with the youngest recorded emplacement age (55 Ma). This shape of this intrusion can be seen in the second panel of Figure 71. The uppermost 3 km of the pluton was emplaced as a silicic melt, with the lower part having a mafic composition. The magma chamber experienced no recharge, but the modelling of the conduit is included as the lower crustal regime experienced more dynamic thermal variation because of the pulsed intrusion. Cooling models of the SCC that were run in the absence of any conduit (i.e. like the model of Rum shown in Figure 70) show no change in the cooling rate at shallow depths ( $< 8$  km) and cooling at depth ( $> 15$  km) is only negligibly slower ( $< 0.25$  Myr). Once emplaced the pluton was allowed to cool, with "screen dump" time slices taken at regular intervals.

## F

## Geological maps of the central complexes of the HIP & sample localities

The following maps show simplified geological maps of the Central Complexes, and shows the localities of all plutons investigated using low temperature thermochronology. The localities of the samples collected during this study, and those supplied by Drs Mike Hamilton, Lynne Chambers, and John Valley are shown on the relevant maps and listed in Table 28.

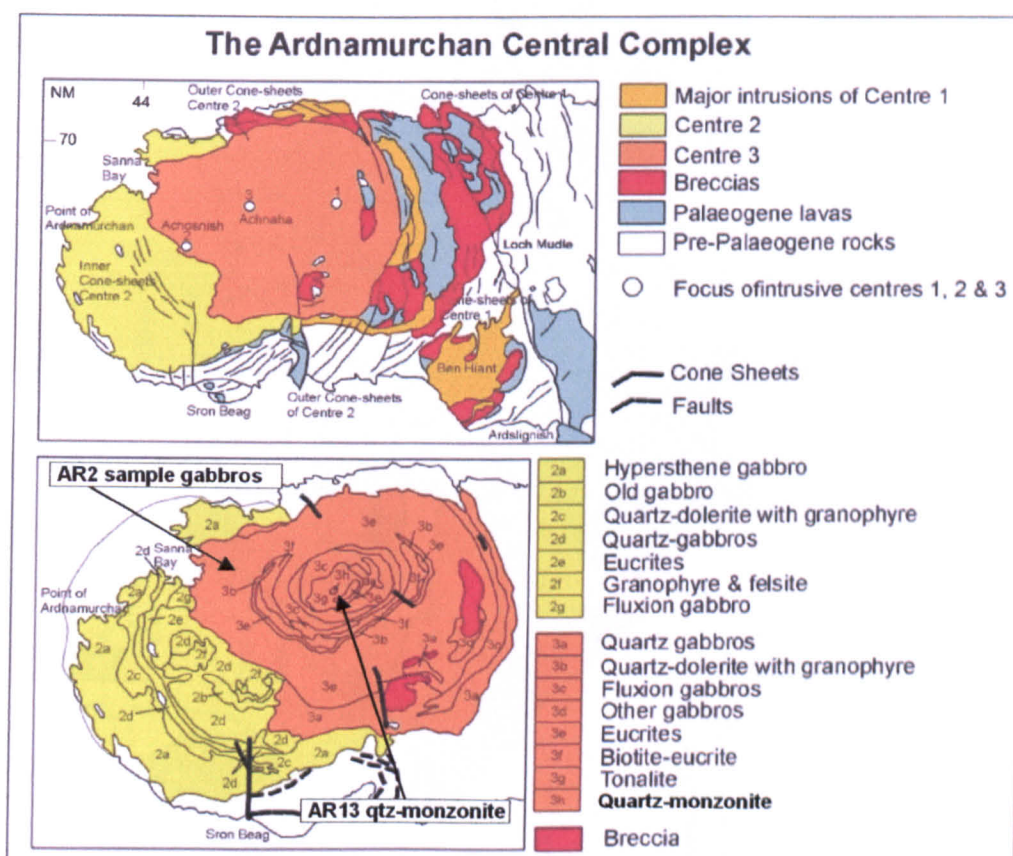


**Figure 103 - The geology of the Ardnamurchan Central Complex and surrounding area. The exact localities of the sample are unknown. Sample AR2 comes from a gabbro within C3 (see figure). Sample AR13 comes from the Quartz Monzonite (3h).**

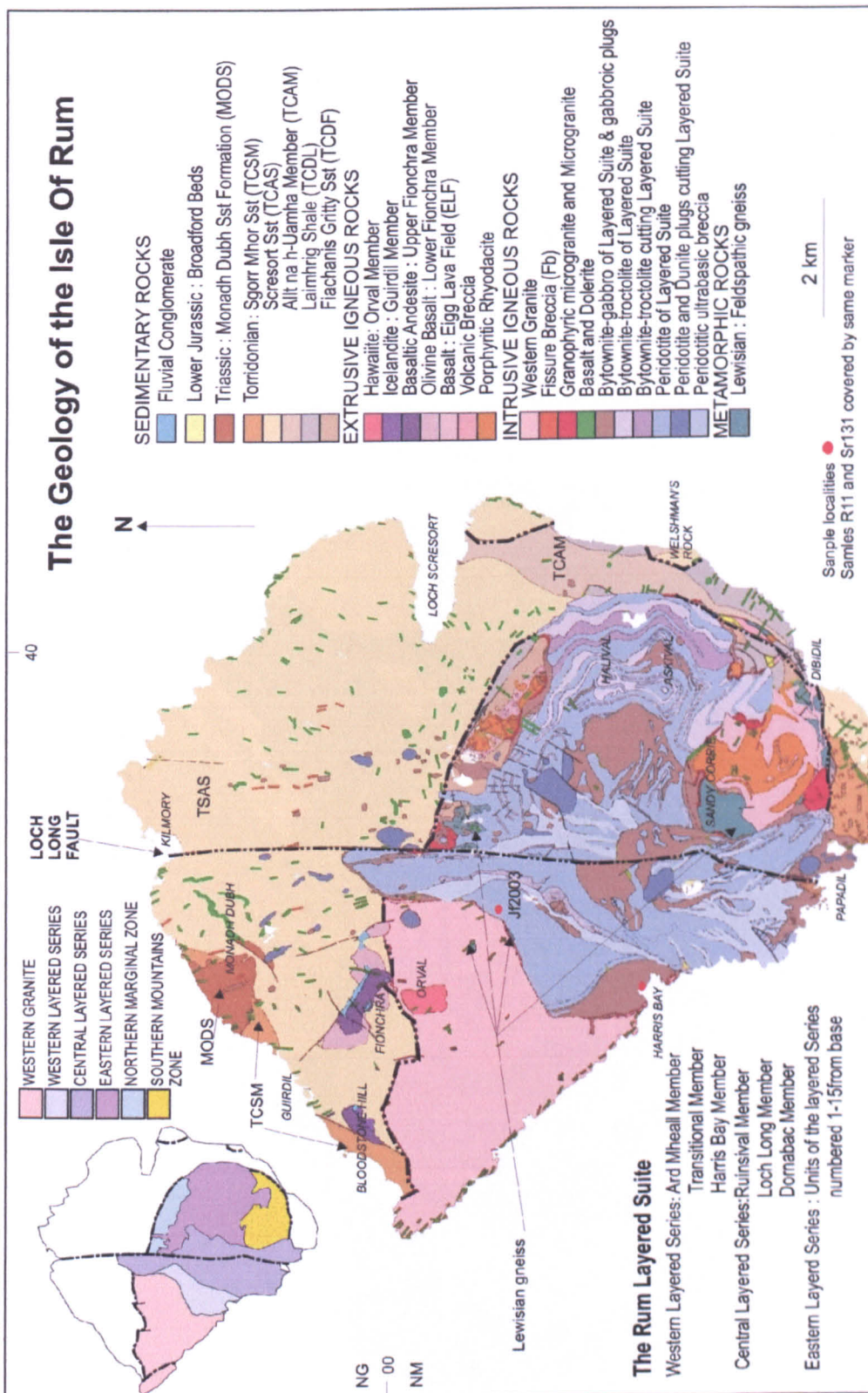


Figure 104 - The geology of Rum, after BGS 1994 inset shows extent and location of each of the main intrusive series. Both samples R03-11 and SR131 were taken from Harris Bay.

# The Skye Central Complex

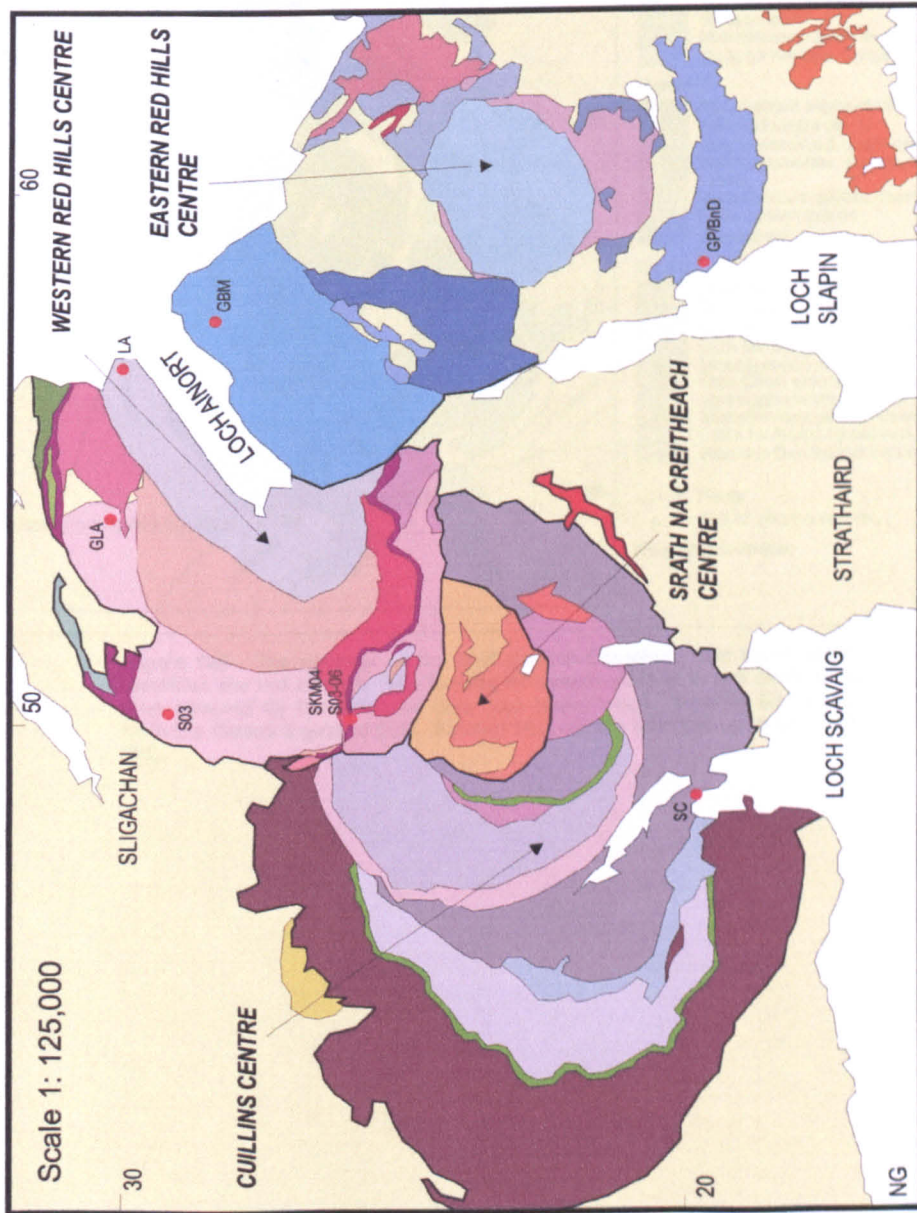
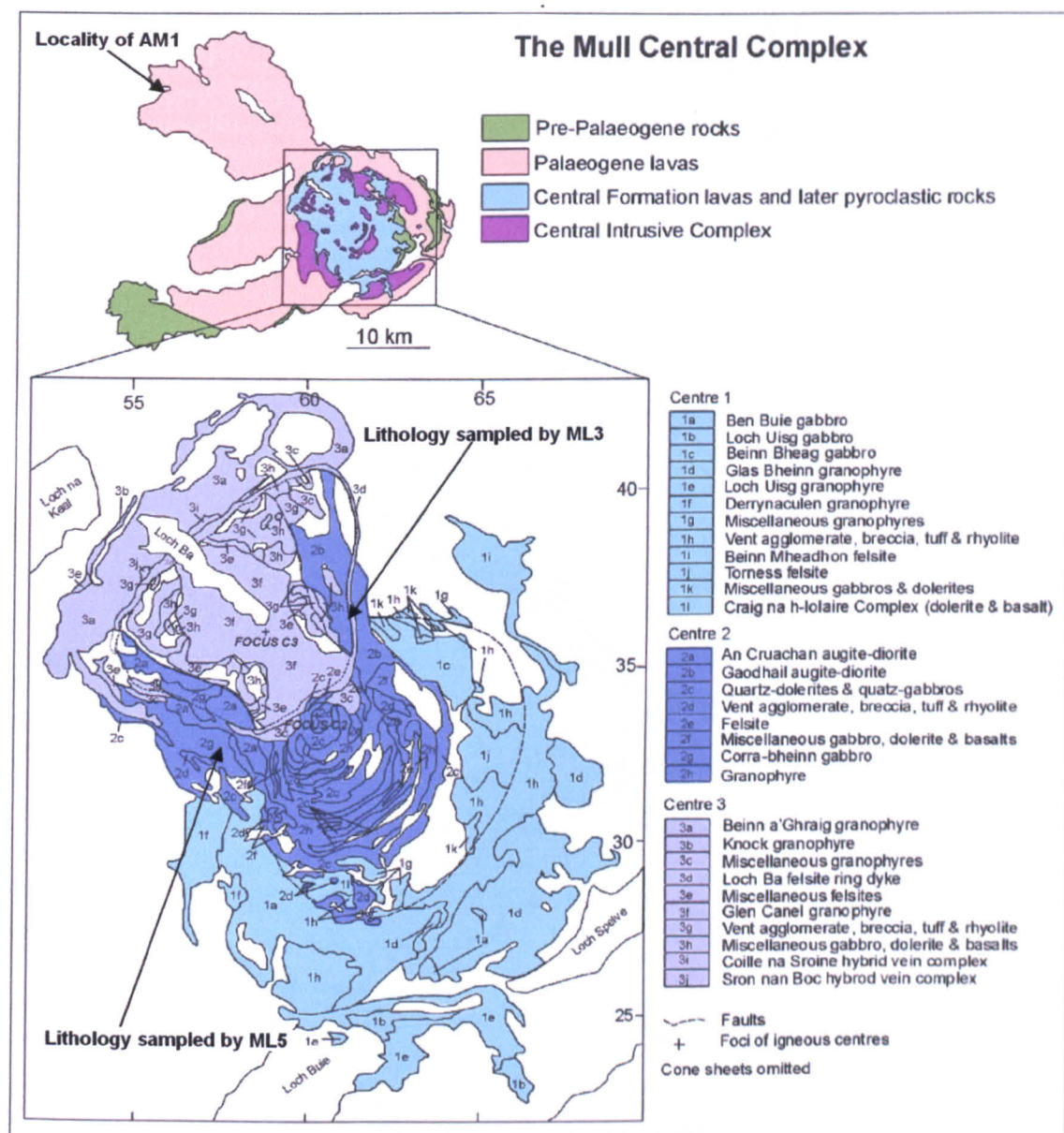
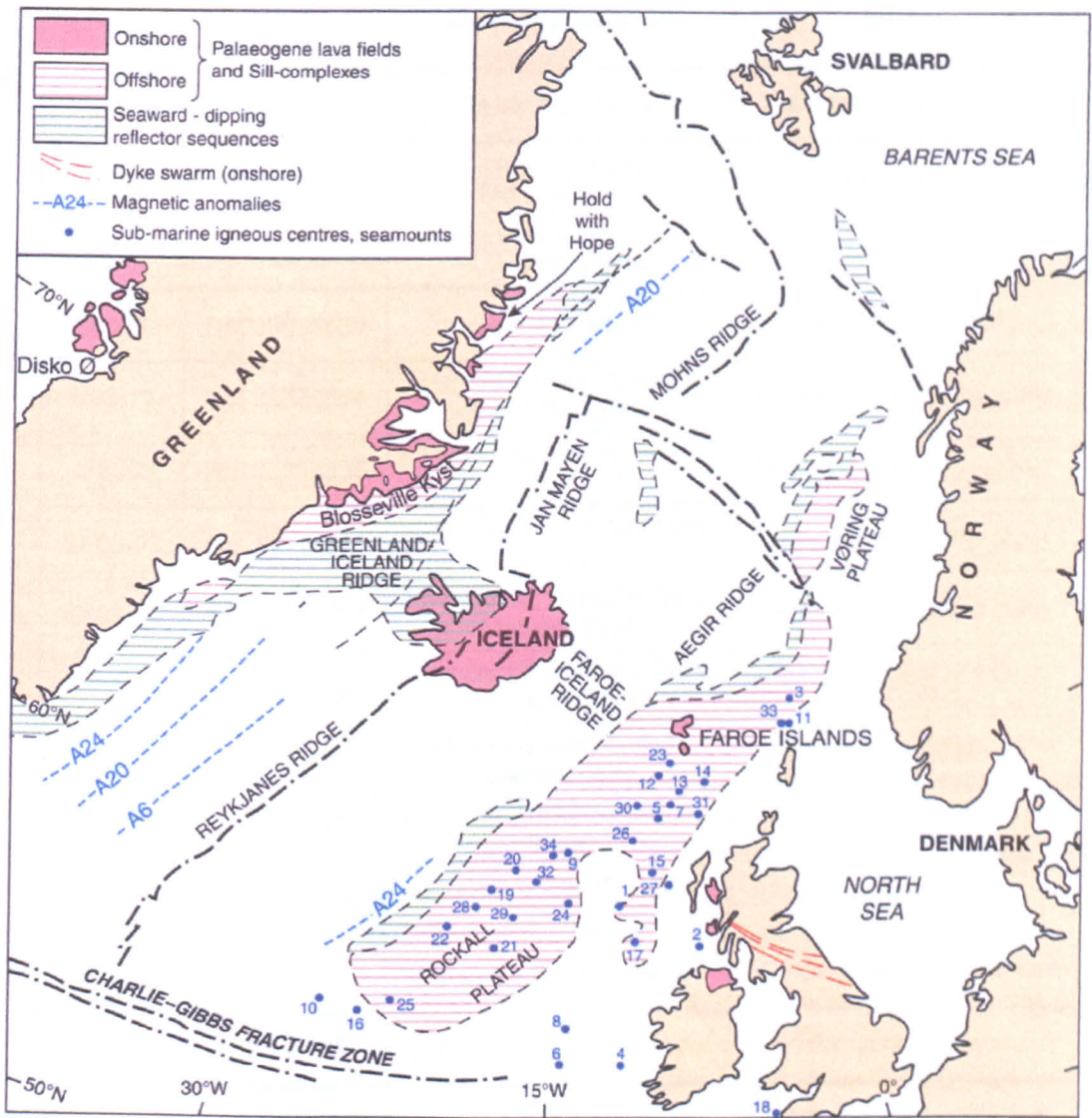


Figure 105 - The geology of the Skye Central Complex [modified from Bell & Williamson, 2002]. Red circles mark sample localities (as labelled).



**Figure 106 - The geology of the Mull Central Complex. The exact sample localities are not known. The locality of sample AM1 is to the north of the area covered by the enlarged map (see upper map). Sample ML5 comes from the Centre 2 gabbro (2g). Sample ML3 comes from the Loch Ba Felsite (3d).**



- |                      |                             |                  |                      |
|----------------------|-----------------------------|------------------|----------------------|
| 1 Anton Dohrn        | 11 Eriend                   | 21 Mentone       | 31 Sula Sgeir        |
| 2 Blackstones        | 12 Faroe Bank               | 22 Owlsgard      | 32 Swithin           |
| 3 Brendan (Shetland) | 13 Faroe Bank Channel Knoll | 23 Regin Smidur  | 33 West Erlend       |
| 4 Brendan (Ireland)  | 14 Fraenir                  | 24 Rockall       | 34 West George Bligh |
| 5 Darwin             | 15 Geikie                   | 25 Rohan         |                      |
| 6 Donn               | 16 Gondor                   | 26 Rosemary Bank |                      |
| 7 Drekaegya          | 17 Hebrides Terrace         | 27 St Kilda      |                      |
| 8 Drol               | 18 Lundy                    | 28 Sandarro      |                      |
| 9 East George Bligh  | 19 Lyonesse                 | 29 Sandastre     |                      |
| 10 Eriador           | 20 Mammal                   | 30 Sigmundur     |                      |

**Figure 107 - The offshore Seamounts in the Northeast Atlantic [from Green et al., 1999]**

<b>Sample</b>	<b>Grid Reference</b>	<b>Lithology, location</b>	<b>Source</b>
MT2	NM 418785	Muck Tuff, Muck	Dr. Lynne Chambers
AR2	unknown	Centre 3 gabbro, Ardnamurchan	Dr. Mike Hamilton
AR13	unknown	Quartz Monzonite, Centre 3, Ardnamurchan	Dr. Mike Hamilton
SR131	NM 33809560	Harrisite, Rum	Dr. Mike Hamilton
R03-11	NM 33829564	Pegmatitic vein material, Harris Bay, Rum	Fieldwork during this study
JF2003	NM 35359839	Pegmatitic vein material, Rum	Fieldwork during this study
SK03-03	NG 51312946	Glamaig Granite, Glamaig, Skye	Fieldwork during this study
SK03-06	NG 49882588	Ferrodiorite, Harker's Gully, Marsco, Skye	Fieldwork during this study
SKM-04	NG 50102580	Ferrodiorite, Harker's Gully, Marsco, Skye	Fieldwork during this study
SC	NG 487196	Outer Layered Series, Cuillins, Skye	Dr. Mike Hamilton
GP422 BnD	NG 583195	Beinn an Dubhaich Granite, Skye	Dr. Mike Hamilton Dr. John Valley
GBM	NG 5688274	Glas Beinn Mhor Granite, Skye	Dr. Mike Hamilton
GLA	NG 548303	Glamaig Granite, Skye	Dr. Mike Hamilton
LA	NG 565298	Loch Ainort Granite, Skye	Dr. John Valley
AM1	unknown	Calgary Tuff, North Mull	Dr. Mike Hamilton
ML5	unknown	Centre 2 Gabbro, Mull	Dr. Mike Hamilton
ML3	unknown	Loch Ba felsite, Mull	Dr. Mike Hamilton
STK1	NF 10479897	Conachair Granite, St Kilda	Chris Reavy

**Table 28 - A summary of the samples and lithologies analysed during this study.**

## Apatite fission track data

$N_D$  is 4973 for all samples except SKM04 where it is 6368. Ages measured by Dr. C. Persano with a zeta of  $368 \pm 8$ . All samples are etched with for 15 seconds in 5 M  $HNO_3$

### G.1 The radial plots for HIP samples

This appendix presents the “screen dumps” of the radial plots calculated using the TrackKey fission track age software [Dunkl, 2002].

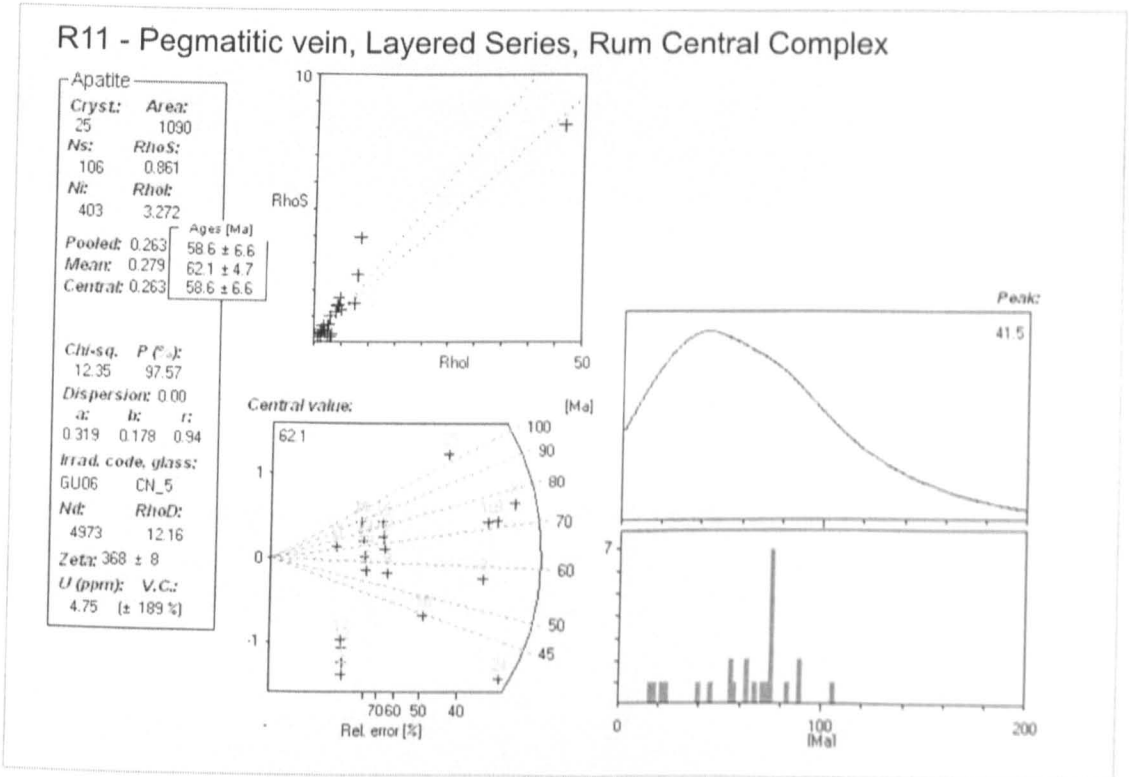
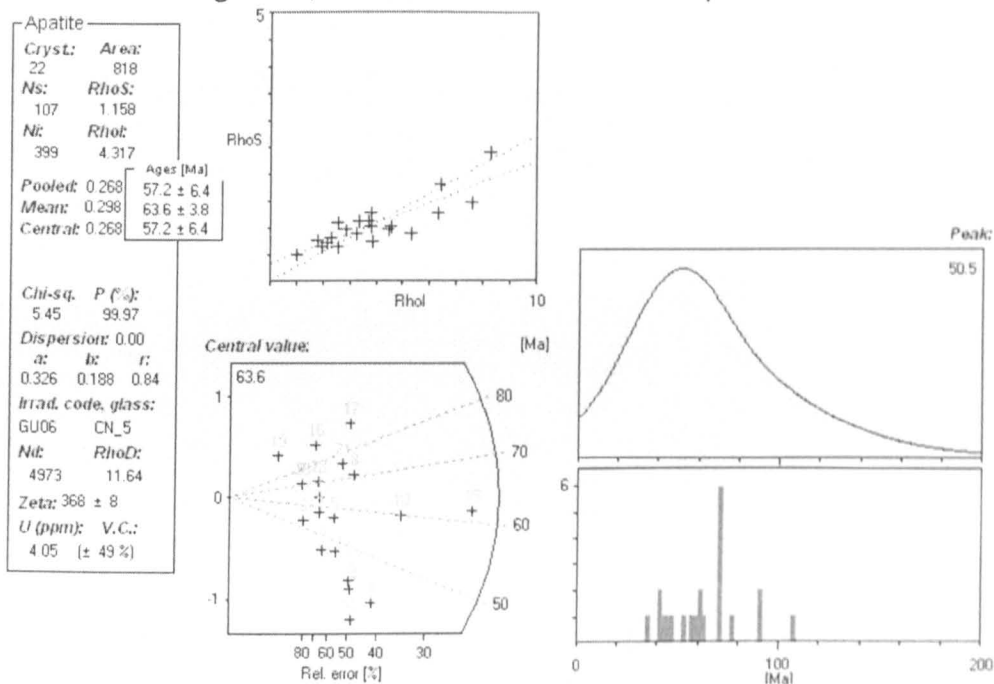


Figure 108 - Radial plots for apatite from the Rum Central Complex. Sample R03-11. Screen shot from TrackKey

## AR2 - Centre 2 gabbro, Ardnamurchan Central Complex



## AR13 - Qtz Monzonite Centre 3, Ardnamurchan Central Complex

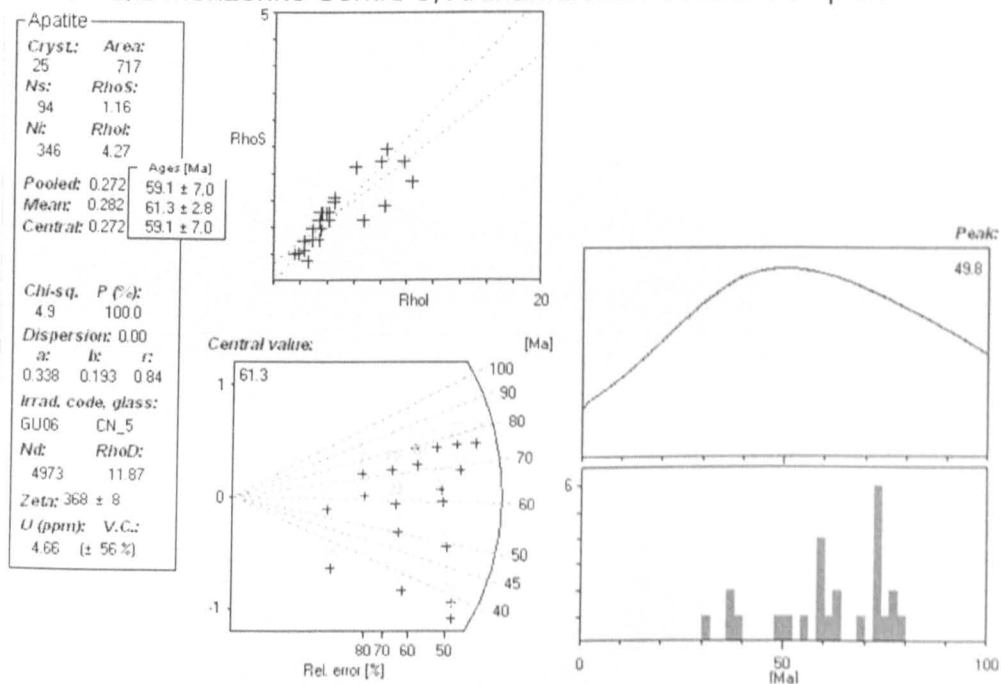
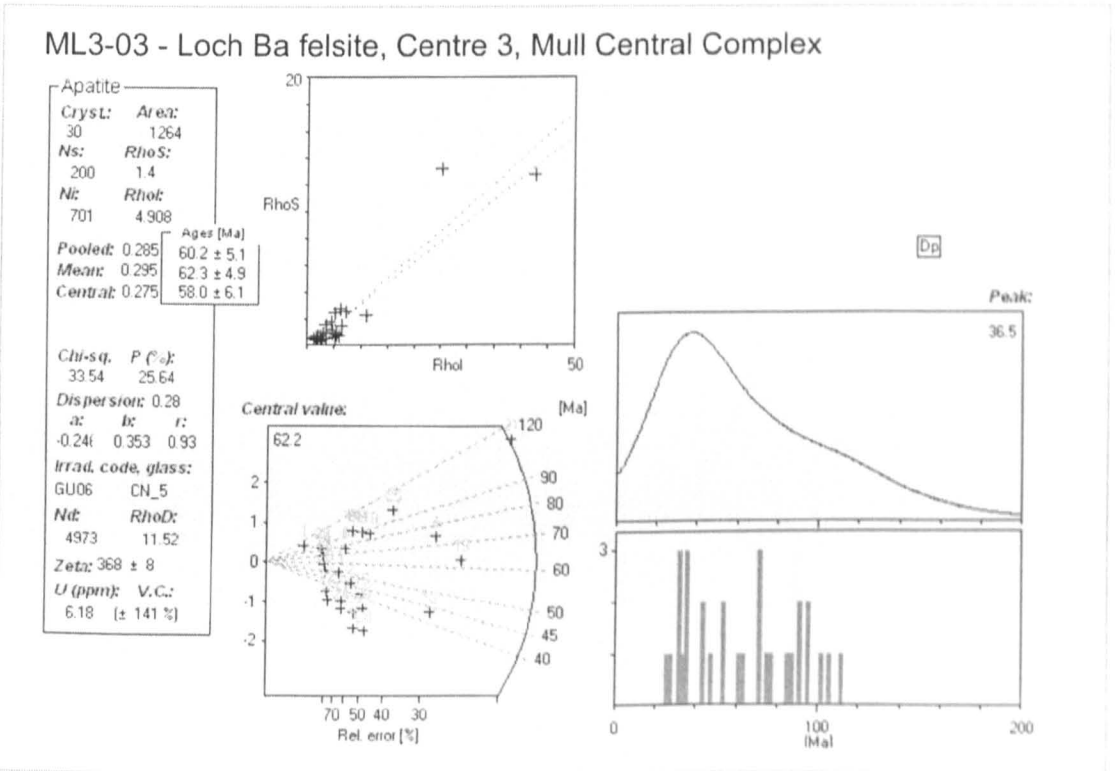
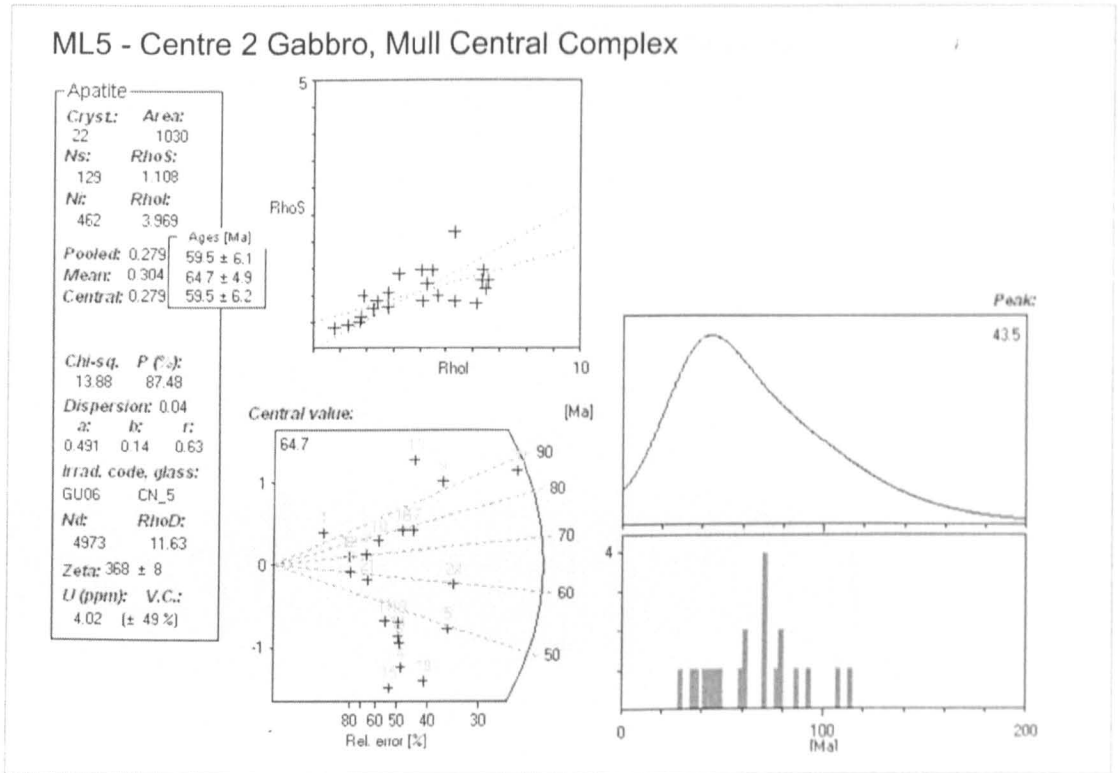
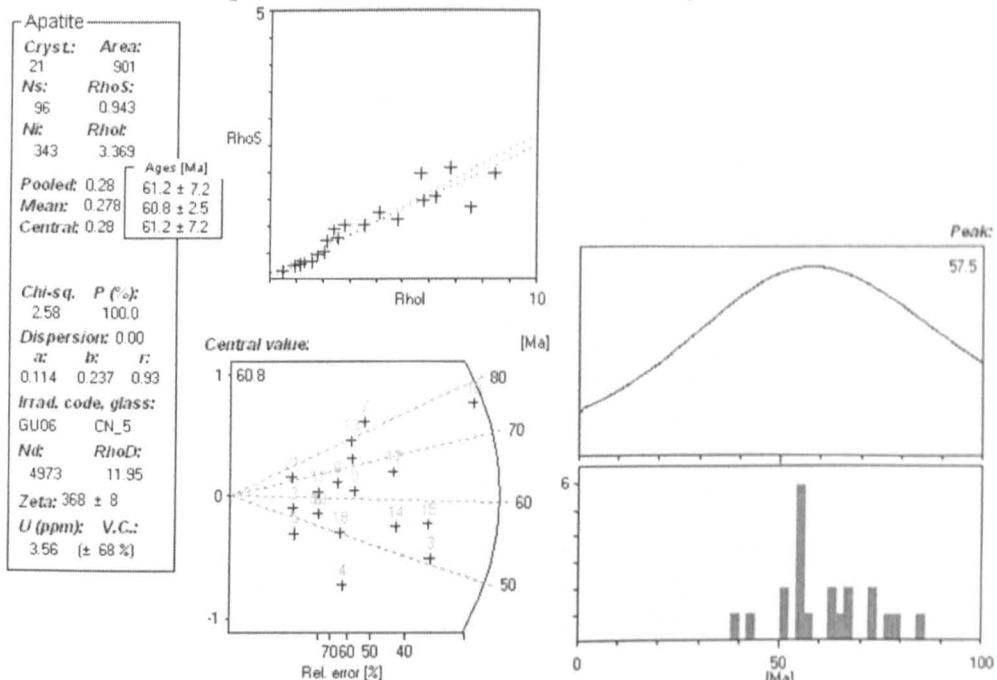


Figure 109 - Radial plots for apatite from the Ardnamurchan Central Complex. Samples AR2 and AR13. Screen shot from TrackKey



**Figure 110 - Radial plots for apatite from the Mull Central Complex. Samples ML5 and ML3. Screen shot from TrackKey**

## S03-03 - Glamaig Granite, Western Red Hills Complex



## SKM-04 - Marscoite ferrodiorite, Western Red Hills Complex

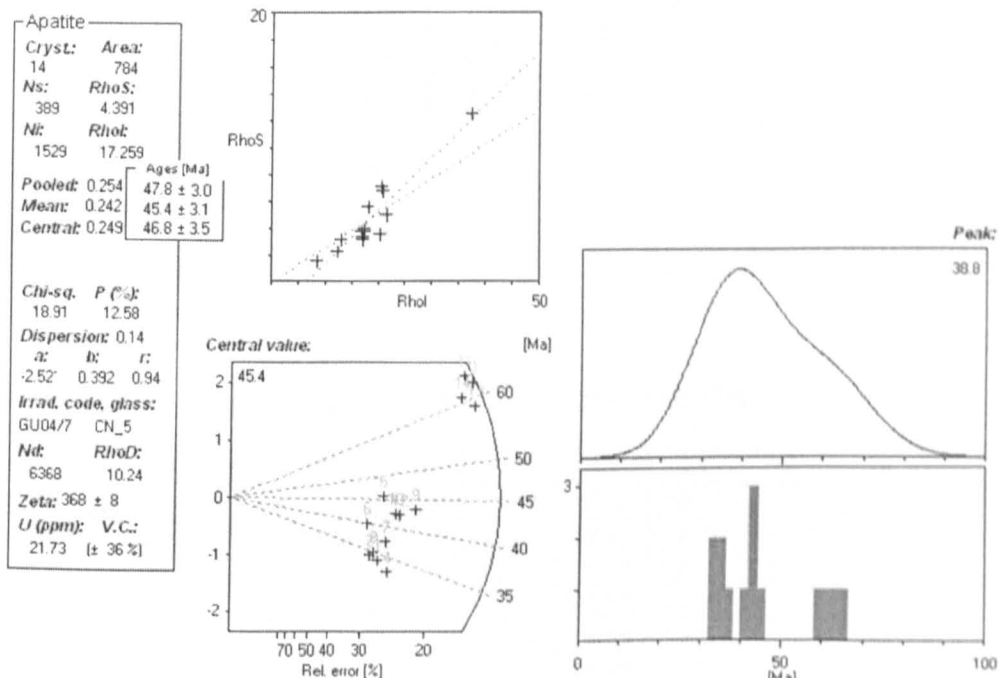


Figure 111 - Radial plots for apatite from the Skye Central Complex. Samples S03-03 and SKM04. Screen shot from TrackKey

## G.2 Raw AFT data for Rum

### G.2.1 Single grain age data

n (list)	n (cryst.)	Ns	Ni	Sum Ns	Sum Ni	Grain age	$\pm 1s$	Chi-sq.	Sum age	$\pm 1s$
1	4	1	15	1	15	14.9	15.4	---	>14.9	>15.4
2	1	1	13	2	28	17.2	17.8	92.2	16.0	11.7
3	12	1	11	3	39	20.3	21.2	97.8	17.2	10.3
4	17	1	10	4	49	22.3	23.4	99.3	18.2	9.5
5	24	11	63	15	112	38.9	12.8	80.0	29.9	8.2
6	18	5	25	20	137	44.6	21.9	84.1	32.6	7.8
7	8	3	12	23	149	55.7	36.0	85.7	34.4	7.8
8	6	2	8	25	157	55.7	44.1	89.5	35.5	7.7
9	3	10	39	35	196	57.1	20.3	85.7	39.8	7.4
10	19	2	7	37	203	63.6	51.0	89.2	40.7	7.3
11	7	2	7	39	210	63.6	51.0	92.0	41.4	7.3
12	5	3	10	42	220	66.8	44.0	93.4	42.6	7.2
13	10	11	34	53	254	72	25.0	88.5	46.5	7.1
14	9	12	37	65	291	72.2	24.0	85.9	49.8	6.9
15	23	3	9	68	300	74.2	49.5	88.7	50.5	6.9
16	22	2	6	70	306	74.2	60.6	91.5	51.0	6.8
17	20	3	9	73	315	74.2	49.5	93.4	51.6	6.8
18	13	2	6	75	321	74.2	60.6	95.2	52.1	6.8
19	11	1	3	76	324	74.2	85.6	96.7	52.3	6.8
20	2	1	3	77	327	74.2	85.6	97.7	52.5	6.7
21	16	14	41	91	368	76	23.6	97.3	55.1	6.6
22	14	3	8	94	376	83.4	56.5	97.8	55.7	6.5
23	21	2	5	96	381	88.9	74.4	98.3	56.1	6.5
24	15	2	5	98	386	88.9	74.4	98.7	56.6	6.5
25	25	8	17	106	403	104.4	44.9	97.6	58.6	6.5

Table 29 - Single grain ages from sample R11, Harris Bay, Rum

## G.3 Confined track length measurements

Categories	9	10	11	12	13	14	15	16	17
Lengths ( $\mu\text{m}$ )	9.11	10.73	11.61	12.79	13.6	14.05	15.92		
		10.52	11.12	12.42	13.11	14.69	15.27		
			11.44	12.54	13.02	14.11	15.01		
				12.2	13.62	14.31			
				12	13.36	14.42			
					13.75	14.95			

Table 30 – Confined track length measurements from sample R11, Harris Bay, Rum

### G.3.1 Frequency plot of track length measurements

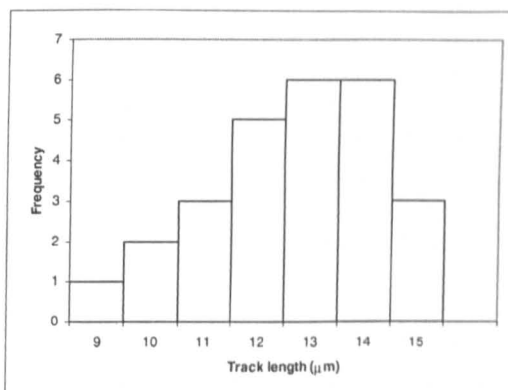


Figure 112 - The apatite fission track frequency distribution

### G.4 Raw AFT data for Mull

n (list)	n (cryst.)	Ns	Ni	Sum Ns	Sum Ni	Grain age	± 1s	Chi-sq.	Sum age	± 1s
1	15	4	29	4	29	29.4	15.7	---	>29.4	>15.7
2	4	5	30	9	59	35.6	17.2	79.2	32.6	11.7
3	19	7	41	16	100	36.4	14.9	94.7	34.1	9.2
4	6	5	26	21	126	41.0	20.1	97.5	35.6	8.4
5	14	5	25	26	151	42.7	20.9	98.8	36.7	7.8
6	11	4	19	30	170	44.9	24.7	99.4	37.7	7.5
7	18	5	23	35	193	46.4	22.9	99.7	38.7	7.2
8	5	10	43	45	236	49.6	17.5	99.5	40.7	6.7
9	21	3	11	48	247	58.1	37.9	99.6	41.5	6.6
10	22	11	39	59	286	60.1	20.6	98.8	44.0	6.4
11	3	2	7	61	293	60.9	48.8	99.3	44.4	6.3
12	12	2	6	63	299	70.9	58.0	99.5	44.9	6.3
13	8	2	6	65	305	70.9	58.0	99.6	45.4	6.3
14	7	3	9	68	314	70.9	47.3	99.6	46.2	6.3
15	2	2	6	70	320	70.9	58.0	99.7	46.6	6.2
16	10	4	11	74	331	77.3	45.2	99.7	47.7	6.2
17	17	7	19	81	350	78.4	34.7	99.4	49.3	6.2
18	16	6	16	87	366	79.8	38.2	99.1	50.7	6.1
19	20	22	54	109	420	86.6	22.0	94.1	55.3	6.1
20	9	11	25	120	445	93.5	33.9	90.6	57.4	6.0
21	1	1	2	121	447	106.1	130.0	92.5	57.7	6.0
22	13	8	15	129	462	113.1	49.6	87.5	59.5	6.1

Table 31 - Single grain ages from sample ML5, Mull

n (list)	n (cryst.)	Ns	Ni	Sum Ns	Sum Ni	Grain age	$\pm 1s$	Chi-sq.	Sum age	$\pm 1s$
1	5	4	33	4	33	25.6	13.6	—	>25.6	>13.6
2	28	5	39	9	72	27.1	12.9	93.7	26.4	9.4
3	24	3	21	12	93	30.2	18.7	98.0	27.3	8.4
4	18	2	14	14	107	30.2	22.9	99.6	27.7	7.9
5	20	4	27	18	134	31.3	16.8	99.9	28.4	7.2
6	17	3	19	21	153	33.4	20.8	100.0	29.0	6.8
7	26	5	30	26	183	35.2	17.0	100.0	30.0	6.3
8	22	2	12	28	195	35.2	26.9	100.0	30.4	6.2
9	7	5	30	33	225	35.2	17.0	100.0	31.0	5.8
10	16	5	25	38	250	42.3	20.7	100.0	32.1	5.6
11	13	15	73	53	323	43.4	12.4	99.9	34.7	5.2
12	2	4	18	57	341	46.9	26.0	99.9	35.3	5.1
13	30	2	8	59	349	52.8	41.7	99.9	35.7	5.1
14	3	3	12	62	361	52.8	34.1	99.9	36.3	5.1
15	12	2	7	64	368	60.3	48.4	99.9	36.8	5.0
16	19	23	77	87	445	63.0	15.1	97.0	41.3	4.9
17	27	2	6	89	451	70.3	57.4	97.5	41.7	4.9
18	23	2	6	91	457	70.3	57.4	98.0	42.1	4.9
19	15	2	6	93	463	70.3	57.4	98.4	42.4	4.9
20	4	18	51	111	514	74.4	20.5	92.6	45.6	4.9
21	6	4	11	115	525	76.6	44.8	92.8	46.3	4.9
22	29	2	5	117	530	84.2	70.5	93.7	46.6	4.9
23	10	7	17	124	547	86.7	39.0	90.9	47.9	4.9
24	11	6	14	130	561	90.2	44.1	88.4	48.9	4.9
25	9	6	14	136	575	90.2	44.1	86.2	49.9	4.9
26	14	5	11	141	586	95.6	51.6	84.4	50.8	4.9
27	8	5	11	146	597	95.6	51.6	82.9	51.6	4.9
28	25	11	23	157	620	100.6	37.0	73.6	53.5	4.9
29	1	1	2	158	622	105.1	128.8	76.7	53.6	4.9
30	21	42	79	200	701	111.7	21.5	25.6	60.2	5.0

Table 32 - Single grain ages from sample ML2, Mull

## G.5 Raw AFT data for Ardnamurchan

n (list)	n (cryst.)	Ns	Ni	Sum Ns	Sum Ni	Grain age	$\pm 1s$	Chi-sq.	Sum age	$\pm 1s$
1	12	5	30	5	30	35.6	17.2	—	> 35.6	> 17.2
2	14	5	26	10	56	41.1	20.1	83.5	38.1	13.1
3	4	7	36	17	92	41.5	17.2	96.7	39.5	10.5
4	3	5	25	22	117	42.7	20.9	99.3	40.1	9.4
5	2	3	14	25	131	45.7	29.1	99.8	40.7	8.9
6	11	4	18	29	149	47.4	26.2	99.9	41.6	8.5
7	6	2	8	31	157	53.3	42.2	100	42.2	8.3
8	5	4	15	35	172	56.9	32.0	99.9	43.4	8.1
9	9	3	11	38	183	58.1	37.9	99.9	44.3	8
10	10	11	39	49	222	60.1	20.6	99.8	47.1	7.5
11	15	22	76	71	298	61.7	15.0	99.5	50.8	6.8
12	1	3	10	74	308	63.9	42.1	99.7	51.3	6.7
13	22	3	9	77	317	71.0	47.4	99.8	51.8	6.7
14	20	2	6	79	323	71.0	58.0	99.9	52.2	6.6
15	18	2	6	81	329	71.0	58.0	99.9	52.5	6.6
16	13	3	9	84	338	71.0	47.4	100	53.0	6.6
17	8	6	18	90	356	71.0	33.5	100	53.9	6.5
18	7	2	6	92	362	71.0	58.0	100	54.2	6.4
19	21	5	14	97	376	76.0	39.7	100	55.0	6.4
20	17	6	14	103	390	91.1	44.5	100	56.3	6.4
21	16	3	7	106	397	91.1	62.9	100	56.9	6.3
22	19	1	2	107	399	106.2	130.1	100	57.2	6.3

Table 33 - Single grain ages from sample AR13, Ardnamurchan

n (list)	n (cryst.)	Ns	Ni	Sum Ns	Sum Ni	Grain age	$\pm 1s$	Chi-sq.	Sum age	$\pm 1s$
1	15	4	29	4	29	29.4	15.7	—	> 29.4	> 15.7
2	4	5	30	9	59	35.6	17.2	79.2	32.6	11.7
3	19	7	41	16	100	36.4	14.9	94.7	34.1	9.2
4	6	5	26	21	126	41.0	20.1	97.5	35.6	8.4
5	14	5	25	26	151	42.7	20.9	98.8	36.7	7.8
6	11	4	19	30	170	44.9	24.7	99.4	37.7	7.5
7	18	5	23	35	193	46.4	22.9	99.7	38.7	7.2
8	5	10	43	45	236	49.6	17.5	99.5	40.7	6.7
9	21	3	11	48	247	58.1	37.9	99.6	41.5	6.6
10	22	11	39	59	286	60.1	20.6	98.8	44.0	6.4
11	3	2	7	61	293	60.9	48.8	99.3	44.4	6.3
12	12	2	6	63	299	70.9	58.0	99.5	44.9	6.3
13	8	2	6	65	305	70.9	58.0	99.6	45.4	6.3
14	7	3	9	68	314	70.9	47.3	99.6	46.2	6.3
15	2	2	6	70	320	70.9	58.0	99.7	46.6	6.2
16	10	4	11	74	331	77.3	45.2	99.7	47.7	6.2
17	17	7	19	81	350	78.4	34.7	99.4	49.3	6.2
18	16	6	16	87	366	79.8	38.2	99.1	50.7	6.1
19	20	22	54	109	420	86.6	22.0	94.1	55.3	6.1
20	9	11	25	120	445	93.5	33.9	90.6	57.4	6.0
21	1	1	2	121	447	106.1	130.0	92.5	57.7	6.0
22	13	8	15	129	462	113.1	49.6	87.5	59.5	6.1

Table 34 - Single grain ages from sample AR2, Ardnamurchan

## G.6 Raw AFT data for Skye

n (list)	n (cryst.)	Ns	Ni	Sum Ns	Sum Ni	Grain age	± 1s	Chi-sq.	Sum age	± 1s
1	4	3	17	3	17	38.7	24.2	—	>38.7	>24.2
2	5	1	5	4	22	43.8	48.0	92.1	39.9	21.7
3	18	3	13	7	35	50.5	32.4	95.6	43.8	18.2
4	3	10	43	17	78	50.9	17.9	98.3	47.7	12.8
5	20	2	8	19	86	54.7	43.3	99.6	48.4	12.3
6	19	2	8	21	94	54.7	43.3	99.9	48.9	11.9
7	16	2	8	23	102	54.7	43.3	100.0	49.4	11.5
8	14	7	28	30	130	54.7	23.2	100.0	50.5	10.3
9	6	2	8	32	138	54.7	43.3	100.0	50.8	10.0
10	2	1	4	33	142	54.7	61.2	100.0	50.9	9.9
11	15	10	39	43	181	56.1	20.0	100.0	52.0	8.9
12	12	2	7	45	188	62.5	50.2	100.0	52.4	8.8
13	9	4	14	49	202	62.5	35.5	100.0	53.1	8.5
14	8	3	10	52	212	65.6	43.2	100.0	53.7	8.4
15	17	7	23	59	235	66.6	28.8	100.0	55.0	8.1
16	11	7	23	66	258	66.6	28.8	100.0	56.0	7.8
17	21	1	3	67	261	72.9	84.2	100.0	56.2	7.8
18	1	4	12	71	273	72.9	42.1	100.0	56.9	7.7
19	10	16	46	87	319	76.0	22.2	100.0	59.7	7.3
20	13	4	11	91	330	79.5	46.4	100.0	60.4	7.3
21	7	5	13	96	343	84.0	44.3	100.0	61.2	7.2

Table 35 - Single grain ages from sample S03-03, Glamaig, Skye

n (list)	n (cryst.)	Ns	Ni	Sum Ns	Sum Ni	Grain age	± 1s	Chi-sq.	Sum age	± 1s
1	1	1	18	1	18	15.3	15.7	—	> 15.3	> 15.7
2	8	1	15	2	33	18.3	18.9	90	16.7	12.1
3	5	1	14	3	47	19.6	20.3	98.4	17.5	10.5
4	9	1	12	4	59	22.9	23.8	99.4	18.6	9.6
5	11	3	24	7	83	34.3	21	95.6	23.2	9.1
6	10	3	19	10	102	43.3	26.9	93.2	26.9	8.9
7	2	3	19	13	121	43.3	26.9	94.5	29.5	8.6
8	15	6	36	19	157	45.7	20.2	94.5	33.2	8.1
9	13	3	18	22	175	45.7	28.5	96.6	34.5	7.9
10	4	2	12	24	187	45.7	34.9	98.1	35.2	7.7
11	14	8	45	32	232	48.8	18.7	98.3	37.9	7.2
12	3	5	28	37	260	49	23.8	98.9	39.1	6.9
13	7	23	120	60	380	52.5	12	98.4	43.3	6.1
14	6	19	99	79	479	52.6	13.2	98.8	45.2	5.6
15	12	5	26	84	505	52.7	25.8	99.3	45.6	5.5
16	17	4	18	88	523	60.9	33.7	99.5	46.2	5.4
17	16	3	5	91	528	163.1	119.2	95.3	47.3	5.5

Table 36 - Single grain ages from sample SKM04, Marsco, Skye

## References

- AL-KINDI, S., WHITE, N., SINHA, M., ENGLAND, R. W., & TILEY, R. (2003) Crustal trace of a hot convective sheet. *Geology*. **31**. (3), 207-210.
- ARROWSMITH, S. J., KENDALL, M., WHITE, N., & VANDECAR, J. C. (2005) Seismic imaging of a hot upwelling beneath the British Isles. *Geology*. **33**. (5), 345-348.
- BALAN, E., NEUVILLE, D. R., TROCELLIER, P., FRITSCH, E., MULLER, J. P., & CALAS, G. (2001) Metamictization and chemical durability of detrital zircon. *American Mineralogist*. **86**. 1025-1033.
- BARBARAND, J., CARTER, A., WOOD, I., & HURFORD, T. (2003) Compositional and structural control of fission-track annealing in apatite. *Chemical Geology*. **198**. (1-2), 107-137.
- BARBARAND, J. & PAGEL, M. (2001) Importance of the chemistry to characterise apatite fission-track annealing. *Comptes Rendus de l'Academie des Sciences*. **332**. (4), 259-265.
- BARTON, A. J. & WHITE, R. S. (1995) The Edoras Bank Margin - continental break-up in the presence of a mantle plume. *Journal of the Geological Society, London*. **152**. 971-974.
- BELL, B. R. & HARRIS, J. W. (1986) *An excursion guide to the geology of the Isle of Skye*. Geological Society of Glasgow.
- BELL, B. R. & WILLIAMSON, I. T. (2002) Tertiary Igneous Activity. in TREWIN, N. H. (ed) *The Geology of Scotland*. Geological Society, London 371-430.
- BENDER, M. (1973) Helium-Uranium dating of corals. *Geochimica et Cosmochimica Acta*. **37**. 1229-1247.
- BERNET, M., BRANDON, M. T., GARVER, J. I., & MOLITOR, B. (2004) Fundamentals of detrital zircon fission-track analysis for provenance and exhumation studies with examples from the European Alps. in BERNET, M. & SPIEGEL, C. (eds) *Detrital thermochronology - Provenance analysis, exhumation, and landscape evolution of mountain belts: Boulder, Colorado*. Geological Society of America Special Paper **378** 25-36.
- BIGAZZI, G. (1981) The problem of the decay constant  $\lambda_1$  of  $^{238}\text{U}$ . *Nuclear Tracks and Radiation Measurements*. **5**. 35-44.
- BLANC, P., BAUMER, A., CESBRON, F., OHNENSTETTER, D., PANCZER, G., & REMOND, G. (2000) Systematic cathodoluminescence spectral analysis of synthetic doped minerals: anhydrite, apatite, calcite, fluorite, scheelite and zircon. in PAGEL, M., BARBIN, V., BLANC, P., & OHNENSTETTER, D. (eds) *Cathodoluminescence in geosciences*. Springer Verlag 127-160.
- BOTT, M. H. P. & TANTRIGODA, D. A. (1987) Interpretation of the gravity and magnetic anomalies over the Mull Tertiary Intrusive Complex, NW Scotland. *Journal of the Geological Society, London*. **144**. 17-28.

- BOTT, M. H. P. & TUSON, J. (1973) Deep structure beneath the Tertiary volcanic regions of Skye, Mull and Ardnamurchan, NW Scotland. *Nature*. **242**. 114-116.
- BOYCE, J. W. & HODGES, K. V. (2005) U and Th zoning in Cerro de Mercado (Durango, Mexico) fluorapatite: Insights regarding the impact of recoil redistribution of radiogenic He-4 on (U-Th)/He thermochronology. *Chemical Geology*. **219**. (1-4), 261-274.
- BRANDON, M. T., RODEN-TICE, M. K., & GARVER, J. I. (1998) Late Cenozoic exhumation of the Cascadia accretionary wedge in the Olympic Mountains, northwest Washington State. *Geological Society of America Bulletin*. **110**. (8), 985-1009.
- BRAUN, J. (2005) Quantitative constraints on the rate of landform evolution derived from low-temperature thermochronology. in REINERS, P. W. & EHLERS, T. A. (eds) *Thermochronology*. Reviews in Mineralogy and Geochemistry. Mineralogical Society of America **58** 351-374.
- BRAUN, J., VAN DER BEEK, P. A., & BATT, G. (2006) *Quantitative thermochronology*. Cambridge University Press.
- BROWN, D. J. & BELL, B. R. (2006) Intrusion-induced uplift and mass wasting of the Palaeogene volcanic landscape of Ardnamurchan, NW Scotland. *Journal of the Geological Society, London*. **163**. (1), 29-36.
- BROWN, R., GALLAGHER, K., & DUANE, M. (1994) A quantitative assessment of the effects of magmatism on the thermal history of the Karoo sedimentary sequence. *Journal of African Earth Sciences*. **18**. (3), 227-243.
- BRYAN, S. E., RILEY, T. R., JERRAM, D. A., STEPHENS, C. J., & LEAT, P. T. (2002) Silicic volcanism: An undervalued component of large igneous provinces and volcanic rifted margins. in MENZIES, M. A., KLEMPERER, S. L., EBINGER, C. J., & BAKER, J. (eds) *Volcanic Rifted Margins*. Geological Society of America Special Paper **362** 97-118.
- BURAKOV, B. E., HANCHAR, J. M., ZAMORYANSKAYA, M. V., GARBUZOV, V. M., & ZIRLIN, V. A. (2002) Synthesis and investigation of Pu-doped single crystal zircon, (Zr, Pu)SiO<sub>4</sub>. *Radiochimica Acta*. **90**. (2), 95-98.
- BUTLER, R. W. H. & HUTTON, D. H. W. (1994) Basin structure and Tertiary magmatism on Skye, NW Scotland. *Journal of the Geological Society, London*. **151**. 931-944.
- CARLSON, W. D., DONELICK, R. A., & KETCHAM, R. A. (1999) Variability of apatite fission-track annealing kinetics: I. Experimental results. *American Mineralogist*. **84**. (9), 1213-1223.
- CARPENA, J. (1992) Fission-track dating of zircon - zircons from the Mont Blanc Granite (French-Italian Alps). *Journal of Geology*. **100**. (4), 411-421.
- CARPENA, J. & MAILHÉ, D. (1987) Fission-track dating calibration of the Fish Canyon Tuff standard in French reactors. *Chemical Geology*. **66**. 53-59.
- CAYZER, N. J. & HINTON, R. (2002, unpublished data) An EBSD study of the damage to zircon crystals by U decay and the implications for SIMS U/Pb dating. <http://www.geos.ed.ac.uk/facilities/ionprobe/CayzerHinton.pdf>.
- CHAMBERS, L. M. & PRINGLE, M. S. (2001) Age and duration of activity at the Isle of Mull Tertiary igneous centre, Scotland, and confirmation of the existence of subchrons during Anomaly 26r. *Earth and Planetary Science Letters*. **193**. (3-4), 333-345.
- CHAMBERS, L. M., PRINGLE, M. S., & PARRISH, R. R. (2005) Rapid formation of the Small Isles Tertiary centre constrained by precise <sup>40</sup>Ar/<sup>39</sup>Ar and U-Pb ages. *Lithos*. **79**. (3-4), 367-384.

- CLAUSER, C. & HUENGES, E. (1995) Thermal conductivity of rocks and minerals. *in* AHRENS, T. J. (ed) *Rock physics and phase relations - a handbook of physical constants*. American Geophysical Union, Washington 3 105-126.
- CLIFT, P. D. (1997) Temperature anomalies under the Northeast Atlantic rifted volcanic margins. *Earth and Planetary Science Letters*. **146**. (1-2), 195-211.
- CLIFT, P. D., CARTER, A., & HURFORD, A. J. (1998) The erosional and uplift history of NE Atlantic passive margins: constraints on a passing plume. *Journal of the Geological Society, London*. **155**. 787-800.
- CLIFT, P. D. & TURNER, J. (1995) Dynamic support by the Icelandic plume and vertical tectonics of the northeast Atlantic continental margins. *Journal of Geophysical Research*. **100**. (B12), 24473-24486.
- CLIFT, P. D. & TURNER, J. (1998) Paleogene igneous underplating and subsidence anomalies in the rockall-Faeroe-Shetland area. *Marine and Petroleum Geology*. **15**. (3), 223.
- COFFIN, M. F. & ELDHOLM, O. (1994) Large Igneous Provinces - Crustal Structure, Dimensions, and External Consequences. *Reviews of Geophysics*. **32**. (1), 1-36.
- CORFU, F., HANCHAR, J. M., HOSKIN, P. W. O., & KINNY, P. (2003) Atlas of zircon textures. *in* HANCHAR, J. M. & HOSKIN, P. W. O. (eds) *Zircon*. Reviews in Mineralogy and Geochemistry. Mineralogical Society of America 53 468-500.
- CORRIGAN, J. (1991) Inversion of apatite fission-track data for thermal history information. *Journal of Geophysical Research*. **96**. 10347-10360.
- COYLE, D. A. & WAGNER, G. A. (1996) Fission track dating of zircon and titanite from the 9101 m deep KTB: Observed fundamentals of track stability and thermal history reconstruction. *Proceedings of International Workshop on Fission Track Dating*, Ghent, Belgium.
- CROWLEY, K. D., CAMERON, M., & SCHAEFER, R. L. (1991) Experimental studies of annealing of etched fission tracks in fluorapatite. *Geochimica et Cosmochimica Acta*. **55**. (5), 1449-1465.
- DAGLEY, P. & MUSSETT, A. E. (1986) Paleomagnetism and radiometric dating of the British Tertiary Igneous Province - Muck and Eigg. *Geophysical Journal of the Royal Astronomical Society*. **85**. (1), 221-242.
- DAGLEY, P., MUSSETT, A. E., & SKELHORN, R. R. (1985) Paleomagnetic and Radiometric Chronology of the British Tertiary Igneous Province - a Review. *Geophysical Journal of the Royal Astronomical Society*. **81**. (1), 323-323.
- DAGLEY, P., MUSSETT, A. E., & SKELHORN, R. R. (1987) Polarity, stratigraphy and duration of the Tertiary igneous activity of Mull, Scotland. *Journal of the Geological Society, London*. **144**. 985-996.
- DAMON, P. E. & GREEN, W. D. (1963) Investigations of the helium age dating method by stable isotope-dilution technique. *in* *Radioactive Dating*. International Atomic Energy Agency, Vienna 55-71.
- DEMPSTER, T. J., HAY, D. C., & BLUCK, B. J. (2004) Zircon growth in slate. *Geology*. **32**. (3), 221-224.
- DEMPSTER, T. J., JOLIVET, M., TUBRETT, M. N., & BRAITHWAITE, C. J. R. (2003) Magmatic zoning in apatite: a monitor of porosity and permeability change in granites. *Contributions to Mineralogy and Petrology*. **145**. (5), 568-577.

- DODSON, M. H. (1973) Closure temperatures in cooling geochronological and petrological systems. *Contributions to Mineralogy and Petrology*. **40**, 259-274.
- DONELICK, R. A. (1991) Crystallographic orientation dependence of mean etchable fission-track length in apatite - an empirical model and experimental observations. *American Mineralogist*. **76**, (1-2), 83-91.
- DONELICK, R. A. (1995) A method of fission track analysis utilizing bulk chemical etching of apatite. Australia Patent 658,800.
- DONELICK, R. A., FARLEY, K. A., O'SULLIVAN, P., & ASIMOV, P. (2003) Experimental evidence concerning the pressure dependence of He diffusion and fission-track annealing kinetics in apatite. *On Track*. **13**, (26), 19-21.
- DONELICK, R. A., KETCHAM, R. A., & CARLSON, W. D. (1999) Variability of apatite fission-track annealing kinetics: II. Crystallographic orientation effects. *American Mineralogist*. **84**, (9), 1224-1234.
- DONELICK, R. A. & MILLER, D. S. (1991) Enhanced TINT fission-track densities in low spontaneous track density apatites using Cf-252 derived fission fragment tracks - a model and experimental observations. *Nuclear Tracks and Radiation Measurements*. **18**, (3), 301-307.
- DONELICK, R. A., O'SULLIVAN, P. B., & KETCHAM, R. A. (2005) Apatite fission-track analysis. *in* REINERS, P. W. & EHLERS, T. A. (eds) *Thermochronology*. Reviews in Mineralogy and Geochemistry. Mineralogical Society of America **58** 49-94.
- DONELICK, R. A., RODEN, M. K., MOOERS, J. D., CARPENTER, B. S., & S., M. D. (1990) Etchable length reduction of induced fission tracks in apatite at room temperature (~23°C): crystallographic orientation effects and "initial" mean lengths. *Nuclear Tracks and Radiation Measurements*. **17**, 261-265.
- DUDDY, I. R., GREEN, P. F., & LASLETT, G. M. (1988) Thermal annealing of fission tracks in apatite III: Variable temperature behavior. *Chemical Geology*. **73**, (1), 25-38.
- DUNKL, I. (2002) Trackkey: a Windows program for calculation and graphical presentation of fission track data. *Computers & Geosciences*. **28**, (1), 3-12.
- EHLERS, T. A., CHAUDHRI, T., KUMAR, S., FULLER, C. W., WILLETT, S. D., KETCHAM, R. A., BRANDON, M. T., BELTON, D. X., KOHN, B. P., GLEADOW, A. J. W., DUNAI, T. J., & FU, F. Q. (2005) Computational tools for low-temperature thermochronometer interpretation. *in* REINERS, P. W. & EHLERS, T. A. (eds) *Thermochronology*. Reviews in Mineralogy and Geochemistry. Mineralogical Society of America **58** 589-622.
- EMELEUS, C. H. (1973) Granophyre pebbles in Tertiary conglomerates on the Isle of Canna, Inverness-shire. *Scottish Journal of Geology*. **9**, 157-159.
- EMELEUS, C. H. (1985) The Tertiary lavas and sediments of Northwest Rhum, Inner Hebrides. *Geological Magazine*. **122**, (5), 419-437.
- EMELEUS, C. H. (1997) *Geology of Rum and the adjacent islands*. Memoir of the British Geological Survey. **Sheet 60 (Scotland)**.
- EMELEUS, C. H. & BELL, B. R. (2005) *The Palaeogene volcanic districts of Scotland*. British Geological Survey.
- EWING, R. C., MELDRUM, A., WANG, L. L., WEBBER, W. J., & CORRALES, L. R. (2003) Radiation effects in zircon. *in* HANCHAR, J. M. & HOSKIN, P. W. O. (eds) *Zircon*. Reviews in Mineralogy and Geochemistry. Mineralogical Society of America **53** 387-425.

- FANALE, F. & KULP, J. L. (1961) Helium in limestone and marble. *American Mineralogist*. **46**. (1-2), 155-167.
- FARLEY, K. A. (2000) Helium diffusion from apatite: General behavior as illustrated by Durango fluorapatite. *Journal of Geophysical Research*. **105**. (B2), 2903-2914.
- FARLEY, K. A. (2002) (U-Th)/He dating: techniques, calibrations, and applications. in PORCELLI, D., BALLANTINE, C. K., & WIELER, R. (eds) *Noble gases in geochemistry and cosmochemistry*. Reviews in Mineralogy and Geochemistry. Mineralogical Society of America **47** 819-843.
- FARLEY, K. A., KOHN, B. P., & PILLANS, B. (2002) The effects of secular disequilibrium on (U-Th)/He systematics and dating of Quaternary volcanic zircon and apatite. *Earth and Planetary Science Letters*. **201**. (1), 117-125.
- FARLEY, K. A. & STOCKLI, D. F. (2002) (U-Th)/He dating of phosphates: Apatite, monazite, and xenotime. in *Phosphates: Geochemical, Geobiological, and Materials Importance*. Reviews in Mineralogy and Geochemistry. Mineralogical Society of America **48** 559-577.
- FARLEY, K. A., WOLF, R. A., & SILVER, L. T. (1996) The effects of long alpha-stopping distances on (U-Th)/He ages. *Geochimica et Cosmochimica Acta*. **60**. (21), 4223-4229.
- FINCH, R. J. & HANCHAR, J. M. (2003) Structure and chemistry of zircon and zirconium-group minerals. in HANCHAR, J. M. & HOSKIN, P. W. O. (eds) *Zircon*. Reviews in Mineralogy and Geochemistry. Mineralogical Society of America **53** 1-25.
- FITZGERALD, P. G., BALDWIN, S. L., WEBB, L. E., & O'SULLIVAN, P. B. (2006) Interpretation of (U-Th)/He single grain ages from slowly cooled crustal terranes: A case study from the Transantarctic Mountains of southern Victoria Land. *Chemical Geology*. **225**. (1-2), 91.
- FLEISCHER, R. L. & PRICE, P. B. (1964) Techniques for geological dating of minerals by chemical etching of fission fragment tracks. *Geochimica et Cosmochimica Acta*. **28**. 1705-1714.
- FLEISCHER, R. L., PRICE, P. B., & WALKER, R. M. (1965) Effects of temperature, pressure, and ionization on the formation and stability of fission tracks in minerals and glasses. *Journal of Geophysical Research*. **70**. 1497-1502.
- FLEISCHER, R. L., PRICE, P. B., & WALKER, R. M. (1975) *Nuclear Tracks in Solids*. University of California Press.
- FOEKEN, J. P. T. (2004) *Tectono-morphology of the Ligurian Alps and adjacent basins (NW Italy). An integrated study of their Neogene to present evolution*. Vrije Universiteit. Ph.D Thesis.
- FOEKEN, J. P. T., STUART, F. M., DOBSON, K. J., PERSANO, C., & VILBERT, D. (2006) A diode laser system for heating minerals for (U-Th)/He chronometry. *Geochemistry Geophysics Geosystems*.
- FORESTER, R. W. & TAYLOR, J., HUGH P. (1976) 18O-depleted igneous rocks from the Tertiary complex of the Isle of Mull, Scotland. *Earth and Planetary Science Letters*. **32**. (1), 11-17.
- FOULGER, G. R., NATLAND, J. H., & ANDERSON, D. L. (2005) A source for Icelandic magmas in remelted Iapetus crust. *Journal of Volcanology and Geothermal Research*. **141**. (1-2), 23-44.
- GALBRAITH, R. F. & LASLETT, G. M. (1997) Statistical modelling of thermal annealing of fission tracks in zircon. *Chemical Geology*. **140**. (1-2), 123-135.
- GALLAGHER, K. (1995) Evolving temperature histories from apatite fission-track data. *Earth and Planetary Science Letters*. **136**. (3-4), 421-435.
- GALLAGHER, K., BROWN, R., & JOHNSON, C. (1998) Fission track analysis and its applications to geological problems. *Annual Review of Earth and Planetary Sciences*. **26**. 519-572.

- GAMBLE, J. A., WYSOCZANSKI, R. J., & MEIGHAN, I. G. (1999) Constraints on the age of the British Tertiary Volcanic Province from ion microprobe U-Pb (SHRIMP) ages for acid igneous rocks from NE Ireland. *Journal of the Geological Society, London*. **156**. 291-299.
- GARVER, J. I. (2003) Etching zircon age standards for fission-track analysis. *Radiation Measurements*. **37**. (1), 47-53.
- GEISLER, T., RASHWAN, A. A., RAHN, M. K. W., POLLER, U., ZWINGMANN, H., PIDGEON, R. T., SCHLEICHER, H., & TOMASCHEK, F. (2003) Low-temperature hydrothermal alteration of natural metamict zircons from the Eastern Desert, Egypt. *Mineralogical Magazine*. **67**. (3), 485-508.
- GEORGE, T. N. (1966) The Geomorphic evolution of Hebridean Scotland. *Scottish Journal of Geology*. **2**. 1-34.
- GLEADOW, A. J. & BROWN, R. W. (2000) Fission track thermochronology and the long term denudation response to tectonics. in SUMMERFIELD, M. A. (ed) *Geomorphology and Global Tectonics*. John Wiley & Sons Ltd. 57-75.
- GLEADOW, A. J. & DUDDY, I. R. (1981) A natural long term track annealing experiment for apatite. *Nuclear Tracks and Radiation Measurements*. **5**. (1/2), 169-174.
- GLEADOW, A. J. W., DUDDY, I. R., GREEN, P. F., & HEGARTY, K. A. (1986a) Fission track lengths in the apatite annealing zone and the interpretation of mixed ages. *Earth and Planetary Science Letters*. **78**. (2-3), 245-254.
- GLEADOW, A. J. W., DUDDY, I. R., GREEN, P. F., & LOVERING, J. F. (1986b) Confined fission track lengths in apatite - a diagnostic tool for thermal history analysis. *Contributions to Mineralogy and Petrology*. **94**. (4), 405-415.
- GLEADOW, A. J. W., DUDDY, I. R., & LOVERING, J. F. (1993) Fission track analysis: A new tool for the evaluation of thermal histories and hydrocarbon potential. *Australian Petroleum Exploration Association Journal*. **23**. 93-102.
- GREEN, P. F. & DUDDY, I. R. (2006) Interpretation of apatite (U-Th)/He ages and fission track ages from cratons. *Earth and Planetary Science Letters*. **244**. (3-4), 541.
- GREEN, P. F., DUDDY, I. R., & BRAY, R. J. (1995) Low-temperature thermal history of Eastern Ireland - effects of fluid flow - Discussion. *Marine and Petroleum Geology*. **12**. (7), 773-776.
- GREEN, P. F., DUDDY, I. R., GLEADOW, A. J. W., TINGATE, P. R., & LASLETT, G. M. (1985) Fission-Track Annealing in Apatite - Track Length Measurements and the Form of the Arrhenius Plot. *Nuclear Tracks and Radiation Measurements*. **10**. (3), 323-328.
- GREEN, P. F., DUDDY, I. R., GLEADOW, A. J. W., TINGATE, P. R., & LASLETT, G. M. (1986) Thermal annealing of fission tracks in apatite I: A qualitative description. *Chemical Geology*. **59**. (4), 237-253.
- GREEN, P. F., DUDDY, I. R., HEGARTY, K. A., & BRAY, R. J. (1999) Early Tertiary heat flow along the UK Atlantic margin and adjacent areas. in FLEET, A. J. & BOLDY, S. A. R. (eds) *Petroleum Geology of Northwest Europe: Proceedings of the 5th Conference*. Geological Society, London 349-357.
- GREEN, P. F., DUDDY, I. R., LASLETT, G. M., HEGARTY, K. A., GLEADOW, A. J. W., & LOVERING, J. F. (1989) Thermal annealing of fission tracks in apatite IV: Quantitative modeling techniques and extension to geological timescales. *Chemical Geology*. **79**. (2), 155-182.
- GREEN, P. F., HEGARTY, K. A., DUDDY, I. R., FOLAND, S. S., & GORBACHEV, V. (1996) Geological constraints on fission track annealing in zircon. *Proceedings of International Workshop on Fission Track Dating*, Ghent, Belgium, August 1996.

- GREEN, P. F. & HURFORD, A. J. (1984) Thermal-Neutron Dosimetry For Fission-Track Dating. *Nuclear Tracks and Radiation Measurements*. **9**. (3-4), 231-241.
- HAMES, W. E. & BOWRING, S. A. (1994) An empirical evaluation of the argon diffusion geometry in muscovite. *Earth and Planetary Science Letters*. **124**. 161-169.
- HAMILTON, M. A., PEARSON, D. G., THOMPSON, R. N., KELLEY, S. P., & EMELEUS, C. H. (1998) Rapid eruption of Skye lavas inferred from precise U-Pb and Ar- Ar dating of the Rum and Cuillin plutonic complexes. *Nature*. **394**. 260-263.
- HANCHAR, J. M. & HOSKIN, P. W. O. (eds) (2003) (eds) *Zircon*. Reviews in Mineralogy and Geochemistry. Mineralogical Society of America, **53**
- HANCHAR, J. M. & MILLER, C. F. (1993) Zircon zonation patterns as revealed by cathodoluminescence and backscattered electron images: Implications for interpretation of complex crustal histories. *Chemical Geology*. **101**. 1-13.
- HARLOV, D. E. & FORSTER, H. J. (2003) Fluid-induced nucleation of (Y+REE)-phosphate minerals within apatite: Nature and experiment. Part II. Fluorapatite. *American Mineralogist*. **88**. 1209-1229.
- HARLOV, D. E., FÖRSTER, H. J., & NIJLAND, T. G. (2002) Fluid-induced nucleation of (Y+REE)-phosphate minerals within apatite: Nature and experiment. Part I. Chlorapatite. *American Mineralogist*. **87**. 245-261.
- HARRISON, T. M., DUNCAN, I., & MCDUGALL, I. (1985) Diffusion of  $^{40}\text{Ar}$  in biotite: temperature, pressure and compositional effects. *Geochimica et Cosmochimica Acta*. **49**. 2461-2468.
- HASEBE, N., BARBARAND, J., JARVIS, K., CARTER, A., & HURFORD, T. (2002) Can FT ages be derived using LA-ICP-MS? *Geochimica et Cosmochimica Acta*. **66**. (15A), 314.
- HASEBE, N., MORI, S., TAGAMI, T., & MATSUI, R. (2003) Geological partial annealing zone of zircon fission-track system: additional constraints from the deep drilling MITI-Nishikubiki and MITI-Mishima. *Chemical Geology*. **199**. (1-2), 45-52.
- HASEBE, N., TAGAMI, T., & NISHIMURA, S. (1994) Towards Zircon Fission-Track Thermochronology - Reference Framework For Confined Track Length Measurements. *Chemical Geology*. **112**. (1-2), 169-178.
- HILL, R. I. (1991) Starting plumes and continental break-up. *Earth and Planetary Science Letters*. **104**. 398-416.
- HILL, R. I., CAMPBELL, I. H., DAVIES, G. F., & GRIFFITHS, R. W. (1993) Mantle plumes and continental tectonics. *Science*. **256**. 186-193.
- HITCHEN, K., MORTON, A. C., MEARNS, E. W., WHITEHOUE, M., & STOKER, M. S. (1997) Geological implications from geochemical and isotopic studies of Upper Cretaceous and Lower Tertiary igneous rocks around the northern Rockall Trough. *Journal of the Geological Society, London*. **154**. 517-521.
- HOLFORD, S. P., GREEN, P. F., & TURNER, J. P. (2005) Palaeothermal and compaction studies in the Mochras borehole (NW Wales) reveals early Cretaceous and Neogene exhumation and argue against regional Palaeogene uplift in the southern Irish Sea. *Journal of the Geological Society, London*. **162**. 829-840.
- HOLNESS, M. B. (1997) Fluid flow paths and mechanisms of fluid infiltration in carbonates during contact metamorphism: the Beinn an Dubhaich aureole, Skye. *Journal Of Metamorphic Geology*. **15**. (1), 59.

- HOLNESS, M. B. (1999) Contact metamorphism and anatexis of Torridonian arkose by minor intrusions of the Rum Igneous Complex, Inner Hebrides, Scotland. *Geological Magazine*. **136**. (5), 527-542.
- HOLNESS, M. B. & ISHERWOOD. (2003) The aureole of the Rum Tertiary Igneous Complex, Scotland. *Journal of the Geological Society, London*. **160**. 15-27.
- HOSKIN, P. W. O. & IRELAND, T. R. (2000) Rare earth element chemistry of zircon and its use as a provenance indicator. *Geology*. **28**. 627-630.
- HOIRIGAN, J. K., REINERS, P. W., & BRANDON, M. T. (2005) U-Th zonation-dependent alpha-ejection in (U-Th)/He chronometry. *Geochimica et Cosmochimica Acta*. **69**. (13), 3349-3365.
- HOUSE, M. A., FARLEY, K. A., & STOCKLI, D. (2000) Helium chronometry of apatite and titanite using Nd-YAG laser heating. *Earth and Planetary Science Letters*. **183**. (3-4), 365-368.
- HURFORD, A. J. (1985) On the closure temperature for fission tracks in zircon. *Nuclear Tracks and Radiation Measurements*. **10**. (3), 415-415.
- HURFORD, A. J. (1986) Cooling And Uplift Patterns In The Lepontine Alps South Central Switzerland And An Age Of Vertical Movement On The Insubric Fault Line. *Contributions to Mineralogy and Petrology*. **92**. (4), 413-427.
- HURFORD, A. J. & GREEN, P. F. (1981) A reappraisal of neutron dosimetry and  $^{238}\text{U}$  gamma-f values in fission track dating. *Nuclear Tracks and Radiation Measurements*. **5**. (1-2), 53-61.
- HURFORD, A. J. & GREEN, P. F. (1982) A users guide to fission track dating calibration. *Earth and Planetary Science Letters*. **59**. (2), 343-354.
- HURFORD, A. J. & HAMMERSCHMIDT, K. (1985)  $^{40}\text{Ar}/^{39}\text{Ar}$  and K/Ar dating of the Bishop and Fish Canyon Tuffs: Calibration ages for fission-track dating standards. *Chemical Geology*. **58**. 23-32.
- HURLEY, P. M. (1954) The helium age method and the distribution and migration of helium in rocks. in FAUL, H. (ed) *Nuclear Geology*. John Wiley 301-329.
- HURLEY, P. M., LARSEN, E. S. J., & GOTTFRIED, D. (1956) Comparison of radiogenic helium and lead in zircon. *Geochimica et Cosmochimica Acta*. **9**. (98-102).
- IRELAND, T. R. & WILLIAMS, I. S. (2003) Considerations in zircon geochronology by SIMS. in HANCHAR, J. M. & HOSKIN, P. W. O. (eds) *Zircon. Reviews in Mineralogy and Geochemistry*. Mineralogical Society of America **53** 215-241.
- JOLLEY, D. W. (1997) Palaeosurface palynofloras of the Skye lava field and the age of the British Tertiary volcanic province. in WIDDOWSON, M. (ed) *Palaeosurfaces: Recognition, Reconstruction and Palaeoenvironmental Interpretation*. Geological Society, London. Special Publications **120** 67-94.
- JONCKHEERE, R. & GOGEN, K. (2001) A Monte-Carlo calculation of the size distribution of latent alpha-recoil tracks. *Nuclear Instruments & Methods In Physics Research*. **183**. 347-357.
- JONES, S. M., WHITE, N., CLARKE, B. J., ROWLEY, E., & GALLAGHER, K. (2002) Present and past influence of the Iceland plume on sedimentation. in DORE, A. G., CARTWRIGHT, J. A., STOKER, M. S., TURNER, J. P., & WHITE, N. (eds) *Exhumation of the North Atlantic Margin: Timing, mechanisms and implications for petroleum exploration*. Special Publication. Geological Society, London **196** 13-25.
- JUDD, J. W. (1874) On the ancient volcanoes of the Highlands and the relations of their products to the Mesozoic strata. *Journal of the Geological Society, London*. **30**. 220-302.

- JUDD, J. W. (1889) The Tertiary volcanoes of the Western Isles of Scotland. *Journal of the Geological Society, London*. **45**. 187-218.
- KASUYA, M. & NAESER, C. W. (1988) The effect of alpha-damage on fission track annealing in zircon. *Nuclear Tracks and Radiation Measurements*. **14**. (4), 477-480.
- KEMPE, U., GOTZE, J., NASDALA, L., & WOLF, D. (2000) Relevance of cathodoluminescence for the interpretation of U-Pb zircon ages, with an example of an application to a study of zircons from the Saxonian Granulite Complex, Germany. in PAGEL, M., BARBIN, V., BLANC, P., & OHNENSTETTER, D. (eds) *Cathodoluminescence in geosciences*. Springer Verlag 425-456.
- KETCHAM, R. A. (2005) Forward and inverse modeling of low-temperature thermochronometry data. in REINERS, P. W. & EHLERS, T. A. (eds) *Thermochronology*. Reviews in Mineralogy and Geochemistry. Mineralogical Society of America **58** 275-314.
- KETCHAM, R. A., DONELICK, R. A., & CARLSON, W. D. (1999) Variability of apatite fission-track annealing kinetics: III. Extrapolation to geological time scales. *American Mineralogist*. **84**. (9), 1235-1255.
- KETCHAM, R. A., DONELICK, R. A., & DONELICK, M. B. (2000) AFTSolve: A program for multi-kinetic modeling of apatite fission-track data. *Geological Materials Research*. **2**. (1).
- KIRBY, E., REINERS, P. W., KROL, M. A., WHIPPLE, K. X., HODGES, K. V., FARLEY, K. A., TANG, W. Q., & CHEN, Z. L. (2002) Late Cenozoic evolution of the eastern margin of the Tibetan Plateau: Inferences from Ar-40/Ar-39 and (U-Th)/He thermochronology. *Tectonics*. **21**. (1), art. no.-1001.
- KIRSTEIN, L. A. & TIMMERMANN. (2000) Evidence for the proto-Iceland plume in northwestern Ireland at 42 Ma from helium isotopes. *Journal of the Geological Society, London*. **157**. 923-927.
- KLINGELHÖFER, F., EDWARDS, R. A., HOBBS, R. W., & ENGLAND, R. W. (2005) Crustal structure of the NE Rockall Trough from wide-angle seismic data modeling. *Journal of Geophysical Research*. **110**. (B11105).
- LAMPHERE, M. A. & BAADSGAARD, H. (2001) Precise K-Ar, <sup>40</sup>Ar/<sup>39</sup>Ar, Rb-Sr and U/Pb mineral ages from the 27.5 Ma Fish Canyon Tuff reference standard. *Chemical Geology*. **175**. 653-671.
- LARSEN, H. C. & SAUNDERS, A. D. (1988) Tectonism and volcanism at the southeast Greenland rifted margin: a record of plume impact and later continental rupture. in SAUNDERS, A. D., LARSEN, H. C., & WISE, S. W. (eds) *Proceedings of the Ocean Drilling Program, Scientific Results*. 503-534.
- LASLETT, G. M., GREEN, P. F., DUDDY, I. R., & GLEADOW, A. J. W. (1987) Thermal annealing of fission tracks in apatite II: A quantitative analysis. *Chemical Geology*. **65**. (1), 1-13.
- LAWVER, L. A. & MÜLLER, R. D. (1994) Iceland hotspot track. *Geology*. **22**. (4), 311-314.
- LEWIS, C. L. E., CARTER, A., & HURFORD, A. J. (1992) Low-temperature effects of the Skye Tertiary intrusions on Mesozoic sediments in the Sea of Hebrides Basin. in PARNELL, J. (ed) *Basins on the Atlantic Seaboard: Petroleum Geology, Sedimentology and Basin Evolution*. Special Publication. Geological Society, London **62** 175-188.
- LIPPOLT, H. J., LEITZ, M., WERNICKE, R. S., & HAGEDORN, B. (1994) (Uranium + Thorium)/ Helium dating of Apatite: experience with samples from different geochemical environments. *Chemical Geology*. **112**. (1-2), 179-191.
- LORENCAK, M., KOHN, B. P., OSADETZ, K. G., & GLEADOW, A. J. W. (2004) Combined apatite fission track and (U-Th)/He thermochronometry in a slowly cooled terrane: results from a 3440-m-deep drill hole in the southern Canadian Shield. *Earth and Planetary Science Letters*. **227**. (1-2), 87.

- LOVERA, O. M., GROVE, T. L., & HARRISON, T. M. (1997) Systematic analysis of K-feldspar  $^{40}\text{Ar}/^{39}\text{Ar}$  step heating results. I. Significance of activation energy determinations. *Geochimica et Cosmochimica Acta*. **61**. 3171-3192.
- LOVERA, O. M., GROVE, T. L., & HARRISON, T. M. (2002) Systematic analysis of K-feldspar  $^{40}\text{Ar}/^{39}\text{Ar}$  step heating results. II: Relevance of laboratory argon diffusion properties to nature. *Geochimica et Cosmochimica Acta*. **66**. 1237-1255.
- LOVERA, O. M., RICHTER, F. M., & HARRISON, T. M. (1989) The  $^{40}\text{Ar}/^{39}\text{Ar}$  thermochronometry for slowly cooled samples having a distribution of diffusion domain sizes. *Journal of Geophysical Research*. **94**. 17917-17935.
- LUNDIN, E. & DORE, A. G. (2002) Mid-Cenozoic post-breakup deformation in the 'passive' margins bordering the Norwegian-Greenland Sea. *Marine and Petroleum Geology*. **19**. (1), 79-93.
- MAHONEY, J. J. & COFFIN, M. F. (eds) (1997) *Large igneous province: Continental, oceanic and planetary volcanism*. American Geophysical Union Geophysical Monograph. **100**
- MEESTERS, A. G. C. A. & DUNAI, T. J. (2002a) Solving the production-diffusion equation for finite diffusion domains of various shapes - Part I. Implications for low-temperature (U-Th)/He thermochronology. *Chemical Geology*. **186**. (3-4), 333-344.
- MEESTERS, A. G. C. A. & DUNAI, T. J. (2002b) Solving the production-diffusion equation for finite diffusion domains of various shapes - Part II. Application to cases with alpha-ejection and nonhomogeneous distribution of the source. *Chemical Geology*. **186**. (1-2), 57-73.
- MEIGHAN, I., HUTCHISON, R., WILLIAMSON, I., & MACINTYRE, R. M. (1982) Geological evidence for the different relative ages of the Rhum and Skye Tertiary central complexes. *Journal of the Geological Society, London*. **139**. 659-659.
- MELDRUM, A., ZINCLE, S. J., BOATNER, L. A., & EWING, R. C. (1998) Displacement-cascade amorphization and phase decomposition in zircon, hafnon, and thorite. *Nature*. **395**. 56-58.
- MENZIES, M. A., KLEMPERER, S. L., EBINGER, C. J., & BAKER, J. (eds) (2002) *Volcanic Rifted Margins*. Geological Society of America Special Paper, **362**
- MITCHELL, J. G. & REEN, K. P. (1973) Potassium-argon ages from the Tertiary ring complexes of the Ardnamurchan Peninsula, western Scotland. *Geological Magazine*. **110**. (4), 331-340.
- MITCHELL, S. G. & REINERS, P. W. (2003) Influence of wildfires on apatite and zircon (U-Th)/He ages. *Geology*. **31**. (12), 1025-1028.
- MONANI, S. (1999) *An oxygen isotope study of granites from the British Tertiary Igneous Province, Western Scotland*. M.Sc. Thesis.
- MONANI, S. & VALLEY, J. W. (2001) Oxygen isotope ratios of zircon: magma genesis of low delta O-18 granites from the British Tertiary Igneous Province, western Scotland. *Earth and Planetary Science Letters*. **184**. (2), 377-392.
- MOSAR, J., LEWIS, G., & TORSVIK, T. H. (2002) North Atlantic sea-floor spreading rates: implications for the Tertiary development of inversion structures of the Norwegian-Greenland Sea. *Journal of the Geological Society, London*. **159**. 503-515.
- MOSER, J. & TORSVIK, T. H. (2002) Opening the Norwegian and Greenland Seas: Plate tectonics in Mid Norway since the Late Permian. In EIDE, E. A. (ed) *BATLAS - Mid Norway plate reconstructions atlas with global and Atlantic*. Geological Survey of Norway 48-59.
- MURAKAMI, T., CHAKOUMAKOS, B. C., EWING, R. C., LUMPKIN, G. R., & WEBBER, W. (1991) Alpha-decay event in zircon. *American Mineralogist*. **76**. (9-10), 1510-1533.

- MURRELL, G. R. (2003) *The long-term thermal evolution of central Fennoscandia, revealed by low-temperature thermochronometry*. Vrije Universiteit Amsterdam. Ph.D. Thesis.
- MUSSETT, A. E., DAGLEY, P., & SKELHORN, R. R. (1988) Time and duration of activity in the British Tertiary Igneous Province. in MORTON, A. C. & PARSON, L. M. (eds) *Early Tertiary volcanism and the opening of the North Atlantic*. Geological Society of London, Special Publication 39 337-348.
- NAESER, C. W. & FAUL, H. (1969) Fission track annealing in apatite and sphene. *Journal of Geophysical Research*. 74. (2), 705-710.
- NASDALA, L., HANCHAR, J. M., KRONZ, A., & WHITEHOUSE, M. J. (2005) Long-term stability of alpha particle damage in natural zircon. *Chemical Geology*. 220. (1-2), 83-103.
- NASDALA, L., REINERS, P. W., GARVER, J. I., KENNEDY, A. K., STERN, R. A., BALAN, E., & WIRTH, R. (2004) Incomplete retention of radiation damage in zircon from Sri Lanka. *American Mineralogist*. 89. (1), 219-231.
- NASDALA, L., WENZEL, M., VAVRA, G., IRMER, G., WENZEL, T., & KOBER, B. (2001) Metamictization of natural zircon; accumulation vs. thermal annealing of radioactivity-induced damage. *Contributions to Mineralogy and Petrology*. 141. 125-144.
- NASDALA, L., ZHANG, M., KEMPE, U., PANCZER, G., GAFT, M., ANDRUT, M., & POLOTZE, M. (2003) Spectroscopic methods applied to zircon. in HANCHAR, J. M. & HOSKIN, P. W. O. (eds) *Zircon*. Reviews in Mineralogy and Geochemistry. Mineralogical Society of America 53 427-467.
- O'CONNOR, J. M., STOFFERS, P., WIJBRANS, J. R., SHANNON, P. M., & MORRISSEY, T. (2000) Evidence from episodic seamount volcanism for pulsing of the Iceland plume in the past 70 Myr. *Nature*. 408. (6815), 954-958.
- O'SULLIVAN, P. B. & PARRISH, R. R. (1995) The importance of apatite composition and single-grain ages when interpreting fission track data from plutonic rocks: a case study from the Coast Ranges, British Columbia. *Earth and Planetary Science Letters*. 132. (1-4), 213-224.
- PALENIK, C. S., NASDALA, L., & EWING, R. C. (2003) Radiation damage in zircon. *American Mineralogist*. 88. 770-781.
- PARRISH, R. R. & KROUGH, T. E. (1987) Synthesis and purification of  $^{205}\text{Pb}$  for U-Pb geochronology. *Chemical Geology*. 66. 103-110.
- PARRISH, R. R., RODDICK, J. C., LOVERIDGE, W. D., & SULLIVAN, R. W. (1987) Uranium-lead analytical techniques at the geochronology laboratory, Geological Survey of Canada. in *Radiogenic Age and Isotopic studies*. Geological Survey of Canada Report. Paper 87-2 3-7.
- PEARSON, D. G., EMELEUS, C. H., & KELLEY, S. P. (1996) Precise  $^{40}\text{Ar}/^{39}\text{Ar}$  age for the initiation of Palaeogene volcanism in the Inner Hebrides and its regional significance. *Journal of the Geological Society, London*. 153. 815-818.
- PERSANO, C., BARFOD, D. N., STUART, F. M., & BISHOP, P. (submitted) Tertiary denudation of Scotland during impact of the Proto-Iceland plume from low temperature thermochronometry. *Earth and Planetary Science Letters*.
- PERSANO, C., BISHOP, P., & BARFOD, D. N. (2002) Apatite (U-Th)/He age constraints on the development of the Great Escarpment on the southeastern Australian passive margin. *Earth and Planetary Science Letters*. 200. (1-2), 79-90.
- POLLER, U., HUTH, J., HOPPE, P., & WILLIAMS, I. S. (2001) REE, U, Th, and Hf distribution in zircon from western Carpathian variscan granitoids: a combined Cathodoluminescence and ion microprobe study. *American Journal of Science*. 301. 858-876.

- PRESTON, R. J. (1982) Igneous Rocks of the British Isles. in SUTHERLAND, D. S. (ed) *Eruptive Volcanism*. John Wiley & Sons 351-368.
- RAHL, R. M., REINERS, P. W., CAMPBELL, I. H., NICOLESCU, S., & ALLEN, C. M. (2003) Combined single-grain (U-Th)/He and U/Pb dating of detrital zircons from the Navajo Sandstone, Utah. *Geology*. **31**. (9), 761-764.
- RAHN, M. K., BRANDON, M. T., BATT, G. E., & GARVER, J. I. (2004) A zero-damage model for fission-track annealing in zircon. *American Mineralogist*. **89**. (4), 473-484.
- REINERS, P. W. (2005) Zircon (U-Th)/He thermochronometry. in REINERS, P. W. & EHLERS, T. A. (eds) *Thermochronology*. Reviews in Mineralogy and Geochemistry. Mineralogical Society of America **58** 151-179.
- REINERS, P. W., CAMPBELL, I. H., NICOLESCU, S., ALLEN, C. M., HOURIGAN, J. K., GARVER, J. I., MATTINSON, J. M., & COWAN, D. S. (2005) (U-Th)/(He-Pb) double dating of detrital zircons. *American Journal of Science*. **305**. (4), 259-311.
- REINERS, P. W. & EHLERS, T. A. (eds) (2005) *Thermochronology*. Reviews in Mineralogy and Geochemistry. Mineralogical Society of America, **58**
- REINERS, P. W. & FARLEY, K. A. (1999) Helium diffusion and (U-Th)/He thermochronometry of titanite. *Geochimica et Cosmochimica Acta*. **63**. (22), 3845-3859.
- REINERS, P. W. & FARLEY, K. A. (2001) Influence of crystal size on apatite (U-Th)/He thermochronology: an example from the Bighorn Mountains, Wyoming. *Earth and Planetary Science Letters*. **188**. (3-4), 413-420.
- REINERS, P. W., FARLEY, K. A., & HICKES, H. J. (2002) He diffusion and (U-Th)/He thermochronometry of zircon: initial results from Fish Canyon Tuff and Gold Butte. *Tectonophysics*. **349**. (1-4), 297-308.
- REINERS, P. W. & SPELL, T. L. (2002) Intercalibration of zircon (U-Th)/He and K-feldspar  $^{40}\text{Ar}/^{39}\text{Ar}$  thermochronometry. *Geochimica et Cosmochimica Acta*. **66**. (15A), 631.
- REINERS, P. W., SPELL, T. L., NICOLESCU, S., & ZANETTI, K. A. (2004) Zircon (U-Th)/He thermochronometry: He diffusion and comparisons with  $^{40}\text{Ar}/^{39}\text{Ar}$  dating. *Geochimica et Cosmochimica Acta*. **68**. (8), 1857-1887.
- REMOND, G., BLANC, P., CESBRON, F., OHNENSTETTER, D., & ROUER, O. (1995) Cathodoluminescence of rare earth doped zircons. II. Relationship between the distribution of the doping elements and the contrasts of images. *Scanning Microscopy Supplemental*. (9), 57-76.
- RENNE, P. R., DEINO, A. L., WALTER, R. C., TURRIN, B. D., SWISHER, C. C., BECKER, T. A., CURTIS, G. H., SHARP, W. D., & JAOUNI, A. R. (1994) Intercalibration of astronomical and radioisotopic time. *Geology*. **22**. 783-786.
- RICHEY. (1961) *The Tertiary volcanic districts of Scotland*. British Geological Survey.
- RITCHIE & HITCHEN. (1996) Early paleogene offshore igneous activity to the northwest of the UK and its relationship to the NAIP. in KNOX, CORFIELD, & DUNAY (eds) *Correlation of the early Paleogene in Northwest Europe*. Special Publication. Geological Society, London **101** 63-78.
- RUTHERFORD, E. (1905) Present problem in radioactivity. *Popular Science Monthly*. **May**. 1-34.
- SAUNDERS, A. D., FITTON, J. G., KERR, A. C., NORRY, M. J., & KENT, R. W. (1997) The North Atlantic Igneous Province. in MAHONEY, J. J. & COFFIN, M. F. (eds) *Large Igneous Provinces: Continental, Oceanic, and Planetary Flood Volcanism*. American Geophysical Union **100** 45-93.

- SCHMITZ, M. D. & BOWRING, S. A. (2001) U-Pb zircon and titanite systematics of the Fish Canyon Tuff: an assessment of high-precision U-Pb geochronology and its application to young volcanic rocks. *Geochimica et Cosmochimica Acta*. **65**. (15), 2571-2587.
- SHUSTER, D. L., FLOWERS, R. M., & FARLEY, K. A. (2006) The influence of natural radiation damage on helium diffusion kinetics in apatite. *Earth and Planetary Science Letters*. **249**. (3-4), 148-161.
- SMITH, N. J. (1985) The age and structural setting of limestones and basalts on the Main Ring Fault in SE Rhum. *Geological Magazine*. **122**. (5), 439-445.
- STOREY, M., PEDERSEN, A. K., STECHER, O., BERNSTEIN, S., LARSEN, H. C., LARSEN, L. M., BAKER, J. A., & DUNCAN, R. A. (2004) Long-lived postbreakup magmatism along the East Greenland margin: Evidence for shallow-mantle metasomatism by the Iceland plume. *Geology*. **32**. (2), 173-176.
- STRUTT, R. J. (1905) On the radioactive minerals. *Proceedings of the Royal Society of London*. **A76**. 88-101.
- STRUTT, R. J. (1910a) The accumulation of helium in geologic time III. *Proceedings of the Royal Society of London*. **83**. 398-301.
- STRUTT, R. J. (1910b) The accumulation of helium in geologic time: II. *Proceedings of the Royal Society of London*. **83**. 96-99.
- STRUTT, R. J. (1910c) Measurements of the rate at which helium is produced in thoranite and pitchblende, with a minimum estimate of their antiquity. *Proceedings of the Royal Society of London*. **83**. 386-388.
- TAGAMI, T. (1990) Thermal annealing characteristics of spontaneous fission tracks in zircon. *Chemical Geology*. **80**. 159-169.
- TAGAMI, T. (2005) Zircon fission-track thermochronology and applications to fault studies. in REINERS, P. W. & EHLERS, T. A. (eds) *Thermochronology*. Reviews in Mineralogy and Geochemistry. Volume 58. Mineralogical Society of America **58** 95-122.
- TAGAMI, T., CARTER, A., & HURFORD, A. J. (1996) Natural long-term annealing of the zircon fission-track system in Vienna Basin deep borehole samples: Constraints upon the partial annealing zone and closure temperature. *Chemical Geology*. **130**. (1-2), 147-157.
- TAGAMI, T., FARLEY, K. A., & STOCKLI, D. F. (2003) (U-Th)/He geochronology of single zircon grains of known Tertiary eruption age. *Earth and Planetary Science Letters*. **207**. (1-4), 57-67.
- TAGAMI, T., GALBRAITH, R. F., YAMADA, K., & LASLETT, G. M. (1998) Revised annealing kinetics of fission tracks in zircon and geological implications. in VAN DEN HAUTE, P. & DE CORTE, F. (eds) *Advances in fission-track geochronology*. Solid earth sciences library. Kluwer, Dordrecht, The Netherlands. **10**.
- TAGAMI, T. & O'SULLIVAN, P. B. (2005) Fundamentals of fission-track thermochronology. in REINERS, P. W. & EHLERS, T. A. (eds) *Thermochronology*. Reviews in Mineralogy and Geochemistry. Mineralogical Society of America **58** 19-47.
- TAGAMI, T. & SHIMADA, C. (1996) Natural long-term annealing of the zircon fission track system around a granitic pluton. *Journal of Geophysical Research*. **101**. (B4), 8245-8255.
- TAYLOR, R. N. & FORSTER, H. J. (1977)  $^{18}\text{O}/^{16}\text{O}$ , D/H and  $^{13}\text{C}/^{12}\text{C}$  studies of the Tertiary igneous complex of Skye, Scotland. *American Journal of Science*. **277**. (136-177).
- TEGNER, C., DUNCAN, R. A., BERNSTEIN, S., BROOKS, C. K., BIRD, D. K., & STOREY, M. (1998)  $^{40}\text{Ar}$ - $^{39}\text{Ar}$  geochronology of Tertiary mafic intrusions along the East Greenland rifted margin: Relation to flood basalts and the Iceland hotspot track. *Earth and Planetary Science Letters*. **156**. (1-2), 75-88.

- THOMPSON, R. N. (1969) Tertiary granites and associated rocks of the Marsco area, Isle of Skye. *Journal of the Geological Society, London*. **124**. 349-385.
- THOMPSON, R. N. (1974) Primary basalts and magma genesis, I: Skye, Northwest Scotland. *Contributions to Mineralogy and Petrology*. **45**. 317-341.
- THOMPSON, R. N. & GIBSON, S. A. (1991) Subcontinental mantle plumes, hotspots and pre-existing thinspots. *Journal of the Geological Society, London*. **148**. 973-978.
- THRASHER, J. (1992) Thermal effect of the Tertiary Cuillins Intrusive Complex in the Jurassic of the Hebrides: an organic geochemical study. in PARNELL, J. (ed) *Basins on the Atlantic Seaboard: Petroleum Geology, Sedimentology and Basin Evolution*. Special Publication of the Geological Society, London **62** 35-49.
- TILEY, R., WHITE, N. J., & AL-KINDI, S. (2004) Linking Pleistocene denudation and magmatic underplating beneath the British Isles. *Geological Magazine*. **141**. (3), 345-351.
- TORSVIK, T. H., VAB DER VOO, R., MEERT, J. G., MOSAR, J., & WALDERHAUG, H. J. (2001) Reconstruction of the continents around the North Atlantic at about the 60th parallel. *Earth and Planetary Science Letters*. **187**. 55-69.
- TROLL, V. R., EMELEUS, C. H., & DONALDSON, C. H. (2000) Caldera formation in the Rum Central Igneous Complex, Scotland. *Bulletin of Volcanology*. **62**. 301-317.
- VALLEY, J. W. & GRAHAM, C. M. (1996) Ion microprobe analysis of oxygen isotope ratios in quartz from Skye granite: Healed micro-cracks, fluid flow, and hydrothermal exchange. *Contributions to Mineralogy and Petrology*. **124**. (3-4), 225-234.
- WAGNER, G. A. (1968) Fission track dating of apatites. *Earth and Planetary Science Letters*. **4**. 411-415.
- WAGNER, G. A. (1981) Fission-Track Ages and Their Geological Interpretation. *Nuclear Tracks and Radiation Measurements*. **5**. (1-2), 15-25.
- WAGNER, G. A. & VAN DER HAUTE. (1992) *Fission track dating*. Kluwer Acad.
- WALKER, G. W. P. (1971) The distribution of amygdale minerals in Mull and Morvern (Western Scotland). in MURTY, T. V. V. G. R. K. & RAO, S. S. (eds) *Studies in Earth Sciences, a volume in honour of William Dixon West*. New Delhi: Today and Tomorrow's Printers and Publishers 181-194.
- WARNOCK, A. C., ZEITLER, P. K., WOLF, R. A., & BERGMAN, S. C. (1997) An evaluation of low-temperature apatite U-Th/He thermochronometry. *Geochimica et Cosmochimica Acta*. **61**. (24), pp5371-5377.
- WATT, G. R., GRIFFIN, B. J., & KINNY, P. D. (2000) Charge contrast imaging of geological materials in the environmental scanning electron microscope. *American Mineralogist*. **85**. 1784-1974.
- WEBER, W. J., EWING, R. C., & MELDRUM, A. (1997) The kinetics of alpha-decay-induced amorphization in zircon and apatite containing weapons-grade plutonium or other actinides. *Journal Of Nuclear Materials*. **250**. (2-3), 147-155.
- WENDT, A. S., VIDAL, O., & CHADDERTON, L. T. (2002) Experimental evidence for the pressure dependence of fission track annealing in apatite. *Earth and Planetary Science Letters*. **201**. (3-4), 593-607.
- WHITE, N. & LOVELL, B. (1997) Measuring the pulse of a plume within the sedimentary record. *Nature*. **387**. (6636), 888-891.

- WHITE, R. S. & MORTON, A. C. (1995) The Iceland Plume and Its Influence on the Evolution of the Ne Atlantic. *Journal of the Geological Society, London*. **152**. 933-933.
- WILLIAMSON, I. T. & BELL, B. R. (1994) The Paleocene Lava-Field of West-Central Skye, Scotland - Stratigraphy, Paleogeography and Structure. *Transactions of the Royal Society of Edinburgh*. **85**. 39-75.
- WILLIAMSON, I. T., BELL, B. R., & JOLLEY, D. (in prep) Graben-emplaced volcanism, sedimentation and landscape evolution: The early development of the Palaeogene Mull lava field, NW Scotland. *Transactions of the Royal Society of Edinburgh*.
- WOHLETZ, K., CIVETTA, L., & ORSI, G. (1999) Thermal evolution of the Phlegraean magmatic system. *Journal of Volcanology and Geothermal Research*. **91**. 381-414.
- WOHLETZ, K. & HEIKEN, G. (1992) *Volcanology and Geothermal Energy*. University of California Press, Berkeley.
- WOLF, R. A., FARLEY, K. A., & KASS, D. M. (1998) Modeling of the temperature sensitivity of the apatite (U-Th)/He thermochronometer. *Chemical Geology*. **148**. (1-2), 105-114.
- WOLF, R. A., FARLEY, K. A., & SILVER, L. T. (1996) Helium diffusion and low-temperature thermochronometry of apatite. *Geochimica et Cosmochimica Acta*. **60**. (21), 4231-4240.
- YAMADA, R., TAGAMI, T., & NISHIMURA, S. (1993) Assessment of overetching factor for confined fission track length measurement in zircon. *Chemical Geology*. **104**. (1-4), 251-259.
- YAMADA, R., TAGAMI, T., & NISHIMURA, S. (1995a) Confined fission track length measurement of zircon - assessment of factors affecting the paleotemperature estimate. *Chemical Geology*. **119**. (1-4), 293-306.
- YAMADA, R., TAGAMI, T., NISHIMURA, S., & ITO, H. (1995b) Annealing kinetics of fission tracks in zircon - an experimental study. *Chemical Geology*. **122**. (1-4), 249-258.
- YOUNG, D. A., MYERS, A., MUNSON, E., & CONKLIN, N. (1969) Mineralogy and geochemistry of fluorapatite from Cerro de Mercado, Durango, Mexico. U.S. Geological Survey, Professional Paper 650D. D84-D93.
- ZAUN, P. & WAGNER, G. A. (1985) The Potential Of Zircon Fission-Track Studies For Deep-Drilling Projects - Results From Borehole Urach-iii. *Naturwissenschaften*. **72**. (3), 143-144.
- ZEIGLER, J. F. (1977) *Helium: Stopping powers and ranges in all elemental matter*. Pergamon.
- ZEITLER, P. K., HERCZEG, A. L., MCDUGALL, I., & HONDA, M. (1987) U-Th-He dating of apatite: A potential thermochronometer. *Geochimica et Cosmochimica Acta*. **51**. 2865-2868.

